The Effect of Modified AuNPs on the Morphology and Nanostructure Orientation of PPMA-*b*-PMMA Block Copolymer Thin Films

DISSERTATION

zur Erlangung des akademischen Grades

Doktor rerum naturalium
(Dr. rer. nat.)

vorgelegt

der Fakultät Mathematik und Naturwissenschaften
der Technischen Universität Dresden

von
Guping He 何谷平

geboren am 20 Juni 1984 in Guangxi, China

Eingereicht am: 24/07/2014
Tag der Verteidigung: 06/10/2014

Die Dissertation wurde in der Zeit von Februar 2011 bis Juni 2014 im Leibniz-Institut für Polymerforschung Dresden e.V. angefertigt

Acknowledgement

I want to express my “great thanks” to Prof. Brigitte Voit for giving me the opportunity to study as PhD student at TUD and in IPF as well as I am deeply grateful for her guidance on my scientific research.

I own my “big and many thanks” to Dr. Doris Pospiech for her very patient and professional guidance and advice on my study and research. I highly appreciate her encouragement on my academic research as well as daily life.

High appreciation is expressed to Dr. Hartmut Komber for his deeply professional analysis of NMR, which is critical for this PhD work.

Special thanks go to Dr. Dieter Jehnichen for his great help on the measurements of T-SAXS and GISAXS and professional explanation of the analysis data.

A delivery of “many thanks” goes to Mr. Andreas Janke for his great help and instruction on AFM measurements.

I want to express my “great thanks” to Dr. Petr Formanek and Mrs. Uta Reuter for their delicate TEM analysis.

“Many thanks” is delivered to Mrs. Petra Treppe for GPC measurements, Mrs. Christina Harnisch for GC-MS measurements, Mrs. Liane Häußler for TGA measurements,

I want to highly thank Mrs. Kathrin Eckstein for her guidance in living anionic polymerization when I start my PhD work here.

I want to say “many thanks” to Dr. Oliver Fischer and Mrs. Romy Selinger for their big help on setting up the anionic polymerization equipment also for the later great help in the lab. And I want to thank all members in P2, Mr. Tim Erdmann, Mr. Berndt Andreas and Mrs. Sandra Starke for their kind help.

Many thanks to the other colleagues in IPF: Mrs. Carmen Krause, Dr. Andriy Horechyy, Mr. Lazaros Tzounis, Dr. Peter Friedel, Mr. Andreas Korwitz, Dr. Klaus-Jochen Eichhorn, Dr. Dietmar Appelhans. And thanks to my Chinese friends in IPF.

The financial support by IPF is gratefully acknowledgement.

Finally, great and special thanks to my families, my dear mother and father, my dear two brothers for their support and love and patience. Very special thanks to my grandma for her care and company and love for the past 30 years. And thank you, my lovely niece, Mengxi, I am so happy and lucky to be with you.

Content

1 Introduction and aim of this work

Block copolymer/inorganic nanoparticle hybrids draw great attention of scientists due to their potential applications in diverse fields such as microelectronics, sensors, solar cells[1,2,3,4,5]. Due to the self-assembly of block copolymers (BCPs), well-defined nanostructures of spherical, cylindrical, lamellar and gyroidal morphology can be obtained in bulk as well as in thin films. The size and shape parameters are adjustable depending on the molecular weight, segmental interaction parameter and block volume ratio[6]. Inorganic nanoparticles (NPs) can be expected to be incorporated into block copolymers with order and selectivity by self-assembly of NPs and/or by synergistic self-assembly between NPs and block copolymers. The morphology and nanostructure order of block copolymers can be also adjusted and directed by incorporation of NPs. Some examples are illustrated in **Figure 1-1**, which shows that CdSe nanoparticle directed the cylindrical domains of PSt-*b*-P2VP normal to the substrate. The ordered arrangement and selective location of NPs in highly ordered and oriented nanostructures of block copolymers are still challenging issues to get for instance, controlled and optimized electrical, photonic and magnetic properties for functional materials.

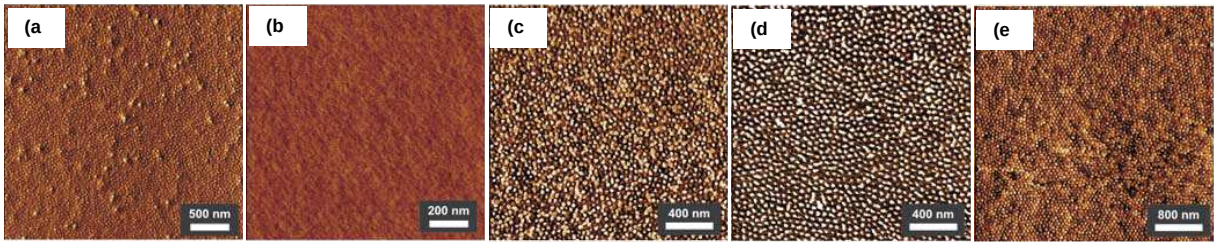

Figure 1-1. Scanning force microscopy (SFM) phase images of thin films. Pure polystyrene-*b*-poly(2-vinyl pyridine) (PSt-*b*-P2VP) (a) after spin-coating, (b) after thermal annealing at 170 ℃ for 2 days; PSt-b-P2VP/CdSe nanoparticle composites of (c) as-spun film, (d) after thermal annealing at 170 ℃ for 2 days, (e) after annealing in saturated chloroform solvent vapour for 1 day. (Taken from ref. 5)

Block copolymers with precisely controlled molecular weight and segmental ratio are always the pursued target of synthetic scientists to get delicate nanostructures. Living anionic polymerization (LAP) is superior in synthesis of well-defined and desired block copolymers to the other controlled polymerization methods such as ATRP, RAFT and NMP. The low dispersity (Đ) of block copolymers by LAP, usually < 1.10, ensures self-assembled nanostructures with uniformed size, which is critical in the application of nanotechnology[7]. Besides the low dispersity, high molecular weight (> 1,000,000 g/mol) and predetermined block ratio, end-functionality is available by end-capping anionic polymer chains with

electrophiles so as to get telechelic polymers[8,9].

Noble metal, gold nanoparticles (AuNPs) attract great interests due to their superior character in surface plasmon resonance, catalysis, and bio-compatibility and thus in diverse applications such as surface enhanced Raman scattering (SERS), chemical sensor, effective catalyst, solar cells, imaging and diagnosis[10,11]. To incorporate inorganic NPs into BCPs in ordered manner, modification of NPs with organic species and also with polymeric species is necessary. AuNPs stabilized by thiol-terminated polymers chemically similar or equal to one component of BCPs have preferential interaction with the specific domains and ordered NP arrays can be expected[12,13,14,15,16].

The preparation of gold colloids owns a long history tracing back to over 2000 years ago for decoration and cure. A simple way to prepare monolayer-protected AuNPs by reducing tetrachloroauric acid ($HAuCl_4$) with sodium borohydride ($NaBH_4$) in the presence of alkylthiol, was discovered in 1994 by Brust and Schiffrin[17]. The modification and functionalization of AuNPs by organic species is thus easily to achieve under mild conditions. However, some points are still not clear or not yet investigated systematically, for instance, how high molecular weight thiols behave in stabilizing AuNPs, and how other species which can coordinate with Au^{3+}, like pyridine derivatives, function in stabilizing AuNPs. These points are studied in this work.

The microphase separation behavior of block copolymers in thin films received extensive study in last decades and this is facilitated by using advanced characterizing technologies, such as transmission electron microscopy (TEM)[18], atomic force microscopy (AFM)[5,19], grazing-incidence small-angle X-ray scattering experiments (GISAXS)[20,21]. The self-assembly of BCP in thin films, usually on Si substrate by spin- or dip-coating, not only depends on the chain parameters including molecular weight, block ratio and segmental interaction as in bulk state, but also relates to the thin film parameters, like film thickness, substrate modification and external fields[22,23].

The challenging task is to get nanostructured thin films with uniformed and highly ordered microdomains. From the application view, thin films with nanostructures perpendicular to substrate and film surface is especially attractive due to the high aspect ratio of nanostructure either as template or as delivery channels. Solvent annealing was found to be effective in preparation near-perfect ordered nanostructures by imparting mobility of polymer chains[24]. Standing microdomains can be achieved by employing solvent annealing where the solvent tunes the segment/air surface interaction. This is similar to the substrate modification by grafting a polymer layer so that non-preferential substrate interaction facilitates perpendicular orientation of microdomains.

Incorporation of inorganic NPs is another way to direct the nanostructure orientation by mediating the segment/NPs and NPs/substrate interaction. Besides, adding NPs can overcome the film thickness limit to get standing nano-cylinders in several hundreds nanometers length[5]. There are theoretical simulations about the NP size and selectivity on the effect of thin film morphology and orientation[25,26,27]. However, only a few research groups studied experimentally the NP size and modification effect on BCP thin films[5,18,28]. **Figure 1-2** shows the controlled orientation of PSt-*b*-PMMA thin films by introducing Au-PEO nanoparticles. In this work, we systematically investigated how the size and modification of AuNP affect the morphology and nanostructure orientation of block copolymer PPMA-*b*-PMMA thin films. The results can serve as a general guide for the other BCP/inorganic NP hybrid systems.

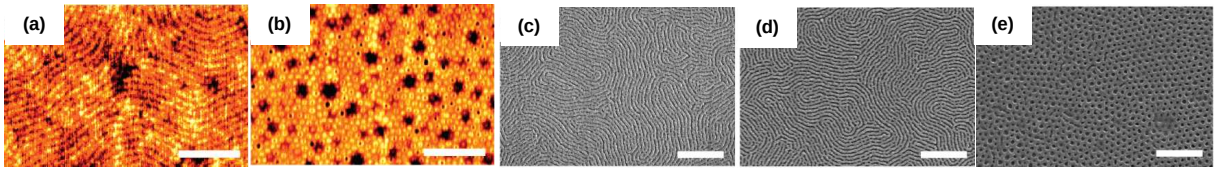

Figure 1-2. SFM height images of polystyrene-*block*-poly(methyl methacrylate) (PSt-*b*-PMMA) thin films containing Au-PEO particles of (a) 0 and (b) 4.5 v% after solvent annealing and rapid solvent evaporation under high humidity conditions (90%). SEM images of PSt-*b*-PMMA thin films containing Au-PEO particles of (c) 0, (d) 0.6, (e) 4.5 % after solvent annealing and rapid solvent evaporation under high humidity conditions (90 %), followed by UV irradiation and then rinsing with acetic acid and water to remove the PMMA microdomains. Scale bar is 500 nm. (Taken from ref. 18)

To achieve these goals mentioned above, experimental work carried out in this study included the following aspects. Block copolymers poly(pentyl methacrylate)-*b*-poly(methyl methacrylate) (PPMA-*b*-PMMA) were synthesized by living anionic polymerization to get high molecular weight and narrow dispersity aiming at nanostructures in uniform size by phase separation in bulk as well as in thin films.

Poly(4-vinyl pyridine)-based block copolymers including P4VP-*b*-PMMA and –PPMA were synthesized by living anionic polymerization in order to get short P4VP-block (degree of polymerization n < 10) as well as long P4VP-block. The P4VP-based BCPs were used to stabilize AuNPs by 4VP/Au^{3+} interaction.

As thiol-based species are strong ligands for stabilizing Au nanomaterials, thiol-terminated PMMA and PPMA with controlled molecular weight were synthesized by reversible addition-fragmentation chain transfer (RAFT) polymerization followed by aminolysis with hexylamine.

The as-synthesized block copolymers and end-functionalized polymers were characterized by ^{1}H- and ^{13}C NMR and GPC (chapter 3).

AuNPs stabilized by different species, including low molecular weight thiol, the synthesized

thiol-terminated polymers, and P4VP-based block polymers were prepared either by two-phase (Brust-Schiffrin method) or one-phase procedure (chapter 4). These AuNPs with controlled size were prepared aiming to investigate the effect of nanoparticle size and stabilizing species on the morphology and nanostructure orientation of PPMA-*b*-PMMA block copolymer thin films.

Finally, PPMA-*b*-PMMA/AuNP hybrid thin films were prepared and studied (chapter 5). The morphology evolution and nanostructure orientation of the hybrid thin films were investigated by T-SAXS, GISAXS, AFM, SEM and TEM. Besides, the conductivity behavior of BCP/AuNP hybrid thin films was analyzed (chapter 5.7).

All topics discussed in this work focused on the investigation how the nanostructures of block copolymer/gold nanoparticle hybrids could be understood and improved. These results are summarized in chapter 6.

2 Theoretical background

2.1 Block copolymers by living anionic polymerization (LAP)

2.1.1 Discovery of living anionic polymerization

In the early 19th century Ziegler and Schlenk first developed the concept of anionic polymerization[29]. They found that dienes became viscous in the presence of alkali metals. The mechanism of anionic polymerization of styrene was clearly demonstrated by Michael Szwarc in 1956[30,31]. Sodium naphthalenide was used to initiate the polymerization of styrene in THF and the color changed from green to red immediately, indicating formation of styryl anions. The red color was insistent until the monomers depleted. The polymerization was initiated by electron transfer from sodium naphthalenide radical to styrene to form the styryl radical anion which dimerized into a dianion and the dianion reinitiated the styrene and propagated until all monomers were consumed **(Scheme 2-1)**. A second portion of styrene was added and polymerization was reinitiated by the intact styryl anions, which was confirmed by the increased relative viscosity compared to the first solution. Such polymerization behavior was characterized by Szwarc as “living polymerization” and the polymers were called as “living polymers”[3]. The term “living” here refers to that the chain-ends of the polymers can maintain the reactivity for a sufficient time and propagate without termination and transfer reactions. The first report of living anionic polymerization of styrene in THF at low temperature, free from termination and transfer reactions, marked the beginning of lively research activities in this field[1].

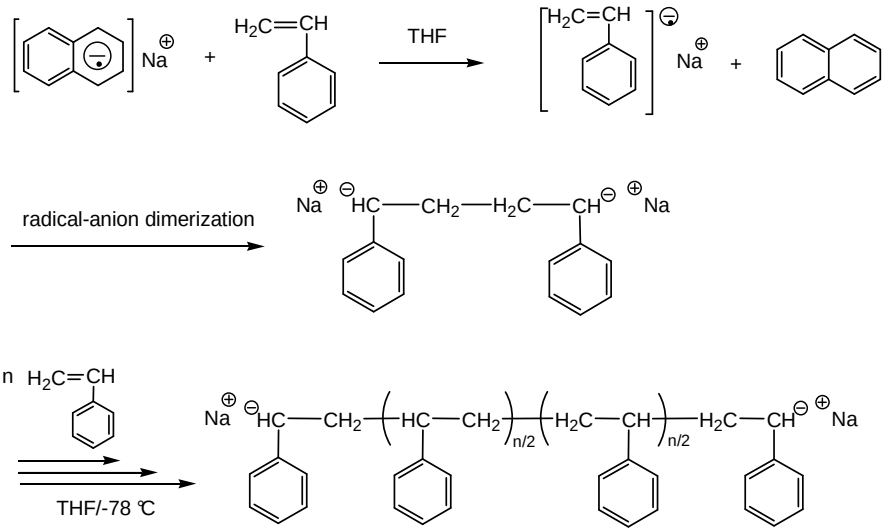

Scheme 2-1. Anionic polymerization of styrene using sodium naphthalenide as initiator in THF[29].

2.1.2 Initiation and propagation of anionic polymerization

Besides naphthalenide, other aromatic compounds, such as diphenylethene (DPE), α-methylstyrene, anthracene, biphenyl and pyrene[2,32], were used as initiators in anionic polymerization with the similar mechanism that interact with alkali metals in polar solvents to form radical anions. Another series of compounds, alkyllithium, have been studied extensively and found to be effective as initiator in anionic polymerization of vinyl monomers[33,34]. Their commercial availability makes them most often used.

Alkyllithiums exist in different aggregated forms depending on the polarity of the used solvent[1]. The degree of intermolecular aggregation affects the efficiency of initiation[35]. The highly aggregated ones, like *n*-butyllithium (*n*-BuLi), may have a considerable unreacted part even when all the monomers are consumed. The less aggregated *sec*-butyllithium (*s*-BuLi) owns fast initiation and nearly ~100 % consumption of *s*-BuLi at ~1 % monomer conversion. Since alkyllithiums are highly reactive and unstable in polar solvent, it is necessary to perform the initiation at low temperature, such as at -78 ℃.

For alkyl(meth)acrylates, alkyllithium is too reactive. Thus, it has to be conjugated with ligands, such as 1,1-diphenylhexyl[36], triphenylmethyl anions[37], fluorenyl anions[38,39], to attenuate the nucleophilicity of the carboanion so as to prevent the attack of the ester carbonyl group.

The ion-pairs are known to exist in different forms in polar solvent, aggregated ion pairs, contact ion pairs, solvent-separated ion pairs and free ions, which are in equilibrium with each other as proposed by Fuoss[40] and Winstein[41] (**Scheme 2-2**). The equilibrium shifts to the formation of free ions at low concentration and in highly solvating media. Free ions, even in a small quantity, can accelerate the propagation tremendously[42,43]. Another form of ion pair, “triple ion“, was supposed to exist at higher concentration of ion-pairs based on the behaviour of high equilibrium conductance[44].

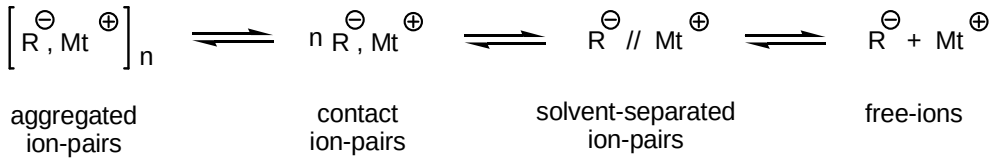

Scheme 2-2. Fuoss-Winstein spectrum of ion pairs in polar solvents[40,41].

The co-existence of free ions, solvent-separated ion pairs, contact ion pairs, aggregated ion pairs and triple ions plays an important role in anionic polymerization in polar solvents. The apparent propagation rate constant of styrene with sodium counterion depended strongly on the dielectric constant of the polar solvent, decreasing from dimethoxyethane (DME) over THF and tetrahydropyran (THP) to dioxane[45,46,47]. Such behavior was attributed to the

equilibrium between free ions and ion-pairs because the propagation rate constant for free anions is much higher than that for the ion-pairs.

From the kinetics study of the propagation of polystyrylsodium in various solvents and a wide range of temperature, Arrhenius plots of the ion pair propagation rate constant ($k_{\pm}$) for various solvents, showed “S-shaped” curves as seen in **Figure 2-1**[48], which suggested that there was another temperature-dependent equilibrium between the contact ion pairs and solvent-separated ion-pairs[49]. As the polarity of the solvent increases with decreasing temperature, the solvent-separated ion pairs with higher reactivity are favored, leading to an increasing overall propagation rate constant at lower temperature.

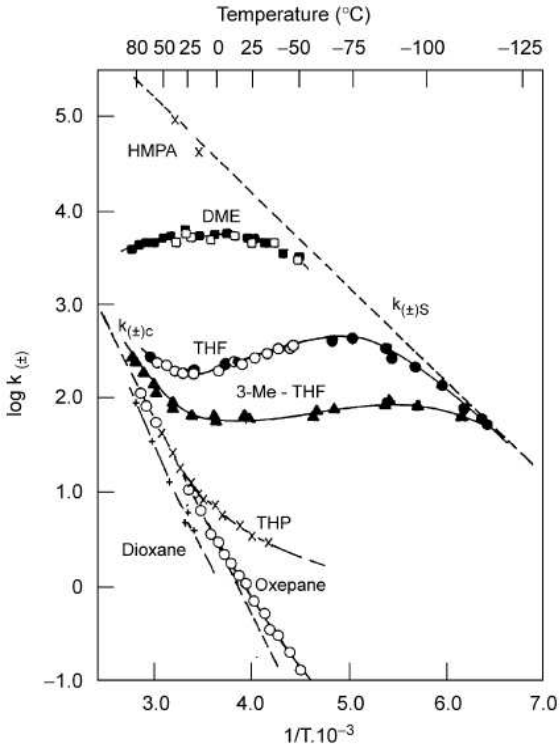

Figure 2-1. Arrhenius plot of the ion pair propagation rate constant in the polymerization of styrene with sodium counterion in polar solvents. (Taken from ref. 48)

2.1.3 Polyalkylmethacrylates by LAP

The anionic polymerization of polar monomers such as alkyl (meth)acrylates, turned out to be more complicated compared to styrene. The initiators with good controllability for styrene and dienes, such as sodium naphthalenide and butyllithium, were not suitable for acrylic monomers[50,51,52,53]. The propagation cannot go further after adding a new portion of monomers and several side reactions existed, leading to low conversion and broad dispersity. The much higher nucleophilicity of the initiators can attack the carbonyl group of the monomer. The carbanion of the active chain may also attack the ester group of the

monomer or of the propagating polymer chain, known as “back biting”[51-53,54,55,56,57,58] (**Scheme 2-3**).

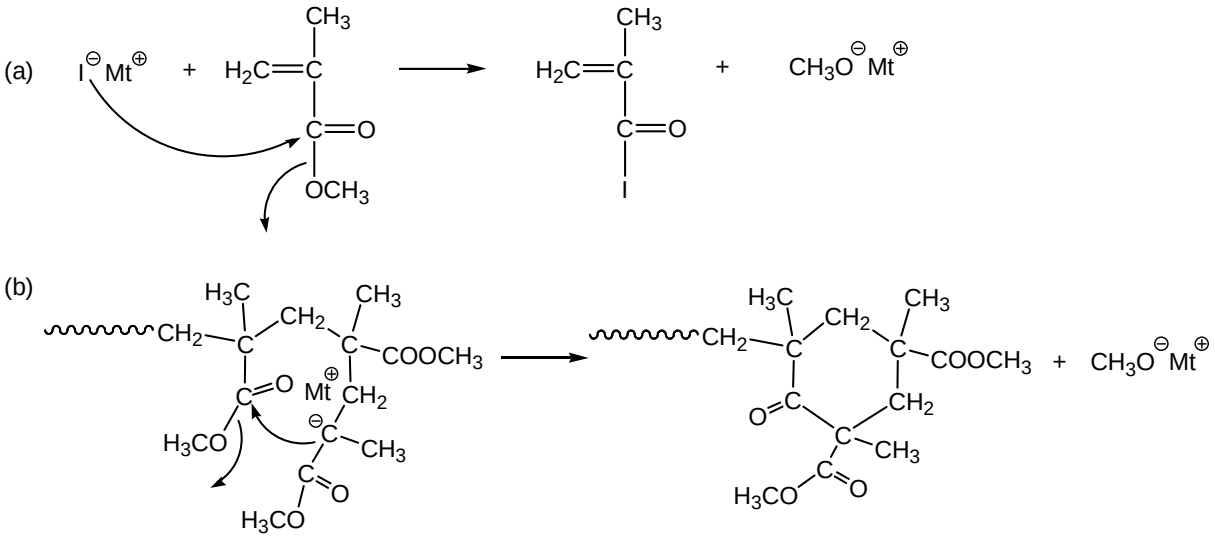

Scheme 2-3. Side reactions in the anionic polymerization of methyl methacrylate. (a) initiator attacks the ester group of the monomer, (b) propagating anionic polymer chain attacks the in-chain ester group, also known as back-biting[29].

Diphenylethylene (DPE) was used to conjunct with BuLi to attenuate the nucleophilicity of the initiator for the anionic polymerization of MMA in polar solvent at -78 ℃ [59,60]. Other aromatic compounds ligated anions (**Scheme 2-4**), like triphenylmethyl anions (conjunction of triphenylmethyl sodium with *p*-chloromethyl styrene)[37] and fluorenyl anions[38,39], also have a good controllability for anionic polymerization of MMA. The phenyl rings here can dissipate and stabilize the charge of the carbanion so to decrease the nucleophilicity.

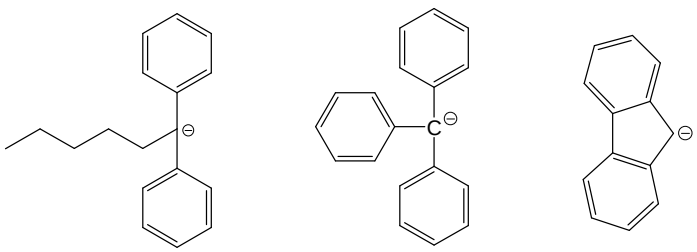

Scheme 2-4. Initiators with phenyl rings for anionic polymerization of MMA.

A useful guide to choose an appropriate initiator for a given monomer in anionic polymerization is that the chemical structure and reactivity of the initiator is similar to that of the propagating anionic species, i.e., the pK_a of the conjugated acid of the propagating anion should be close to that of the initiating species[61]. As seen in **Table 2-1**, the pK_a of

diphenylmethane is 32.2, which is close to that of ethyl acetate (pK_a = 30–31).

For synthesis of block copolymers by sequential anionic polymerization, pK_a should also be taken into consideration. The base of the propagating carbanion should be equal or slightly higher than that of the newly formed carbanion of the sequentially added monomer.

Table 2-1. Acidities of carbon acids[a] in DMSO at 25 ℃ [62].

Monomer	Propagating species	Compound[a]		pK_a [references]
		Fluorene	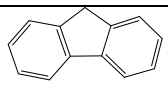	22.6[63]
		Triphenylmethane	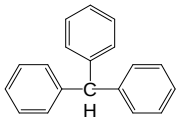	30.6[34]
		diphenylmethane	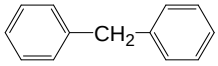	32.2[64]
Ethylene		Methane	CH_4	56[35]
Butadiene	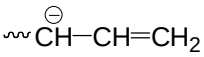	Propene	CH_3-CH=CH_2	44[35]
Styrene	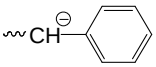	Toluene	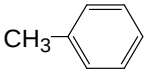	43[35]
Acrylonitrile	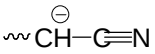	Acetonitrile	CH_3-C≡N	31[35]
Alkylmethacrylate	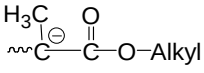	Ethyl acetate	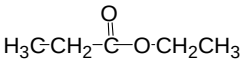	30–31[35]
Oxirane	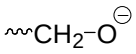	Methanol	CH_3OH	29[65]
Lactone	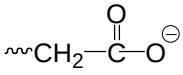	Acetic acid	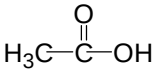	12[35]
Siloxane	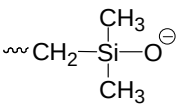	Trimethylsilanol	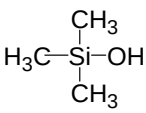	10-11[66]

[a] A carbon acid has a carbon-hydrogen covalent bond which can dissociate to form a carbanion and a proton; a carbon acid is the conjugated acid of the corresponding carbanion ([61], p.33)

In contrast to the kinetics of anionic polymerization of styrene in THF (**Figure 2-1**), linear Arrhenius plots for propagation rate constants of PMMA in THF were obtained and the rate constant depended on the counterion size **(Figure 2-2)**[67,68], which indicates that only one kind of active species, assigned as peripherally solvated contact ion pairs, is involved in the

MMA polymerization. There is equilibrium between different types of contact ion pairs depending on the polarity of solvents as shown in **Scheme 2-5**[69]. In the medium polar solvent THF, the externally solvated contact ion pairs (c) exists competitively with intramolecular solvated contact ion pairs (a, b). In the high polar solvent DME, the equilibrium shifts to externally solvated contact ion pairs (c) or even solvent-separated ion pairs (d).

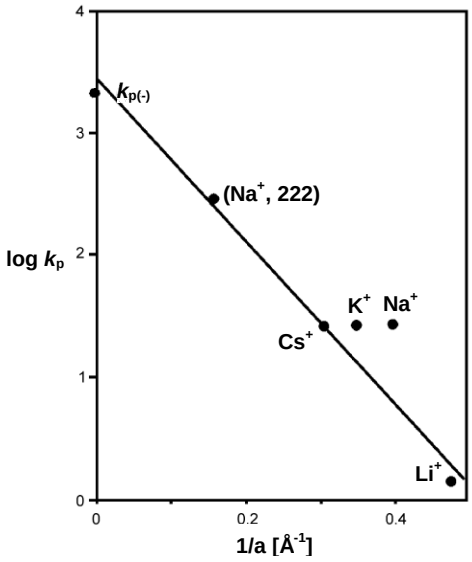

Figure 2-2. The propagation rate constant (k_P) of different PMMA$^-$Mt$^+$ ion pairs in THF at -98 ℃ depending on the reciprocal interionic distance a. (Na+, 222) cryptated sodium. (Taken from ref. 68)

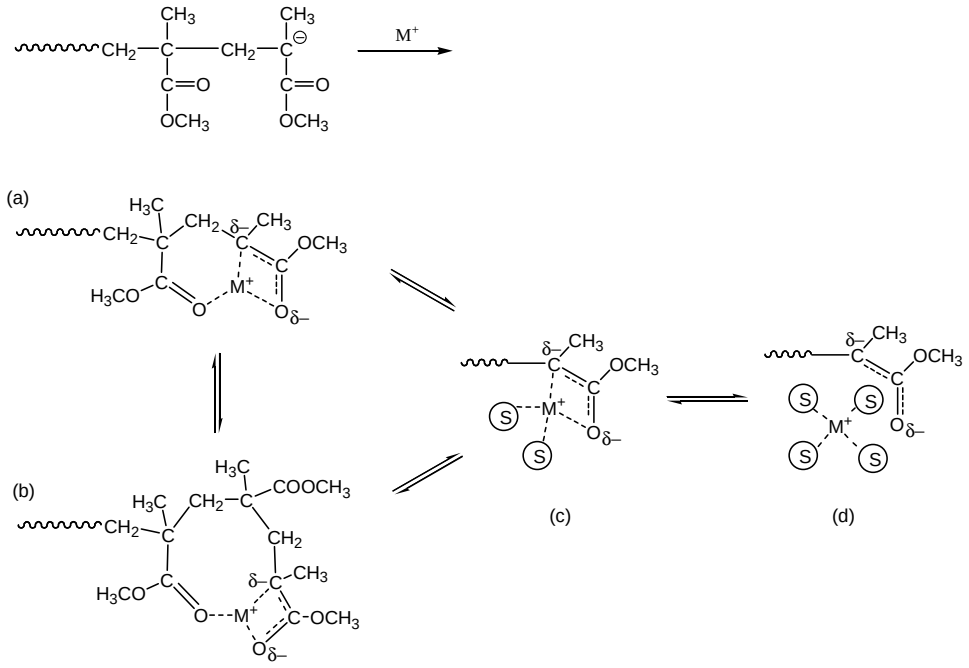

Scheme 2-5. Intramolecularly solvated contact ion pairs (a) and (b), externally solvated contact ion pairs (c), and solvent-separated ion pairs (d)[69]. (S: solvent)

The experimental propagation rate constant, k_{app}, was found to be strongly dependent on the concentration of living ends, [P*], indicating the coexistence of associated and nonassociated ion pairs[70,71,72] (**Scheme 2-6**).

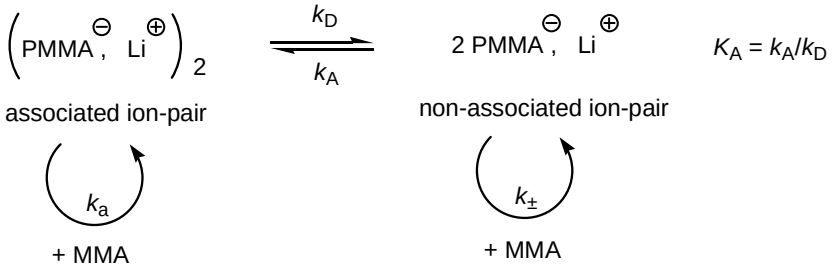

Scheme 2-6. Equilibrium between the associated and non-associated ion pairs[29].

Due to the much higher reactivity of the non-aggregated ion pairs than that of associated ones, the equilibrium has a profound effect on the PDI. A high rate of association and high monomer conversion are needed to get a narrow dispersity.

In 1987, Teyssié et al. reported for the first time the living anionic polymerization of *tert*-butyl acrylate in THF in the presence of excess lithium chloride[73]. Based on the kinetic study of the anionic polymerization of MMA in THF at -65 ℃ with LiCl, the propagating rate constant decreased with increasing LiCl/[P*] ratio after passing a slight maximum and PDI decreased by increasing LiCl and bellow 1.1 at addition 2/1 of LiCl/[P*]. Müller et al. suggested the formation of 1:1 and 2:1 adducts of propagating chain/LiCl(**Scheme 2-7**)[29]. The fast equilibrium from the adducts towards to the associated ion-pair of $(PMMA^-/Li^+)_2$ and the slow disassociation into non-associated ion-pair gives a higher fraction of associated ion-pair (α), thus a narrow dispersity.

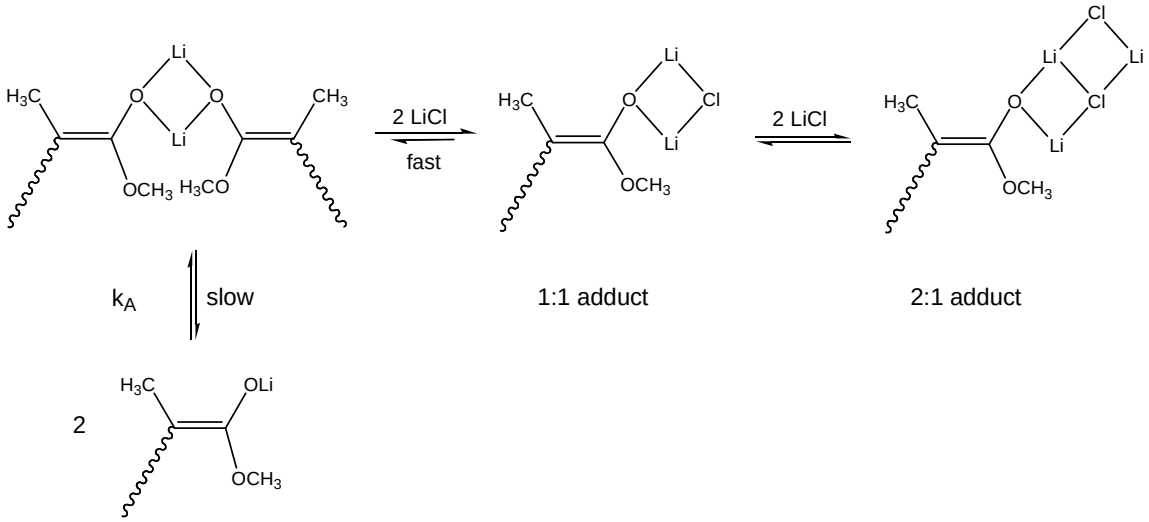

Scheme 2-7. Equilibriums in the polymerization of MMA at the presence of LiCl[29].

Other ligands, known as σ-type (Lewis base), μ-type (Lewis acid), and σ,μ-type can also coordinate with the cation or the enolate ion pairs, thus enhancing the living character of alkyl(meth)acrylate polymerization[29].

2.1.4 End-functionality by LAP

Living anionic polymerization offers a versatile way to make end-functionalized polymers[74,75,76]. **Scheme 2-8** shows end-functionalized polymers using functional initiator (a), substituted DPE (b), and functional terminator (c).

(a) using functional initiator

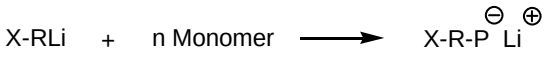

(b) using substitued DPE

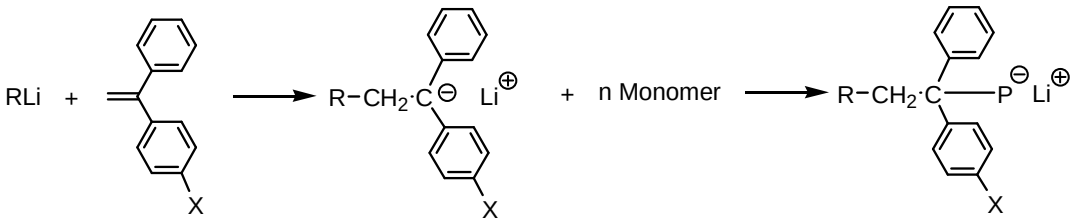

(c) using functional terminator

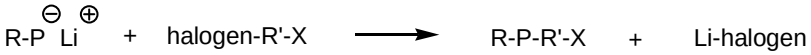

X: Protected functional group

Scheme 2-8. End-functionalized polymers using functional initiator (a), substituted DPE (b), and functional terminator (c).

Functional initiator

Initiators with protected hydroxyl, amine, alkyl group have been developed for prepared α-functionalized polymers[77,78,79]. The advantage to use functionalized initiator in anionic polymerization is that every polymer chain owns a functional group from the initiator. However the poor solubility of some functional initiators in desired hydrocarbon solvent limited the versatility. Like N,N-bis(trimethylsilyl)amine derivative, usually as a solution in diethyl ether or as a dispersion in toluene, is not applicable to prepared polydienes with high 1,4-microstructure in diethyl ether solution.

Substituted diphenylethylene

Substituted diphenylethylene (DPE) is an excellent methodology to prepare α- or ω-functionalized polymers in anionic polymerization by using the diphenylalkyllithium as initiator or end-capping agent as the reaction of alkyllithium and DPE is irreversible and monoadditional[75,76]. Hydroxyl, carboxyl, amine, halogen functionalized DPE have been used in anionic polymerization.

In-chain functionalized polymers can be prepared by using substituted DPE. Polystyrene or polydiene is first polymerized and end-capped with substituted DPE, then copolymerized with another monomer of alkyl (methyl)acrylate[76].

Hetero- and mikro-arm, star branched polymers can also be obtained by applying multifunctionalized DPE[76].

Functional terminator

The reaction of polymeric organolithium with homologous ethylene oxide is a simple way to produce hydroxyl functionalized polymers in anionic polymerization. Ethylene oxide, propylene oxide and 1-butene oxide have been successfully used to end-cap anionic polystyrene with high efficiency[80,81,82] as seen in **Scheme 2-9**. Longer reaction time and larger excesses of ethylene oxide should be prevented to get pure ω-hydroxyethylated functionalized polymers (mono-addition of ethylene oxide)[80].

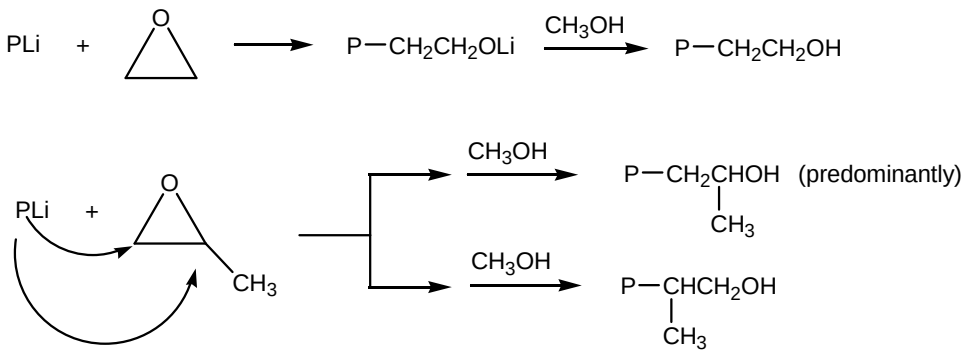

Scheme 2-9. Reaction of polystryryllithium with homologous ethylene oxide and propylene oxide[74].

Similarly, thiiranes were used to produce thiol end-functionalized polymers. Alkyllithium compounds were known to react with thiiranes in “sulfur extrusion” mechanism[83]. However, until recently, polystyryllithium was reported to undergo ring-opening mechanism as shown in **Scheme 2-10**[84].

(a) Thiirane with alkyllithium compounds

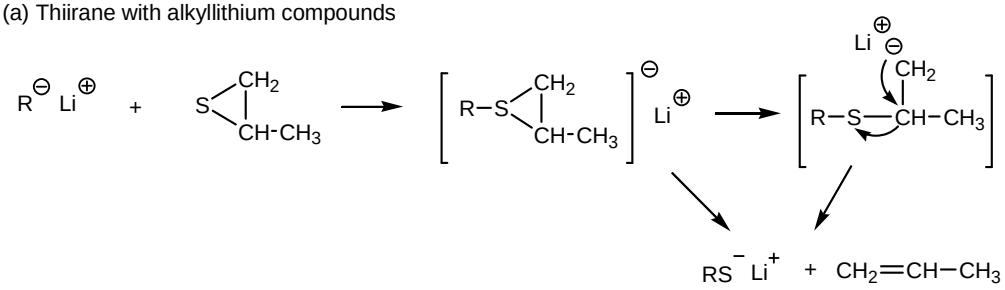

(b) Thiirane with polystyryllithium compounds

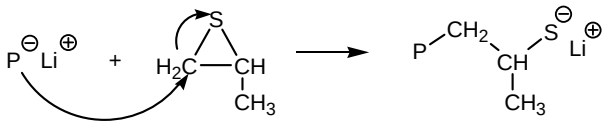

Scheme 2-10. Reaction of thiiranes with alkyllithium compounds (a) and polystyryllithium (b)[84].

The electrophiles, alkyl halides and silyl halides, provide two general functionalization methods to prepared ω-functionalized polymers. Hirao and co-workers[8-9,85] developed a series of α-halo-ω-functional alkanes to end-cap the anionic polymer chains as shown in **Scheme 2-11**. The hydroxyl group can be introduced quantitatively to the end of polystyrenes and polyisoprenes regardless of the kind of halogen atom and the length of methylene spacer[9]. The successful end-functionalization with high efficiency (~100%) is free from side reactions, such as α-metalation, β-elimination, meta-halogen exchange, which are competitive in the reaction of organolithium and haloalkanes. This was attributed to the high enough nucleophilicity of the living polymer anions, although not as high as the typical organolithium compounds such as *n*- and *s*-butyllithium.

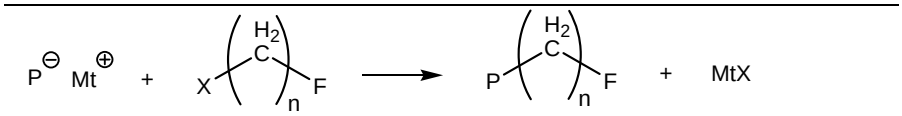

F: protected functional group
X: halogen, Cl, Br, I
n: 2, 3, 4

Functional Group	Protected Functionality
-OH	—O—Si(CH3)3 —O—Si(CH3)2C(CH3)3
-NH2	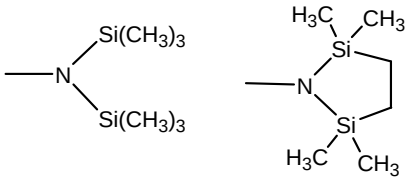
-SH	—S—Si(CH3)2C(CH3)3
-CHO	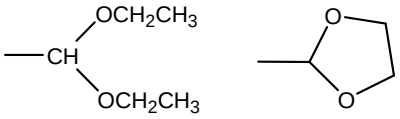
-COCH3	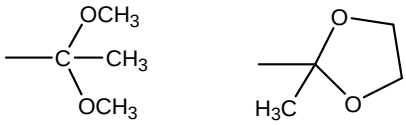
-COOH	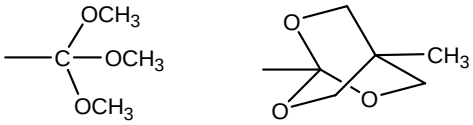
-C≡CH	—C≡C—Si(CH3)3

Scheme 2-11. α-halo-ω-functional alkanes as terminators for anionic polymerization and various protected groups[74].

Termination of living anionic polymerization with chlorosilane derivatives is another general synthetic methodology for synthesis of end-functionalized polymers. By using the similar group-protecting method as in α-halo-ω-functional alkanes, developed by Nakahama and Hirao[85], chlorosilanes with protected amino and hydroxyl groups successfully terminate PSt, PI and PDMS anions, as shown in **Scheme 2-12**[86].

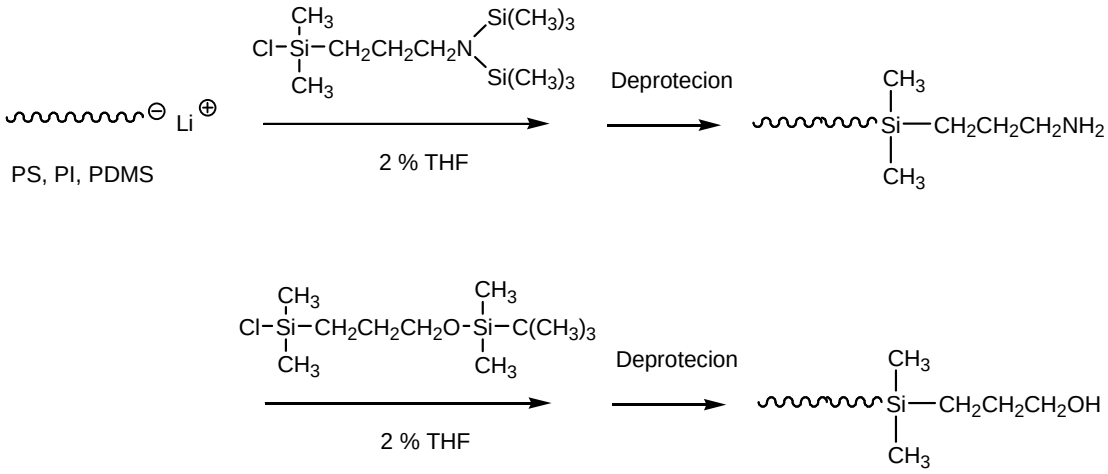

Scheme 2-12. Chlorosilane derivatives as terminators in anionic polymerization[86].

2.1.5 Poly(4-vinyl pyridine) by LAP

The anionic polymerization of 4-vinyl pyridine turned out to be complicated by several aspects. The pyridine unit of the propagating chain suffers the nucleophilic attack from the active anion and the newly generated active centers are capable of reinitiating, which leads to broad dispersity and mixtures of linear and branched polymers[87].

The poor solubility of P4VP in common solvents that are mostly used in anionic polymerization, such as toluene and THF, arises as huge hindrance for the development of anionic polymerization of 4VP. Homopolymeric P4VP is not dissolvable in THF above a critical molecular weight of 20 repeating units[88] and turned out to give a yellow-opaque solution above 5000 g/mol[89]. Mixed solvent systems of THF/dimethylformamide (DMF) or hexamethylphosphoric triamide, were used to improve the solubility[89]. 1 % of HMPT in THF yielded a controlled polymerization of 4VP up to M_n of 14000 g/mol when initiated by α-methylstyryllithium at -78 ℃ with 1 wt% of polymer concentration. Higher molecular weight of P4VP, 67000 g/mol, with narrow dispersity of 1.18, was obtained by applying THF/DMF (8/2 v/v) mixed solvent at -78 ℃ with diphenylmethylpot assium ($Ph_2CH^-K^+$) as initiator and 2 wt.% of polymer concentration. Pyridine as good solvent for P4VP was found to be a better choice due to the lower boiling point and easier purification. Jérôme et al.[90] investigated the homopolymerization of 4VP with pyridine as solvent and co-solvent THF initiated by diphenylmethyllithium. P4VP of ~10000 g/mol with narrow dispersity of 1.1 was obtained in pyridine/THF (60/40 v/v) at -78 ℃. An increasing a mount of pyridine was needed for higher M_n. As the freezing point of pyridine is -42 ℃, elev ated temperature is necessary for working in higher amounts of pyridine or in pure pyridine. Unexpectedly, polymerization of 4VP in a controlled way even at room temperature was realized with dispersity of ~1.2, which indicated no noticeable side reactions even at such high temperature with consideration that anionic polymerization was usually conducted at very low temperature, like -78 ℃. Pyridine

was proposed to act not just as solvent but also as propagating species, like in the mechanism in anionic polymerization of MMA with σ-type ligand of pyridine, as shown in **Scheme 2-13**[91].

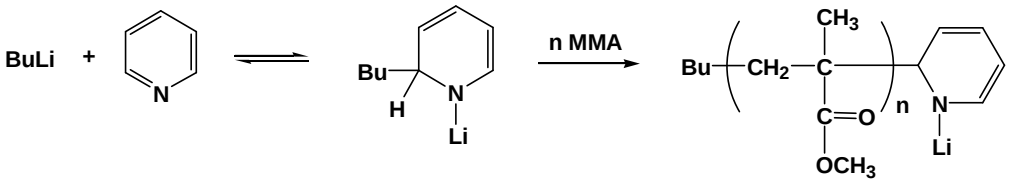

Scheme 2-13. Pyridine-ligated anionic polymerization of MMA[91].

Sequential polymerization of 4VP with another block, which is dissolvable in THF, is another solution to improve the solubility so as to carry out the polymerization in THF. The maximum amount of 4VP depends on the molar ratio of each block and higher amounts of the first block can accommodate more 4VP. Carbanions of polystyrene and polyisoprene with higher base strength than that of P4VP, were successful in reinitiating 4VP and produced P4VP-based block copolymers with narrow dispersity. This indicated that the initiation step from PSt^- and PI^- to 4VP is much faster than the propagation of 4VP to make sure the final results with a narrow dispersity[92,93]. As the base strength of the corresponding anion is lower than that of P4VP anion, PtBMA and PMMA were also used as first block to copolymerize 4VP[88,89,94].

Homo-P4VP and P4VP-based copolymers cannot be eluted or partially eluted through GPC columns with the mostly used eluents such as THF, $CHCl_3$, or DMF[95]. The absorption of P4VP onto the column (usually cross-linked polystyrene gels) can lead to retarded elution time and thus unreliable characterization. Eisenberg and co-workers[89] observed no noticeable adsorption by using N-Methyl-2-pyrrolidone as eluent at elevated temperature of 90 ℃. The block copolymers even with very low 4VP contents (5 %) could not be eluted either in THF or in $CHCl_3$ at 40 ℃. A few amount of triethylamine was found to be efficient to avoid absorption of poly(dimethylamino)ethyl methacrylate and poly(2-vinylpyridine)[96], however not successful for P4VP. Jérôme et al.[63] applied TEA/pyridine/DMF (10/10/80 v/v/v) as eluents at -45 ℃ to characterize P4VP.

Diphenylethylene is efficient to attenuate the activity of alkyllithium to anionic polymerization of MMA to prevent side reactions, but is not applicable for styrene. However, DPE was also used in combination with alkyllithium as initiator for 4VP to prevent side reactions[89,97,98].

2.2 Thiol end-functionalized polymers by RAFT

2.2.1 Mechanism of RAFT

Reversible addition-fragmentation chain transfer (RAFT) polymerization is a reversible deactivation radical polymerization[99]. The basic polymerization process is similar to the normal radical polymerization including initiation, propagation and termination, but involves the RAFT chain transfer agent (CTA) dictating addition, fragmentation and reinitiation[100,101,102,103] as shown in **Scheme 2-14**.

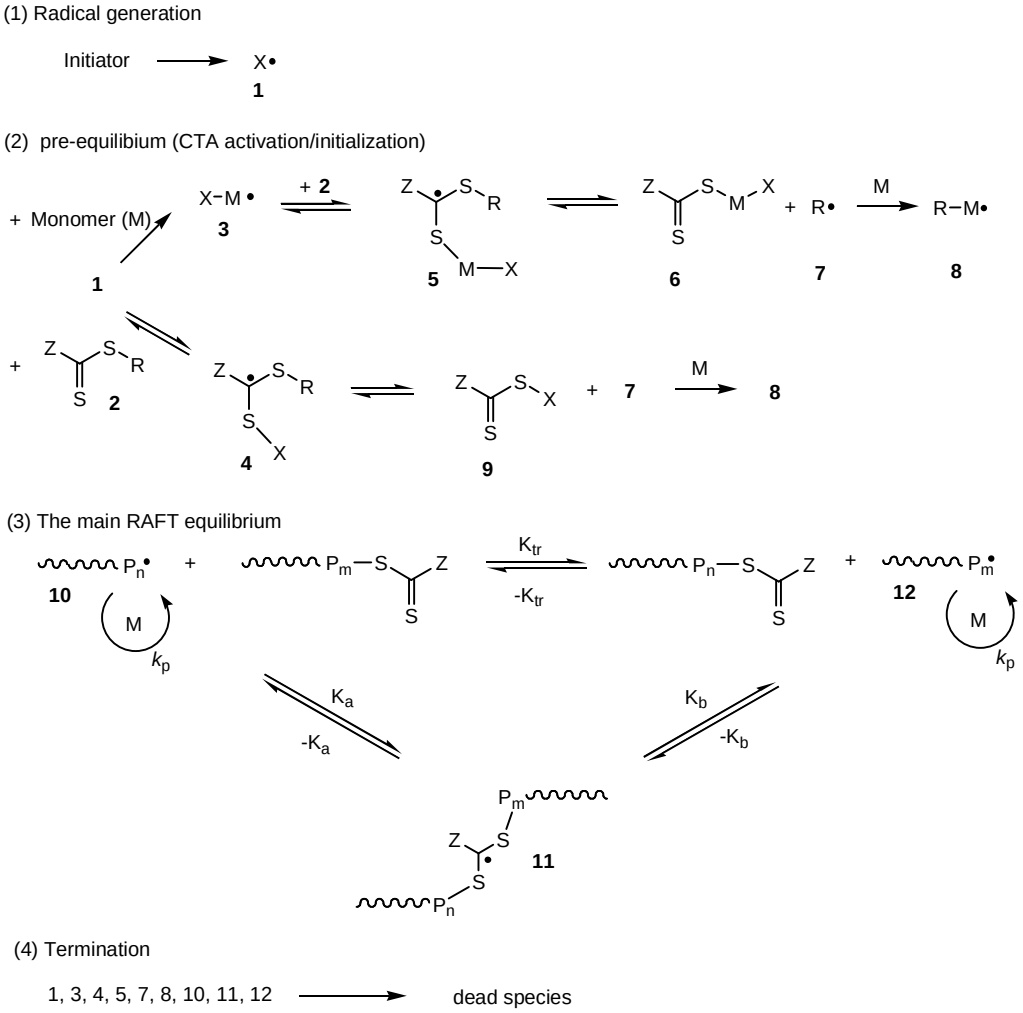

Scheme 2-14. The mechanism of RAFT with thiocarbonylthio-based CTA[104].

2.2.2 Thiol end-functionalized polymers prepared by RAFT

It is not possible to suppress all side reactions in the radical polymerization. However, with proper choice of CTA, the majority of polymer chains (> 95 %) will possess thiocarbonylthio functional groups at the ω-end. The polymers with thiocarbonylthio end-group made by

RAFT have intense color, such as red for dithiobenzoates, which was noted as drawback in the early time of research. Various methods have been developed to remove the end-groups to obtain colorless polymers[104,105] as shown in **Scheme 2-15**. The introduce of –H, –OH and –CN based end-groups by radical processes, transformation into ene end-group by thermal elimination, hetero Diels-Alder reaction with a diene to get dithioacetal derivatives and nucleophilic reaction, usually with amine or hydrazine, to give thiol end-group.

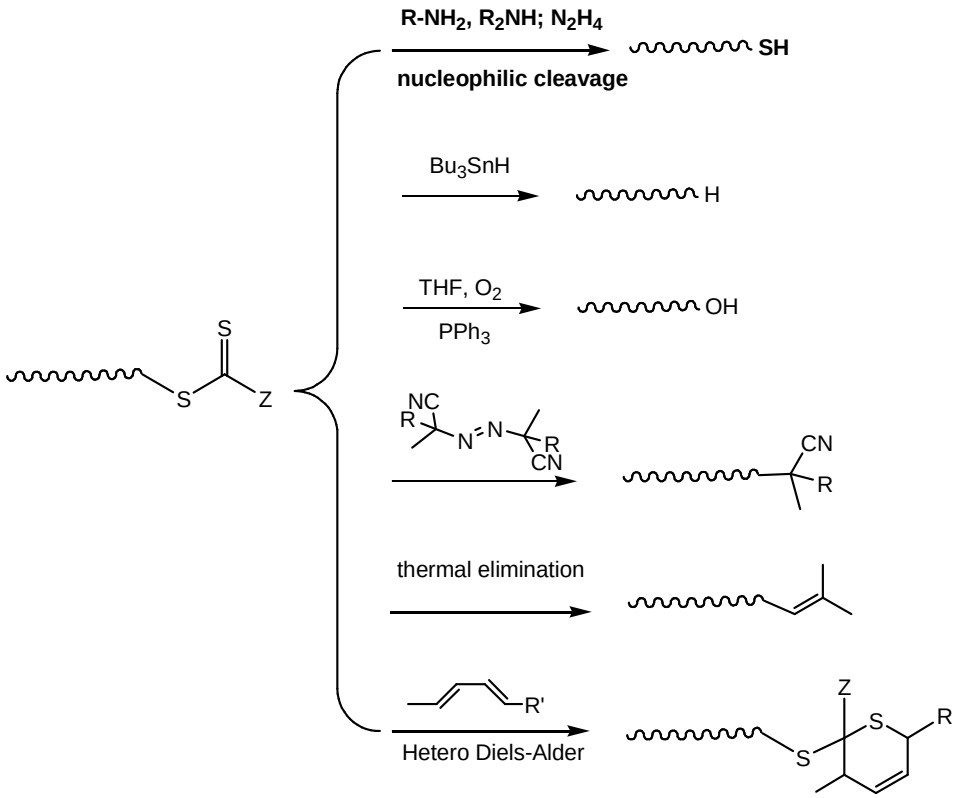

Scheme 2-15. Methods to remove or transform the thiocarbonylthio end-group[104,105].

The reaction with primary or secondary amine (aminolysis)[106,107], or with hydrazine (hydrazinolysis)[108] is the commonly employed method to get thiol end-functionalized polymers. The processes are well known and understood, usually complete in a few minutes at room temperature[107].The polymeric thiol can be employed in the versatile thiol chemistry and also as stabilizing species for the inorganic nanomaterials.

2.3 AuNPs synthesis by Brust-Schiffrin method and by one-phase method in THF

2.3.1 History of the preparation of AuNPs

Gold nanoparticles (AuNPs) owned an old history in the human's civilization, dating from the "soluble" gold which appeared around the 5th or 4th century B.C. in Egypt and China, serving as aesthetic and curative purposes, for coloring glass and ceramics, and which is also used in modern industry[10,11]. Gold colloids were de-veiling gradually in later extended application, mostly in the medicine, known as drinkable gold. In the 20th century, various methods were reported for preparing gold colloids[10]. The hydrophilic gold nanoparticles are prepared in polar/aqueous solvent, best known is the citrate reduction of $HAuCl_4$ in water, which was introduced by Turkevitch[109] in 1951 and improved by Frens[110] in 1973. AuNPs with controlled size from 16–147 nm, were synthesized by varied ratio of trisodium citrate to gold. The hydrophobic (sometimes also hydrophilic) AuNPs were prepared in nonpolar/organic solvent in the presence of various ligands, as the cluster Au_{55} discovered by Schmid[111] in 1981, which marks the opening of chemical nanotechnology in the gold world. The AuNPs stabilized by alkanethiols were first reported by Mulvaney and Griesig[112] in 1993. Later in 1994, Brust and Schiffrin discovered the monolayer protected AuNPs, known as Brust-Schiffrin method (BSM), in which the Au colloids were prepared by reduction of $HAuCl_4$ with sodium borohydride by employing dodecanethiol as stabilizing agent in the two phases of toluene and water[17]. The synthesis procedure is facile and the AuNPs have reduced dispersity and controlled size bellow 5 nm, thermal and air stability, and the possibility of repeated isolation and re-dissolving in common organic solvents. Thus, the as-prepared AuNPs can be handled like stable organic and molecular compounds. Brust-Schiffrin method was widely used for preparing monolayer-protected clusters with various thiol ligands, such as with amine, alkene, and fluorescence functionalized molecules with thiol group.

2.3.2 Brust-Schiffrin Method

The monolayer protected gold nanoparticles, size of 1-3 nm, discovered by Brust and Schiffrin in 1994, were prepared by reducing tetrachloroauric acid ($HAuCl_4$) with sodium borohydride ($NaBH_4$) in the presence of alkanethiol in water/toluene two-phase system[17]. $HAuCl_4$ was first dissolved in water and $AuCl_4^-$ was transfered from aqueous phase to toluene by using tetraoctylammonium bromide as the phase-transfer agent and reduced with aqueous $NaBH_4$ in the presence of dodecathiol. A typical color change from orange to deep brown can be seem within a few seconds, indicating the formation of gold nanoparticles. The

overall reaction is shown in **Formula (2-1)** and **(2-2)**:

$$\mathbf{HAuCl_{4(aq)} + N(C_8H_{17})_4Br_{(tol)} \rightarrow [N(C_8H_{17})_4][AuCl_4]_{(tol)}} \qquad \mathbf{(2\text{-}1)}$$

$$\mathbf{m[AuCl_4]^-_{(tol)} + nC_{12}H_{25}SH_{(tol)} + 3me^- \rightarrow [(Au_m)(SC_{12}H_{25})_n]_{(tol)} + 4mCl^-_{4\,(aq)}} \qquad \mathbf{(2\text{-}2)}$$

Later in 1995 they developed the procedure in a single phase of methanol by employing *p*-mercaptophenol as stabilizing ligand[113]. The solution turned brown immediately upon the addition of freshly prepared aqueous $NaBH_4$ and finally AuNPs in size of 2.4-7.6 nm were obtained.

Brust-Schiffrin method has become the most widely used method for synthesizing metal NPs < 5 nm stabilized by thiolates[114,115,116,117,118,119,120,121,122] and by other organochalcogenates[123,124,125]. The long-held assumption was that the addition of thiol reduces Au^{3+} to Au^{1+} and forms polymeric $[AuSR]_n$ species in both the one-phase and two-phase BSM (**Formula (2-3)**). Until in 2010 Goulet and Lennox found that $[TOA]^+[AuX_2]^-$ complex (tetraoctylammonium gold(1) halide), which was formed from the reduction of $[AuX_4]^-$ by thiol, was actually the gold precursor in the BSM (**Formula (2-4)**)[126].

$$\mathbf{[NR_4][AuX_4] + 3R'SH \rightarrow [AuSR']_n + R'SSR' + NR_4X + 3HX} \qquad \mathbf{(2\text{-}3)}$$

$$\mathbf{[NR_4][AuX_4] + 2R'SH \rightarrow [NR_4][AuX_2] + R'SSR' + 2HX} \qquad \mathbf{(2\text{-}4)}$$

The stoichiometry of the reduction of $[NR_4][AuX_4]$ to $[NR_4][AuX_2]$ (Au^{3+} to Au^{1+}) was confirmed by UV-vis monitoring the disappearance of the absorption band at 402 nm (Au^{3+}) upon addition of alkanethiol and the solution changed from intense orange to colorless. The species present during the reaction were quantitatively monitored by ^1H NMR spectroscopy. The spectrum of the mixture of TOAX and $[TOA][AuX_4]$ is similar to that of pure TOAB but some shifts of all the resonance peaks due to the association with the AuX_4^- anion. Addition of 2 equiv of dodecanethiol generates 1 equiv of dodecyl disulfide. Finally upon addition of 3 and 4 equiv of the thiol, all $[TOA][AuX_4]$ converted to $[TOA][AuX_2]$ with the associated generation of 1 equiv of the disulfide. However, 1 and 2 equiv of free thiol are also observed respectively. The results clearly show that polymeric $[AuSR]_n$ species are not generated in measurable quantities. Rather, the intermediate step of the Brust-Schiffrin synthesis proceeds via **Formula (2-4)**, where Au^{1+} tetraalkylammonium complex are the relevant Au precursors.

The earlier studies showed that both thiols and disulfides can form self-assembled monolayers (SAMs) on the bulk gold surface[127,128,129] and the thiol was preferred by a factor

of ~75:1 over the disulfide in the competitive adsorbtion of thiols and disulfides[104]. However, disulfide showed a similar activity as thiol in the ligand-exchange reaction of thiolate-protected AuNPs as thiol[130]. Tong and coworkers observed that the Au-S bonds do not form until the last reduction step by $NaBH_4$ in the original BSM[131]. They further identified the co-presence of the residual thiol and the reduction-generated disulfide as found in typical BSM synthesis is a source of size dispersity[132]. In the presence of H_2O, thiol was a better ligand than disulfide make smaller and more homogeneous AuNPs but in water deprived situation disulfide was better.

2.3.3 One-phase procedure in THF

There are two typical procedures of Brust-Schiffrin method for synthesis of AuNPs stabilized by thiol ligand, two-phase procedure[17] and one-phase procedure in methanol[112] as discussed previously. However, some of ω-functionalized alkane- or arenethiols have poor solubitlity in methanol, such as 4'-substituted-4-mercaptobiphenyls[133].

Ulman and coworkers developed a facile one-phase procedure in THF for synthesis of thiol-stabilized AuNPs[132]. Hydrogen tetrachloroaureate(III) trihydrate ($HAuCl_4 \cdot 3H_2O$) was dissolved in freshly distilled THF and lithium triethylborohydride (Superhydride) was used as reducing agent. The solution turned red-brown immediately upon the addition of Superhydride and finally AuNPs of 4 nm (TEM) were obtained at 0.9/1 molar ratio of octadecanethiol/$HAuCl_4 \cdot 3H_2O$.

Later Lennox and co-workers employed thiol-capped polystyrene as macromolecular ligand to stabilize AuNPs in one-phase procedure in THF[134]. AuNPs with a moderate dispersity, core size of 6.2 ± 1.7 nm, were prepared at 1/3.5 molar ratio of thiol/ $HAuCl_4$. Such polystyrene coated gold nanoparticles showed good dispersity in PSt matrix, without aggregates. Whilst $C_{14}H_{29}SH$ coated AuNPs showed aggregates in dimension of several hundreds of nanometers in the PSt matrix.

Since hydrophobic polymers such as PSt, PMMA, PtBMA are unable to coordinate with metal nanoparticles, a coordinating group is necessary to stabilize the metal nanoparticles[134,135,136]. Thiol or disulfide end-capped polymers synthesized either by anionic polymerization or by RAFT method, were widely employed in stabilizing gold nanoparticles by one-phase procedure to improve the dispersity in the corresponding polymer matrix.

Water-soluble polymers such as poly[2-(N,N-dimethylamino)ethyl methacrylate][137], poly(*N*-isopropylacrylamide)[138], poly(2-vinylpyridine)[139], poly(4-vinylpyridine)[140,141,142,143], poly(vinyl alcohol)[144], poly(acrylic acid)[145], and poly(ethylene oxide)[146,147] are well known for their ability to coordinate with metal particles. The gold nanoparticles stabilized by such water-soluble polymers are usually prepared in aqueous solution.

2.4 Block copolymer thin films modified by AuNPs

2.4.1 Block copolymer thin films

The self-assembly of block copolymers has been widely studied from theoretical to experimental aspects in the last decades. It is well known that the microphase separation of BCPs into ordered structure of spherical, cylindrical, gyroidal or lamellar microdomains below an order-disorder transition temperature (T_{ODT}) depends on the segmental interaction, which in the term of Flory-Huggins segmental interaction parameter (χ), degree of polymerization (N), volume fraction (f) and chain architecture (e.g., linear, star, etc.)[6]. In the strong segregation regime (χN >> 10.5), the equilibrium interlamellar spacing (L_0) can be obtained from the balance between the elastic stretching energy and the interfacial energy contribution[148].

$$L_0 \propto \chi^{1/6} N^{2/3} \qquad \textbf{(2-5)}$$

In a weakly segregated system, L_0 is proportional to $N^{1/2}$ [148,149].

In contrast to the bulk, the morphology and ordering of BCP thin films can be further strongly influenced by the surface and interfacial energies and commensurability between the film thickness and the period of the microdomain[22].

2.4.1.1 Film thickness induced incommensurability

Thin films of symmetric diblock copolymer (A-*b*-B) were most studied for their comparably simple structural parameters. When one side of the thin film is attached to a “hard” substrate (such as by spin-coating or dip-coating on Si wafer) referring to free interface of air/copolymers, the topography is determined by the commensurability between the local film thickness (h) and the interlamellar spacing (L_0) as shown in **Figure 2-3**[22,150]. For the case of symmetric wetting, that the same component A or B resides at both interfaces, the film surface is smooth when the local film thickness $h = H_n = nL_0$. For asymmetric wetting, that a different component resides at each interface, the surface is smooth when the local film thickness $h = H_n = (n+1/2)L_0$. If the local film thickness derivates from the commensurable thickness H_n by an amount of $\Delta h > 0$, topographical features, islands, holes or ‘bicontinuous’ patterns appear at the free surface.

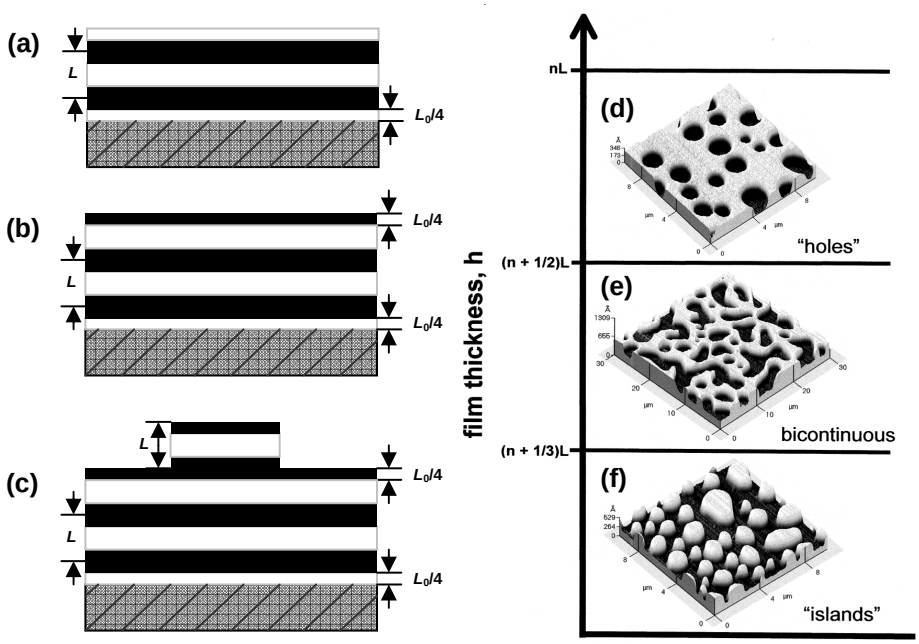

Figure 2-3. Film thickness induced topographical features. Thin film with commensurable thickness under symmetric wetting (a) and asymmetric wetting (b); thin film with incommensurable thichness (c); AFM images (taken from ref. 150) of symmetric PSt-*b*-PMMA thin films with holes (d), bicontinuous (e) and islands (f).

Such forming of discontinuous layers can minimize the free energy of the thin film system. However, the surface topography may also not appear if the film thickness h is not much different from the commensurable value H_n, nL_0 or (n+1/2)L_0 for symmetric and asymmetric wetting respectively, in which case the copolymer chains may stretch or compress to accommodate the small incommensurability[22].

2.4.1.2 Substrate effect

When one component of BCPs preferentially interacts with the substrate or the component of lower surface energy causes the segregation of that block to the free surface or the substrate interface, microdomains paralleled to the substrate form below T_{ODT}. For a neutral substrate, i.e., the interfacial interactions of both blocks are equally favorable and even slight incommensurability may induce the microdomain to orient normal to the substrate.

The substrate can be modified either by self-assembled monolayers through chlorosilane chemistry[151,152] or by random copolymers[153,154]. Nealey and co-workers studied the wetting behavior of symmetric PSt-*b*-PMMA thin film on octadecyltrichlorosilane modified Si/SiO_x substrate[151]. By varying graft density with different deposition time (t) of substrate into the OST solution, asymmetric wetting with PMMA wetting the substrate at t = 1-10 h, neutral wetting with lamellae oriented perpendicular to the substrate at t = 12 h and symmetric

wetting with PSt wetting the substrate at t = 21-24 h were obtained. Russell and co-workers[153] investigated the controlling of the interfacial energy by end-grafted hydroxyl end-functionalized random copolymer PSt-*b*-PMMA (**Scheme 2-16**) onto the silica substrates. By varying the styrene fraction (*f*) from 0-1, preferential wetting of the substrate by PMMA to preferential wetting by PSt can be obtained. The interfacial energies with PSt and PMMA were equal when *f* was about 0.6 as shown in **Figure 2-4**.

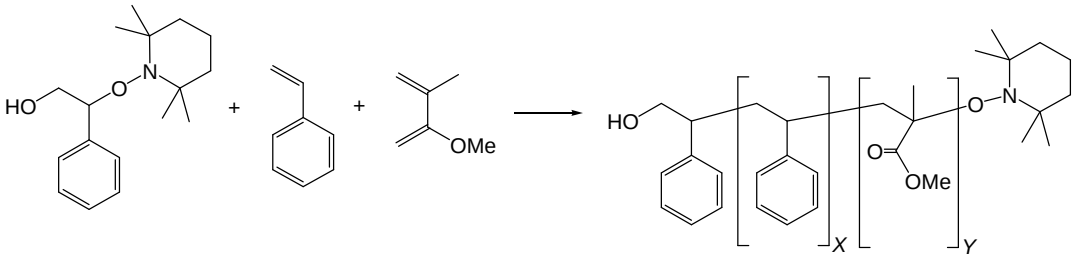

Scheme 2-16. Hydroxyl end-functionalized random copolymer P(St-*r*-MMA)[153].

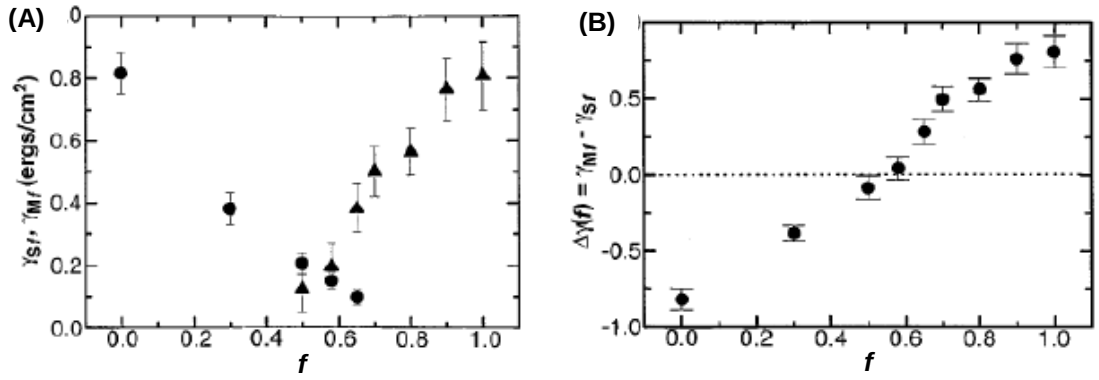

Figure 2-4. (A) Interfacial energies γ_{Sf} and γ_{Mf} and (B) $\Delta\gamma(f) = \gamma_{Mf} - \gamma_{Sf}$ of a random copolymer P(St-r-MMA) brush as a function of styrene fraction *f*. (Taken from ref. 153)

Both the thin films of cylinder- and lamella-forming diblock copolymers PSt-*b*-PMMA with microdomain oriented normal to the substrate were achieved when the substrate owned a balanced interfacial interaction by anchoring a layer of random copolymer P(St-*r*-MMA) with specific PSt volume fraction as seen in **Figure 2-5**[155].

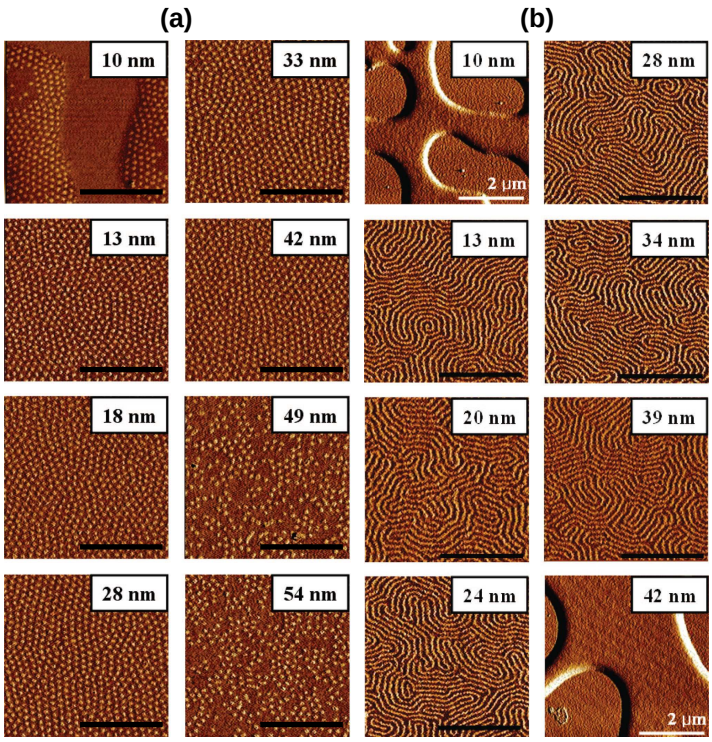

Figure 2-5. SFM phase images for thin films of (a) cylinder-forming PSt-*b*-PMMA on the substrate modified by P(St-*r*-MMA) (with PSt molar fraction of 0.64) and (b) lamella-forming PSt-*b*-PMMA on the substrate modified by R55 (with PSt molar fraction of 0.55) at various film thicknesses. Both series was after thermally annealing at 170 ℃ for 24 h. S cale bar is 0.5 μm unless specified. (Taken from ref. 155)

Nealey and co-workers investigated perpendicular windows for symmetric and asymmetric block copolymers PSt-*b*-PMMA thin films on the substrate modified by random copolymers with terminal hydroxyl group, or a third polar co-monomer of 2-hydroxyethyl methacrylate (HEMA) or cross-linkable glycidyl methacrylate (GMA)[154]. The range of PSt fraction in which the BPCs showed vertical oriented domains was different for each random copolymer composition and block copolymers. PSt-*b*-PMMA with PSt cylinders exhibited vertical structure for a very narrow range of compositions compared to that with PMMA cylinders or lamellae. The incorporation of polar HEMA or GMA monomers in the grafted random copolymers shifted the composition range for the perpendicular orientation to higher fractions of styrene.

2.4.1.3 Solvent vapor annealing

The surface preferentiality at the free surface, referring to the interface of polymer/air, is governed by the surface tensions of the copolymer blocks[23]. Block with lower surface tension preferentially segregates to the free surface to minimize the surface tension. The effect of the

free surface (“soft” interface) on the thin film morphology and orientation is similar to that of the fixed substrate (“hard” interface). By thermal[156] or solvent vapor annealing, the free surface can be tuned to be neutral or preferential to one specific block. As many copolymers are susceptible to thermal degradation, solvent vapor annealing is an attractive alternative to adjust the free surface so as to get desired microstructure ordering and orientation.

Solvent vapor exposure of the BCP thin film in the annealing can serve to several aspects. First, the free surface can be modified to be neutral or interact preferentially with one block by proper solvent selection[157,158]. Han et al. obtained well-ordered hexagonally packed nanocylinders by exposing symmetric PSt-*b*-PMMA to PMMA selective solvent of $CHCl_3$ or acetone[158]. As increasing the annealing time, PSt block with lower surface tension dominated free surface but finally switched to PMMA dominated surface as shown in **Figure 2-6**.

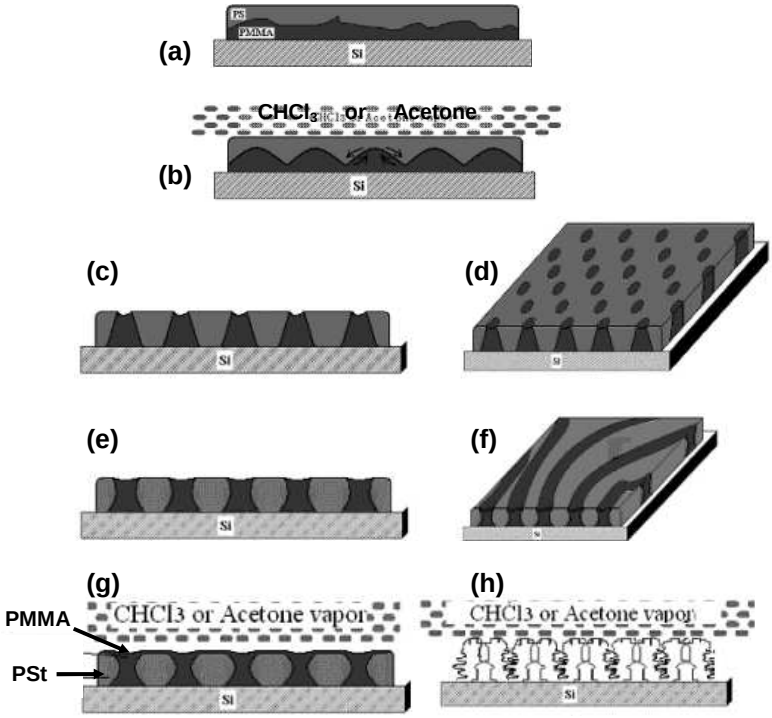

Figure 2-6. Schematic model of morphology development of the symmetric PSt-*b*-PMMA thin film depending on the solvent annealing time. The black regions denote PMMA, the gray regions denote PSt, and the dots denote solvent vapor molecules. (a) Before being exposure to solvent. (b) Exposed for a certain time. Cross-section (c) and plane (d) view of nanocylinder formation. Cross-section (e) and plane (f) view of the lamellar formation. After a long time annealing (g) and when PSt block takes the collapse conformation (h)[158].

As the solvent imparts the chain mobility to the copolymers during annealing procedure, defects can be greatly reduced. Russel and co-workers produced highly oriented, nearly-defeat-free PEO cylinders in PSt matrix by controlling the solvent evaporation rate of benzene as shown in **Figure 2-7**[24]. They proposed that there is a gradient in the

concentration of the solvent as a function of depth and the solvent concentration increases with the depth from free surface to substrate. As the solvent evaporates, an ordering front propagates through the film producing highly ordered and oriented cylinder arrays throughout the entire film.

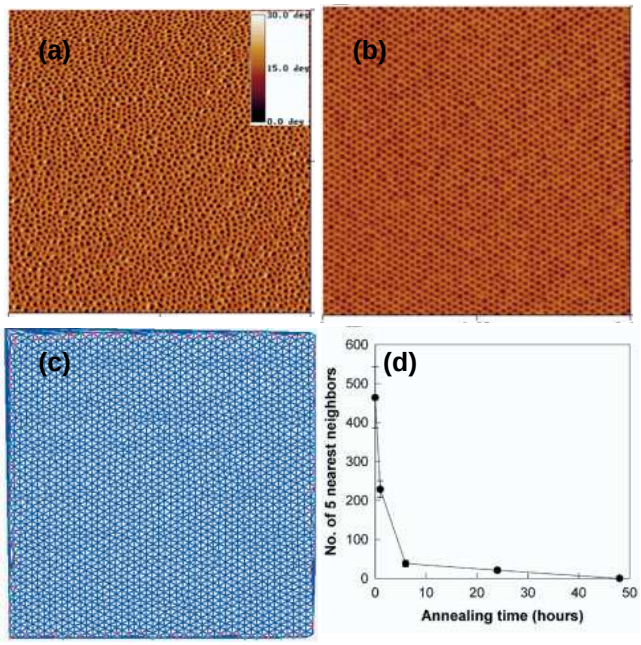

Figure 2-7. AFM images (2*2 μm^2) of PSt-*b*-PEO thin film (255 nm in thickness) by spin-coating before (a) and after (b) annealing for 48 h in benzene, (c) triangulation image of (b), and (d) the number of five-neighbor defects as a function of annealing time in solvent vapor[24].

The solvent in the thin film during annealing also changes the blocks interaction and the relative volume fraction, thus leading to changes in morphology[158,159]. The size of microdomain can be enlarged or reduced due to the film swelling and confinement[160,161].

2.4.1.4 Block copolymer/homopolymer mixtures

Polymer blends are usually produced aiming to get properties superior to each individual component. In the thin film mixtures consisting of diblock copolymer (A-*b*-B) and homopolymer (A or B), the phase behavior depends on the ratio of the degree of polymerization of homopolymer ($N_{H,A}$) to block copolymer ($N_C = N_{C,A} + N_{C,B}$)[162]. For $N_H < N_C$, the homopolymer chains are shorter than the copolymer chains, homopolymers segregate to the appropriate microdomains to minimize the unfavorable segmental A/B contacts. If the molecular weight of homopolymer is significantly less than the appropriate block, the homopolymer chains interpenetrate into the favorable block and distribute throughout the whole domain to form the so-called “wet brush” as shown in **Figure 2-8a**. The lateral swelling

of A-domain necessitates the shrinking of B-domain in order to maintain uniform density throughout the film. The increase in the swelling of A-domain outweighs the shrinking of B-domain, leading to an increase of interlamellar spacing, $L_{\text{distributed}}$, which can be predicted by **Formula (2-)**[163]:

$$L_{\text{distributed}} = \frac{L_0 [g(f,\varphi)]^{-1/3}}{(1-\varphi)} \qquad \textbf{(2-6)}$$

where

$$g(f,\varphi) = \frac{f + (1-f)\varphi^2}{f(1-\varphi)^2} \qquad \textbf{(2-7)}$$

Here, L_0 is the interlamellar spacing of block copolymer A-*b*-B, φ is the volume fraction of homopolymer A, f is the volume fraction of A-block in the block copolymer, which is 1/2 for a symmetric block copolymer. It should be noted that macrophase separation would happen when the homopolymer addition exceeds the critical volume fraction φ_C, the solubility limit for A-block.

When the homopolymer chain has a comparable length to the block copolymer, $N_H \approx N_C$, the homopolymers segregate to the middle of the corresponding microdomain to form a separate phase, leading to a large increase of the interlamellar spacing as seen in **Figure 2-8b**. ("dry brush" condition that homopolymers do not interpenetrate the copolymer "brush" layers). The interlamellar spacing increases with increasing volume fraction of homopolymer, φ, and can be predicted by **Formula (2-8)**[163] when $\varphi < \varphi_C$:

$$L_{\text{localized}} = L_0 / (1-\varphi) \qquad \textbf{(2-8)}$$

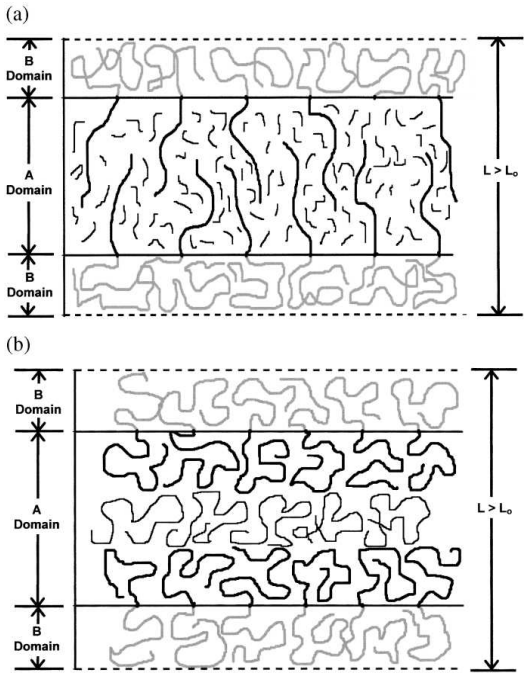

Figure 2-8. Schematics of the copolymer (A-*b*-B) with (a) homopolymer chains distributed throughout one domain and (b) with homopolymer localized in the center of one domain[162].

The spatial distribution of homopolymers in the block copolymer was investigated by neutral reflectivity in the early studies. The selective deuteration of one block can provide detailed information about the domain size and interfacial width[164,165]. Addition of deuterium-labeled homopolymers to an unlabeled copolymer can reveal the homopolymer distributions in the copolymer microdomain. Mayes et al. investigated the distribution of perdeuterated homopolymers PSt and PMMA in the unlabeled symmetric block copolymer PSt-*b*-PMMA by neutral reflectivity[166]. When the molecular weight of homopolymer is comparable to the block molecular weight, the homopolymer is confined to the corresponding microdomain, with a distribution which peaks at the center of the domain. With decreasing molar mass, the homopolymer is more uniformly distributed within the domain. When the molecular weight of the homopolymer is much higher than the block, the homopolymer is excluded from the lamellar microdomains, but does not interfere with the preferred lamellar orientation and is incorporated into the multilayered morphology.

Orso and Green used atomic force microscopy to examine the phase behavior of symmetric block copolymer PSt-*b*-PMMA (N = 650) and homopolymers PSt (N = 20 and 250) as well as symmetric block copolymer PSt-*b*-PMMA (N = 200) thin film blends[167]. When blended with homopolymers, interlamellar spacing increased with increasing volume fraction of the homopolymer and the trend was less extensive for the low molecular weight one. The addition of block copolymer had a converse effect that the lamellar spacing decreased as increasing volume fraction of the block copolymer, as shown in **Figure 2-9a**. The data from AFM measurements were in good agreement with the data from neutral reflectivity by Mayes et al.[168] **Figure 2-9b**, indicate that AFM technique provides a reliable analysis of the size of microdomain by probing the topography of the sample.

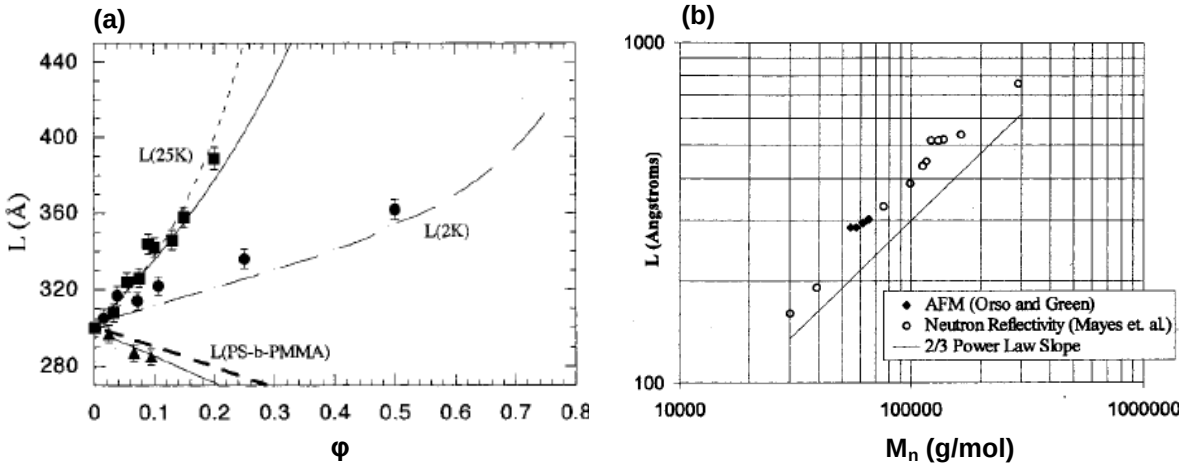

Figure 2-9. (a) Interlamellar spacing (L) versus volume fraction (φ) of PSt homopolymers and PSt-*b*-PMMA diblock copolymers, and (b) Data obtained by AFM versus data obtained by neutron reflectivity. (Taken from ref. 167)

For thin film of block copolymer/block copolymer (A-b-B type) mixtures, the shorter copolymer chains were found to locate preferentially at the interface, while long chains concentrate in the domain centers[167,168]. The lower molecular weight copolymer segregates toward the interfacial region in order to minimize unfavorable A/B contacts. The longer copolymer chains retract in order to maintain a constant segmental density, leading to a shrinking lamellar domain with increasing weight fraction of the shorter copolymers as shown in **Figure 2-10**[162].

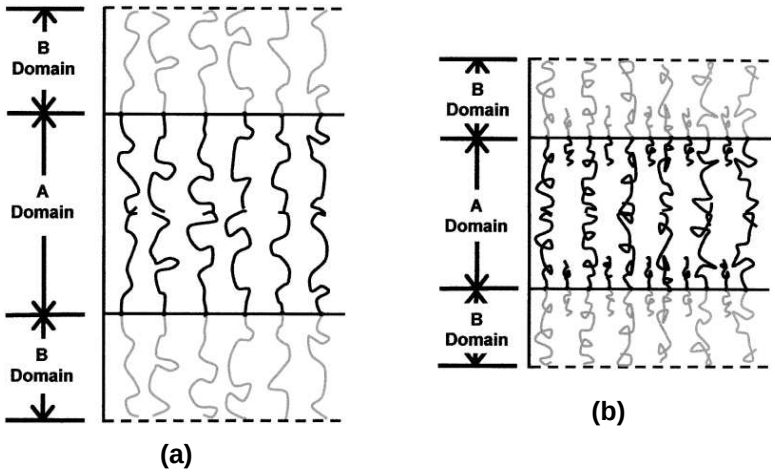

Figure 2-10. Schematics of diblock copolymer mixtures. (a) Longer block copolymer chains and (b) microdomain of longer block copolymers shrinks with addition of shorter block copolymers[162].

2.4.2 Block copolymer/NPs hybrid thin films

2.4.2.1 Theoretical predictions and simulations

Organization of nanoparticles in self-assembled block copolymers can yield hierarchically ordered structures, which are promising functional materials for next generation catalysts, selective membranes and photonic band gap materials[1-4,169]. A variety of methods and techniques, including self-consistent field theory, density functional theory, strong segregation theory, Monte Carlo and molecular dynamics simulation, have been used to get prediction and simulation about the effect of nanoparticles on the morphology of block copolymers and the distributions of NPs in the block copolymer matrix[25-27,170,171,172,173,174,]. A number of parameters, such as the size, shape, volume fraction and modifier of particles, the composition of block copolymer and the interaction between the particles and different blocks, control the final morphology, ordering and particles distribution of the copolymer/nanoparticle composite. Otherwise the interactions between the particles and the substrate also the free air surface as well as the thin film thickness should be in the consideration when the composite dimension is reduced to nanometer-size, as in hybrid thin

film[26].

Thompson and Balazs did pioneering work on the theoretical study and simulation of copolymer/nanoparticle composites[25]. Based on self-consistent field theory (SCFT) and density functional theory (DFT), the free energy of the system A-*b*-B/NPs is given by

$$F = F_{\mathrm{e}} + F_{\mathrm{d}} + F_{\mathrm{p}} \qquad \textbf{(2-9)}$$

The first term F_{e} is the enthalpic interaction in the system:

$$F_{\mathrm{e}} = \frac{1}{V} \cdot \int d\mathrm{r} \cdot \left[\chi_{\mathrm{AB}} \cdot N \cdot C_A(\mathrm{r}) \cdot C_{\mathrm{B}}(\mathrm{r}) + \chi_{\mathrm{BP}} \cdot N \cdot C_B(\mathrm{r}) \cdot C_{\mathrm{P}}(\mathrm{r}) + \chi_{\mathrm{AP}} \cdot N \cdot C_A(\mathrm{r}) \cdot C_{\mathrm{P}}(\mathrm{r}) \right] \qquad \textbf{(2-10)}$$

Where V is the volume of the system, χ is the Flory-Huggins parameter, and $C(\mathrm{r})$ is the dimensionless concentration. The diblock entropic free energy F_{d} is given by:

$$F_{\mathrm{d}} = (1 - \varphi_{\mathrm{P}}) \cdot \ln\left[\frac{V \cdot (1 - \varphi_p)}{Q_{\mathrm{d}}} \right] - \frac{1}{V} \cdot \int d\mathrm{r} \cdot \left[w_{\mathrm{A}}(\mathrm{r}) \cdot C_{\mathrm{A}}(\mathrm{r}) + w_{\mathrm{B}}(\mathrm{r}) \cdot C_{\mathrm{B}}(\mathrm{r}) \right] \qquad \textbf{(2-11)}$$

Where Q_{d} is the partition function of a single diblock subject to the field $w_{\mathrm{A}}(\mathrm{r})$ (the value at point r of the mean field felt by the A segments) and $w_{\mathrm{B}}(\mathrm{r})$, and φ_{P} is the overall volume fraction of particle. Finally the particle entropic free energy F_{p} is given by

$$F_{\mathrm{p}} = \frac{\varphi_{\mathrm{p}}}{\alpha} \cdot \ln\left(\frac{V \cdot \varphi_{\mathrm{p}}}{Q_{\mathrm{p}} \cdot \alpha} \right) - \frac{1}{V} \cdot \int d\mathrm{r} \cdot w_{\mathrm{p}}(\mathrm{r}) \cdot \rho_{\mathrm{p}}(\mathrm{r}) + \frac{1}{V} \cdot \int d\mathrm{r} \cdot \rho_{\mathrm{p}}(\mathrm{r}) \cdot \psi_{\mathrm{hs}} \cdot \left[\overline{\varphi}_{\mathrm{p}}(\mathrm{r}) \right] \qquad \textbf{(2-12)}$$

Where Q_{p} is the partition function of a single particle subject to the field $w_{\mathrm{p}}(\mathrm{r})$. α is the particle-to-diblock volume ratio. $\rho_{\mathrm{p}}(\mathrm{r})$ is the dimensionless centre of mass distribution. $\overline{\varphi}_{\mathrm{p}}(\mathrm{r})$ is the local particle volume fraction. ψ_{hs} is the Carnahan-Starling function for the excess free energy of a hard-sphere fluid. The last term of F_{p} describes the excess steric free energy of the particles through the density functional theory. The particles localize in the preferred domain and the large ones tend to stay in the center of the domain while the small ones stay near the A/B interface.

The thin film morphology of copolymer-nanoparticle confined in walls was investigated by using SCFT/DFT approach and scaling theory which is based on strong segregation model[26]. The particles were found to effectively modify the chemical nature of the wall/copolymer interface thus affect the polymer-wall interactions and consequently the structure of the film. When the nonselective particles localize at the selective walls at a sufficiently high concentration, the surface-parallel lamella structure switches to surface-perpendicular lamella. When the selective particles with affinity for A-component were driven to the nonselective wall, the wall was modified to become more A-like, causing the orientation switch from surface perpendicular to parallel. The results indicate that the entropically driven

effects are relatively robust and can be applied more generally than approaches based on chemistry-specific enthalpic effects.

Strong segregation theory was further developed by Pryamitsyn and Ganesan to calculate and predict the particle distribution and lamella thickness as well as lamella instability for the block copolymer-nanoparticle composites[27]. The approximation is only applicable when BCPs is within the limit of strong segregations that the length scale of interfaces is much small than microphase structures. There are three competing energetic effects for selective particles: (1) the decrease in A/B interfacial tension arising from the localization at the A/B interface; (2) the enthalpic gain in localizing into the A (or B) domain; (3) the reduction in polymer elastic penalty by localizing in the middle of the A (or B) domain. The calculation results of particle density distributions depending on the particle size (R) and selectivity (β) were shown in **Figure 2-11**. The parameter $\beta = (\eta_{AC} - \eta_{BC})/\eta_{AB}$, where η as interfacial tension, represents the particle selectivity for polymer component. For small particles and/or for stronger segregation between A and B phase, the particles can be expected to be more localized at the A/B interface. For larger particles and/or weak segregation, the particles tend to segregate into the preferred domain.

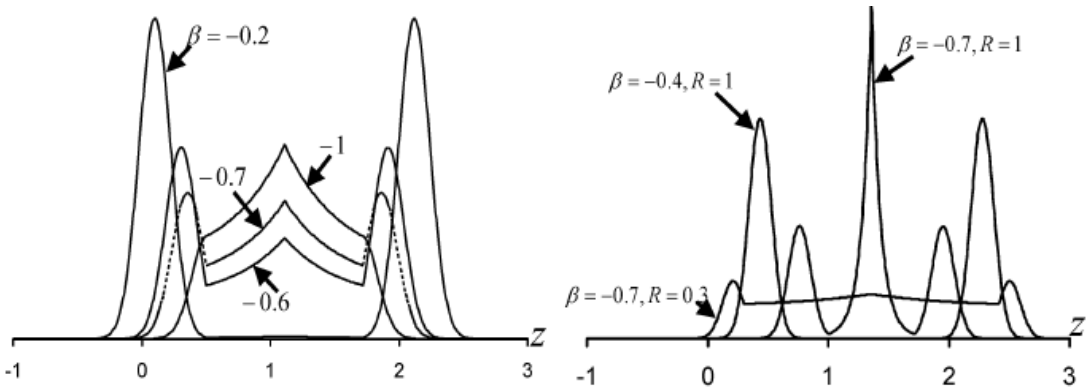

Figure 2-11. Typical particle density distributions (z = 0 corresponds to the AB interface and A segment occupy z>0). (a) Density profiles for R = 0.5, χN = 30, and υ = 0.5 for different selectivity parameters β. (b) Density profiles for different β and R combinations at χN = 100 and υ = 0.5. (Taken from ref. 27)

The variation in lamella thickness, $2(h - h_0)$, can be given by

$$\frac{h - h_0}{h_0} = \varphi_P \left[-\frac{11}{12} + \frac{2\pi R^2 \left(-1 + 5\beta^2\right)\sqrt{\chi N}}{15\upsilon} \right] \quad \textbf{(2-13)}$$

When $\beta \to 0$ (nonselective particles)

$$\frac{h-h_0}{h_0}=-\varphi_P\left[\frac{11}{12}+\frac{2\pi R^2\sqrt{\chi N}}{15\upsilon}\right] \quad \textbf{(2-14)}$$

Where $h_0=\sqrt[3]{2}(\chi N)^{1/6}$ is the height of the polymer brush, υ is the nondimensional occupied volume of the polymer and $\upsilon=N/R_g{}^3\rho_0$ (ρ_0 is the segmental/monomeric density), φ_P is the volume fraction of particles. The calculation indicates that there is a contraction of the lamella thickness due to the addition of nonselective particles. In contrast, for $\beta>>1$ (selective particles),

$$\frac{h-h_0}{h_0}=\varphi_P\left[\frac{2\pi R^2\beta^2\sqrt{\chi N}}{3\upsilon}\right] \quad \textbf{(2-15)}$$

there is a swelling of the lamellae upon the addition of selective particles, similar to the addition of a selective solvent. Over all, the degree of the swelling or contraction are generally dependent on the degree of segregation (χN and υ), the size of the particle R and the selectivity parameter β. It should be noted that the above arguments are strictly applicable only in the limit of dilute concentration of nanoparticles. When the brush height decreased to $h(\varphi_{P,c})<R_g$ (the unperturbed radius of gyration of the copolymer) at a critical particle concentration $\varphi_{P,c}$, corresponding to an over all compression of the polymer chains, lateral instabilities in the brushes and morphological transition can be caused.

2.4.2.2 Block copolymer/AuNPs

The controllability of nanoparticles location and distribution in the block copolymer matrix is the critical issue for the development of functional hybrid materials, which have superior electrical, magnetic, optical and/or photoelectric properties[175,176,177,178]. As theoretical prediction and simulation, nanoparticels can be selectively localized in the preferred domain or at the interface by varying the particle size, selectivity (modification) and volume fraction.

Kramer and co-workers investigated the effect of areal chain density and polymer ligand on the location of polymer-coated gold nanoparticles in block copolymers[12-14]. Thiol-end polystyrene (PSt-SH) coated gold nanoparticles were controlled localized in PSt microdomain or at the PSt/P2VP interface by varying the areal chain density[161]. By decreasing the areal chain density of coated PSt from 2.38 chains/nm^2 to 0.92 chains/nm^2, the AuNPs shifted the location from PSt-domain to PSt/P2VP interface.

Small particles (nonselective and selective) are predicted to localize in the A/B interface while large particles tend to localize at the center of microdomain. The results of experiments were found to be consistent with the theoretical prediction[15,16]. Bockstaller and Thomas

incorporated two kind of nanoparticles, gold particles of d_{core} = 3.5 nm and silica particles of d_{core} = 21.5 nm with the same modifier, into block copolymers[165]. Two distinct types of particles topologies in the block copolymer/nanoparticle blends have been identified, that the small particles localize at the intermaterial dividing surface and the large particles localize at the center of the respective polymer domain.

Incorporation of nanoparticles is an efficient way to guide the ordering and orientation of microstructures in block copolymer thin film by enthalpic and entropic effects[157,160]. Russel and co-workers used CdSe nanoparticles (4 nm) to direct the self-assembly the nanoparticle/copolymer mixture[5]. Upon 1 wt% of CdSe loading, which coated by tri-*n*-octylphosphine oxide, the cylindrical P2VP microdomains in the PSt matrix shifted to normal to the substrate. The particles were found to cap the P2VP cylinders at the air surface, which confirmed by grazing incidence small angle X-ray scattering (GISAXS), thus balanced the free surface interaction. The cylindrical P2VP-domain oriented perpendicularly to the substrate independent of the substrate nature or the film thickness (over 400 nm).

The hydrophilic PEO-coated gold nanoparticles were blended with PSt-*b*-PMMA and the hybrid thin film was further treated by solvent annealing at controlled humidity (~ 90 %) to get cylindrical PMMA domain perpendicular to the substrate[28]. The hydrophilic particles in PMMA domain interact with water vapor under the high humidity in the BCP/solvent swelling procedure which was attributed as the key factor for the change of cylinder orientation from parallel to perpendicular to substrate.

Gold nanoparticles coated by random copolymer P(MMA-*r*-St)-*b*-PSt-N_3-SH were tuned to be selective and nonselective (neutral) in block copolymer PSt-*b*-PMMA template by varying PMMA content in the P(MMA-*r*-St) block[18]. The selective gold particles (with 80 mol% PMMA) located with the PMMA domain and the nonselective particles (with 20 mol% PMMA) stayed at the PSt/PMMA interface, which leading to parallel and perpendicular lamella structure individually, confirmed by top-view and cross-sectional view TEM. The SCFT simulations showed that nonselective nanoparticles at the PSt/PMMA interface can move to the substrate to reduce the entropic penalty of the block copolymer chains.

2.4.3 Methods to investigate BCP hybrids and thin films

SAXS

Small angle X-ray scattering (SAXS) is a technique to study the structural features of colloidal size (one to hundreds of nm). The electrons resonate with the frequency of X-rays passing through the objects and emit coherent secondary waves, which interfere with each other[179]. Small angle X-ray scattering can be only observed when there is electron density inhomogeneity of colloidal size in the sample.

The SAXS patterns is scattering intensity (Lorentz-correlated intensity I*q2) vs. magnitude of the scattering vector q. The scattering vector is defined as

$$q = \left|\vec{q}\right| = \frac{4\pi \sin\Theta}{\lambda} \quad \textbf{(2-16)}$$

Where Θ is Bragg scattering angle, λ is wavelength of the X-rays. The distance of adjacent planes (d_{hkl}) can be determined from Bragg equation as

$$n\lambda = 2d_{hkl} \sin\Theta \quad \textbf{(2-17)}$$

Thus the correlation between the scattering vector q and d_{hkl} spacing (Bragg spacing) (distance between adjacent planes) is determined as

$$d_{hkl} = \frac{2\pi n}{q} \quad \textbf{(2-18)}$$

The relative morphology is estimated from the relative ratios of the observed peak positions with the position of the first existing peak[180].

For hexagonally packed cylinders, the relative ratios of the observed peak positions with the position of the first existing peak (q_{hkl}/q_{100}) are equal to 1, $\sqrt{3}$, $\sqrt{4}$, $\sqrt{7}$, $\sqrt{9}$ for the 1st to 5th scattering maxima (corresponding to hkl of 100, 110, 200, 210, 300). For lamellae morphology, the position ratios of q_{hkl}/q_{100} are equal to 1, 2, 3, 4, 5 corresponding to hkl of 100, 200, 300, 400, 500.

The BCPs phase separate into ordered structure of spherical, cylindrical or lamellar microdomains bellow order-disorder transition temperature **(chapter 2.4.1)**. Chemically distinct microdomains, such as PPMA-domain and PMMA-domain for PPMA-*b*-PMMA, have different electron density thus can be analyzed by SAXS to get information about the microdomain size, shape and arrangement for the BCPs in bulk.

GISAXS

Grazing-incidence small angle X-ray scattering (GISAXS) is a versatile tool for characterizing nanoscale density correlations and/or the shape of nanoscopic objects at surfaces, at buried interfaces, or in thin films[20]. In order to make X-ray scattering surface sensitive, a grazing incidence angle α is chosen between about half the critical angle α_c and several critical angles of the film material. A full penetration of hundreds nm into the sample can be achieved.

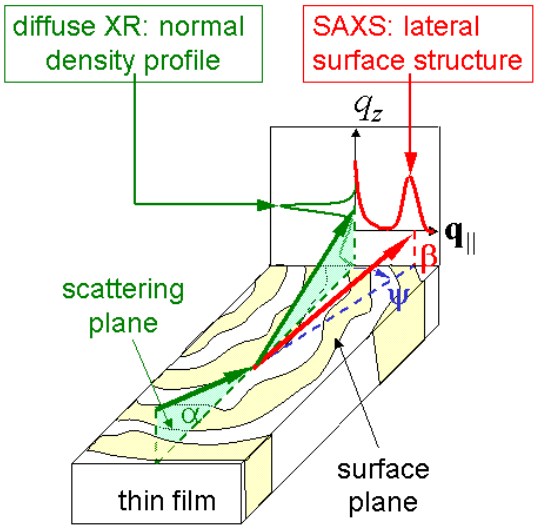

Figure 2-12. GISAXS scattering geometry: incident angle α, in-plane scattering angle ψ, and exit angle β. The cut of the incident plane with the area detector corresponds to a detector scan in diffuse reflectivity. Lateral structure in the films gives rise to SAXS-like scattering parallel to the sample surface. Line scans corresponding to these two special situations are indicated as the red and green curves. (Taken from ref. 21)

GISAXS provides information of both lateral and normal ordering at a surface or inside a thin film[181]. For the extreme cases of symmetric BCP thin films, when the lamellae align parallel to the substrate, typical stripes of intensity at regular spacings along the q_z direction appear in GISAXS. When the lamellae orient perpendicularly to the substrate, correlation peaks parallel to the interface, with a rod-like shape normal to the surface appear. In the case of disordered or partially ordered lamellae where the lamellae have a finite distribution of tilt angles with respect to the interface, rings or partial rings appear in the intensity maps. Each case has a well-defined signature in GISAXS intensity pattern.

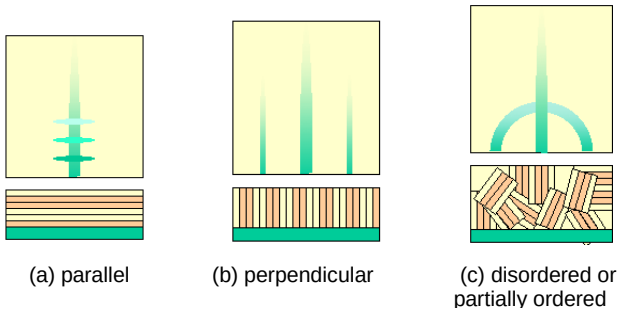

Figure 2-13. The extreme cases of symmetric BCP thin films with lamellar structure in GISAXS[182]. (Lower images: schematic side view; upper images: GISAXS pattern)

Due to the penetration power of x-rays, not only surface structures, but also the internal structure of thin films and buried interfaces can be studied without any need of elaborate

sample preparation, as needed in cross-sectional TEM.

AFM

Atomic force microscopy (AFM) is a form of scanning probe microscopy (SPM) in which a sharp probe is scanned across a sample surface and the probe/sample interaction is monitored. AFM is a versatile tool in polymer film characterization with regard to both surface topography and phase morphology. There are three primary modes of AFM, contact mode AFM, non-contact mode AFM and tapping mode AFM. In tapping mode, the silicon probe tip oscillates at its resonance frequency as it rasters across the sample surface, experiencing only intermittent contact with the surface. Due to the lower forces and less damage to soft samples imaged in air, tapping mode AFM is mostly employed in analysis of polymer films.

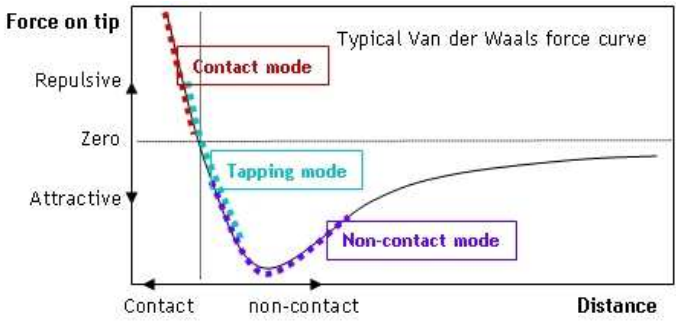

Figure 2-14. The repulsive and attractive force regimes as AFM tip approaching the sample[183].

In tapping mode AFM, a tip attached to the end of an oscillating cantilever lightly “taps” on the sample surface during scanning across the sample surface. The cantilever is oscillated at or slightly below its resonance frequency with amplitude ranging typically from 20 nm to 100 nm. The feedback loop maintains constant oscillation amplitude by maintaining a constant RMS of the oscillation signal acquired by the split photodiode detector. By maintaining constant oscillation amplitude, a constant tip-sample interaction is maintained during imaging. The vertical position of the scanner at each (x,y) data point is stored by the computer to form the topographic image of the sample surface.

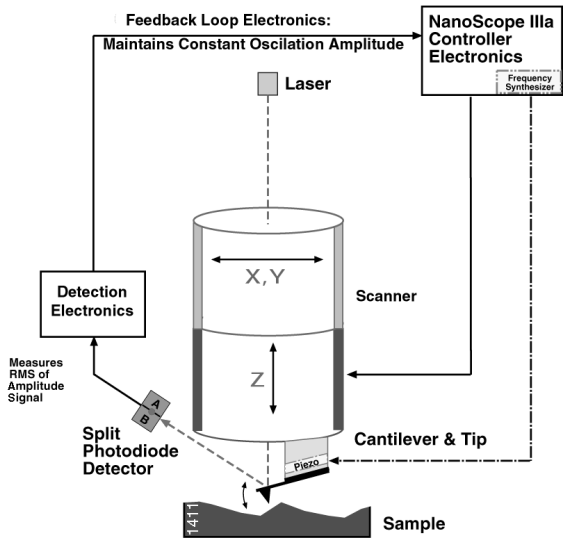

Figure 2-15. Feedback loop electronics in tapping mode AFM[184].

There are three types of data in tapping mode AFM. **Height Data**: The vertical position of the probe tip is monitored by noting changes in the length of the z-axis on the xyz scanning piezo tube. The change in the z-axis is plotted as a topographical map of the sample surface. **Phase Data**: The phase offset, or phase angle, of the input drive signal of piezo with respect to the phase offset of the oscillating cantilever is monitored. The phase offset between the two signals is defined as zero for the cantilever oscillating freely in air. As regions with different elasticity encounter on the sample surface, the phase angle between the two signals changes. These changes in phase offset are due to differing amounts of damping experienced by the probe tip as it rasters across the sample surface. These differences are plotted as the so-called 'phase image'. **Amplitude Data**: The amplitude of the cantilever is monitored by the photo diode detector. The RMS value of the laser signal on the y-axis of the detector is recorded for each segment on a given raster of the probe tip. These values are plotted as an amplitude map of the sample surface. Amplitude images show well the edges of surface features which are not shown in height data.

TEM

Transmission electron microscopy (TEM) is a microscopy technique in which a beam of electrons is transmitted through an ultra-thin specimen, interacting with the specimen as it passes through. An image is formed from the transmitted electrons and focused onto an imaging device[185]. The maximum resolution (d) in light microscope is limited by the wavelength of the photons (λ) and the numerical aperture of the system (NA) as in equation

$$d = \frac{\lambda}{2n\sin\alpha} \approx \frac{\lambda}{2NA} \quad \textbf{(2-19)}$$

TEM is thus capable of imaging at a significantly higher resolution than light microscopy due

to the smaller de Broglie wavelength of electrons[186]. Electrons are generated by thermionic emission from a filament, usually tungsten, or by field electron emission and then accelerated by electric potential and focused onto the sample by electrostatic and electromagnetic lenses. The transmitted beam containing information about electron density, phase and periodicity is used to form an image.

At smaller magnifications TEM image contrast is due to absorption of electrons in the material. The contrast formation is formed directly by occlusion and absorption of electrons in the species. Thicker regions or regions with a higher atomic number appear dark, whilst regions with no sample in the beam path appear bright, as also called "bright field". Samples can exhibit diffraction contrast when the electron beam undergoes Bragg scattering. If the reflections are selected to exclude the unscattered, the image will appear dark wherever no sample scattering arises, called dark-field image.

At higher magnifications, as in high-resolution transmission electron microscopy (HRTEM), the images are formed due to differences in phase of electron waves, known as phase contrast, in which the image is not only dependent on the number of electrons hitting the screen, making direct interpretation of phase contrast images more complex.

For biological and polymeric materials, staining with heavy metals is usually employed to enhance contrast. Compounds of heavy metals, such as osmium, lead, uranium or gold can be used to selectively deposit electron dense atoms to the desired regions of sample.

SEM

Scanning electron microscopy (SEM) is an electron microscopy technique in which a focused electron beam scans over the sample surface and the emitted electrons by atoms excited by the electron beam are detected to produce an image about the sample’s surface topography and composition. The emitted electrons detected in SEM include secondary electrons (by inelastic scattering), back-scattered electrons (by elastic scattering), characteristic X-ray (by removing an inner shell electron). The signals are amplified by an electronic amplifier and displayed as variations in brightness in an image.

The magnification in SEM results from the ratio of the dimensions of the raster on the sample surface and the raster on the display device, which is different from TEM, in which the magnification is a function of the power of the objective lens. Higher magnification is obtained by reducing the size of the raster on the specimen. Thus, the magnification is controlled by the current supplied to the x, y scanning coils.

The detection of secondary electrons (emitted from k-shell of atoms by inelastic scattering) is the most common imaging mode. The electrons are first attracted towards an electrically biased grid and then further accelerated to a phosphor or scintillator to emit flashes of light (cathodoluminescence). The flashes are conducted to a photomultiplier and displayed as a

two-dimensional intensity distribution which can be viewed and saved as digital image. The brightness of the signal depends on the number of the secondary electrons reaching on the detector. As the incident angle of electron beam increase, the “escaped” distance of one side of the beam deceases and more secondary electrons are emitted. Thus, the steep surfaces and edges tend to be brighter than flat surfaces. In the mode of back scattered electrons detection, the heavy elements of higher atomic number backscatter electrons more strongly than light elements of low atomic number and appear brighter in the image.

3 Nanostructured block copolymers and SH-terminated polymers: synthesis and discussion

3.1 Non-functionalized PPMA-*b*-PMMA by living anionic polymerization

Block copolymers poly(pentyl methacrylate)-*b*-poly(methyl methacrylate) (PPMA-*b*-PMMA) were synthesized by living anionic polymerization aiming to get high molecular weight and narrow dispersity. The phase separation behavior of block copolymers in bulk is dominated by the Flory-Huggins interaction parameter, the degree of polymerization and the volume ratio of the segments (**Chapter 2.4**). Block copolymers with narrow dispersity can serve to get nanostructures in uniform size by phase separation in bulk as well as in thin films.

As the propagating species of carbanions in anionic polymerization are vulnerable to oxygen, moisture and any other proton-donors, the synthesis must be carried out under rigorous conditions (**Chapter 2.1**). All reactants, including monomers, solvent and initiator were purified strictly as described in the experimental section. The reaction was carried out under argon with syringe techniques.

As shown in **Scheme 3-1**, diphenylethylene (DPE) was used to combine with sec-BuLi to attenuate the nucleophilicity of initiator so as to avoid the attack to the carbonyl group of monomer pentyl methacrylate (PMA) and of propagating chains[59,60]. 10 molar excess of LiCl with respect to initiator was added as ligand.

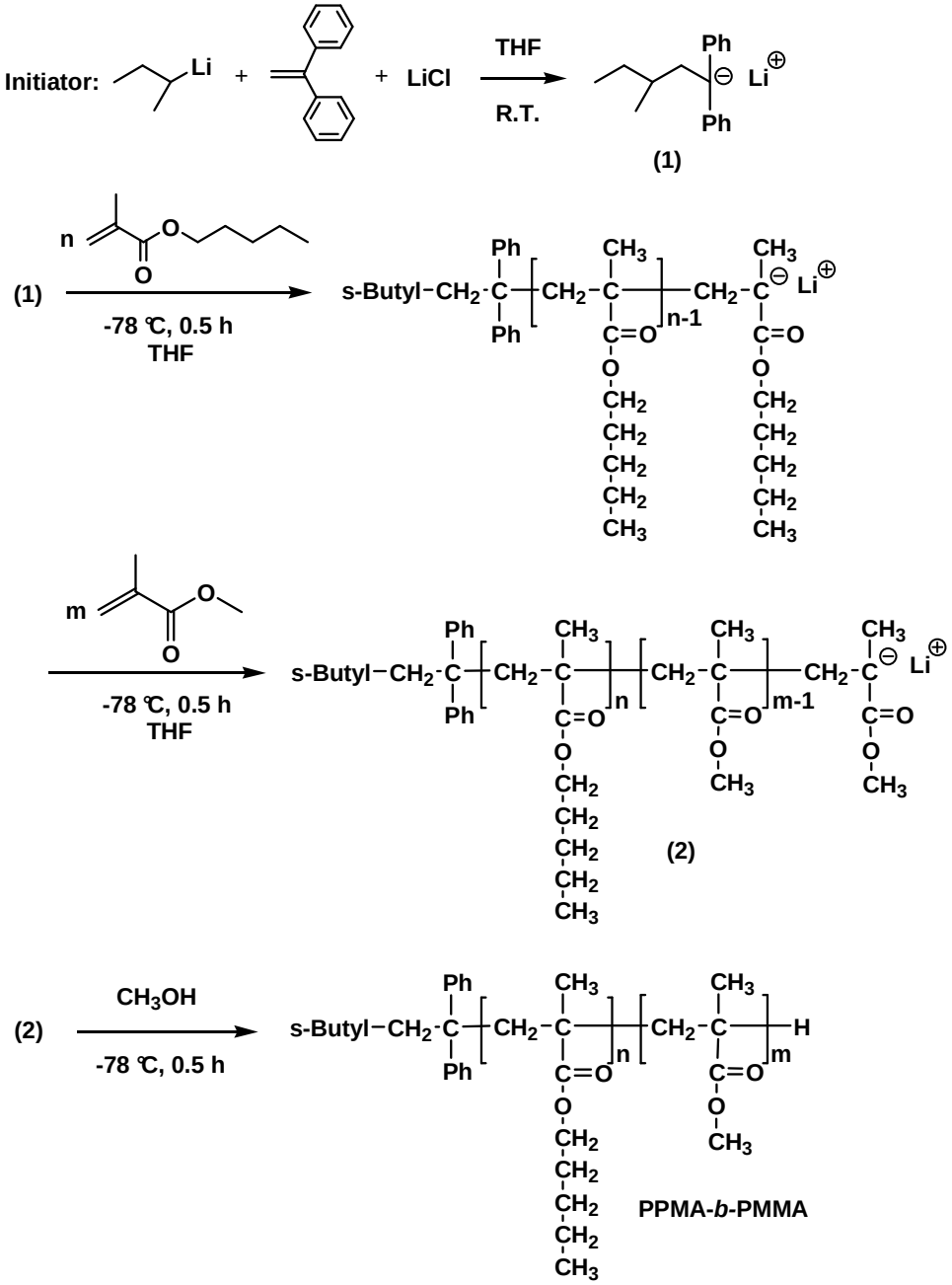

Scheme 3-1. Synthetic route of PPMA-*b*-PMMA by living anionic polymerization.

Excess LiCl was supposed to form 1:1 and 2:1 adducts with propagating chain (**Scheme 2-7**). The fast equilibrium from adducts toward to the associated ion-pair of $(PPMA^-/Li^+)_2$ was attributed to lead to the narrow dispersity. Methyl methacrylate (MMA) was sequentially added after complete consumption of the first monomer PMA (usually after 30 min). The final

copolymer, sample PM4, showed a shorter retention time in GPC analysis than PM4-1 which was withdrawn before adding MMA **(Figure 3-1)**. Both PM4-1 and PM4 had narrow dispersity Đ < 1.10 and the block ratio of PM4 calculated from ^{1}H NMR matched to the feed ratio very well (**Table 3-1**), indicating the polymerization proceeded in a living and controlled way free from side reactions and termination.

Table 3-1. Characterizations of synthesized PPMA-b-PMMA block copolymers.

Sample	**Feed details**		**NMR**[b]				**GPC**[c]	
PPMA$_n$-*b*-PMMA$_m$	**g/mol**	**n/m**	**n**	**m**	**n/m**	**M_n (g/mol)**	**M_n (g/mol)**	**M_w/M_n**
PM5	5000	40/60	38	64	37.2/62.8	14020	9600	1.07
PM5-1	Sampling[a]		--	--	--/--	--	5100	1.09
PM4	10000	70/30	93	43	68.1/31.9	16010	15400	1.07
							18300	1.04[d]
PM4-1	Sampling[a]		--	--	--/--	--	12500	1.07
PM8	5000	40/60	41	64	39.1/60.9	14080	7900	1.09
							10900	1.07[d]
PM7	20000	70/30	151	70	68.2/31.8	26020	21100	1.11
PM84	30000	70/30	83	209	28.4/71.6	40900	30900	1.11[e]
PM11	50000	40/60	--	--	49.3/50.7	--	54600	1.16
PM13	50000	70/30	--	--	72.2/27.8	--	54200	1.14

[a] withdrawing sample before adding second monomer, terminated with MeOH; [b] in $CDCl_3$; [c] in THF with RI detector and PMMA as calibration; [d] in $CHCl_3$, PSt as calibration; [e] in DMAc, PMMA as calibration.

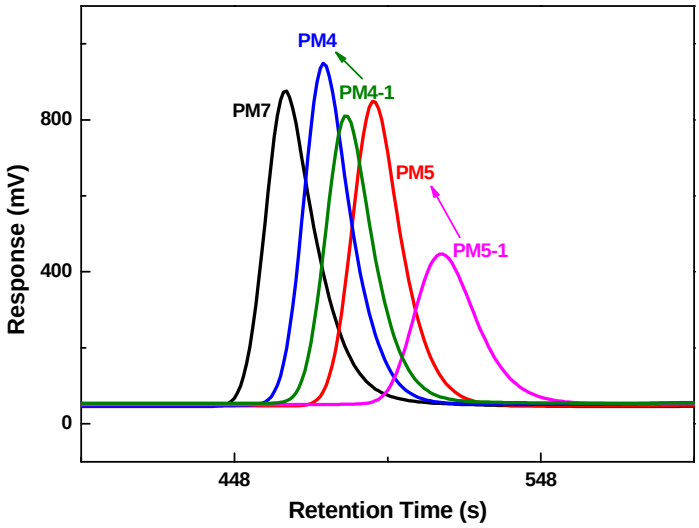

Figure 3-1. GPC curves of PPMA-*b*-PMMA (PM4, PM5 and PM7) and the corresponding withdrawn samples before adding second monomer (PM4-1 and PM5-1). THF was used as elution solvent and PMMA as calibration.

Block copolymers PPMA-*b*-PMMA with varied molecular weight and block ratio were successfully synthesized as shown in **Table 3-1**. The chemical structures were confirmed from ^{1}H NMR as seen in **Figure 3-2**. The molar ratio of PMA/MMA (n/m) was calculated from the integration of OC$\underline{H}_2$ of PPMA-block and OC$\underline{H}_3$ of PMMA-block as $\frac{2n}{3m} = \frac{A_{OCH_2}}{A_{OCH_3}}$. For the case of molecular weight M_n < ~20000 g/mol (**Figure 3-2** PM8), M_n can be calculated from the integration of OC$\underline{H}_2$ and OC$\underline{H}_3$ compared to the phenyl group from initiator as $\frac{10}{2n} = \frac{A_{C_6H_5}}{A_{OCH_2}}$ and $\frac{10}{3m} = \frac{A_{C_6H_5}}{A_{OCH_3}}$. Thus, the molecular weight of block copolymers based on NMR analysis was given by

$$\mathbf{M_n = 156n + 100m + MW_{Ini}} \quad \mathbf{(3\text{-}1)}$$

where MW_{Ini} is the molecular weight of initiator and here $M_{n,Ini}$ = 237 g/mol. For the (co)polymers with higher molecular weight M_n > ~20000 g/mol (**Figure 3-2** PM11), the integration from initiator in ^{1}H NMR was not discernible, thus M_n was evaluated from GPC.

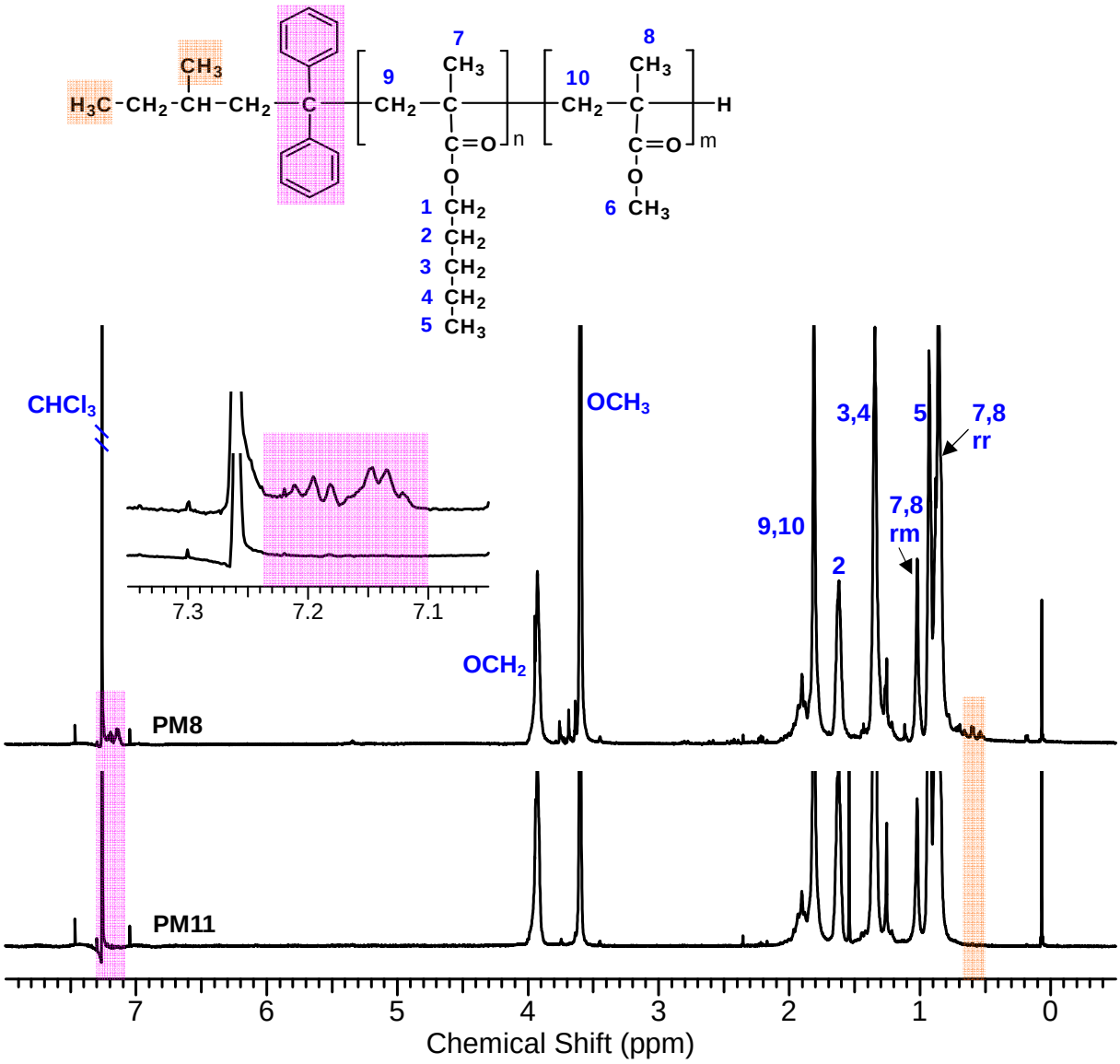

Figure 3-2. ^{1}H NMR (in $CDCl_3$) spectra of PM8 (M_n = 7900 g/mol) and PM11 (M_n = 54600 g/mol, phenyl group from initiator is not discernible).

To conclude here, block copolymers PPMA-*b*-PMMA with predetermined molecular weight and segmental ratio were successfully synthesized by living anionic polymerization under standard conditions of MMA polymerization. PPMA-*b*-PMMA with microphase separation (samples PM11 and PM13) was next chosen as templates in BCP/AuNP hybrid thin films.

3.2 Thiol-terminated polymers by living anionic polymerization

The reaction of polymeric organolithium species with electrophiles in anionic polymerization is a straightforward way to produce end-functionalized polymers. Termination of living anionic polymeric chains with alkyl halides and silyl halides is a general method to prepare ω-functionalized polymers (**Chapter 2.1.4**). The prominent advantage is the high degree of functionality. Each polymer owns a functional end-group given a high purified terminator.

Alkyl halide terminator: *tert*-butyldimethylsilyl 3-chloropropyl sulfide (TDSCS)

tert-Butyldimethylsilyl 3-chloropropyl sulfide was synthesized by reaction of 3-chloro-1-propanethiol with *tert*-butyldimethylsilyl chloride to protect the thiol group[9] (**Scheme 7-1**). There was a high yield of > 95 %. After purification and drying followed by twice distillation over CaH_2, the final product TDSCS was confirmed with high purity by ^{1}H NMR as seen in **Figure 3-3** and further confirmed to have a purity of ~98 % by GC-MS.

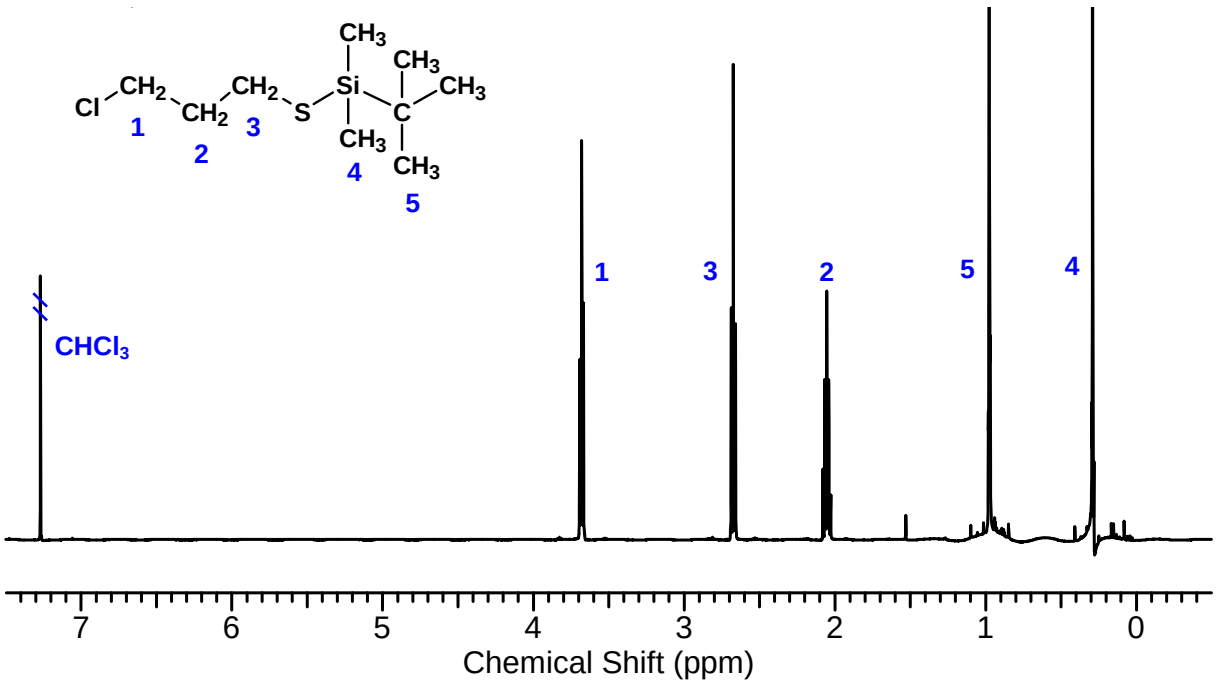

Figure 3-3. ^{1}H NMR (in $CDCl_3$) spectrum of synthesized terminator TDSCS.

The synthesized TDSCS was successful in termination of anionic polymerization of styrene. The end-functionality was confirmed by ^{1}H NMR (**Figure 3-4**) and ^{13}C NMR. The functionality was calculated from the integration of $Si(C\underline{H}_3)_2$ from the end-group and $C\underline{H}_3$ from the starting group (initiator) as $f = \frac{A_{Si(CH_3)_2}/6}{A_{CH_3(Ini)}/6}\%$. However, TDSCS was not successful in

end-capping anionic PMMA⁻ even at large molar excess of TDSCS > 10 PMMA⁻ and at elevated temperature for over 24 h. The functionality was too low to be discernible from ^{1}H NMR. A series of α-halo-ω-functional alkanes were developed to end-cap anionic polystyrenes (PSt) and polyisoprenes (PI) by Hirao and co-workers[8,86]. The high efficiency (~100 %) of functionality free from side reactions was attributed to the high enough nucleophilicity of the living polymer anions. As the nucleophilicity of anionic PMMA⁻ is lower than anionic PSt⁻ and PI⁻ (**Chapter 2.1**), the carbanion of propagating PMMA⁻ is not nucleophilic enough to attack the Cl–C bond of terminator TDSCS. Terminators with higher electrophilicity are needed to end-cap PMMA⁻ in anionic polymerization.

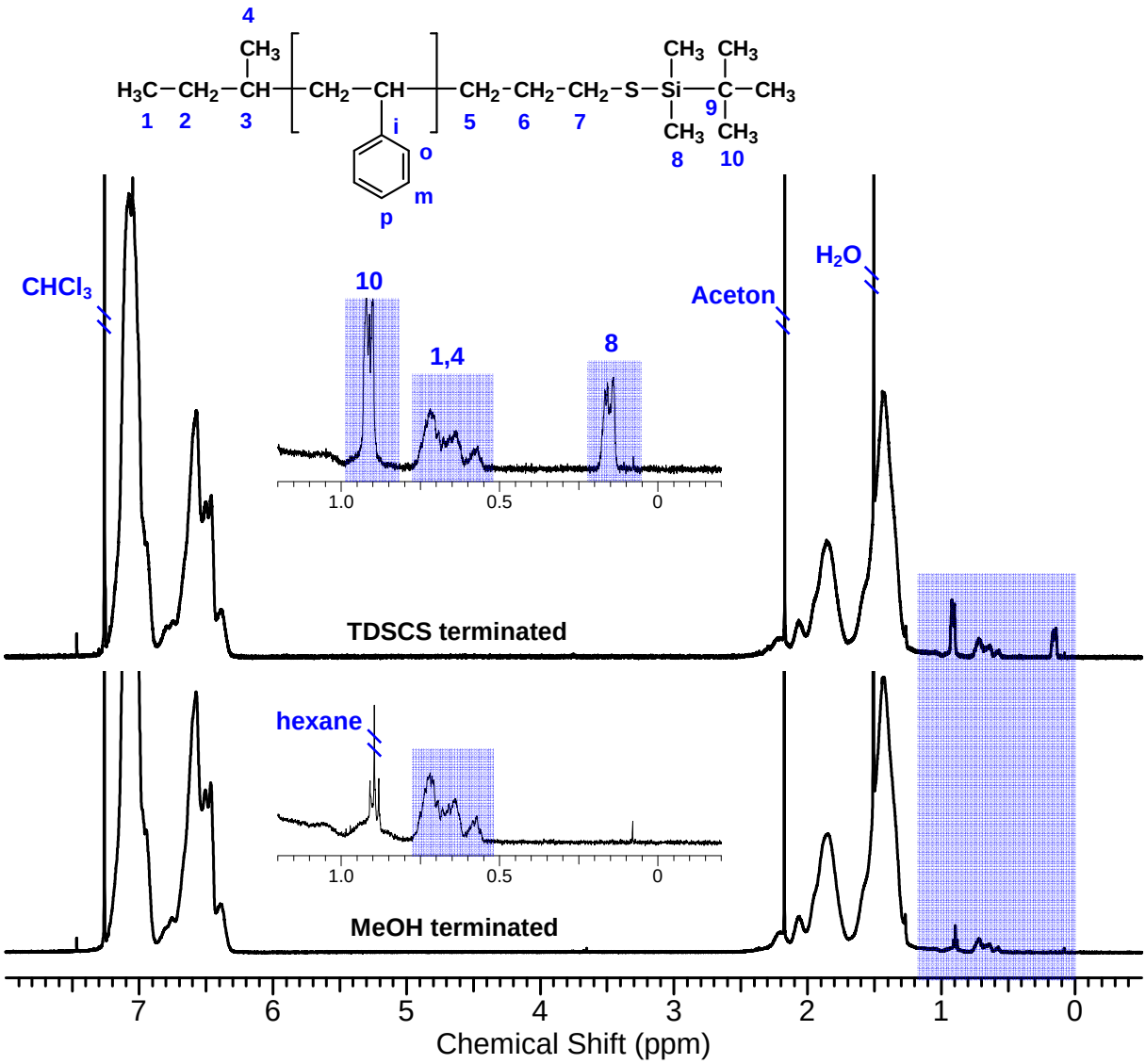

Figure 3-4. ^{1}H NMR (in $CDCl_3$) spectra of polystyrene terminated by TDSCS (PSt27) and by MeOH (PSt8).

Silyl halide terminators: Dimethylsilyl chloride and *tert*-butyldimethylsilyl 3-(chlorodimethylsilyl)propyl sulfide (TSCSPS)

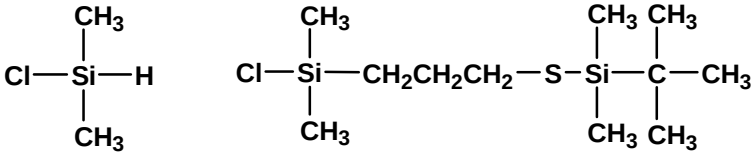

Scheme 3-2. Silyl halide terminators.

Dimethylsilyl chloride was also successful in termination of anionic polymerization of styrene. The end-functionality was confirmed by ^{1}H NMR (**Figure 3-5**) and ^{13}C NMR (**Figure 3-6**). The functionality was calculated from the integration of Si(C<u>H</u>$_3$)$_2$ from the end-group and C<u>H</u>$_3$ from the starting group (initiator) as $f = \frac{A_{Si(CH_3)_2} / 6}{A_{CH_3(Ini)} / 6} \%$. However, dimethylsilyl chloride was again not successful in end-capping anionic PMMA$^-$ even at large molar excess of TDSCS > 10 PMMA$^-$ and at elevated temperature.

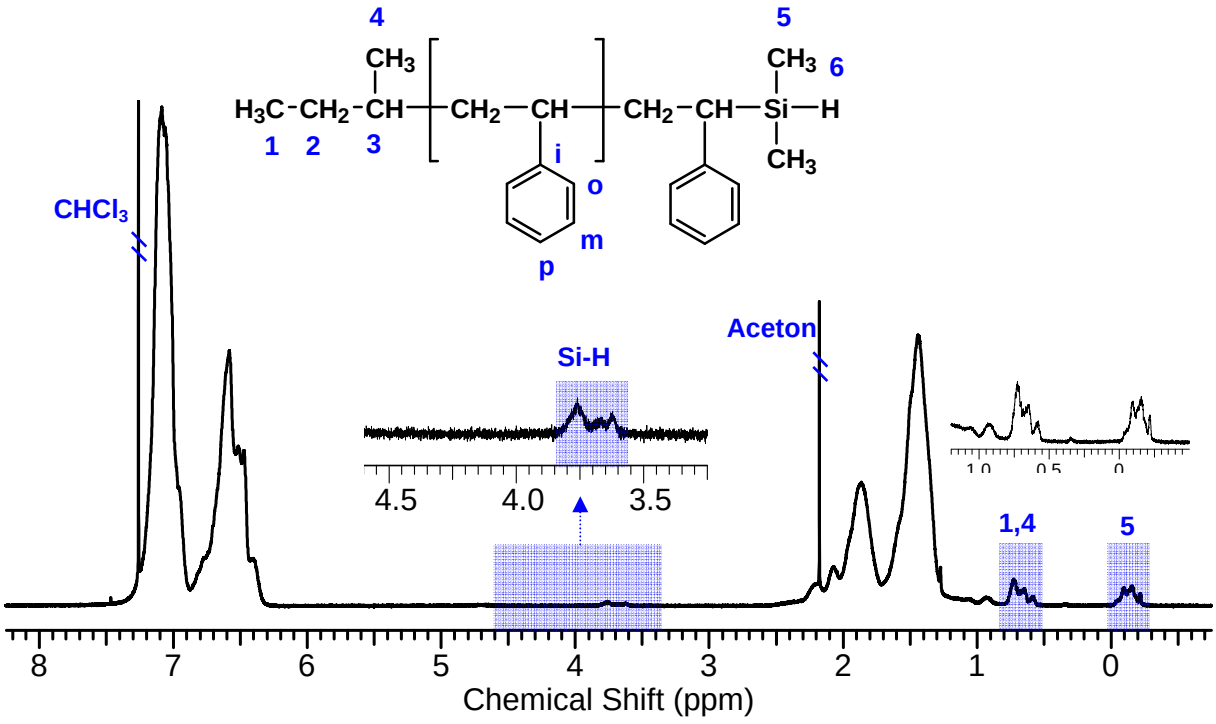

Figure 3-5. ^{1}H NMR (in $CDCl_3$) spectrum of polystyrene (PSt28) terminated by dimethylsilyl chloride.

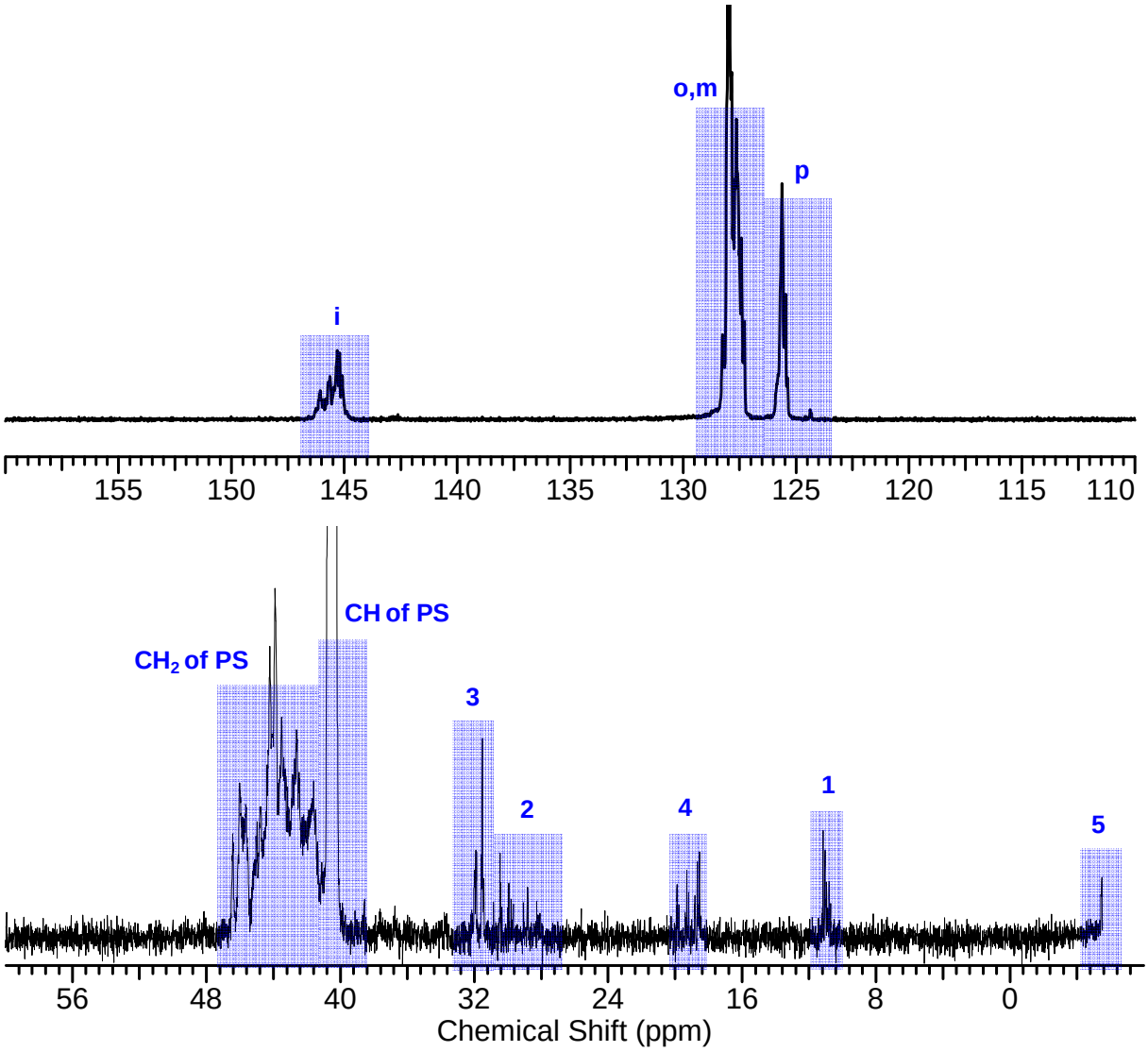

Figure 3-6. ^{13}C NMR (in $CDCl_3$) spectra of polystyrene (PSt28) terminated by dimethylsilyl chloride.

Chlorosilanes with protected amino and hydroxyl groups were used to prepare end-functionalized polymers by anionic polymerization[86,187]. **Scheme 3-2** (right one) shows the chlorosilane derivative with protected thiol group. The methodology is applicable to a wide range of polymeric nucleophiles from polysiloxanolates to polystyrenics. 4-(Chlorodimethylsilyl)-styrene was also successful in end-capping anionic P*t*BA with functionality > 90 %[188]. Due to the presence of the methyl group on the carbanionic site of $PMMA^-$, a slightly higher reactivity can be expected for $PMMA^-$. However, dimethylchlorosilane, here successfully end-capped PSt^- but failed for $PMMA^-$.

To conclude, alkyl chloride with protected thiol group (synthesized) and silyl chloride were successfully used in terminating PSt^- which was confirmed by ^1H and ^{13}C NMR. However, these terminators failed to terminate $PMMA^-$. Thiol end-functionalized PMMA were prepared by RAFT polymerization in the next step (chapter 3.4).

3.3 P4VP-*b*-PMMA/PPMA by living anionic polymerization

As the nitrogen of pyridine group in P4VP can coordinate with Au^{3+}, P4VP-based block copolymers were synthesized to be applied in stabilizing gold nanomaterials and also as template for BCP/AuNP hybrids. P4VP-*b*-PMMA and -PPMA with varied molecular weight and P4VP-content were synthesized by living anionic polymerization.

3.3.1 P4VP-*b*-PMMA with short P4VP-block synthesized in THF

P4VP-*b*-PMMA and -PPMA with 4VP units of n = ~10 were synthesized in THF with similar procedure as polymerization of PPMA-*b*-PMMA. 10 molar excess of LiCl was employed and the polymerization was carried out at -78 ℃. Homop olymer P4VP is not soluble in THF above a critical degree of polymerization of 20 units[88] as discussed in chapter 2.1.5. In our study, short P4VP-block with n < 10 **(Table 3-2)** gave a clear solution in THF and anionic $P4VP^-$ was yellow-green until adding second monomer MMA. Diphenylethylene (DPE) was also used to combine with sec-BuLi followed by adding 4VP. The red solution of initiator turned to yellow-green at first drop of 4VP and completed in several seconds, which indicated the fast initiation of 4VP.

Table 3-2. Characterization of P4VP-based block copolymers by anionic polymerization.

Sample	Solvent	Feed details[a]	NMR		GPC	
$P4VP_n$-*b*-$PMMA_m$		g/mol; n/m	n, m	n/m	M_n (g/mol)	M_w/M_n
P4VPM42	THF	1300; 20/80	11, 46	19.3/80.7	3400	1.25[b]
P4VPM43	THF	7000; 10/90	7,61	10.2/89.8	8400	1.21[b]
P4VPM30	THF	10000; 5/95	6,170	3.4/96.6	11900	1.13[b]
P4VPP85	THF	10000; 5/95	6,107	5.3/94.7	21200	1.14[c]
P4VPM35	THF+pyridine	40000; 20/80	--/--	12/88	16500	1.08[b]
P4VPM37	pyridine[e]	20000; 20/80	--/--	27.8/72.2	38400	1.28[d]

[a] all samples without addition of DPE before adding MMA or PMA except P4VPM30; all with DPE before adding 4VP; [b] in THF, PMMA as calibration, RI detector; [c] in $CHCl_3$, PSt as calibration, RI detector; [d] in DMAc, with LS fit; [e] reaction at ~-12 ℃ (ice + NaCl), and the others a t -78 ℃.

Before adding MMA, DPE was added to combine with $P4VP^-$. However, $P4VP^-$ without combination with DPE also initiated MMA very fast according to the fast color change of the

solution from yellow-green to colorless at first drops of MMA. The molecular weight and block ratio matched well to the feed ratio from ^{1}H NMR analysis as shown in **Table 3-2**. As discussed in **Chapter 2.1.3**, the nucleophilicity of initiator sec-BuLi has to be attenuated by combination with DPE or other clumsy compound so as to avoid the attack to the carbonyl group of MMA[59,60]. The carbanion of P4VP$^-$ had reduced nucleophilicity although not as weak as DPE combined sec-BuLi, so P4VP$^-$ could initiate MMA fast enough and without attack of the carbonyl group of MMA. The final block copolymers with narrow dispersity further confirmed the sequential copolymerization of MMA from P4VP$^-$ free from noticeable side reactions.

The repeating units of P4VP block were calculated from the integration of pyridine group $NC_5\underline{H}_4$ and the phenyl $C_5\underline{H}_5$ from starting group in ^{1}H NMR (**Figure 3-7**) as given by $\frac{2n}{10}=\frac{A_b}{A_c}$. The repeating units of PMMA block were also obtained as given by $\frac{3m}{10}=\frac{A_{OCH_3}}{A_c}$.

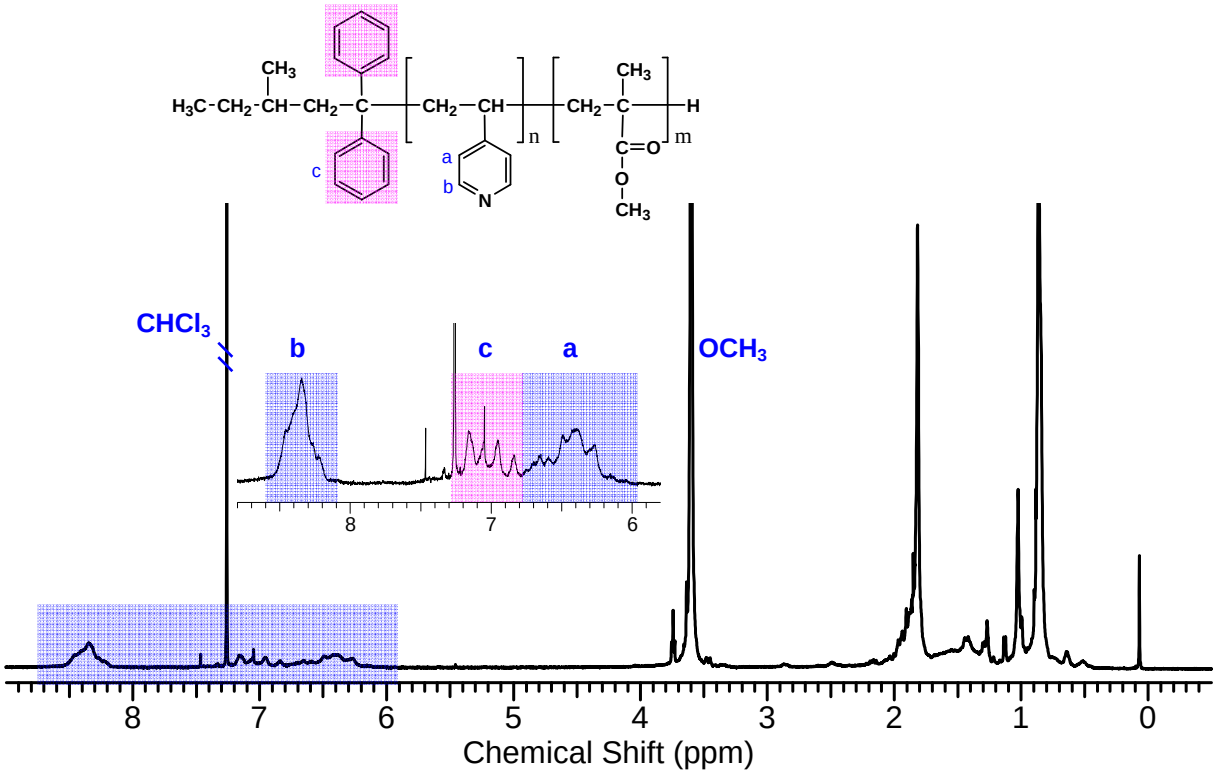

Figure 3-7. ^{1}H NMR (in $CDCl_3$) spectrum of P4VP-*b*-PMMA (P4VPM42) by anionic polymerization.

3.3.2 P4VP-*b*-PMMA with long P4VP-block synthesized in pyridine

Sequential polymerization of 4VP after another living block which is soluble in THF is a solution to improve the solubility so as to carry out the polymerization in THF. However, styrene is not expected to be sequentially added to PMMA$^-$ because of the higher pK_a of the

conjugated acid of PSt^- (pK_a = 43 and 31 respectively for the conjugated acid of PSt^- and $PMMA^-$) as discussed in **Chapter 2.1.3**. Experimentally $PMMA^-$ was not able to initiate the copolymerization of styrene[189]. In our study, 4VP was tried to sequentially copolymerize from $PMMA^-$ in THF but it was not successful. This is attributed to the similar reason as copolymerization of St from $PMMA^-$.

Higher molecular weight P4VP block was then polymerized in pyridine, which is a good solvent for P4VP. As the freezing point of pyridine is -42 ℃, the reaction has to be carried out at elevated temperature compared to -78 ℃ in anionic polymerization MMA in THF. In our study, ~-12 ℃ (ice + NaCl) was maintained to polymerize 4VP in pyridine. The color of $P4VP^-$ in pyridine was yellow-orange, somehow different from $P4VP^-$ in THF (yellow-green). The polymerization of 4VP was maintained for 1 h followed by adding the second monomer MMA. The solution changed into colorless at first drops of MMA indicated the fast initiation from $P4VP^-$ to MMA. The final copolymers showed narrow dispersity, as Đ = 1.28 for P4VPM37 in **Table 3-2**. The block ratio (27.8/72.2 from NMR) was also close to the feed ratio (20/80). The results indicate that the anionic polymerization 4VP in pyridine at elevated temperature proceeded in a controlled way free from noticeable side reactions. Pyridine was proposed to act not only as solvent but also as σ-type ligand like the mechanism in anionic polymerization of MMA, thus directed the polymerization in a controlled way (**Scheme 2-13**)[90,91].

To conclude here, $P4VP_n$-based copolymers with short (n = ~10) and long P4VP-block were synthesized by living anionic polymerization by choosing proper solvent system, THF or pyridine, depending on the P4VP-block length. These P4VP-based block copolymers were employed in stabilizing AuNPs in the next step.

3.4 SH-terminated PMMA and PPMA by RAFT

Homo- and block copolymers were synthesized by RAFT method with dithiolate as chain transfer agent (CTA) followed by aminolysis to get thiol end-functionality. As thiol-based species are strong ligands for stabilizing Au nanomaterials, PMMA-SH and PPMA-SH with varied molecular weight were synthesized for modification of AuNPs.

3.4.1 Homo- and block copolymers by RAFT with dithiolate compound as CTA

MMA was synthesized in toluene at 70 ℃ with 2- phenyl-2-propyl benzodithiolate as chain transfer agent[190] (**Scheme 3.3**). For diblock copolymers, first-synthesized PMMA-SCS with dithioester-end was used as macro-CTA for copolymerization of the second monomer PMA.

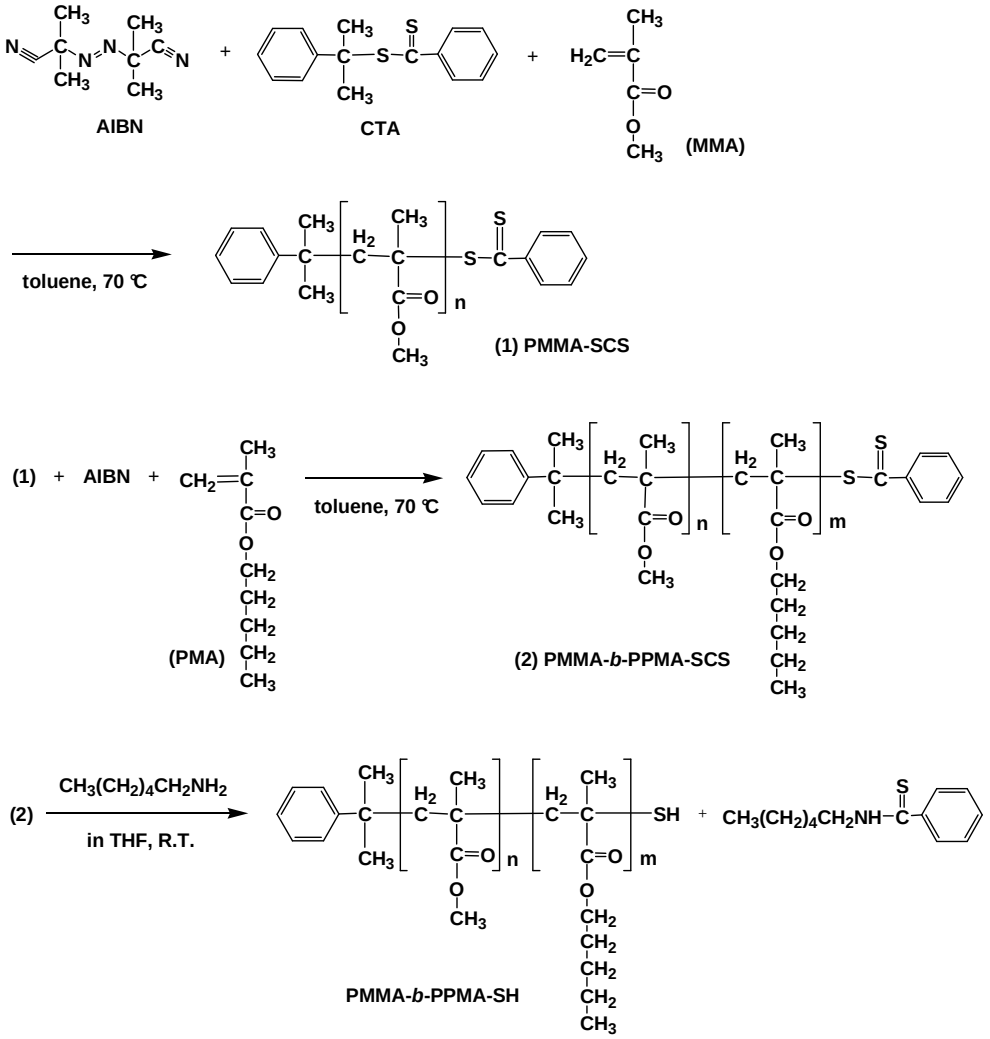

Scheme 3-3. Synthetic route of polymers by RAFT and the aminolysis.

The homopolymerization of MMA was monitored by withdrawing samples through

degassed syringe at differently timed intervals for ^{1}H NMR and GPC analysis. **Figure 3-8** shows the polymerization kinetics of MMA using 2-phenyl-2-propyl benzodithiolate as CTA. There was an induction period of 2 h which was attributed to the pre-equilibrium of CTA activation and initialization in the RAFT process (**Scheme 2-14**). The conversion of MMA was 53.9 % at reaction time of 48 h. However, the first-order polymerization kinetic of MMA was conducted until ~40 %. The molecular weight had a linear evolution versus monomer conversion together with narrow dispersity (~1.2–1.3).

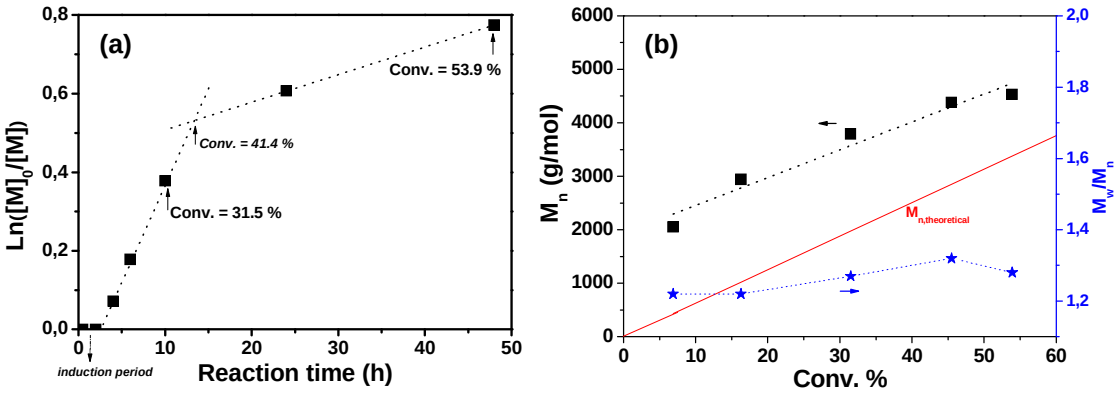

Figure 3-8. (a) Kinetic study of RAFT polymerization of MMA in toluene at 70 ℃. [AIBN] = 8.3 * 10^{-3} M, [CTA] = 4.1 * 10^{-2} M, [MMA] = 2.5 M. (b) Molecular weight (M_n, determined by GPC in $CHCl_3$ with PSt as calibration) versus conversion (■). The theoretical molecular weight (—) is given by **Formula (3-2)**.

Besides, the molecular weight could be controlled by the feed molar ratio of monomer/CTA. **Figure 3-9** shows the homopolymerization of MMA with varied molar ratio of MMA/CTA. With the same reaction time of 16 h (PMMA51 (▼), PMMA56 (▲), PMMA63 (♦)), similar conversions (60–70 %, by weight method) were obtained. The molecular weight (M_n) increased linearly as increasing molar ratio of MMA/CTA. However, M_n determined by NMR and GPC was higher than the theoretical one. Here the theoretical M_n was calculated by

$$M_{n,conv}^{th} = ([M]_0 / [CTA]_0) \cdot MW_{MMA} \cdot Conv + MW_{CTA} \qquad \textbf{(3-2)}$$

where Conv. is the monomer conversion, $[M]_0$ is the initial concentration of monomer, MW_{MMA} = 100 g/mol, MW_{CTA} = 272 g/mol. For sample PMMA56 (▲) with conv. of 61 % by weight method, M_n (NMR) = 4370 g/mol, $M_{n,61\%}$(theoretical) = 2100 g/mol and $M_{n,100\%}$(theoretical) = 3270 g/mol. The obtained M_n (NMR) higher than theoretical one can be either due to the termination of radicals in the RAFT procedure or due to the efficiency of CTA < 100 %. The later one was more reasonable as the dispersity (Đ = 1.22) was fairly narrow indicating no obvious termination happened in the propagation step. The efficiency of CTA was given by

$$M_{n,conv} = ([M]_0 / (f_{CTA} \cdot [CTA]_0)) \cdot MW_{MMA} \cdot Conv + MW_{CTA} \quad \textbf{(3-3)}$$

Thus,

$$f_{CTA} = \frac{([M]_0 / [CTA]_0) \cdot MW_{MMA} \cdot Conv}{(M_{n,conv} - MW_{CTA})} \quad \textbf{(3-4)}$$

For the case of PMMA56, f_{CTA} = 51.2 %. In the previous report by J. Chiefary et al.[98], a higher f_{CTA} (~72 %) was obtained for the polymerization of MMA with the same CTA in methyl ethyl ketone at 60 ℃. The experimental parameters like solvent, temperature, molar ratio of CTA/AIBN can lead to different efficiency of CTA.

The controlled manner of RAFT polymerization is due to the main equilibrium between the propagating polymer radicals and the dithioester group of chain transfer agent (CTA). The extreme case is free radical polymerization (non-controlled) without CTA (only with initiator AIBN). Here by increasing AIBN, PMMA57 (CTA/AIBN = 10/1) had the same conversion (61 %) and similar molecular weight (4000 vs. 4100 g/mol) as PMMA56 (CTA/AIBN = 5/1) at the same reaction time (16 h) and molar ratio of MMA/CTA (30/1) (**Table 3-3**). When AIBN was further increased to CTA/AIBN = 3/1 (PMMA54), reasonable M_n and narrow Đ were still obtained. This indicated that the polymerization proceeded in a controlled way (the main equilibrium of RAFT procedure predominated) in this range of CTA/AIBN (10/1 to 3/1).

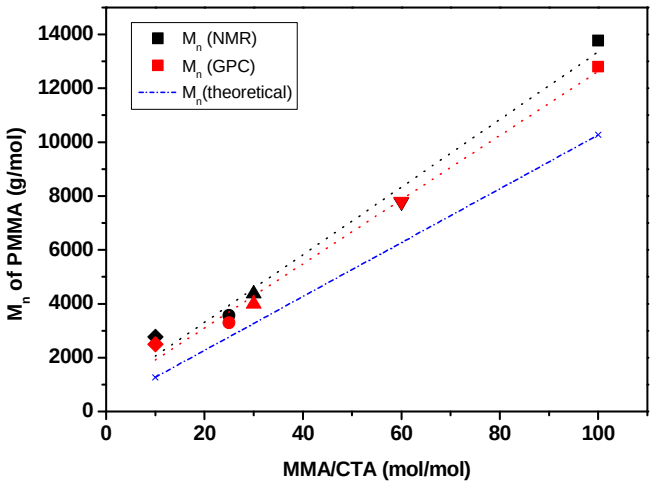

Figure 3-9. Molecular weight (M_n) of PMMA versus the molar ratio of MMA/CTA. Polymerization in toluene at 70 ℃ for 16 h except sample ■ (20.5 h) and ●(21.5 h). The other details see Table 4-4. PMMA54 (■), PMMA51 (▼), PMMA56 (▲), PMMA59 (●), PMMA63 (♦). Theoretical M_n at monomer conversion of 100 % as given by **Formular (3-2)**.

Table 3-3. Characterization of polymers by RAFT and after aminolysis.

Sample	Feed details	Time	Conv.[b]	NMR			GPC	
	AIBN/CTA/M[a]	h	%	n[c]	M_n(g/mol)[d]	%(SCS)[e]	M_n(g/mol)	M_w/M_n
PMMA54	1/3/300	20.5	~80	135	13770	--	12800	1.20[f]
PMMA51	1/5/300	16	62	75	7770	150	7800	1.22[g]
PMMA56	1/10/300	16	61	41	4370	115	4000	1.22[f]
PMMA59	1/5/75	21.5	78	33	3570	~85	3300	1.20[f]
PMMA63	1/10/100	16	67	25	2770	110	2500	1.14[f]
PMMA57	1/5/150	16	61	42	4470	110	4100	1.22[f]
PMMA55	1/10/300	6	30	28	3070	~97	2900	1.20[f]
PPMA52	1/5/192	19.5	60	30	4950	--	7900	1.17[g]
PPMA58	1/5/96	23	62	15	2610	115	2900	1.42[f]
$PMMA_n$-*b*-$PPMA_m$ with first-synthesized PMMA as macro-CTA								
				n[j]	m[k]	M_n(g/mol)[l]	%(scs)	
PMS61	1/5/160[h]	16	31	34	24	7420	~48	7100	1.22[f]
PMS62	1/5/320[h]	16	19	31	84	16480	--	12700	1.06[f]
PMS93	1/5/135[i]	21	95	135	48	21260	--	18700	1.21[f]

[a] molar ratio; MMA/toluene = 1/5 (vol/vol); [b] conversion from weight method; [c] the degree of polymerization; [d] $M_n = n * MW_{monomer} + MW_{CTA}$; [e] the integration ratio of dithioester group/phenyl of starting group, (%(SCS) **=** 150 % means each polymer chain owned dithioester end-group but 33 % of polymer had starting group from AIBN); [f] in $CHCl_3$, PSt as calibration, RI detector; [g] in THF, PSt as standard, RI detector; [h] PMMA59 as macro-CTA; [i] PMMA54 as macro-CTA; [j] degree of polymerization of PMMA block; [k] degree of polymerization of PPMA block; [l] $M_n = n * MW_{MMA} + m * MW_{PMA} + MW_{CTA}$ (g/mol).

The chemical structure of PMMA by RAFT was confirmed by ^1H and ^{13}C NMR. The starting group ($C_6\underline{H}_5C(CH_3)_2$) and ending group ($S(C=S)C_6\underline{H}_5$) from CTA were well discernible in ^1H NMR spectra as following (**Figure 3-10**): **a** (7.14 ppm, 1H), **b**+**c** (7.26 ppm, 4H), **j** (7.88 ppm, 2H), **k** (7.35 ppm, 2H), **l** (7.51 ppm, 1H). From the ^{13}C NMR spectra (**Figure 3-11**), further details of the chain structure were confirmed. The dithioester group ($S(\underline{C}=S)$) appeared at high chemical shift of 225 ppm. The neighboring unit of the start and end-group (**g**, **g***, **p**, **m**, **n**) were also identified as shown in **Figure 3-11**. The dithioester end-functionality (%(SCS)) can be calculated by the integration ratio of dithioester group/phenyl of starting group as summarized in **Table 3-3**. Here, %(SCS) = 85 % means 85 % of polymer chains owned

dithioester end-group and %(SCS) = 150 % means each polymer chain owned dithioester end-group but 33 % of polymer had starting group from AIBN. More than 85 % of homopolymers chains owned dithioester end-group. The high end-functionality makes sure the availability of these homopolymers in stabilizing AuNPs.

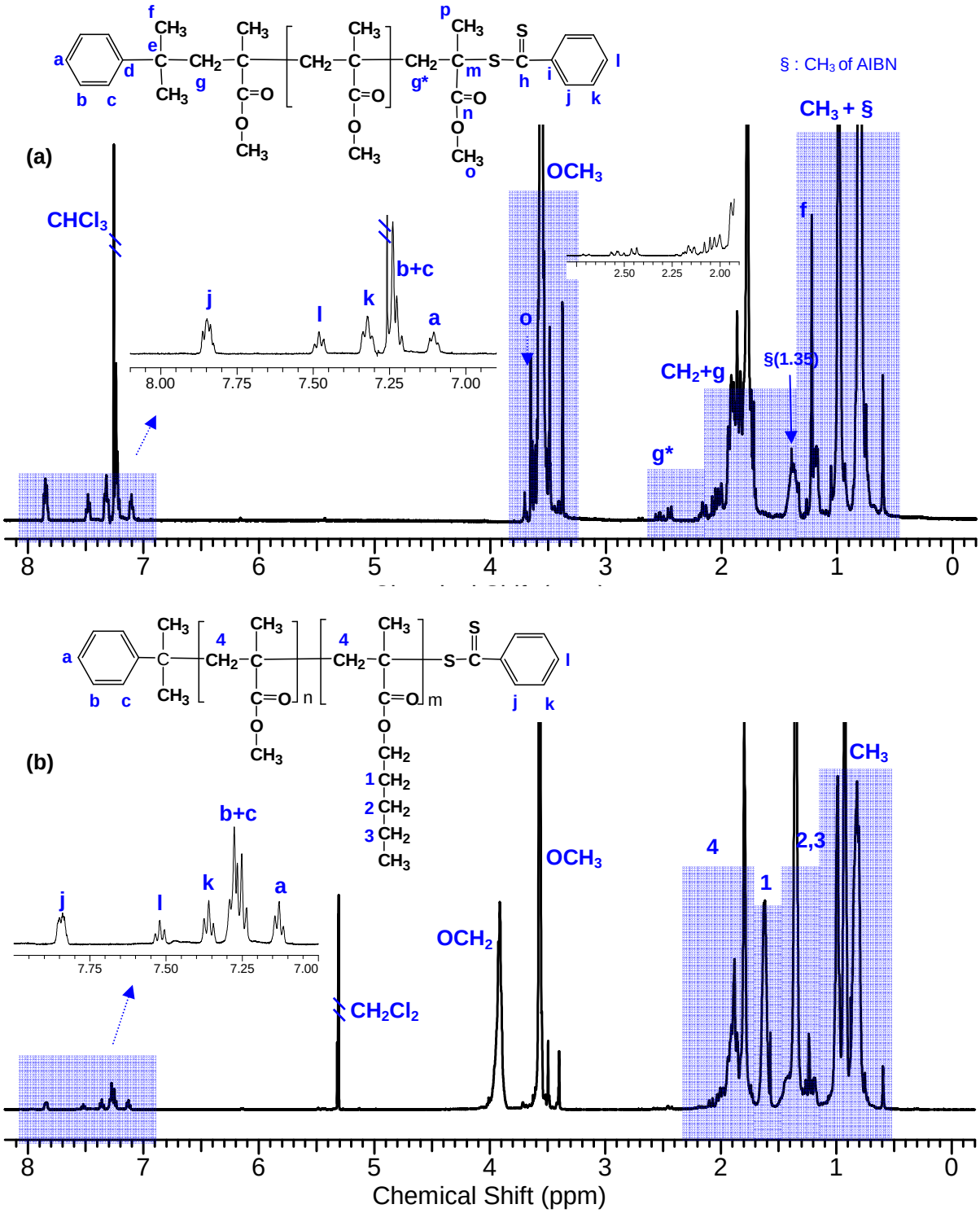

Figure 3-10. ^{1}H NMR spectra of (a) homopolymer PMMA59 (in $CDCl_3$) and (b) block copolymer PMS61 (in CD_2Cl_2) by RAFT.

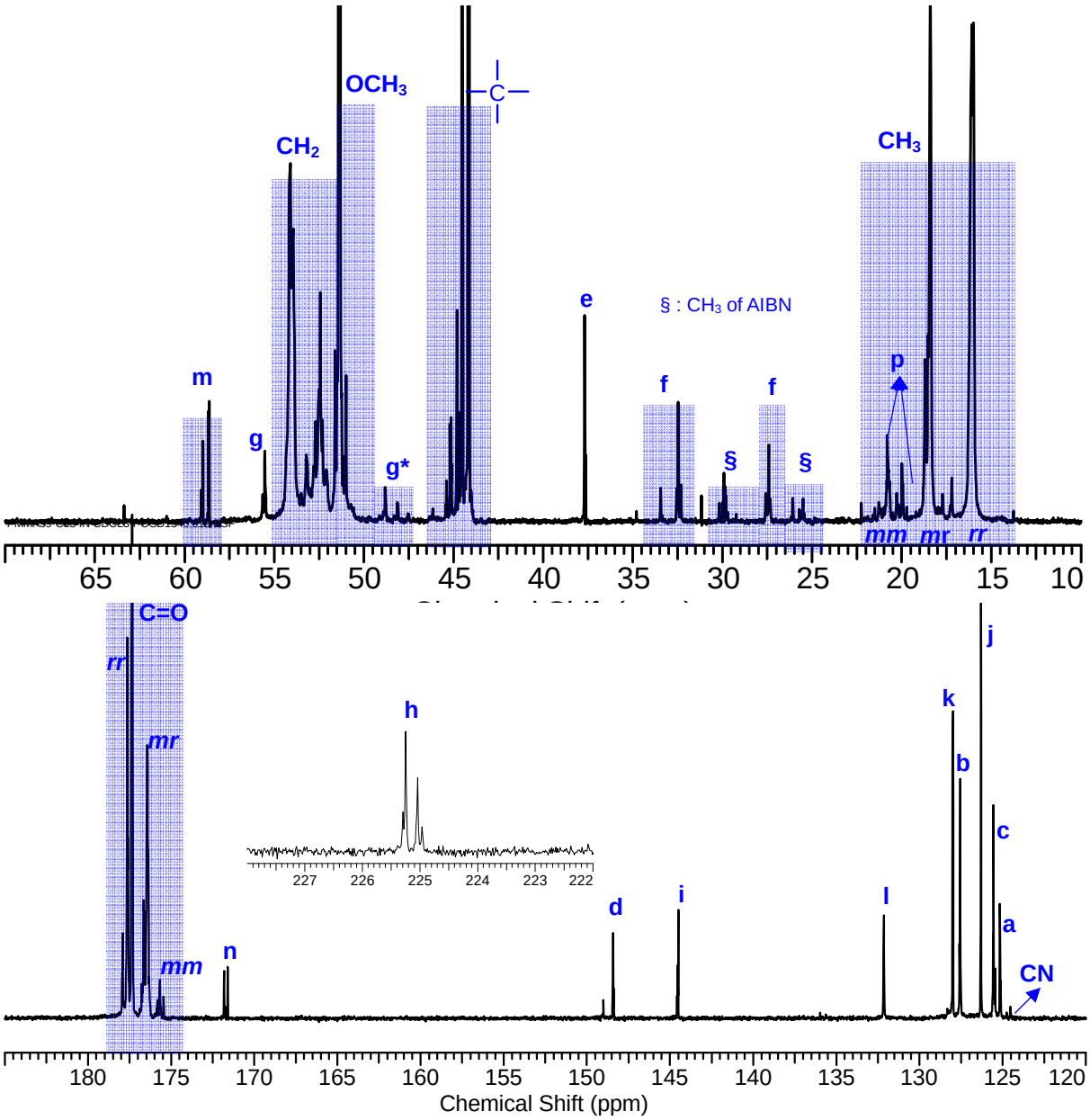

Figure 3-11. ^{13}C NMR (in $CDCl_3$) spectra of homopolymer PMMA59 by RAFT.

The copolymerization of PMA with first-synthesized PMMA54 (the degree of polymerization n = 135) as macro-CTA was studied. The reaction time of PMMA54 was 20.5 h, which deviated not far from the linear region of the kinetic study as shown in **Figure 3-8a**. This made sure that the macro-CTA maintained the dithioester end-group so as to work as chain transfer agent in the copolymerization of the second monomer. As shown in the polymerization kinetics in **Figure 3-12**, copolymerization of PMA with molar ratio of AIBN/PMMA54/PMA = 1/5/300 in toluene at 70 ℃ showe d a first-order kinetic character although conducted until ~30 % in this case. There was also an induction period of 2 h like the homopolymerization of MMA. The resulted block copolymers had narrow dispersity of Đ = ~1.2–1.3. The controlled way of block copolymerization of PMA from PMMA-SCS indicated a

faster or comparably fast fragmentation of the intermediated radical PMMA-S-C(Ph)-S-PPMA from PMMA side in the RAFT procedure.

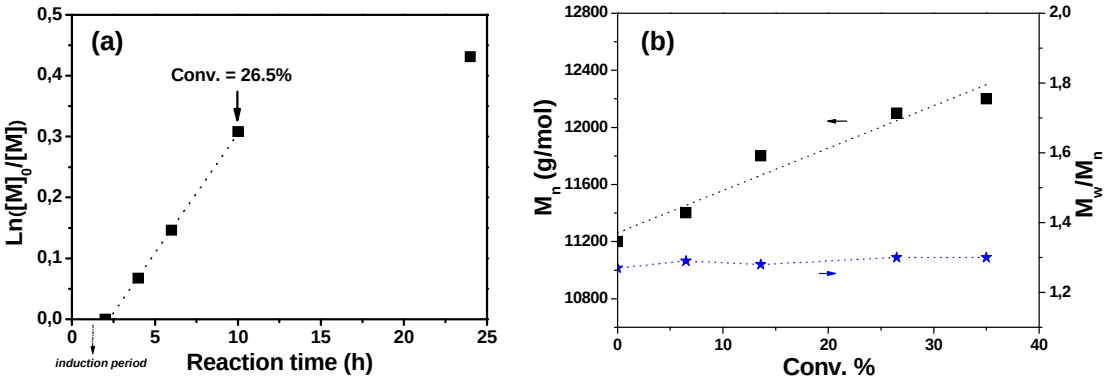

Figure 3-12. (a) RAFT polymerization of PMA in toluene at 70 °C with PMMA54 (n = 135, Đ = 1.20) as macro-CTA. [AIBN] = 1.3 * 10^{-3} M, [micro-CTA] = 6.7 * 10^{-3} M, [PMA] = 0.4 M. (b) molecular weight versus conversion (■).

The first-synthesized PMMA, with low and high molecular weight, were both successful in copolymerization of PMA. Block copolymers PMS61, mediated by PMMA59 (M_n = 3300 g/mol) as macro-CTA and with feed molar ratio of AIBN/CTA/PMA = 1/5/160, had a narrow dispersity of Đ = 1.22 and an increase of molecular weight from 3300 to 7100 g/mol as shown from GPC analysis in **Figure 3-13**. By calculation from the integration of $OC\underline{H}_3$ and $OC\underline{H}_2$ in ^{1}H NMR (**Figure 3-10b)** as $\frac{3n}{1} = \frac{A_{OCH_3}}{A_a}$ and $\frac{2m}{1} = \frac{A_{OCH_2}}{A_a}$, the degree of polymerization n (PMMA block) = 34 and m (PPMA block) = 24. The dithioester end-functionality was calculated by the integration ratio of dithioester group/phenyl of starting group. For PMS61, %(SCS) = 48 % which means 48 % of block copolymer chains owned dithioester end-group. When higher molecular weight of PMMA54 (n^{NMR} = 135, M_n^{NMR} = 13770 g/mol) as macro-CTA, the obtained block copolymer PMS93 also had narrow dispersity of Đ = 1.21 (**Figure 3-13**) and the second block length m = 48 based on NMR analysis.

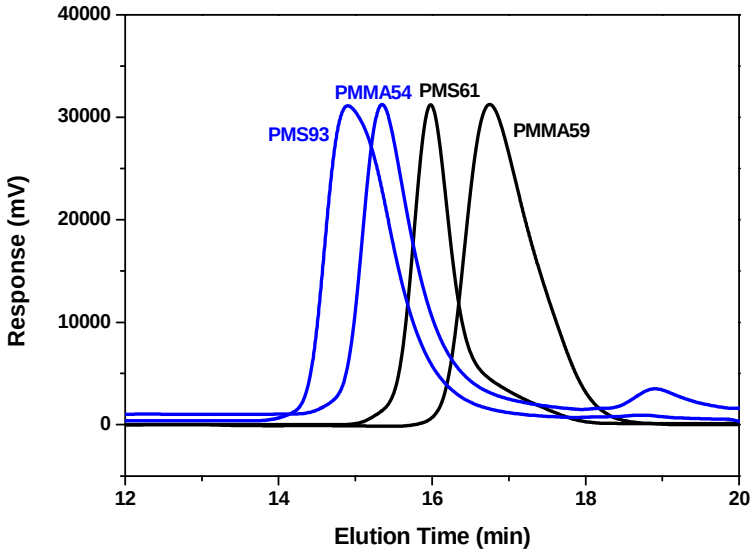

Figure 3-13. GPC curves of homopolymer (PMMA59, PMMA54) and block copolymer (PMS61, PMS93) by RAFT. PMS61 was produced with PMMA59 as macro-CTA and PMS93 with PMMA54 as macro-CTA. In $CHCl_3$, RI detector and PSt as calibration.

As shown in **Table 3-3**, the molecular weight (M_n) of PMMA determined from GPC with PSt calibration was close to that determined from NMR. The deviation $\Delta = \left|M_n^{GPC} - M_n^{NMR}\right| / M_n^{NMR}$ = 5~10 %. Such as for PMMA56, $M_n^{NMR} = 4370$ g/mol and $M_n^{GPC} = 4000$ g/mol, so the deviation Δ = 8 %. The small deviation of M_n^{GPC} from M_n^{NMR} is attributed to the slightly different hydrodynamic volume between PMMA and the calibration PSt in GPC analysis, as well as the dithioester end-group of PMMA can also affect the hydrodynamic volume.

For homopolymer PPMA, M_n^{GPC} with PSt calibration deviated much more far from M_n^{NMR}. For PPMA52, $M_n^{NMR} = 4950$ g/mol and $M_n^{GPC} = 7900$ g/mol, so the deviation Δ = 60 %. For PPMA58, $M_n^{NMR} = 2610$ g/mol and $M_n^{GPC} = 2900$ g/mol, so Δ = 11 %. This is due to the big difference of hydrodynamic volume between PPMA and PSt.

3.4.2 Aminolysis of dithioester end-capped polymers

3.4.2.1 Model reaction of aminolysis

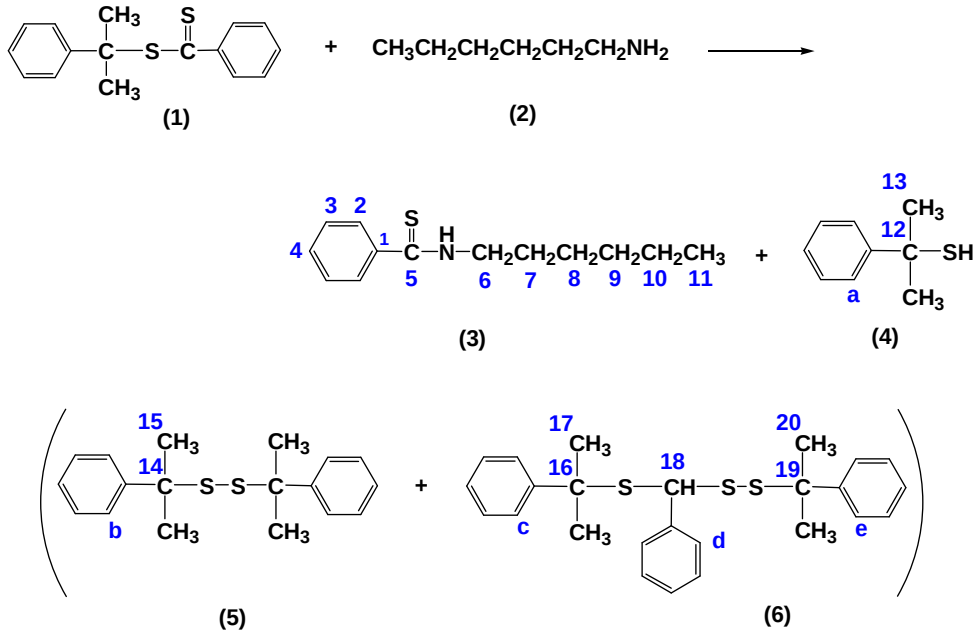

Scheme 3-4. Model reaction between dithioester and hexylamine in THF.

A model reaction between dithioester and amine was carried out. 2-Phenyl-2-propyl benzodithiolate **(1)** reacted with hexylamine **(2)** in dilute solution of THF (0.05 mol/L of amine) under argon. The product of the aminolysis was expected to include thioamide and thiol[191]. Thioamide compound **(3)** with 100 % conversion was confirmed by ^{1}H NMR spectroscopy (**Figure 3-14**). By-products were present according to the four signals of C$\underline{H}_3$ at 1.70 ppm (**17**, CH_3), 1.61 ppm (**20**, CH_3), 1.55 ppm (**17'**, CH_3), and 1.51 ppm (**20'**, CH_3) in **Figure 3-14**. With the help of ^{1}C NMR spectroscopy (**Figure 3-15**), disulfide compounds of **(5)** and **(6)** derivate from thiol **(4)** (**Scheme 3-4**) were identified. Compound of **(5)** was the oxidized product of thiol **(4)**.

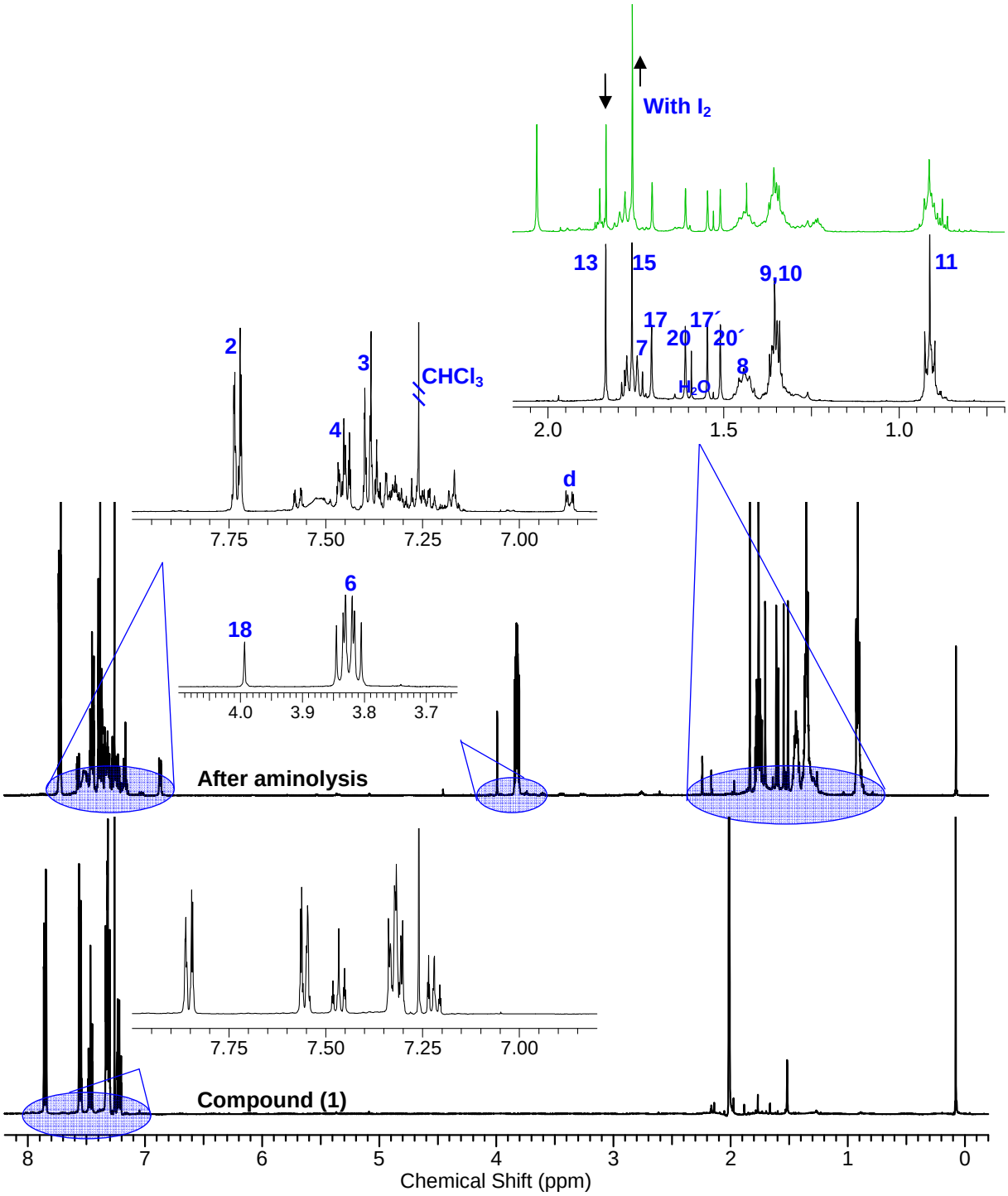

Figure 3-14. ^{1}H NMR (in $CDCl_3$) spectra of aminolysis model reaction. The green spectrum (at top) was the product after adding I_2 which was supposed to oxidize thiol.

To confirm the co-existence of thiol **(4)** and disulfide **(5)**, iodine was added to the product. As seen in the ^{1}H NMR spectroscopy (**Figure 3-14** green one), the signal at 1.84 ppm (**13**, CH_3) decreased and correspondingly the signal at 1.76 ppm (**15**, CH_3) increased. This was attributed to the oxidation of thiol **(4)** into disulfide **(5)**, which may also happen in the presence of O_2. Compound **(6)** resulted from the reaction of **(4)** with **(1)**.

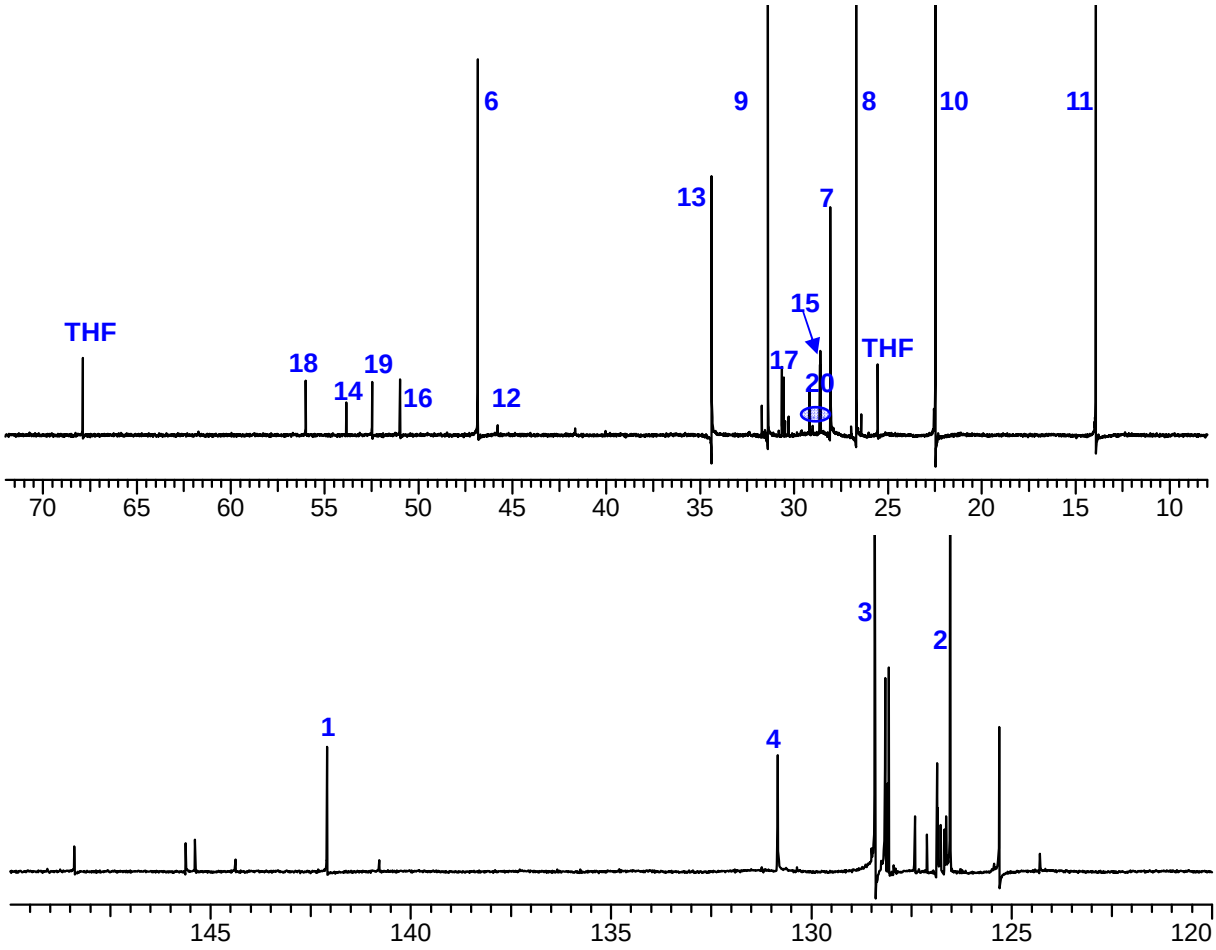

Figure 3-15. ^{13}C NMR (in $CDCl_3$) spectra of the aminolysis model reaction.

For the aminolysis of dithioester end-capped polymers, oxidation of thiol into disulfide can be avoided by carrying out the reaction under inert atmosphere. If necessary the purification and storage of the thiol-terminated polymers were also done under inert gas. The side-reaction between thiol **(4)** and dithioester **(1)** in the model reaction was expected to be minimized due to only one reactive thiol group at each long polymer chain and also further diluted thiol and dithioester concentration.

3.4.2 Aminolysis of dithioester end-capped polymers

Thiol-terminated polymers were prepared by cleaving the dithioester end-capped polymers with hexylamine in THF. The aminolysis was carried out in dilute solution under Ar at room temperature. As for PMMA55 (n = 28), 0.9 g of polymer (0.3 mmol of S(C=S) end-group) and 45 mg (0.45 mmol) of hexylamine were dissolved in 5 ml of dry THF. Dithioester end-capped polymer solution with typical red color changed into orange in 15 min and finally yellow-orange in 2 h. The disappearance of the red color indicated the dithioester group was cleaved[104,105]. The final product was precipitated out of hexane and turned out to be colorless

powder. The procedure of aminolysis of PPMA was the same with PMMA. The red color disappeared in 2 h with addition of hexylamine.

From ^{1}H NMR spectra of PMMA55 in **Figure 3-16**, the phenyl (**j**, **k**, and **l**) from end-group disappeared after aminolysis. The phenyl (**a**, **b**, and **c**) from the starting group was intact. Results of ^{13}C NMR spectroscopy showed further details of the aminolysis (**Figure 3-17**). Thiocarbonyl S(C=S) (**h**) disappeared. The neighboring unit of S(C=S) (**p**, **m**, **n**) also disappeared because of the cleavage of dithioester group. For PPMA52, the aminolysis was also successful based on ^{1}H NMR analysis that the phenyl from end-group was removed.

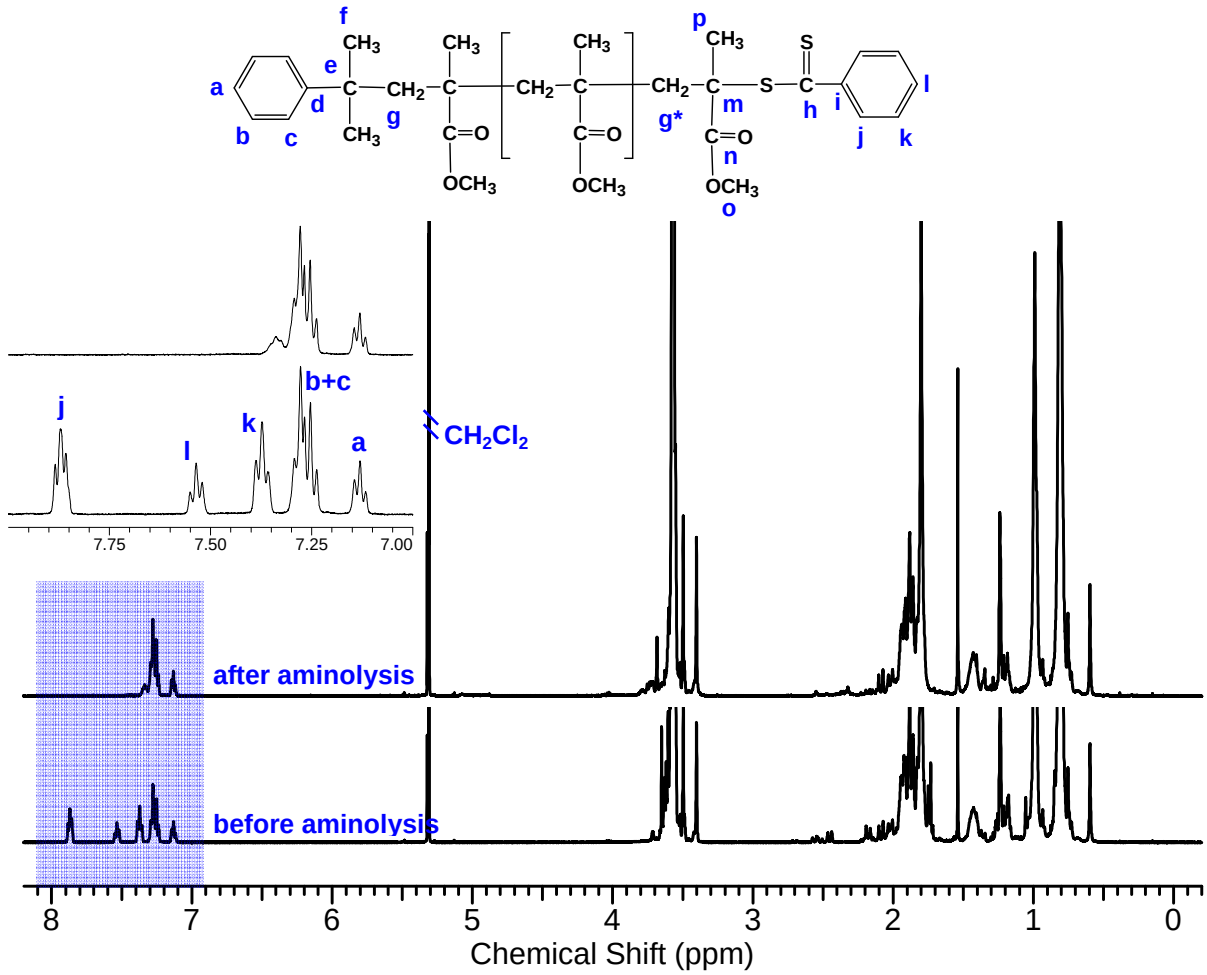

Figure 3-16. ^{1}H NMR (in CD_2Cl_2) spectra of PMMA55 before and after aminolysis.

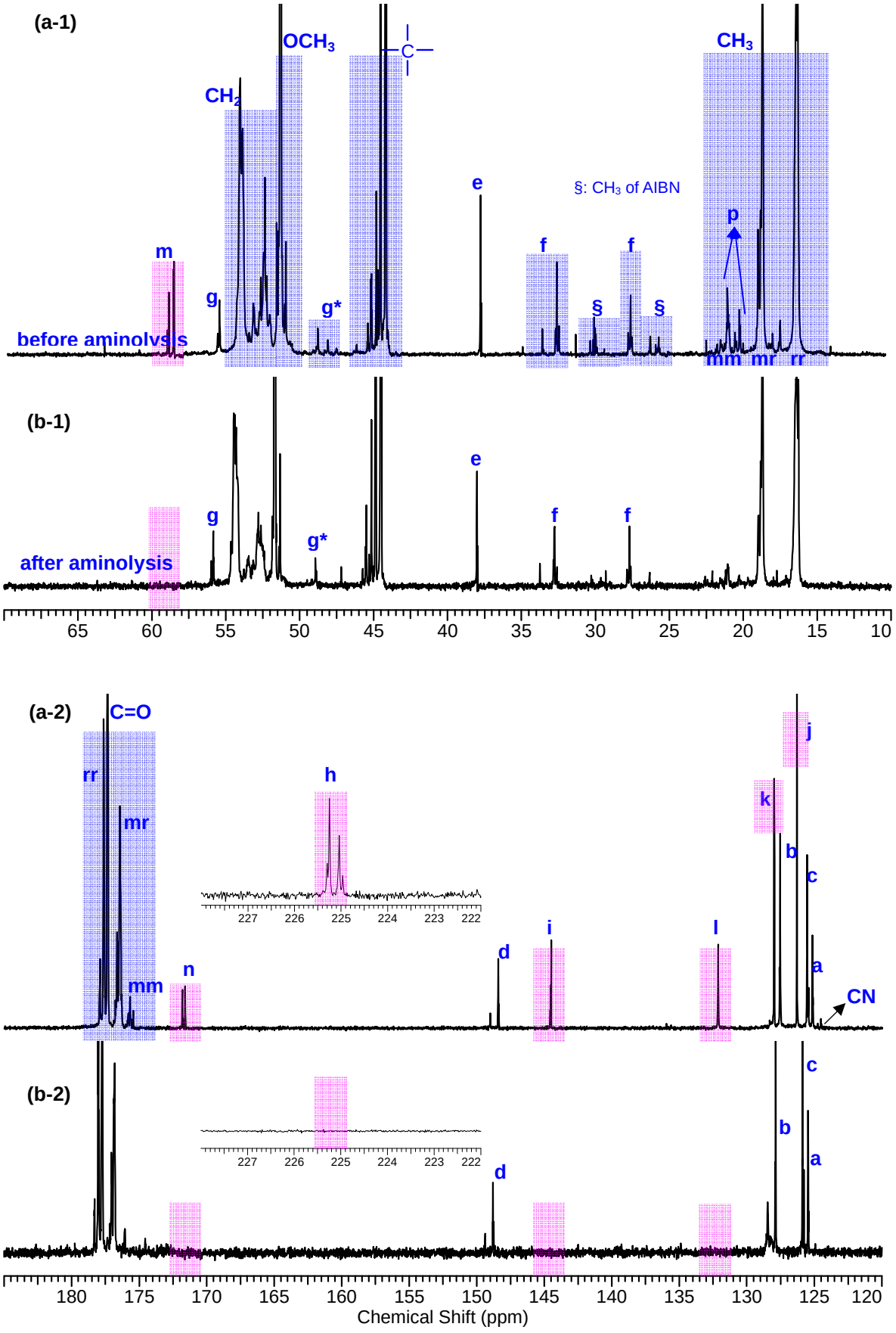

Figure 3-17. ^{13}C NMR (in $CDCl_3$) spectra of PMMA59 before (a) and after aminolysis (b).The red color marked groups disappeared after aminolysis.

To further confirm the polymers with thiol end-group after aminolysis, iodine (I_2) was added to PMMA55SH (PMMA55 after aminolysis) solution in $CHCl_3$. The polymers with thiol end-group were expected to be oxidized into dimers via disulfide linkage (-SS-) at the presence of iodine[84,192]. **Figure 3-18** showed GPC analysis of polymers before and after aminolysis and oxidation by I_2. PMMA55SH had lower molecular weight compared to PMMA55 ($M_{n,PMMA55SH} = M_{n,PMMA55}$ - 120) but showed shorter elution time. This can be due to the thiol end-group which caused the difference of chain polarity thus the difference of hydrodynamic volume. After oxidation by I_2, PMMA55-I2 shifted to a shorter elution time than PMMA55 indicating increased molecular weight thus the formation of dimers.

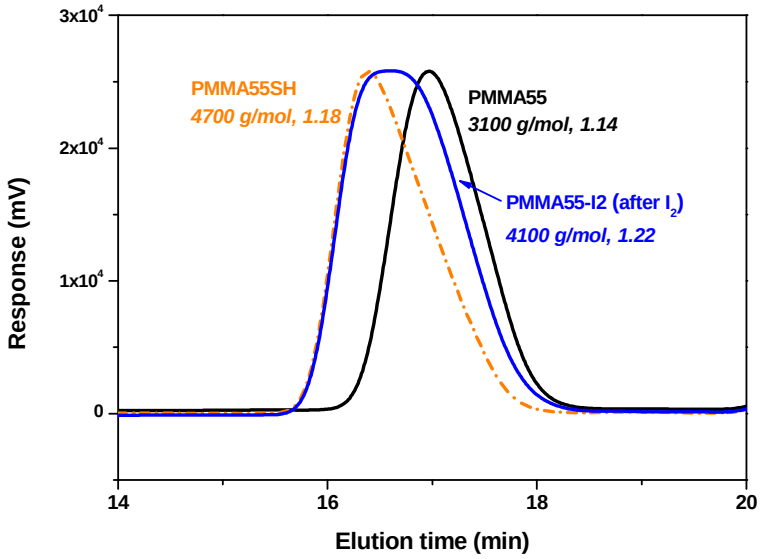

Figure 3-18. GPC curves of PMMA55 (before aminolysis) (—), PMMA55SH (after aminolysis) (– ·), and PMMA55-I2 (after oxidation of PMMA55SH by I_2 for 24 h) (—).

If PMMA55-I2 was dimer via disulfide linkage from PMMA55, $M_n^{PMMA55\text{-}I2}$ was double of M_n^{PMMA55}. From the GPC analysis (**Figure 3-18**), $M_n^{PMMA55\text{-}I2}$ = 4100 g/mol, which was less than the double of M_n^{PMMA55} (3100 g/mol). Besides, PMMA55-I2 showed obviously broad evolution curve and the dispersity (Đ = 1.22) was higher than PMMA55 (Đ = 1.14). This can be either due to the partially oxidation or due to partially SH end-functionality. The previous one was excluded as the reaction time (24 h) was long enough for the thiol oxidation by I_2. The percentage of dimers via disulfide bond (f_{SS}) after I_2 oxidation is given by

$$M_n^{PMMA\text{-}I2} = \frac{f_{SS} \cdot \left(2 \cdot M_n^{PMMA^*} - 242\right) + M_n^{PMMA^\#} \cdot (1 - f_{SS})}{0.5 f_{SS} + (1 - f_{SS})} \quad \textbf{(3-5)}$$

where $M_n^{PMMA\text{-}I2}$ is the molecular weight of polymers after I_2 oxidation, PMMA* is the polymers with SH end-group and form dimers via disulfide bond after I_2 oxidation, and

PMMA$^{\#}$ represents two parts, one part is the polymers without SH end-group, and the other part is the polymers with SH end-group but do not form dimers during I_2 oxidation. For PMMA55, M_n^{PMMA*} was 3100 g/mol and $M_n^{PMMA^{\#}}$ = M_n^{PMMA*}-152. Thus, for PMMA55, f_{SS} = 22.8 %, which was much lower than the dithioester end-functionality f_{SCS} = 97 % (**Table 3-3**). This indicated that at least 22.8 % of PMMA55 owned SH end-group after aminolysis. We suppose that a part of polymers with SH end-group do not form dimers during I_2 oxidation although this has to be further verified by other analysis method such as mass spectroscopy.

To conclude, thiol-terminated PMMA was synthesized by RAFT polymerization following aminolysis which was confirmed by ^{1}H and ^{13}C NMR and GPC. PPMA-SH was also produced in the similar procedure as PMMA-SH. The functionality of dithioester end-group was > 85 %. PMMA-*b*-PPMA was also synthesized by RAFT by using the first-produced PMMA as macro-CTA. The thiol-terminated polymers were employed to stabilize AuNPs in the next step.

4 AuNPs stabilized with different species: synthesis and discussion

Gold nanoparticles (AuNPs) stabilized with different species and with controlled size were prepared. To control the nanoparticle location in nanostructured block copolymer PPMA-*b*-PMMA, species with varied hydrophobicity, including PEO-SH, $C_{12}H_{25}$-SH, $CF_3(CF_2)_5CH_2CH_2$-SH, PPMA-SH, PMMA-SH, P4VP-based PPMA and PMMA block copolymers were employed as stabilizing agents for AuNPs (**Scheme 4-1**). The nanoparticles were expected to disperse into preferred microdomains of BCP. AuNPs with controlled size were prepared aiming to investigate the particle size effect on the morphology and orientation evolution of BCP thin films in the next step.

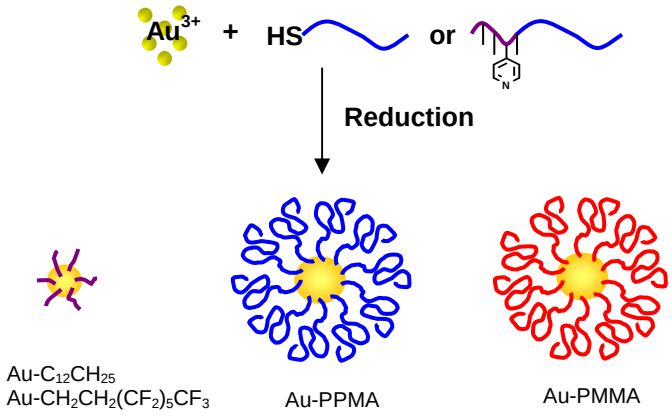

Scheme 4-1. AuNPs stabilized by various ligands.

In this chapter for the synthesis of AuNPs, UV-vis, DLS, and TEM were used to analyze the NPs size and size dispersity. Both UV-vis and DLS give information of AuNPs in solution state. DLS provides the average size (Au-core + ligand-shell) and size dispersity of NPs in solution. TEM gives the direct images of NPs in dry state thus the Au-core size and size dispersity can be measured (the ligand-shell is not discernible due to the much lower contrast of organic species compared to Au-core).

4.1 Model reaction of Brust-Schiffrin method: Au-TOAB and Au-P4VP

Tetraoctylammonium bromide (TOAB) was employed as phase-transfer agent in Brust-Schiffrin method (BSM). Without thiol ligand, TOAB also served as stabilizing agent and AuNPs were obtained from $HAuCl_4$ after reduction by $NaBH_4$. By varying the molar ratio of TOAB/Au^{3+} from 12/1 to 1/1, AuNPs had average core size ~3–5 nm based on TEM analysis (**Table 4-1**). The particle size had no dependence on the ratio of TOAB/Au^{3+} in the range from 12/1 to 1/1. Our results are comparable with a previous report by Ibañez et al.[193], in which AuNPs of 4.39 ± 1.25 nm were obtained with TOAB/Au^{3+} of 1.2/1.

Table 4-1. AuNPs stabilized by TOAB and P4VP-based block copolymers by Brust-Schiffrin method.

Sample	Feed N/Au^{3+} mol/mol	d_{core} (TEM) nm	$d_{core+shell}$ (DLS)[a] nm	PDI
Au-TOAB	**$N(C_8H_{17})_4Br$ (TOAB)** as stabilizer			
Au36G	12/1	4.5	4.4	1.000
Au36H	6/1	4.8	7.9	0.137
Au36I	2/1	--	5.9	0.197
Au36J	1/1	3.8	4.5	0.916
Au-P4VP	**TOAB/$P4VP_{\sim10}$-*b*-PMMA** as stabilizer[b]			
Au37	0.75/1	4.9	14.6	0.249
Au38	0.49/1	5.3	12.7	0.295
Au39	0.88/1	6.2	10.6	0.184

[a] the size was from "number averaged" in DLS measurements; [b] $P4VP_8$-*b*-$PMMA_{148}$ for Au37, $P4VP_6$-*b*-$PMMA_{170}$ (P4VPM30) for Au38, $P4VP_9$-*b*-$PMMA_{139}$ for Au39, see Table 3-2 for P4VPM30. The feed ratio of TOAB/Au^{3+} in synthesis of Au37–39 was the same as for Au36H.

As the nitrogen of 4-vinyl pyridine (4VP) can coordinate with Au^{3+}, $P4VP_{\sim10}$-*b*-PMMA was applied as ligand in Brust-Schiffrin method with TOAB as phase-transfer agent. The resulting AuNPs had core size range from 4.9–6.2 nm as determined by TEM (**Figure 4-1 d–f**) at molar ratio of 4VP/Au^{3+} from 0.5–1 as summarized in **Table 4-1**. There was a slight increase compared to Au36H (core of 4.8 nm) with the same feed ratio of TOAB/Au^{3+}. DLS analysis showed an increasing diameter (core+shell) when P4VP-based block copolymers was

applied (10–15 nm) compared to TOAB (4–8 nm) (**Table 4-1**). The AuNPs with some enlargement of core+shell size in solution state indicated that P4VP partially grafted to the Au surface. Besides, under the same feed ratio of TOAB/Au^{3+} of 6/1, the size dispersity of Au-P4VP (PDI = 0.184–0.295 for Au37–39) was broader than that of Au-TOAB (PDI = 0.137 for Au36H) (**Table 4-1**). Thus, P4VP was supposed to serve as stabilizer for AuNPs in Brust-Schiffrin method and were comparable with TOAB in stabilizing AuNPs. P4VP-based block copolymers with short P4VP-block (units ~10) produced larger particles than TOAB did in the same procedure. The coexistence of P4VP and TOAB could induce broader size dispersity.

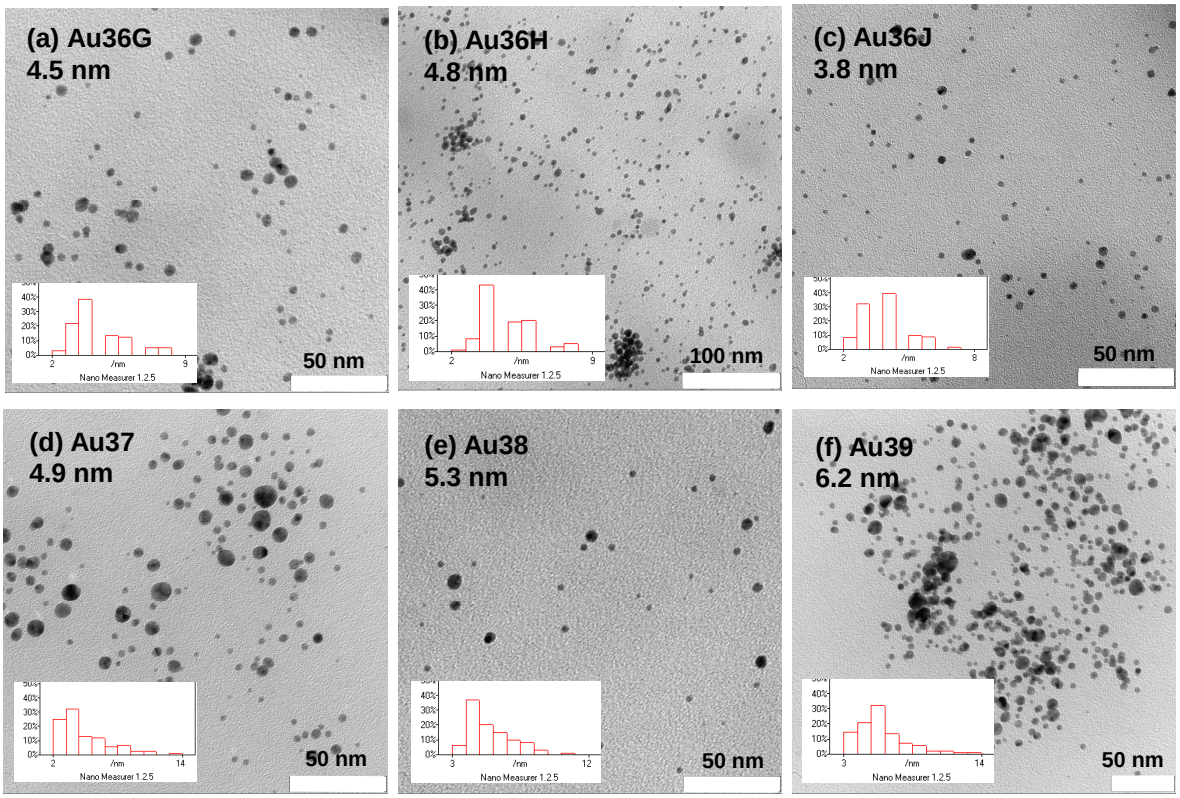

Figure 4-1. TEM analysis of AuNPs stabilized by TOAB (a–c) and P4VP$_{\sim 10}$-*b*-PMMA (d–f) by Brust-Schiffrin method.

To conclude here, from the probe reaction of Brust-Schiffrin method, the phase-transfer agent tetraoctylammonium bromide (TOAB) was capable in stabilizing AuNPs and competed with P4VP-based block copolymers. This provided a guide that TOAB and similar nitrogen based compounds should be avoided in synthesis of AuNPs when weak ligands such as P4VP or SH-terminated polymers are employed. Thus in the next part, AuNPs stabilized by P4VP-based block copolymers and SH-terminated homopolymers were prepared in one-phase method in which TOAB were not needed.

4.2 Low molecular weight thiol stabilized AuNPs by Brust-Schiffrin method

In this study, the low molecular weight thiol applied for stabilizing AuNPs by Brust-Schiffrin method (BMS) included $CH_3(CH_2)_{10}CH_2$-SH (denoted as C12-SH), $CF_3(CF_2)_5CH_2CH_2$-SH (denoted as F6-SH) and $CH_3O(CH_2CH_2O)_6CH_2CH_2$-SH (denoted as PEO-SH). When dodecanethiol was employed, AuNPs with core size of 1.8–2.4 nm were prepared by varying the molar ratio of SH/Au^{3+} from 6/1, 3/1, to 1/1 (**Table 4-2**). The nanoparticles had narrow size dispersity as shown from TEM images (**Figure 4-2 c-e**). By further decreasing SH ligand with SH/Au^{3+} < 1/1, the nanoparticle size increased dramatically above 7 nm (**Figure 4-2a,b**). The characteristic surface plasmon resonance (SPR) of AuNPs depends on the size[194,195,196]. AuNPs bellow 3 nm do not show absorbance in UV-vis. The larger ones exhibit a sharper and more intense absorbance at ~525 nm. Our results were in good agreement with previous reports. The samples Au17–19 with size ~2nm did not show plasmon band or a very weak one. Whilst Au15 and Au14 with size ~8 nm showed obvious SPR absorbance at ~525 nm (**Figure 4-2f**).

Table 4-2. AuNPs stabilized by $C_{12}H_{25}SH$ by Brust-Schiffrin method.

Sample	Feed details SH/Au^{3+} (mol/mol)	d_{core} (TEM) nm	$d_{core+shell}$ (DLS)[a] nm	PDI
$C_{12}H_{25}$-SH as stabilizer				
Au14	0.25/1	7.6	6.4	0.238
Au15	0.5/1	8.7	7.7	0.338
Au17	1/1	2.4	32.2	0.461
Au18	3/1	2.0	4.0	0.773
Au19	6/1	1.8	2.2	0.533
$CF_3(CF_2)_5CH_2CH_2$-SH as stabilizer				
AuF6c	0.25/1	6.4	8.4	0.355
AuF6a	1/1	1.9	2.6	1.000
$CH_3O(CH_2CH_2O)_6$-SH as stabilizer				
Au21	0.5/1	6.6	8.5	0.329
Au22	1/1	--	6.7	0.191
Au23	3/1	5.9	5.8	0.423

[a] the size is from “number averaged” in DLS.

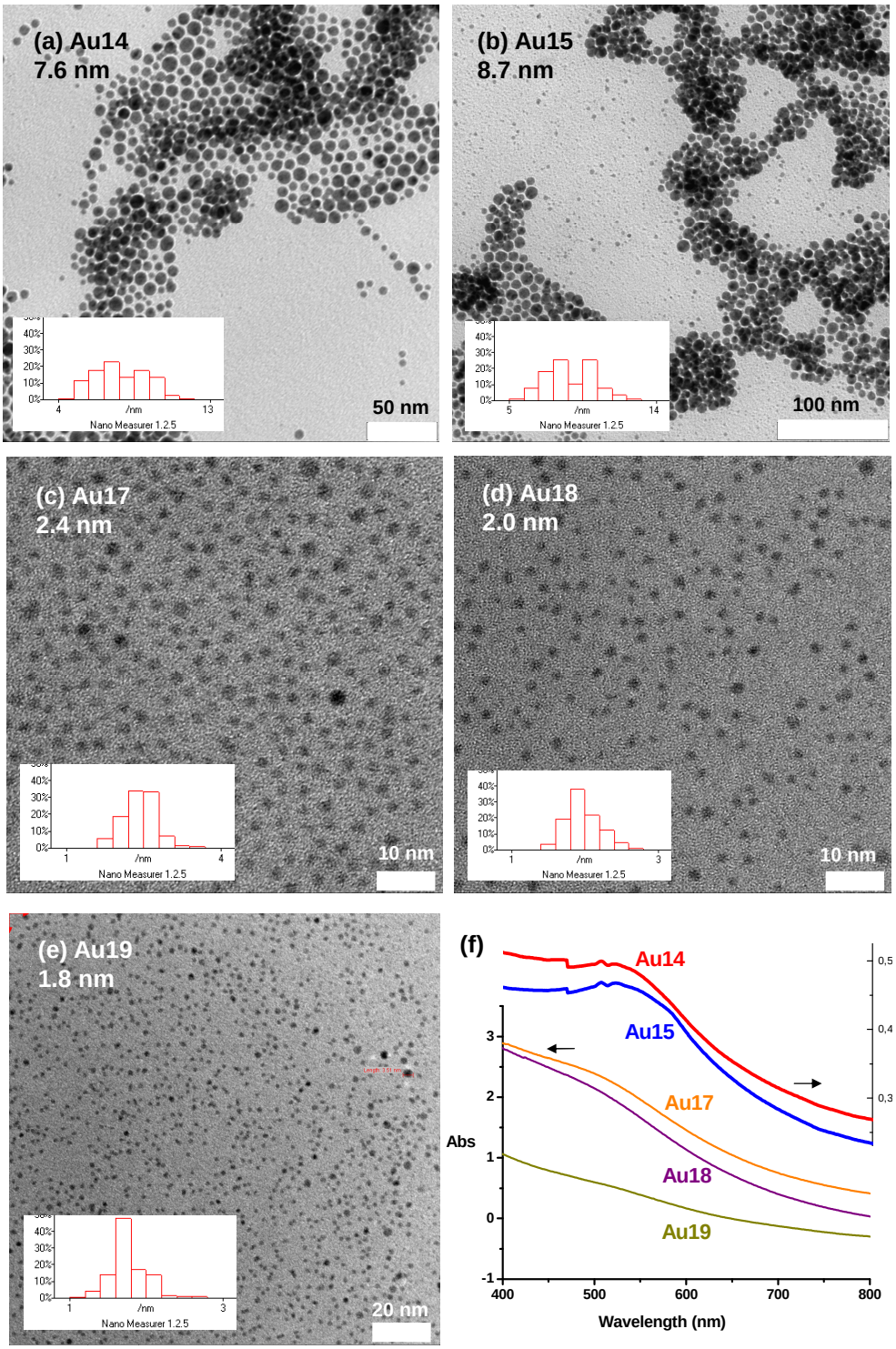

Figure 4-2. TEM analysis of AuNPs stabilized by $C_{12}H_{25}$-SH with molar ratio SH/Au^{3+} of (a) 0.25/1, (b) 0.5/1, (c) 1/1, (d) 3/1, (e) 6/1 and the corresponding UV-vis analysis (f).

Tridecafluoro-1-octanethiol ($CF_3(CF_2)_5CH_2CH_2$-SH) had similar effect in stabilizing AuNPs as dodecanethiol. The nanoparticle size depended on the molar ratio of SH/Au^{3+} and increased as SH decreased. When SH/Au^{3+} < 1/1, the nanoparticle size had a dramatically enlargement over 6 nm (AuF6c with SH/Au^{3+} = 0.25, **Figure 4-3a**). When SH/Au^{3+} ≥ 1/1, the size decreased well below 3 nm (AuF6a with SH/Au^{3+} = 0.25, **Figure 4-3b**).

The hydrophilic thiol ligand $CH_3O(CH_2CH_2O)_6CH_2CH_2$-SH (PEO-SH) showed some different character in stabilizing AuNPs. Before reduction, $[N(C_8H_{17})_4][AuCl_4]$ stayed in toluene phase. The nanoparticles formed after reduction by $NaBH_4$ and transferred to the aqueous phase due to the hydrophilic stabilizing shell of PEO. When $SH/Au^{3+} < 1/1$, the particle size was above 6 nm (**Figure 4-3c**). When $SH/Au^{3+} \geq 1/1$, the nanoparticles showed better dispersity but are still larger than 6 nm, which was different from dodecanethiol and semi-fluorinated thiol. Two reasons could be attributed. The longer chain of PEO-SH can stabilize larger particles at the same SH molar amount compared to dodecanethiol and semi-fluorinated thiol[146,147]. Besides, in Brust-Schiffrin method (including two phases of H_2O and toluene), AuNPs stabilizing by different ligands were reduced and formed in different phase, respectively, Au-PEO in aqueous phase, Au-C12 ($CH_3(CH_2)_{10}CH_2$-SH) and Au-F6 ($CF_3(CF_2)_5CH_2CH_2$-SH) in toluene phase. This can also cause the resulting AuNPs with different size at the same SH/Au^{3+} ratio.

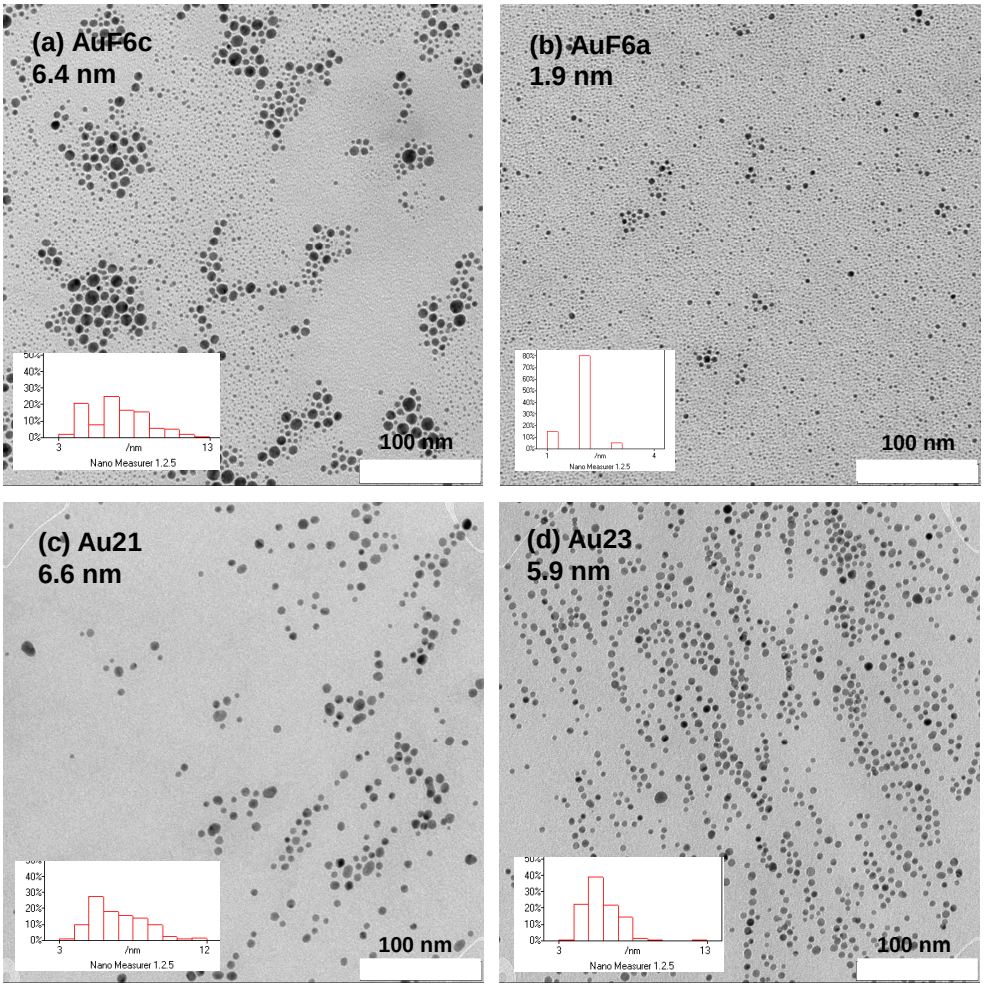

Figure 4-3. TEM analysis of AuNPs stabilized by $CF_3(CF_2)_5CH_2CH_2$-SH with molar ratio SH/Au^{3+} of (a) 0.25/1, (b) 1/1 and by PEO-SH (c) 0.5/1, (d) 3/1. Synthesized by Brust-Schiffrin method with TOAB as phase-transfer agent.

There is a long-held assumption for the mechanism of Brust-Schiffrin method. Polymeric $[AuSR]_n$ species form by addition of thiol which reduces Au^{3+} to Au^{1+} (**Formula (2-3)** in chapter 2). Until in 2010 Goulet and Lennox[126] found that $[NR_4]^+[AuX_2]^-$ complex (Au^{1+}), which formed from the reduction of $[AuX_4]^-$ by thiol, was actually the gold precursor in BSM (**Formula (2-4)** in chapter 2). Thus the reduction of $HAuCl_4$ into Au^0 is as follows:
Firstly $AuCl_4^-$ was transferred from aqueous phase (aqu) to toluene phase (tol) as

$$H\overset{+3}{Au}Cl_4\ (aqu) + [(C_8H_{17})_4N]Br\ (tol) \rightarrow [\overset{+3}{Au}Cl_4]^-[(C_8H_{17})_4N]^+\ (tol) + HBr \quad \textbf{(4-1)}$$

$\overset{+3}{Au}$ was firstly reduced into $\overset{+1}{Au}$ with adding R-SH as

$$[\overset{+3}{Au}Cl_4]^-[(C_8H_{17})_4N]^+\ (tol) + 2\ R\text{-}SH \rightarrow [\overset{+1}{Au}Cl_2]^-[(C_8H_{17})_4N]^+\ (tol) + R\text{-}SS\text{-}R\ (tol) + 2\ HCl \quad \textbf{(4-2)}$$

Finally $\overset{+1}{Au}$ was reduced into $\overset{0}{Au}$ by $NaBH_4$ as

$$[\overset{+1}{Au}Cl_2]^-[(C_8H_{17})_4N]^+\ (tol) + NaBH_4 \rightarrow \overset{0}{Au} + (C_8H_{17})_4NCl + NaCl + (BH_3)_x + ½\ H_2 \quad \textbf{(4-3)}$$

The stoichiometry of the reduction of Au^{3+} to Au^{1+} was confirmed by UV-vis monitoring the disappearance of the absorption band at 402 nm (Au^{3+}). At addition of tetraoctylammonium bromide (TOAB), Au^{3+} was transferred to toluene layer in the form of $[N(TOA)_4][AuCl_4]$ (orange) and there was absorption at ~400 nm in UV-vis. After adding dodecanethiol (into separated toluene phase), the solution became colorless (inset **(b)E** in **Figure 4-4**) at SH/Au^{3+} = 3/1 indicating all Au^{3+} were reduced into Au^{1+}. The other cases with $SH/Au^{3+} < 2$ were still orange (inset **(b)F–H**). Here F was light orange because the ratio SH/Au^{3+} had slight deviation < 2. From UV-vis, the absorbance at 402 nm disappeared for sample **E** which further confirmed the complete reduction of Au^{3+} to Au^{1+} (**Figure 4-4**). There was no absorbance at ~520 nm indicating that no Au^0 formed even at excess R-SH in the step of **Formula (4-2)**. Besides, the solution was clear as seen in the insets **(b)** in **Figure 4-4**. This indicated that no polymeric $[AuSR]_n$ formed which is not soluble in toluene. The solution became dark brown immediately after addition of $NaBH_4$ indicating that AuNPs formed. After diluted into 0.1 mg/ml, the AuNPs were discernible brown for sample **E, F, G** and brown with slight red for **H** (inset **c**).

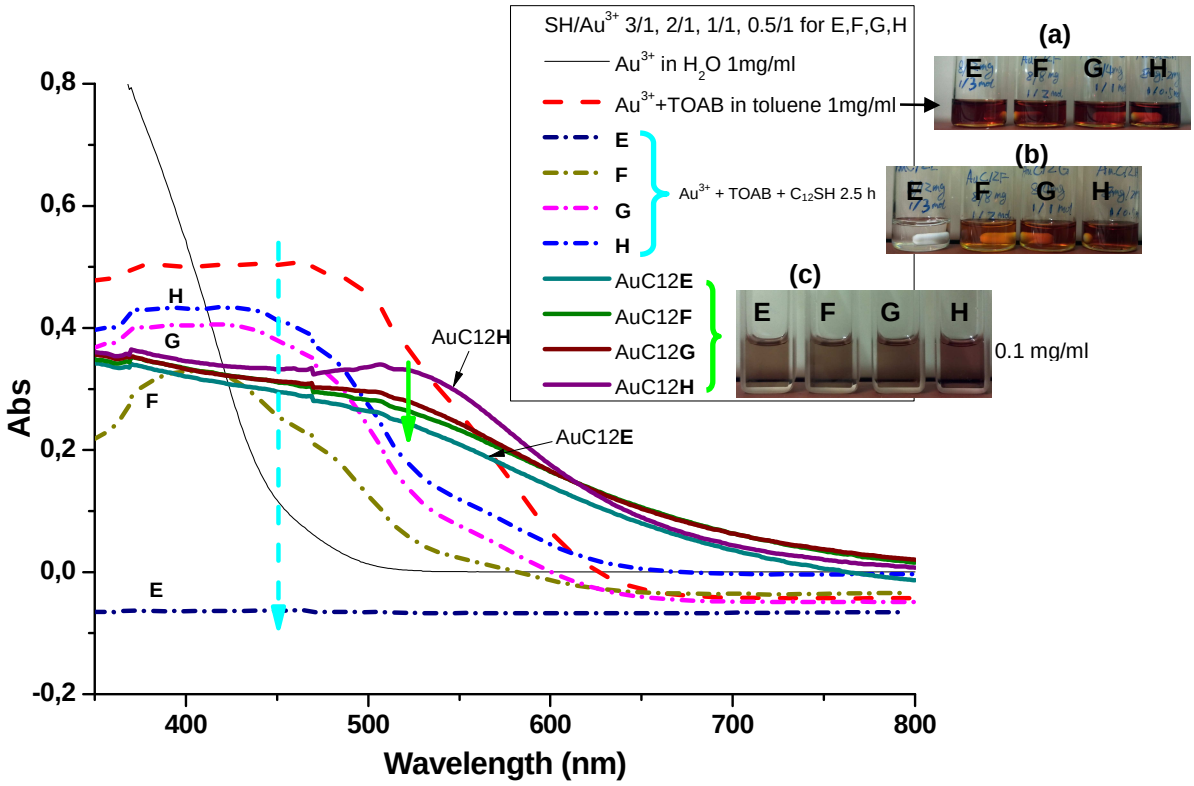

Figure 4-4. UV-vis analysis of AuNPs stabilized with $CH_3(CH_2)_{10}CH_2$-SH by Brust-Schiffrin method. Sample E, F, G, H corresponded to the molar ratio SH/Au^{3+} = 3/1, 2/1, 1/1, 0.5/1. The solution is 0.1 mg/ml in toluene for UV analysis unless specified. The inset (a–c) shows the pictures by camera.

The outcomes of AuNPs solution color depended on the size and shape, and showed brown at d < 3 nm and shifted to wine-red as size increasing[197]. The UV absorbance at ~525 nm also confirmed the formation of AuNPs. As SH decreased (SH/Au^{3+} = 3/1, 2/1, 1/1, 0.5/1 for E, F, G, H) the strength of absorbance peak increased indicating the nanoparticle size increased. As Au further evoluted into non-round shape, the solution turned into purple and further into blue and also with a red shift in UV-vis depending on the shape and aspect ratio[198,199], which will be discussed in the next step of polymer stabilized Au materials.

4.3 P4VP-based block copolymers stabilized AuNPs by one-phase procedure in THF

4.3.1 Short P4VP-block based copolymers as stabilizers for AuNPs

P4VP-based block copolymers were employed as stabilizer for AuNPs in one-phase procedure in THF. The Au^{3+} was reduced by $(Et)_3SiH$ or $Li(CH_2CH_2)_3BH$ (Superhydride) at presence of P4VP-based block copolymers. Any other competitive stabilizer, like TOAB used as phase-transfer agent in Brust-Schiffrin method, was avoided.

Table 4-3 showed that with higher molar ratio of $4VP/Au^{3+}$ longer time was needed to reduce Au^{3+} into Au^0 by $(Et)_3SiH$. The solution color changed into brown-red within 10 min when $4VP/Au^{3+} < 1/1$ (Au85G,H). Higher amount of 4VP needed longer time for reduction, 2 h and 20 h for Au85E ($4VP/Au^{3+} = 2/1$) and Au85F ($4VP/Au^{3+} = 4/1$), respectively. The UV-vis (**Figure 4-5**) showed that Au85E and F had maximum absorbance at ~530 nm. Au85G and H had a broad shoulder peak shift to higher wavelength ~700 nm, indicating big particles or non-round shape of Au formed[197,198]. The DLS analysis confirmed that larger Au particles (d of 200~300 nm) formed for sample Au85G and H. Higher amount of 4VP ($4VP/Au^{3+} > 1/1$) produced small particles with d = 20–30 nm.

Table 4-3. AuNPs stabilized by $P4VP_6$-*b*-$PPMA_{107}$ via one-phase method in THF with $(Et)_3SiH$ as reducing agent.

Sample	$4VP/Au^{3+}$	Au^{3+}+4VP	Au^{3+} + 4VP + $(Et)_3SiH$					
	mol/mol	2 h	5 min	10 min	30 min	1 h	2 h	20 h
Au85F	**4/1**							
Au85E	**2/1**							
Au85G	**1/1**					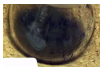		
Au85H	**0.5/1**							

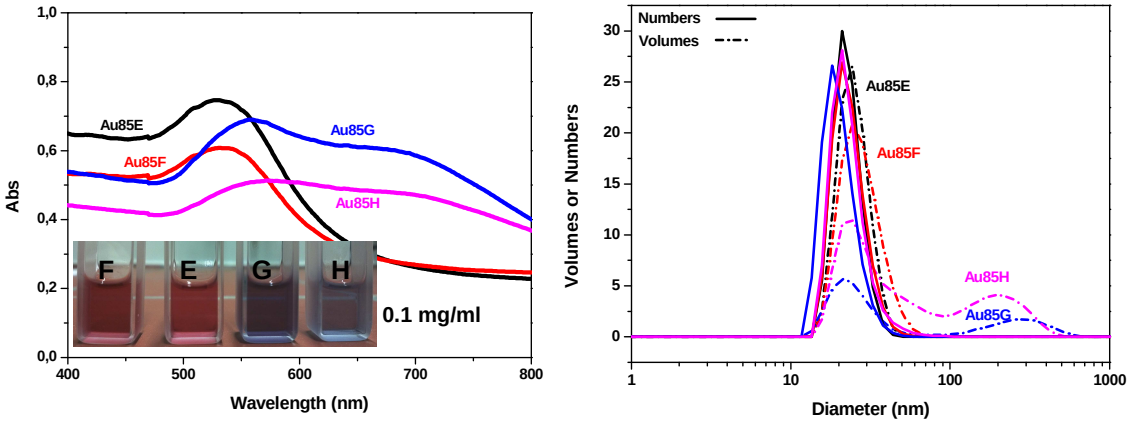

Figure 4-5. UV-vis (left) and DLS (right) analysis of AuNPs stabilized with P4VP$_5$-*b*-PPMA$_{107}$ by one-phase method in THF. Molar ratio 4VP/Au^{3+} = 4/1, 2/1, 1/1, and 0.5/1 for Au85F, E, G, H respectively.

To get a fast reduction of Au^{3+} to Au^0, the stronger reducing agent $Li(CH_2CH_2)_3BH$ (Superhydride) was applied. The solution changed into brown-red immediately at addition of Superhydride. The fast reduction finished in 10 min meaning that there was no obvious size evolution after that (**Figure 4-6,7** Au43F). The growth of NPs was monitored by withdrawing samples at different timed intervals for DLS and TEM analysis. DLS results in **Figure 4-6** showed that the AuNPs owned a large size over 100 nm (Au core + polymer shell) which was different from Au85E–F (~20 nm) reduced by weaker reducing agent $(Et)_3SiH$ (**Figure 4-5**). TEM images in **Figure 4-7** showed that small Au core < 5 nm was obtained. Based on DLS and TEM, the AuNP in solution, such as for sample Au43F owned a polymer shell of ~60 nm by $(d_{DLS} - d_{TEM})/2$, indicating that the P4VP-based block copolymers grafted to AuNP surface.

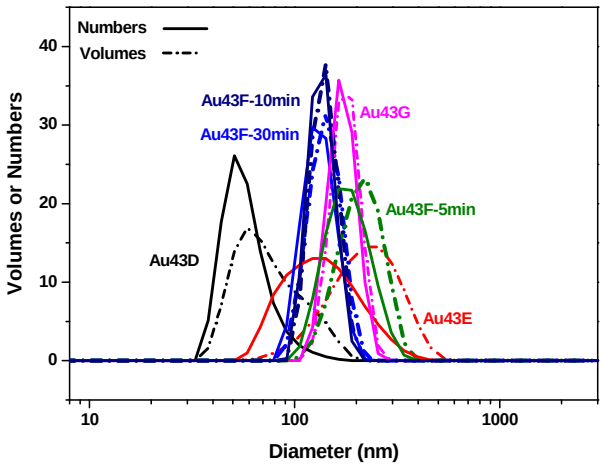

Figure 4-6. DLS analysis (a) of AuNPs stabilized by P4VP$_7$-*b*-PMMA$_{61}$ with molar ratio of 4VP/Au^{3+} of 8/1, 4/1, 2/1 and 1/1 for Au43D, E, F, G respectively.

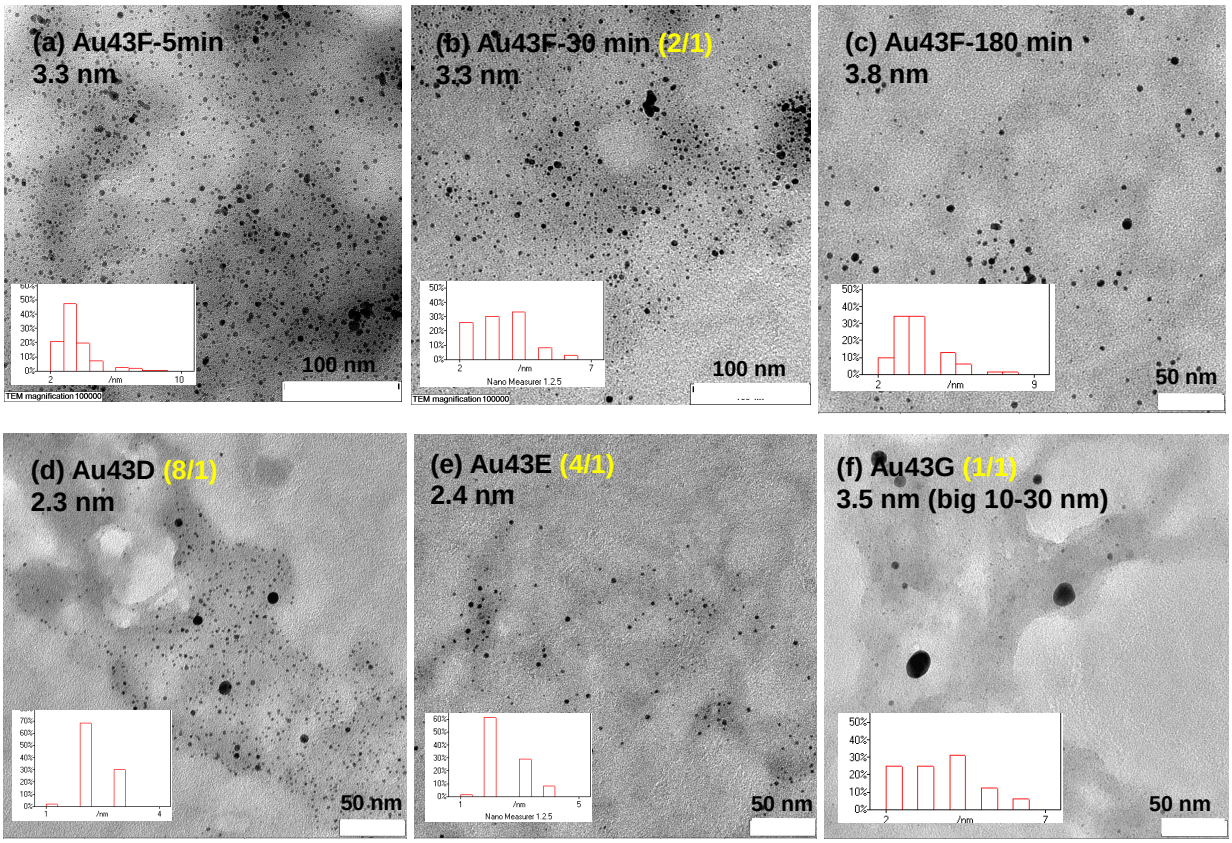

Figure 4-7. TEM images of AuNPs stabilized by $P4VP_7$-*b*-$PMMA_{61}$ with molar ratio of $4VP/Au^{3+}$ of (a-c) 2/1, (d) 8/1, (e) 4/1, (f) 1/1; (a) and (c) show the withdrawn samples from (b) with reaction time of 5 min and 3 h, the rest are the samples after 30 min.

Besides, AuNPs had narrow size dispersity at molar ratio of $4VP/Au^{3+}$ = 2/1 (Au43F stabilized by $P4VP_7$-*b*-$PMMA_{61}$ in **Figure 4-6,7**). Higher or lower amount of 4VP caused some big particles formation (10–30 nm) as shown in **Figure 4-7d–f**, 8/1, 4/1, 1/1 for Au 43D, E, and G respectively. However the big particles were in very low amount of < 1% in number by counting from TEM images. Other short-P4VP based block copolymers, $P4VP_6$-*b*-$PPMA_{107}$ and $P4VP_6$-*b*-$PMMA_{170}$ had similar effect in stabilizing AuNPs and proved that a molar ratio of $4VP/Au^{3+}$ = 2/1 was the optimal condition to get AuNPs with narrow size dispersity.

4.3.1 Long P4VP-block based copolymers as template: one-step preparation of PMMA-*b*-P4VP@AuNPs hybrids

As long P4VP-block (M_n > ~2000 g/mol) has poor solubility in THF which is good solvent for PMMA-block, PMMA-*b*-P4VP can self-assemble into nanostructures in THF with P4VP as core and PMMA as shell. $PMMA_{135}$-*b*-$P4VP_{73}$ (denoted as M135V73) with dispersity Đ = 1.25 was dissolved in THF with ~10 mg/ml under stirring to form stable micelles. Gold precursor Au^{3+} ($HAuCl_4$) was then incorporated into P4VP-core of the micelles by N:Au^{3+} interaction. **Figure 4-8a–d** shows the M135V73 block copolymer micelles formed in THF. The spherical micelles had an averaged size of d_{AFM} = 51 nm which was comparable with the size determined by DLS measurements (d_{DLS} = 55 nm from "number averaged"). After incorporation with Au^{3+}, the micelles M135V73@Au^{3+} maintained the spherical shape as M135V73 (**Figure 4-8a,b**). But the micelle size decreased from 51 nm to 40 nm. The Au^{3+} was supposed to act as cross-linker for the P4VP-core by N:Au^{3+} interaction and induced the shrinking of the micelles. The tendency was more pronounced with further increasing Au^{3+}. As shown in **Figure 4-8c,d**, by increasing Au^{3+} to molar ratio of 4VP/Au^{3+} = 73:5 and 73:10, the micelle size further decreased to d = 31 nm and 25 nm.

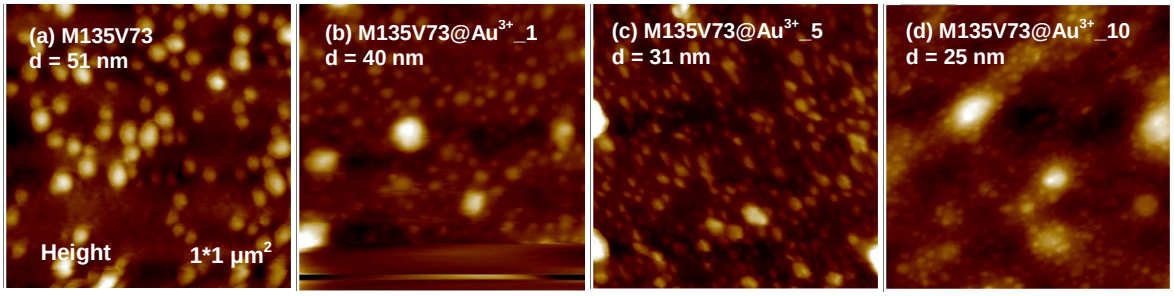

Figure 4-8. AFM height images (1*1 μm^2) of $PMMA_{135}$-*b*-$P4VP_{73}$ (denoted as M135V73) micelles in THF. (a) 13mg/ml of M135V73 in THF; M135V73 micelles incorporated with $HAuCl_4$ and molar ratio of (b) 4VP/Au^{3+} = 73:1, (c) 4VP/Au^{3+} = 73:5, (d) 4VP/Au^{3+} = 73:10.

Strong reducing agent $Li(CH_2CH_2)_3BH$ (1M in THF) was added to M135V73@Au^{3+}_1 micelle solution in THF under argon to get fast reduction of Au^{3+} into Au^0. The solution changed into grey-brown immediately indicating the formation of AuNPs. Due to the contrast between Au and polymers, the AuNP areas were easily identified in AFM images (**Figure 4-9a,b)**. TEM analysis provided more details about the size and location of AuNPs in the micelles. From **Figure 4-9c**, the micelles M137V73@Au maintained spherical shape with averaged size of d = 40 nm which was the same as that before reduction (M135V73@Au^{3+}) (**Figure 4-8b**). TEM with higher magnification (**Figure 4-9d**) shows that AuNPs formed in the spherical areas and with small size of d = 1.8 nm. Most of micelles (~90 %) were filled with

5–10 AuNPs per micelle. The gathering of several AuNPs on individual micelles contributed to the grey color of M137V73@Au solution since AuNPs with d_{core} < 3 nm solution appears brown (**Figure 4-4)**.

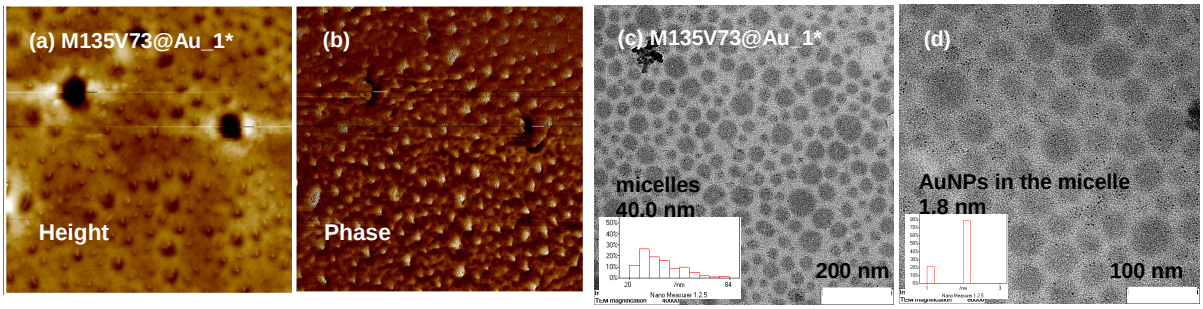

Figure 4-9. M135V73@Au hybrids by in-situ reduction from M135V73@Au3+_1 (4VP/ Au^{3+} = 73/1) in dry THF under argon. (a,b) AFM height and phase images (1*1 μm^2), (c) TEM image and (d) in high magnification.

The micelle size and shape depend on the block copolymer structure parameters[200,201,202]. Incorporation of Au^{3+} induced the shrinking of micelles. With self-assembly of PMMA-*b*-P4VP as template, micelles with incorporated uniform AuNPs were prepared in one-step by in-situ reduction.

4.4 Thiol-terminated polymers stabilized AuNPs prepared by one-phase procedure in THF

Thiol-terminated polymers PMMA-SH and PPMA-SH were employed in stabilizing AuNPs aiming to get NPs with grafted layer chemically equal to the components of PPMA-*b*-PMMA, thus controlled location of NPs in BCP thin films can be achieved.

Homopolymers $PMMA_{28}$-SH with n_{MMA} = 28 and dispersity Đ = 1.20 were polymerized by RAFT and followed by aminolysis to give thiol end-group. $PMMA_{28}$-SH and $HAuCl_4$ were mixed in dry THF followed by reduction with Superhydride ($Li(CH_2CH_2)_3BH$). The solution changed into brown-red immediately at addition of Superhydride indicating fast reduction. The reaction was maintained for 0.5 h under stirring to ensure complete reduction and then stopped by adding fresh THF.

Table 4-4. AuNPs stabilized with $PMMA_{28}$-SH by one-phase method in THF reduced by Superhydride.

Sample	**Feed details** SH/Au^{3+} mol/mol	**d_{core} (TEM)** nm	**$d_{core+shell}$ (DLS)**[a] nm	PDI
Au55a	4/1	1.4	141	0.221
Au55b	2/1	4.4	175	0.261
Au55c	1/1	3.9	208	0.189
Au55d	0.5/1	3.5	168	0.132

[a] the size is from “number averaged” in DLS.

Au-$PMMA_{28}$ in solution state was investigated by DLS and UV-Vis. **Figure 4-10** showed that the nanoparticles had diameter d > 100 nm (gold core + polymer shell) except Au55a (~50 nm), whilst there was a maximum absorbance at λ = 519 nm for Au55b,c,d and λ = ~500 nm for Au55a in UV-vis. The weak absorbance peak at ~520 nm indicated that the nanoparticles owned small gold core d_{core} < 10 nm. The AuNPs with d_{core} < 4 nm had no obvious absorbance according to previous reports[197,198]. The results of UV-Vis were consistent with TEM analysis which showed the core size below 5 nm (**Figure 4-11**) (due to the low contrast of polymer shell $PMMA_{28}$ only Au core could be seen by electron microscopy). The big difference in size from TEM (< 5 nm) (Au core) and DLS (> 100 nm) (Au core + shell) confirmed that the AuNPs were grafted by polymer $PMMA_{28}$.

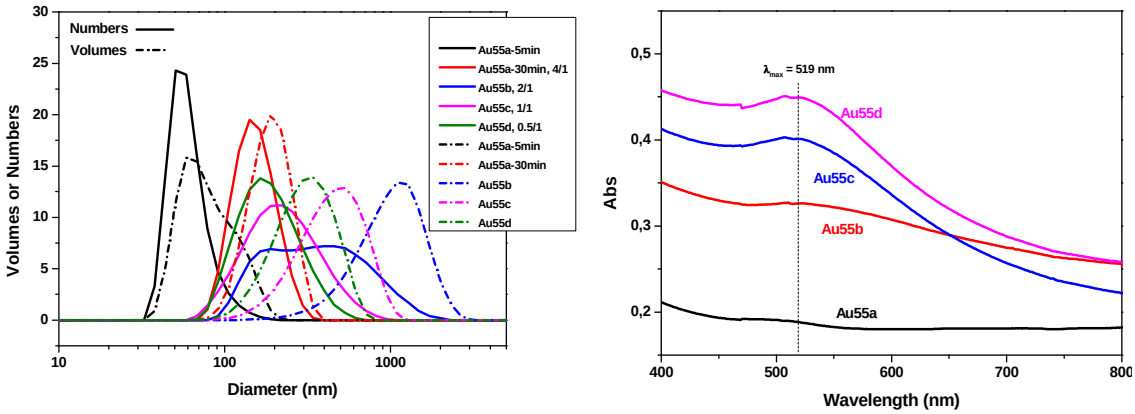

Figure 4-10. DLS (left) and UV-Vis (right) analysis of AuNPs stabilized by $PMMA_{28}$-SH with molar ratio of SH/Au^{3+} of 4/1, 2/1, 1/1, 0.5/1 for Au55a, b, c, d, respectively. 0.1 mg/ml in THF.

With decreasing SH amount from 4/1, 2/1, 1/1 to 0.5/1 (SH/Au^{3+}, mol/mol), the AuNP size increased obviously, with d_{core} = 1.4 nm for SH/Au^{3+} = 4/1 (Au55a) and d_{core} = 3.5 nm for SH/Au^{3+} = 0.5/1 (Au55d) (**Figure 4-11a,d**). High molecular weight thiol ligand $PMMA_{28}$-SH obtained smaller particles compared to dodecanethiol at same SH amount. For SH/Au^{3+} = 0.5/1, Au-$C_{12}H_{25}$ had d_{core} = 8.7 nm (**Figure 4-2b**) and Au-$PMMA_{28}$ had d_{core} = 3.5 nm (**Figure 4-11d**).

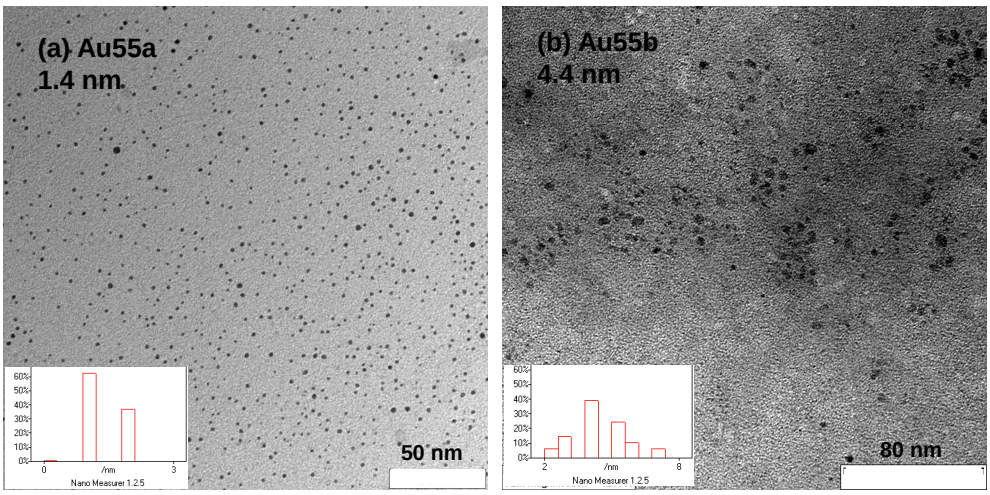

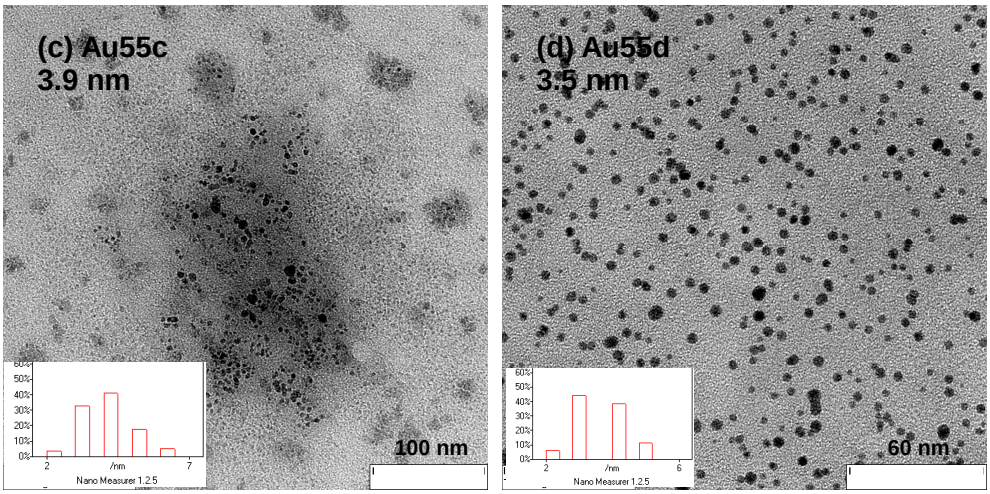

Figure 4-11. TEM images of AuNPs stabilized by $PMMA_{28}$-SH with molar ratio of SH/Au3+ of (a) 4/1, (b) 2/1, (c) 1/1, (d) 0.5/1.

The nanoparticles size depended on SH amount. However, the variations were in a very small range of d_{core} between 1.5–4.5 nm when SH amount decreased from 4/1 to 0.5/1 (SH/Au^{3+}). Further decrease of SH amount, SH/Au^{3+} = 0.1/1, was tried. The solution changed into wine-red after adding Superhydride but became dark and totally precipitated out within 1 h. When the AuNPs with $PMMA_{28}$-SH as stabilizer were prepared in Brust-Schiffrin method with SH/Au^{3+} = 1/1, small AuNPs were obtained with d_{core} < 5 nm. Our results were comparable to the previously reported that d_{core} = 4.4 nm resulted when PSt_{19}-SH/Au^{3+} = 1/1 in one-phase in THF[203] and d_{core} = ~2.5 nm resulted when PSt_{34}-SH/Au^{3+} = 1/1 in Brust-Schiffrin method[12]. It was supposed that the steric effect of grafted polymers prevented the further growth of AuNP, thus small AuNPs were obtained.

The AuNPs stabilized by thiol-end polymers dispersed in THF very well and were stable for over months under room temperature as low molecular weight thiol stabilized AuNPs did. Homogeneous AuNPs solution without precipitation can be discerned easily by un-aided eyes as well as from DLS and UV analysis (**Figure 4-12**). This further confirmed that polymer grafted AuNPs via S-Au bond are much more stable compared to P4VP-based block copolymers stabilized AuNPs. The AuNPs coated by P4VP-*b*-PMMA were stable in THF only for hours to weeks, then precipitation appeared gradually.

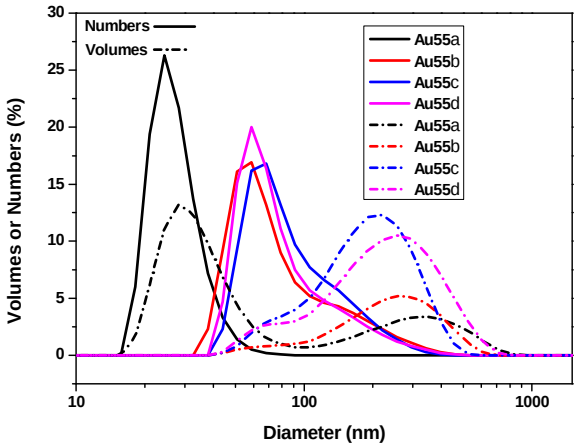

Figure 4-12. DLS analysis of Au-PMMA$_{28}$ (one month after synthesis). The molar ratio of SH/Au^{3+} is 4/1, 2/1, 1/1, 0.5/1 for Au55a, b, c, d respectively. 0.1 mg/ml in THF.

Conclusion for this part:

AuNPs with varied size and stabilizing species were synthesized in controlled manner by two-phase method (Brust-Shiffrin method) or one-phase in THF and characterized by DLS, UV-Vis and TEM. P4VP-based block copolymers were employed successfully in stabilizing AuNP with P4VP-block as inner shell due to the coordination of pyridine group with Au^{3+} and the other block as outer shell. Thiol-terminated polymers were weaker ligands than small thiol molecules in stabilizing AuNPs due to steric effect, thus were used in one-phase method in stabilizing AuNPs in order to avoid phase-transfer agent TOAB. Thiol-terminated polymers were grafted to AuNP surface via S-Au bond and were stronger ligands compared to P4VP-based species. The nanoparticle size depended on the molar ratio of SH/Au^{3+} and increased as SH decreased.

5 PPMA-*b*-PMMA based hybrid thin films modified by AuNPs: characterization and discussion

The effects of AuNPs with varied size and coated species on the morphology evolution and nanostructure orientation of block copolymer thin films were investigated. The classic approach to control the microdomain orientation in thin films is to modify the substrate by introducing a random copolymer layer or by applying an external field like solvent and thermal annealing, electrical field (**Chapter 2.4.1**). Introducing of NPs in BCP thin films is an easy method to direct the morphology and orient the nanostructure to get standing cylinders perpendicular to the substrate. Such highly ordered nanostructure with high aspect ratio is critical for further application such as in electronics and sensors. The following discussions will show how the nanostructure and orientation of PPMA-*b*-PMMA thin films were improved by adding AuNPs of varied size and stabilizing species.

5.1 Microphase separation of PPMA-b-PMMA

5.1.1 PPMA-*b*-PMMA in bulk

Two synthesized block copolymers of PPMA-*b*-PMMA, denoted as PM11 and PM13, were employed in this study. PM13 has a molar ratio of n/m = 72:28, molecular weight of M_n = 54200 g/mol, dispersity of Đ = 1.14, and PM11 has a molar ratio of n/m = 49:51, M_n = 54600 g/mol, Đ = 1.16 as shown in **Table 3-1**. Block volume fraction is one of parameters which dominate the microphase separation of block copolymers and is given by

$$\varphi_{PPMA} = \frac{n_{PPMA} V_{mol,PPMA}}{n_{PPMA} V_{mol,PPMA} + m_{PMMA} V_{mol,PMMA}} \quad \textbf{(5-1)}$$

where φ_{PPMA} is the volume fraction of PPMA block, n and m is the degree of polymerization of PPMA and PMMA respectively, V_{mol} is the molar volume and $V_{mol,PPMA}$ = 146.3 cm^3/mol, $V_{mol,PMMA}$ = 81.9 cm^3/mol[180]. Thus for PM13, φ_{PPMA} = 82 %, and for PM11, φ_{PPMA} = 63 %.

SAXS was used to investigate the phase separation of BCP in bulk with regard to morphology and domain size. The relative morphology is estimated from the relative ratio of the observed peak positions to the position of the first existing peak[180]. The d_{hkl} spacing (Bragg spacing) (distance between adjacent reflecting net planes of the morphology) is calculated from q value (magnitude of the scattering vector) as given by **Formula (2-18)** (chapter 2) that

$$d_{hkl} = \frac{2\pi}{q_{hkl}} \quad \textbf{(2-18)}$$

Figure 5-1a,b showed the temperature-dependent SAXS (T-SAXS) patterns of the samples PM13 and PM11. The d_{hkl} spacing was T-dependent and mostly increased as T was elevated (q shift to lower value) for both samples.

For PM13, beginning with ~120 ℃, the results were phase-modeled as lamellar as well as hexagonally close packed cylinders. Last version should be more realistically because of the volume ratio of PPMA/PMMA = 82/18. Specifically after 1st heating/cooling run of 30-200-30 ℃ and cooling to room temperature (RT) (**Figure 5-1c**), d_{100} spacing was calculated as $d_{100} = \frac{2\pi}{q} = \frac{2\pi}{0.1632} = 38.5$ nm.

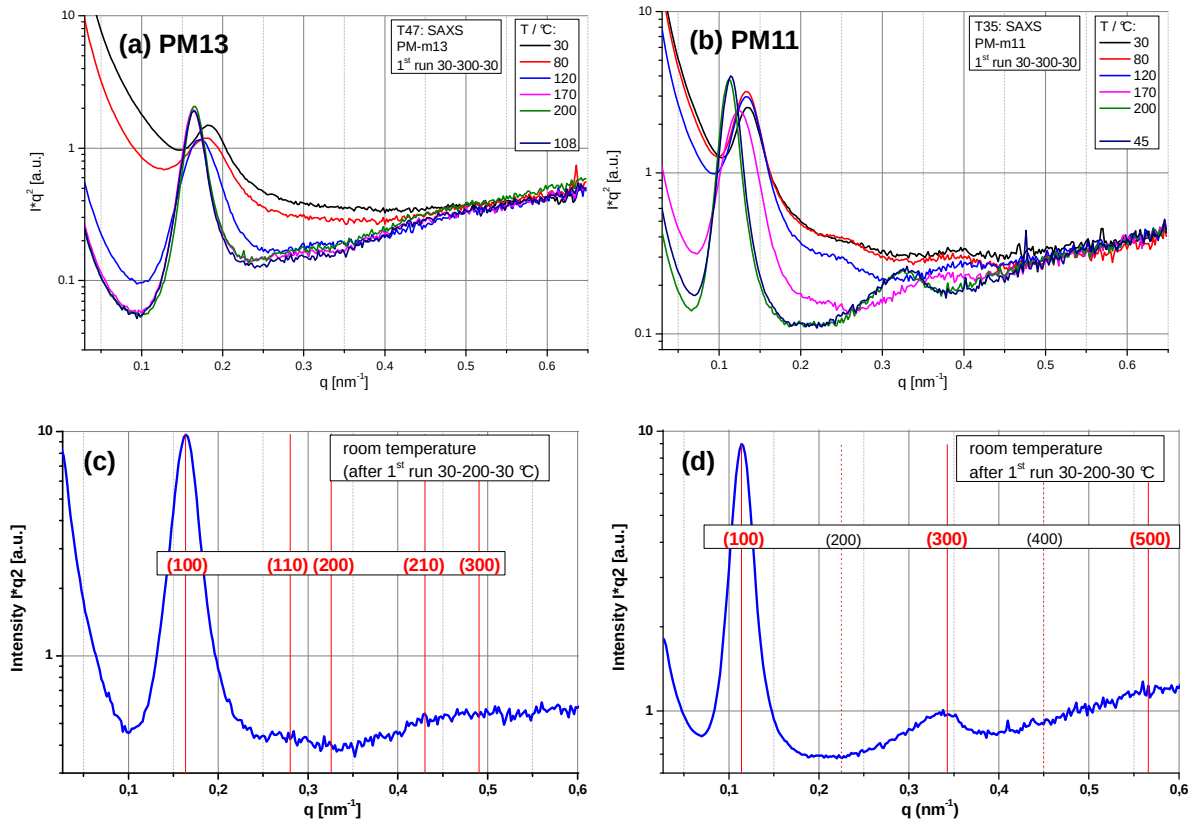

Figure 5-1. T-SAXS patterns of PPMA-*b*-PMMA in bulk. Curves with scattering intensity (Lorentz-correlated intensity $I*q^2$) vs. magnitude of the scattering vector q. (a) PM13; (b) PM11; specifically after 1st run 30-200-30 °C and cooling to RT (c) PM13 with h exagonal close-packed cylinder morphology of d_{100} = 38.5 nm, corresponding a_{hex} = 44.5 nm; and (d) PM11 with lamellar morphology of d_{100} = 55.5 nm.

For PM11, the results were phase-modeled as lamellar. The quality of lamellae ordering at T < 120 °C was not very high as indicated by the lo w intensities of higher indexed reflections. The quality is slightly increased during heating. Beginning with ~120 °C, the intensity of the (002) reflection (the first even reflection) was decreasing. This gives a hint onto the more and more identically thick sub-layers of PMMA and PPMA. Due to extinction condition[204,205], the second peak should be absent from the scattering profile when the volume fraction φ is ~0.5 for lamella. The volume fraction of PM11 is φ_{PPMA} = 0.63, therefore, the extinction condition is approximately satisfied. After 1st heating/cooling run of 30-200-30 °C and cooling to RT (**Figure 5-1d**), d_{100} spacing was calculated as $d_{100} = \frac{2\pi}{q} = \frac{2\pi}{0.1132} = 55.5$ nm.

5.1.2 PPMA-*b*-PMMA in thin films

The morphology and nanostructure orientation of block copolymer in thin films were investigated by AFM measurements. Due to stiffness contrast in tapping-mode AFM, the harder PMMA-domain (higher modulus) is brighter than PPMA-domain in the AFM phase contrast images. Correspondingly, PMMA-domain is brighter than PPMA-domain in the height images.

Figure 5-2a–d shows the AFM images of PM13 thin films with film thickness of t_{film} = ~20 nm (~0.5d_{100}) and ~45 nm (~d_{100}). Both the thin films showed stripes-like pattern which can be recognized as lying cylinders (parallel to the substrate) as well as standing lamellas (perpendicular to the substrate). Since PM13 in bulk had phase separation into cylindrical morphology at equilibrium state (T > T_g) (**Figure 5-1a,c**), in PM13 thin films the typical stripes-like pattern was recognized as phase separation of lying PMMA-cylinders in PPMA matrix. The substrate of Si-wafer pre-cleaned by Piranha solution exhibited hydrophilic matrix with silanol group on the surface. Thus, the more hydrophilic PMMA-domains had preferential interaction with the substrate. This induced that the PMMA-cylinders oriented parallel to the substrate.

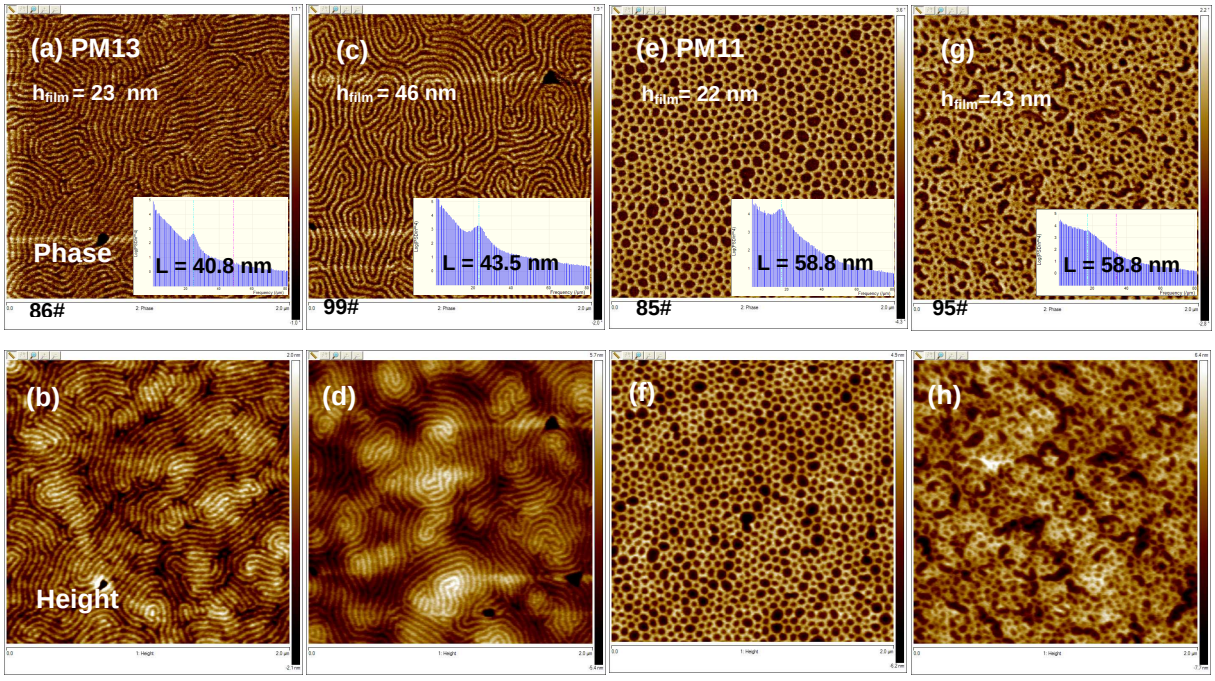

Figure 5-2. AFM images (2*2 µm^2) of PPMA-*b*-PMMA thin films on Si-substrate as-prepared by dip-coating. (a–d) PM13, (e–h) PM11. (a,e) film thickness of ~20 nm, (c,g) film thickness of ~45 nm. (a,c,e,g) are phase images and the rest are height images. The inset image is the Fast Fourier Transition (FFT) of the corresponding AFM and L is lateral distance obtained by the first-order peak (maximum intensity peak) in FFT.

Figure 5-2e,f shows that PM11 thin film had dots-like pattern. The darker dots were recognized as PPMA-cylinders in PMMA matrix. As discussed previously, PM11 with φ_{PPMA} = 63 % (volume fraction) has lamellar morphology of domain size d_{100} = 55.5 nm in bulk from T-SAXS analysis. The different phase separation behaviors in thin film and in bulk were attributed to the substrate effect. The pre-cleaned Si-wafer was hydrophilic and preferential to PMMA-domain. PPMA-block with lower surface energy than PMMA-block preferred the free surface (γ_{PMMA} = ~40 mN/m and γ_{PPMA} = ~25 mN/m[180]). Thus PPMA-cylinders oriented perpendicularly to the substrate to get minimum contact areas with the substrate. The substrate effect deteriorated as the film thickness increased. **Figure 5-2g,h** shows that PM11 thin film of ~45 nm had less pronounced standing PPMA-cylinders with mixed structures of lying PPMA-cylinders or standing lamellas.

The following discussions were about how the nanostructures of PM13 and PM11 in thin films were improved by adding AuNPs and how the AuNPs affect the morphology and nanostructure orientation of the BCP thin films.

5.2 The size effect of AuNPs on the morphology of PPMA-*b*-PMMA thin films

5.2.1 AuNPs stabilized by low molecular weight species

The morphology and nanostructure orientation of block copolymer thin films were investigated by AFM measurements. Due to stiffness contrast (in tapping-mode AFM), PMMA-phase which was harder than PPMA-phase turned out to give brighter areas in the AFM phase images.

Table 5-1. Small AuNPs stabilized by low molecular weight species.

	d_{core}(TEM) nm	**stabilizing species**	**SH/Au[a] mol/mol**
Au18	2	$CH_3(CH_2)_{11}$-SH	3/1
Au15	8.7	$CH_3(CH_2)_{11}$-SH	0.5/1
AuF6a	1.9	$CF_3(CF_2)_5CH_2CH_2$-SH	1/1
AuF6c	6.4	$CF_3(CF_2)_5CH_2CH_2$-SH	0.26/1

[a] feed in AuNP synthesis.

The effects of AuNPs stabilized with $CH_3(CH_2)_{11}$-SH on the morphology and nanostructure orientation of PM13 thin films were investigated. **Au18** with d_{core} of 2 nm stabilized by $CH_3(CH_2)_{11}$-SH were dispersed in THF and mixed with PM13 in THF solution followed by dip-coating onto the pre-cleaned Si-wafer to get hybrid thin films denoted as PM13/Au18. Some dots appeared among the stripes-like pattern in the AFM images of thin film PM13/Au18 (**Figure 5-3b**). This indicated that a part of lying PMMA-cylinders (parallel to the substrate) turned to standing PMMA-cylinders (perpendicular to the substrate). As the nanoparticles increased to 5 wt%, an increasing amount of lying cylinders switched to standing cylinders according to the increasing dots appearing in the morphology (**Figure 5-3c)**. The quality of the thin film nanostructures was improved by the incorporation of Au18. From the Fast Fourier Transition (FFT) (insets in **Figure 5-3a–c**) of the corresponding AFM images, the lateral distance (L) of the nanostructures (PMMA-cylinders) had a decreasing tendency from 40.8 nm to 37.7 nm when Au18 increased from 0 to 5 wt%.

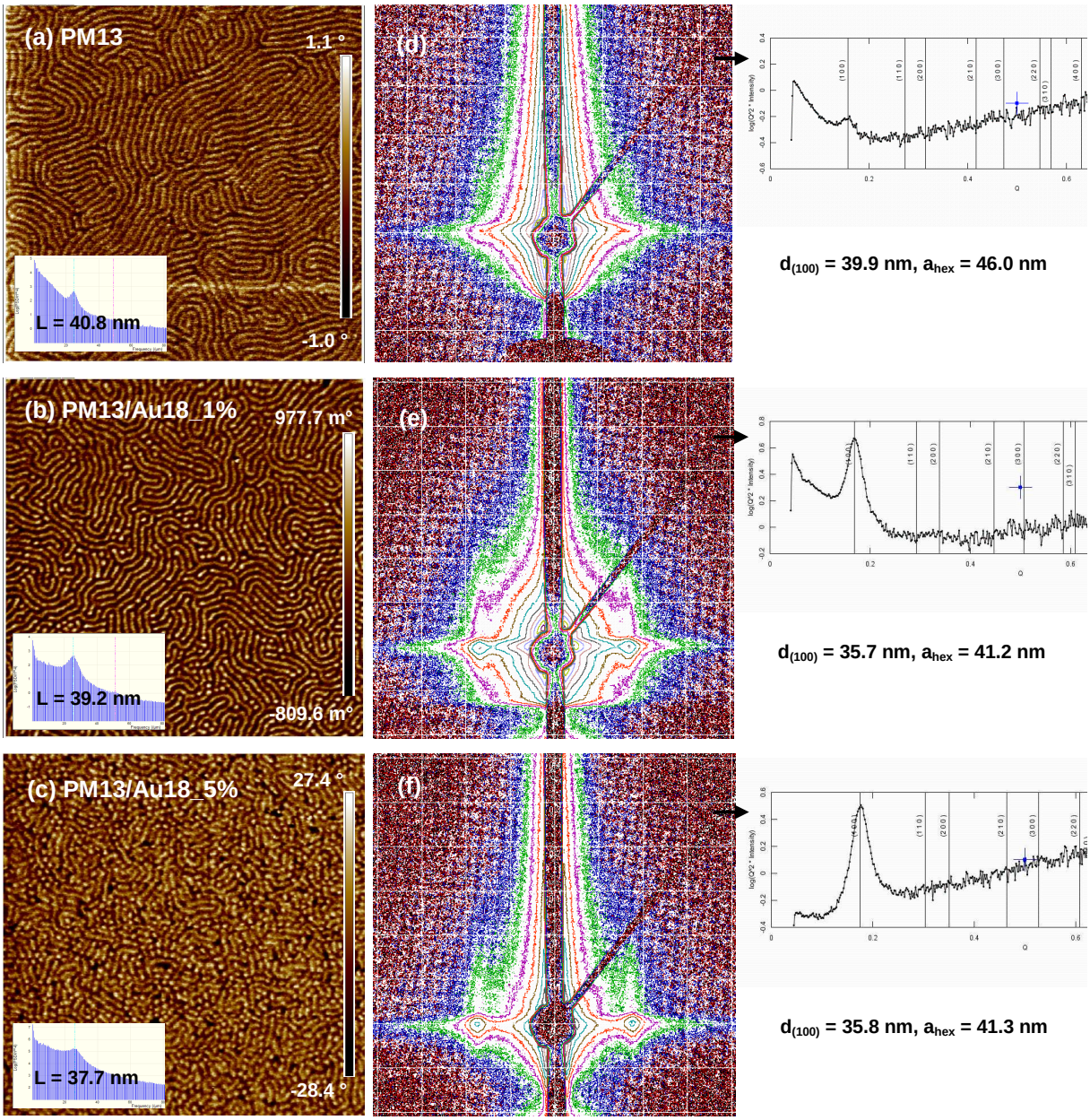

Figure 5-3. AFM phase images (2*2 μm^2) of PM13/Au18 hybrid thin films (thickness ~20 nm) containing (a) 0 wt%, (b) 1 wt%, and (c) 5 wt% of Au18 (d_{TEM} = 2 nm) stabilized by dodecanethiol. AuNPs % = Au/PM13, m/m. The brighter area is PMMA-domain and darker area is PPMA-domain due to stiffness contrast. GISAXS patterns (mesh size Δq = 0.1 nm^{-1}) (incidence angle α_i = 0.18 °) of the corresponding hybrid thin films containing (d) 0 wt%, (e) 1 wt%, and (f) 5 wt% of Au18. a_{hex} is unit cell parameter, derived from lateral correlation peak (set as (100) reflection); not faultless in case of mixed arrangements of lying and standing cylinders[206].

To further investigate the morphology evolution of BCP thin films with incorporation of varied amount of AuNPs, Grazing Incidence Small Angle X-ray Scattering (GISAXS)[207] measurements were carried out. GISAXS data were collected at different incidence angle from 0.10 ° to 0.40 °. **Figure 5-3d–f** shows the GISAXS pattern with incidence angle α_i = 0.18 ° (≈ $\alpha_{i,BCP}$). The correlation peak became sharper and stronger with adding Au18

indicating enhanced lateral structures in the thin films. The lateral distance of the nanostructures decreased from 39.9 nm to 35.7 nm and 35.8 nm ($d_{(100)}$ value) corresponding to 1 and 5 wt% of Au18 (a_{hex} value from 46.0 nm, 41.2 nm to 41.3 nm). The lateral distance determined by AFM were comparable with the results from GISAXS ($d_{(100)}$ value). The contraction of microdomains (L decreased) was attributed to the decreased interfacial tension by the segregation of NPs near the interface of the two blocks, leading to decreased chain stretching[208,209,210].

Nanoparticles **Au15** stabilized by $CH_3(CH_2)_{11}$-SH but with larger size of d_{core} = 8.7 nm were compared. Hybrid thin films of PM13/Au15 were prepared in the same procedure as PM13/Au18. The nanostructures of the thin film were improved with 1 wt% of Au15 according to the enhanced phase contrast (**Figure 5-4a**). However, the orientation of PMMA-cylinders had no change and was still parallel to the substrate when the NPs increased to 5 wt% (**Figure 5-4b**). This is different from Au18 which caused the re-orientation of most PMMA-cylinders. The size difference between Au15 and Au18 was attributed to their distinct effect on the morphology of BCP thin films. From the theoretical prediction about the particles distribution in the BCP thin films[25-27,170,171], the small particles are expected to be more localized at the segment interface and the larger particles tend to segregate into the preferred domain. In this study, Au18 with d_{core} = 2 nm are supposed to have higher tendency to disperse near the segment interface. Larger particles Au15 (d_{core} = 8.7 nm) were more localized to the preferred PPMA-domain. The small particles Au18 near the PPMA/PMMA interface were not discernable in the AFM due to the too low resolution. But some of the larger particles Au15 were identified to appear in the PPMA-domain as shown in the **Figure 5-4b** (green arrows marked). Furthermore, Au18 induced the contraction of microdomains (L decreased) which was consistent with the theoretical prediction that small particles localized at interface tend to decrease the interfacial tension thus reduce the domain size[25-27].

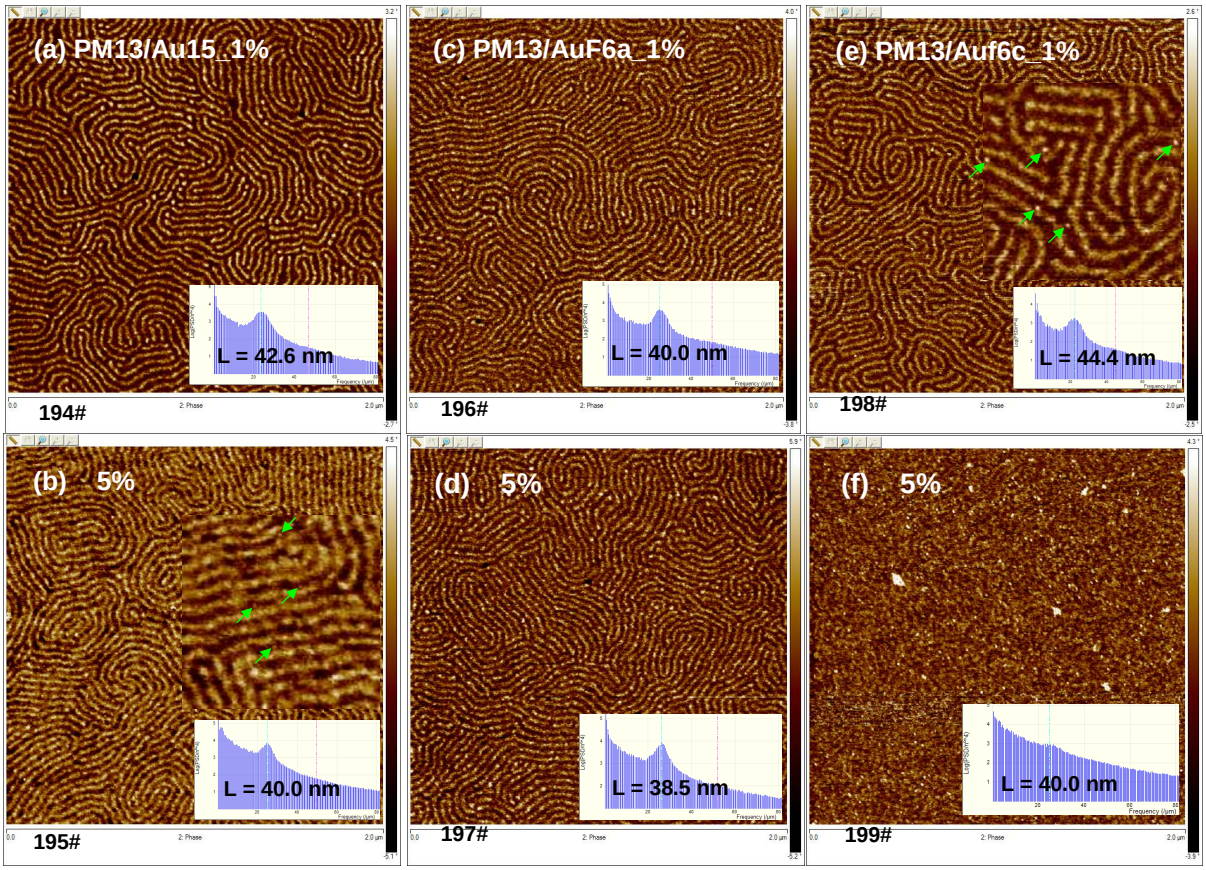

Figure 5-4. AFM phase images (2*2 μm^2) of PM13/AuNPs hybrid thin films (thickness ~20 nm) containing (a) 1 wt%, and (b) 5 wt% of Au15 (d_{core} = 8.7 nm) stabilized by dodecanethiol; (c) 1 wt%, and (d) 5 wt% of AuF6a (d_{core} = 1.9 nm), (e) 1 wt%, and (f) 5 wt% of AuF6c (d_{core} = 6.4 nm) stabilized by $CF_3(CF_2)_5CH_2CH_2$-SH. AuNPs % = Au/PM13, m/m. The inset image is the FFT of the corresponding AFM.

To further verify the size effect of NPs on BCP thin films, AuNPs stabilized by hydrophobic species of $CF_3(CF_2)_5CH_2CH_2$-SH were studied. AuF6a (d_{core} = 1.9 nm) improved the lateral structure of PM13 thin films according to the enhanced phase contrast and the much stronger 1st order peak in the FFT of AFM images (**Figure 5-4c,d**). The lateral distance of the nanostructures decreased (from 40.8 nm for neat PM13) to 40.0 nm and 38.5 nm corresponding to 1 and 5 wt% of AuF6a, similarly as Au18 did. The larger nanoparticles AuF6c (d_{core} = 6.4 nm) induced the expansion of microdomains and the lateral distance increased to 44.4 nm at 1 wt% of AuF6c (**Figure 5-4e**). The NPs were well discernible near the PPMA-domain center (**Figure 5-4e** green arrows marked). Much more NPs localized near the PPMA-domain centre as AuF6c increased to 5 wt%, but the nanostructures became less pronounced (**Figure 5-4f**). $CF_3(CF_2)_5CH_2CH_2$-SH stabilized AuNPs worked similarly as $CH_3(CH_2)_{11}$-SH stabilized AuNPs for the BCP thin films. The smaller AuF6a segregated more at the segment interface inducing the contraction of microdomains. The larger particles AuF6c preferably located in the PPMA-domain inducing the expansion of microdomains of BCP thin films.

5.2.2 AuNPs stabilized by polymer species

To examine the effect of the nanoparticle size on the BCP thin film morphology and orientation, big AuNPs stabilized by high molecular weight species (polymeric species) were employed. **Table 5-2** summarized the details of AuNPs stabilized by polymeric species.

Table 5-2. Big AuNPs stabilized by high molecular weight species employed in the BCP thin films.

		d_{core} (TEM) nm	**stabilizing species**	**SH or 4VP/Au**[a] mol/mol
Au-PMMA	**Au30a**	1.2	P4VP$_6$-*b*-PMMA$_{170}$	1/1
	Au30a2	2.8	P4VP$_6$-*b*-PMMA$_{170}$	0.5/1
	Au51h	6.5	PMMA$_{75}$-SH	0.5/1
	Au51i	10.0	PMMA$_{75}$-SH	0.25/1
Au-PPMA	**Au85b**	5.4	P4VP$_6$-*b*-PPMA$_{107}$	2/1
	Au85d	~5	P4VP$_6$-*b*-PPMA$_{107}$	0.25/1
Au-PEO	**Au16**	5.7	$CH_3O(CH_2CH_2O)_6CH_2CH_2$-SH	1/1

[a] feed ratio in AuNP synthesis.

P4VP-based block copolymer P4VP$_6$-*b*-PMMA$_{170}$ stabilized nanoparticles Au30a (d_{core} = 1.2 nm) and Au30a2 (d_{core} = 2.8 nm) were employed into PM13 thin films. Au30a induced the expansion of microdomains to L = 41.7 nm at 5 wt% NP loading (**Figure 5-5a,b)**. The lateral quality of the nanostructures was improved at 1 wt% of NPs. The orientation of PMMA-cylinders had a nearly complete change from parallel (stripes pattern in **Figure 5-3a** of neat PM13 thin film) to perpendicular (dots pattern in **Figure 5-5a**) to the substrate. However, some aggregations in the form of clusters (3–5 AuNPs per cluster) appeared at higher NP loading of 5 wt% (**Figure 5-5b**).

The incorporation of Au30a2 (1 and 3 wt%) into PM13 thin films induced a complete orientation change of the PMMA-cylinders from parallel to perpendicular as shown in **Figure 5-5c,d** (dots pattern). The lateral distance of the PMMA-cylinders firstly increased to 42.6 nm at 1 wt% of Au30a2 and then decreased to 40.8 nm at 3 wt% of Au30a2. The quality of the nanostructures was improved obviously at 3 wt% of NPs according to the higher phase contrast (**Figure 5-5d**). The PMMA-cylinders arranged hexagonally with partial distortion. Solvent or thermal annealing were usually needed to impart higher mobility of the segmental chains so as to get BCP thin films with ordered nanostructures[5,28]. Here, gold nanoparticles with polymeric species of PMMA as shell (denoted as Au-PMMA) preferably dispersed into

PMMA-domain of block copolymers and this increased the PPMA/PMMA segmental interaction (corresponding to increased X value–Florry-Huggins interaction parameter). This caused the enhanced phase separation of block copolymers.

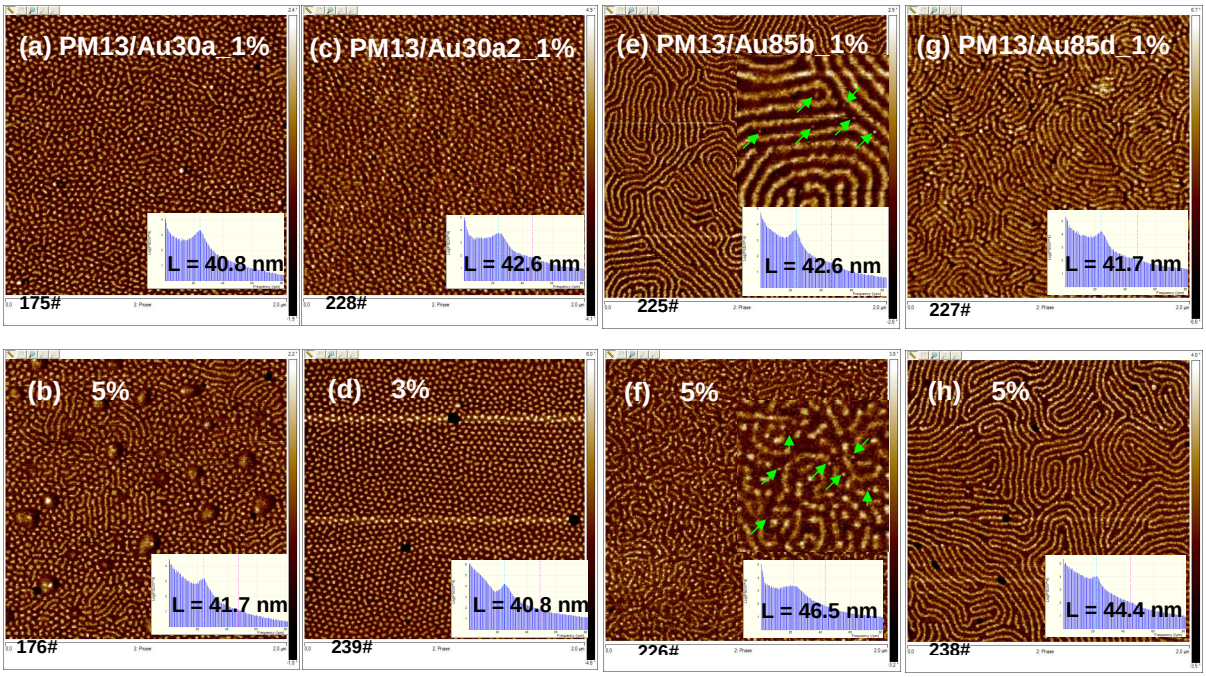

Figure 5-5. AFM phase images (2*2 μm^2) of PM13/AuNPs hybrid thin films (thickness ~20 nm) containing P4VP$_6$-*b*-PMMA$_{170}$ stabilized (a) 1 wt% and (b) 5 wt% of Au30a (d_{core} = 1.2 nm), (c) 1 wt% and (d) 3 wt% of Au30a2 (d_{core} = 2.8 nm); P4VP$_6$-*b*-PPMA$_{107}$ stabilized (e) 1 wt%, and (f) 5 wt% of Au85b (d_{core} = 5.4 nm), (g) 1 wt%, and (h) 5 wt% of Au85d (d_{core} = ~5 nm). AuNPs % = Au/PM13, m/m. The inset image is FFT of the corresponding AFM.

P4VP$_6$-*b*-PPMA$_{107}$ stabilized nanoparticles Au85b and Au85d (denoted as Au-PPMA) (**Table 5-2**) with PPMA as outer shell were mixed with PM13 to make hybrid thin films. The lateral quality of the thin film nanostructures was improved by incorporation of Au-PPMA according to the enhanced phase contrast and the sharper 1st order peak in FFT (**Figure 5-5e–h**). The broader distribution of the lateral distance of nanostructures in **Figure 5-5f** was due to the mixed PMMA-cylinder orientation. Au-PPMA also induced the expansion of microdomains from 40.8 nm to 46.5 nm and 44.4 corresponding to 5 wt% of Au85b and Au85d, respectively. This was similar to the case of PM13 with Au-PMMA discussed previously. The AuNPs with PPMA shell preferably dispersed into PPMA-domain. As seen in the insets in **Figure 5-5e,f**, the nanoparticles appeared in the PPMA-phase (green arrows marked) and near the microdomain centre. The stretching of the segmental chains increased so as to accommodate the incoming NPs[211,212]. However, as shown in **Figure 5-5d**, the lateral distance decreased as Au-PMMA increased. This was attributed to the rearrangement of the nano-cylinders into higher ordered and more closely packed arrays (hexagonally with

partially distorted). The lateral distance of the nanostructures in the BCP thin film decreased when the orientation of the nano-cylinders completely changed from parallel to perpendicular to the substrate (also as shown in the later chapters). This was independent of the NP size and stabilizing species.

Conclusion of the effect of nanoparticle size on BCP thin films:

The small AuNPs stabilized by low molecular weight species had similar effect on the morphology and nanostructure orientation of the BCP thin films. The nanostructures in the thin film were improved by adding AuNPs. The smaller AuNPs (~2 nm) localized more at the segment interface inducing the contraction of microdomains. The contraction was more pronounced as AuNPs increased (**Figure 5-6**). The AuNPs at the interface worked as surfactant that decreased the interface tension thus decreased the chain stretching[25-27]. The larger AuNPs (6-9 nm) preferably dispersed into specific domains inducing the expansion of microdomains. Both the AuNPs improved the nanostrucures (enhanced lateral structure) of the BCP thin film. The PMMA-cylinders re-oriented partially from parallel to perpendicular to the substrate. Higher AuNPs loading (15 wt%) was needed to get complete cylinder re-orientation of the BCP thin films.

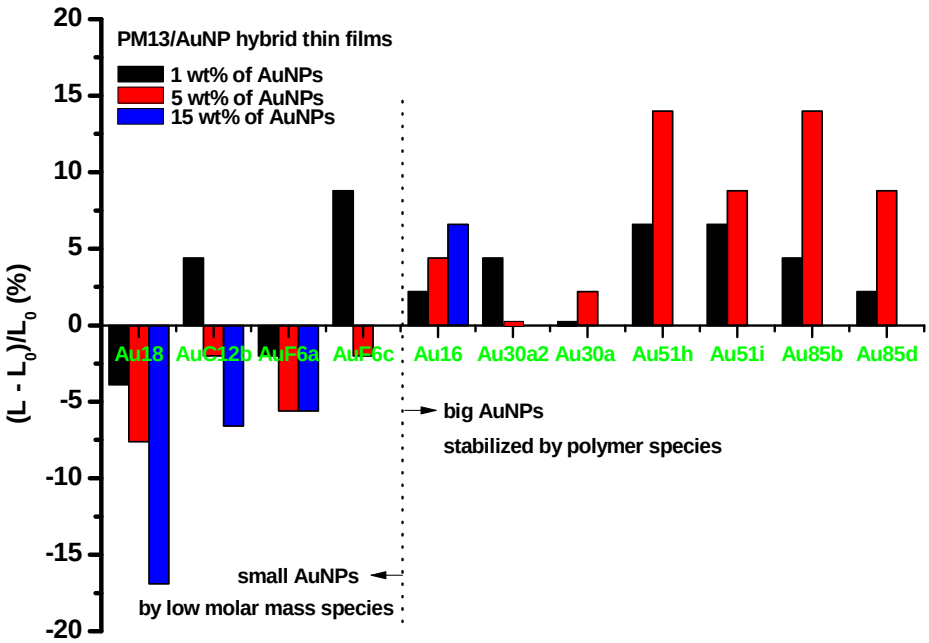

Figure 5-6. Histogram of the change of lateral distance $(L - L_0)/L_0$ (based on AFM) of PM13/AuNP hybrid thin films (thickness ~20 nm). L_0 is the lateral distance of neat PM13 thin film, and L is the lateral distance of PM13/AuNP hybrids. Au18 and Au12b stabilized by $CH_3(CH_2)_{10}CH_2$-SH, Auf6a and Auf6c stabilized by $CF_3(CF_2)_5CH_2CH_2$-SH), Au16 stabilized by $CH_3O(CH_2CH_2O)_6CH_2CH_2$-SH, Au30a2 and Au30a stabilized by P4VP$_6$-*b*-PMMA$_{170}$, Au51h and Au51i stabilized by PMMA$_{75}$-SH, Au85b and Au85d stabilized by P4VP$_6$-*b*-PPMA$_{107}$.

The big AuNPs (d>10 nm) stabilized by high molecular weight species (synthesized polymers) also improved the nanostructures of the BCP thin film. The microdomains expanded and the expansion increased with increasing AuNPs (**Figure 5-6**). The big AuNPs with polymer shell were supposed to preferably locate in the specific microdomains, leading to increased stretching of the segmental chains to accommodate the NPs.

When most of the nano-cylinders in the thin film showed re-orientation from parallel to perpendicular to the substrate in hexagonal arrangement, the microdomains contracted (lateral distance decreased). The trend was more obviously when the nanostructure orientation had a complete change. This was independent of the NP size and stabilizing species.

5.3 The effect of NP stabilizing species on the NP location in PPMA-*b*-PMMA thin films

From the theoretical prediction, the nanoparticle size and selectivity dominate the location of NPs in block copolymers[25-27,170,171]. The selectivity of NPs is referred to the interaction of NPs and the segments of block copolymers and depends on the coated species of NPs. The NPs stabilized by species compatible to one component of BCP are considered as selective. When the stabilizing species are equally compatible to both components of BCP, the NPs are considered as nonselective. Small NPs and nonselective NPs are more localized at the segment interface and tend to reduce the domain size of BCP. Large NPs and selective NPs preferably segregate into the specific domain and induce the domain swelling so as to accommodate the incoming NPs.

5.3.1 AuNPs selectively located at the segment interface

Based on the previous discussions in **chapter 5.2**, the NP size is the main factor in dominating the location of AuNPs in the BCP thin films regardless of the stabilizing species. Small AuNPs tended to segregate at the interface of the two blocks. Correspondingly, the location of small AuNPs at the segment interface induced the contraction of microdomains. The contraction was more pronounced with increasing AuNPs. Our results are consistent with the theoretical prediction that small particles localize more at the segment interface and reduce the interface tension thus, reduce the segment chain stretching[25-27].

5.3.2 AuNPs selectively located in the specific microdomain

According to the surface tension (**Table 5-3**), the species of $CF_3(CF_2)_5CH_2CH_2$-SH, $CH_3(CH_2)_{10}CH_2$-SH, and PPMA were referred as hydrophobic and more compatible with PPMA-domain of block copolymer PPMA-*b*-PMMA. Correspondingly, PEO-SH and PMMA species were referred as hydrophilic and more compatible with PMMA-domain. As discussed in the previous **chapter 5.2**, for the AuNPs stabilized by low molecular weight species, the larger NPs (Au15, AuF6c in **Figure 5-4**) preferably segregated into PPMA-domain. For the AuNPs stabilized by high molecular weight species (polymers), PEO-SH stabilized Au16, $P4VP_6$-*b*-$PMMA_{170}$ and $PMMA_{75}$-SH stabilized Au30a, Au30a2, Au51h, Au51i, preferably segregate into PMMA-domain and no NPs appeared in PPMA-domain based on AFM analysis (Au30a, Au30a2 in **Figure 5-5**).

Table 5-3. Surface tension of the outer layer of AuNPs.

Species for stabilizing AuNPs	Surface tension[a] (mN/m)
$CF_3(CF_2)_5CH_2CH_2$-SH	~17[213]
$CH_3(CH_2)_{10}CH_2$-SH	~30[213]
P4VP$_6$-*b*-**PPMA$_{107}$**	~25[180]
$CH_3O(CH_2CH_2O)_6CH_2CH_2$-SH[b]	~35[213]
P4VP$_6$-*b*-**PMMA$_{170}$**	~40[180]
PMMA$_{75}$-SH	~40[180]

[a] surface tension of the underlined part of species which is the outer layer in stabilizing AuNPs.

[b] $CH_3O(CH_2CH_2O)_6CH_2CH_2$-SH denoted as PEO-SH.

Due to the longer pendant alkyl side chain of PPMA, PPMA-block is more hydrophobic (γ = ~25 mN/m) than PMMA-block (γ = ~40 mN/m). To get AuNPs preferably dispersed into PPMA-domain of PPMA-*b*-PMMA thin film, high surface coverage of AuNPs by hydrophobic species was needed to overcome the hydrophilicity of gold surface (γ_{Au} = ~1410 mN/m). The surface coverage of AuNPs was evaluated by the graft density, ρ, given by

$$\rho = \frac{\frac{m_P}{M_{n,P}} \cdot N_A}{\frac{m_{Au}}{\rho_{Au} \cdot \frac{4}{3}\pi\left(\frac{d_{core}}{2}\right)^3} \cdot 4\pi\left(\frac{d_{core}}{2}\right)^2} \qquad \textbf{(5-2)}$$

The graft density ρ represents how many molecules are grafted on per unit area of nanoparticle surface. The NPs are simplified as ideal round shape in the calculation of **(5-2)**. Here, m_P is the mass of graft species, $M_{n,p}$ is the molecular weight of graft species, N_A is Avogadro constant ($6.02 \cdot 10^{23}$ mol^{-1}), m_{Au} is the mass of gold cores, ρ_{Au} is the density of gold (19.32 g/cm^3), d_{core} is the gold core diameter of AuNPs. From **(5-2)**, ρ is determined by

$$\rho = \frac{1}{6} \cdot \frac{m_P}{m_{Au}} \cdot \frac{d_{core}}{M_{n,P}} \cdot \rho_{Au} \cdot N_A \qquad \textbf{(5-3)}$$

To verify the surface coverage effect, hybrid thin films with P4VP$_6$-*b*-PPMA$_{107}$ stabilized Au85b (4VP/Au = 2/1 (mol/mol) and Au85d (4VP/Au = 0.25/1 (mol/mol) which had similar core size of ~5 nm were compared. By calculation according to **(5-3)**, ρ(Au85b) = 15.3 nm^{-2},

and ρ(Au85d) = 1.75 nm^{-2}. It should be pointed out here that 15.3 nm^{-2} is above the theoretical maximum graft density (~9 nm^{-2})[214]. The extra polymer chains were supposed to be physically coated on the Au surface by polymer/polymer interaction. When 1 wt% of Au85b was added to PM13, some NPs can be seen in PPMA-domain and near the domain centre (**Figure 5-5e**). As Au85b content increased to 5 wt%, more NPs appeared in PPMA-domain (**Figure 5-5f**). For Au85d, no NPs appeared in PPMA-domain (**Figure 5-5g,h)**. This was due to the lower graft density of Au85d. So Au85d were less preferable to PPMA-domain compared to Au85b.

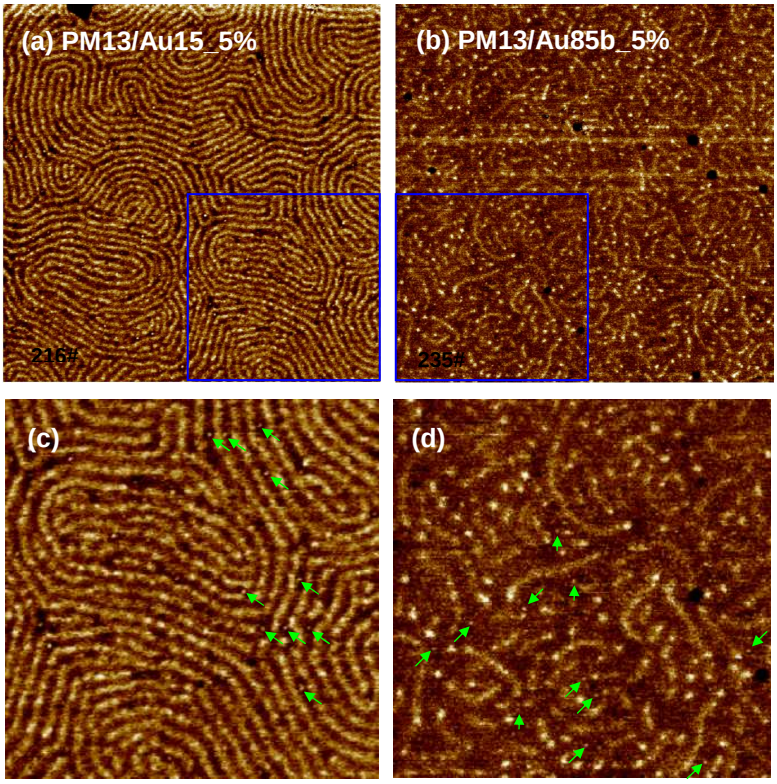

Figure 5-7. AFM phase images (2*2 μm^2) of AuNPs located in PPMA microdomains at film thickness of ~45 nm. (a) 5 wt% of Au15 (d_{core} = 8.7 nm) stabilized by $CH_3(CH_2)_{10}CH_2$-SH; (b) 5 wt% of Au85b (d_{core} = 5.4 nm) stabilized by $P4VP_6$-*b*-$PPMA_{107}$. AuNPs % = Au/PM13, m/m. (c,d) (1*1 μm^2) are the correspondingly enlarged areas from a,b.

The AuNPs were more preferable to PPMA-domain of thicker BCP film. **Figure 5-7** shows that more AuNPs appeared in PPMA-domain for the thin film of ~45 nm compared to that of ~20 nm, Figure **5-7a** vs. **Figure 5-4b** for PM13/Au15, **Figure 5-7b** vs. **Figure 5-5f** for PM13/Au85d.

5.4 The re-orientation of microdomains: lying cylinders completely switched into standing cylinders

5.4.1 Thin film thickness from ~20–70 nm: BCP with 1 wt% of Au-PPMA

To further examine the effect of nanoparticles on the thin film nanostructure orientation, BCP/AuNP hybrid thin films with thickness from 10 to 100 nm were studied. The AuNPs stabilized by dodecanethiol and PMMA-SH facilitated the cylindrical domain orientation from parallel to perpendicular to the substrate at film thickness ~20 nm (~0.5L_0) (**Figure 5-3,5**). However, as film thickness increased to ~45 nm, the cylindrical domains had no change and still oriented parallel to the substrate (**Figure 5-8**).

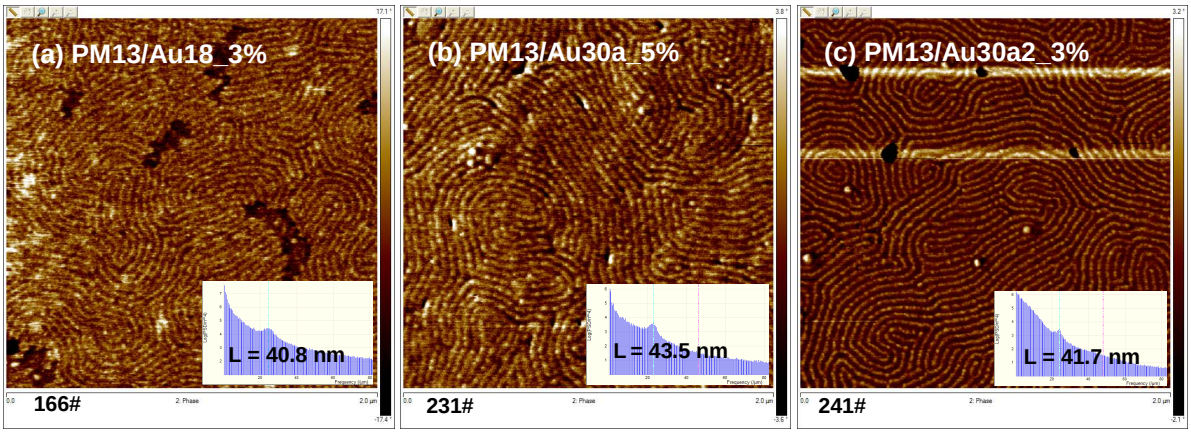

Figure 5-8. AFM phase images (2*2 μm^2) of PM13/AuNP hybrid thin films with film thickness of ~45 nm. (a) 3 wt% of Au18 stabilized by $CH_3(CH_2)_{10}CH_2$-SH, (b) 5 wt% of Au30a and (c) 3 wt% of Au30a2 stabilized by P4VP$_6$-*b*-PMMA$_{170}$. AuNPs % = Au/PM13, m/m. The inset image is FFT of the corresponding AFM.

Au52a (d_{TEM} = ~8 nm, d_{DLS} = 16 nm) stabilized by thiol-terminated PPMA$_{30}$SH (n = 30, synthesized by RAFT) were introduced into PM13 thin films. By adding 1 wt% of Au52a, the PMMA-cylinder orientation changed completely from parallel to perpendicular to the substrate as shown in **Figure 5-9a,b** (neat PM13 shown in Figure 5-2a,c). The nanostructure was obviously improved and in hexagonal order with partial distortion (**Figure 5-9b**). The lateral distance of PMMA-cylinders decreased from 40.8 nm to 37.0 nm at 1 wt% of Au52a (**Figure 5-9b**). Au52a also directed the lying cylinders to standing cylinders at varied film thickness from ~20–70 nm as seen in **Figure 5-9c,d**. The nanoparticles overcame the thickness limit on the nanostructure orientation. Substrate modification by grafting an organic layer was used to get standing cylinders, however, suffered from thickness limit[153-155]. The substrate effect usually deteriorates as the film thickness increases. The NPs which change

the block interface tension were more powerful in directing the nanostructure orientation[5].

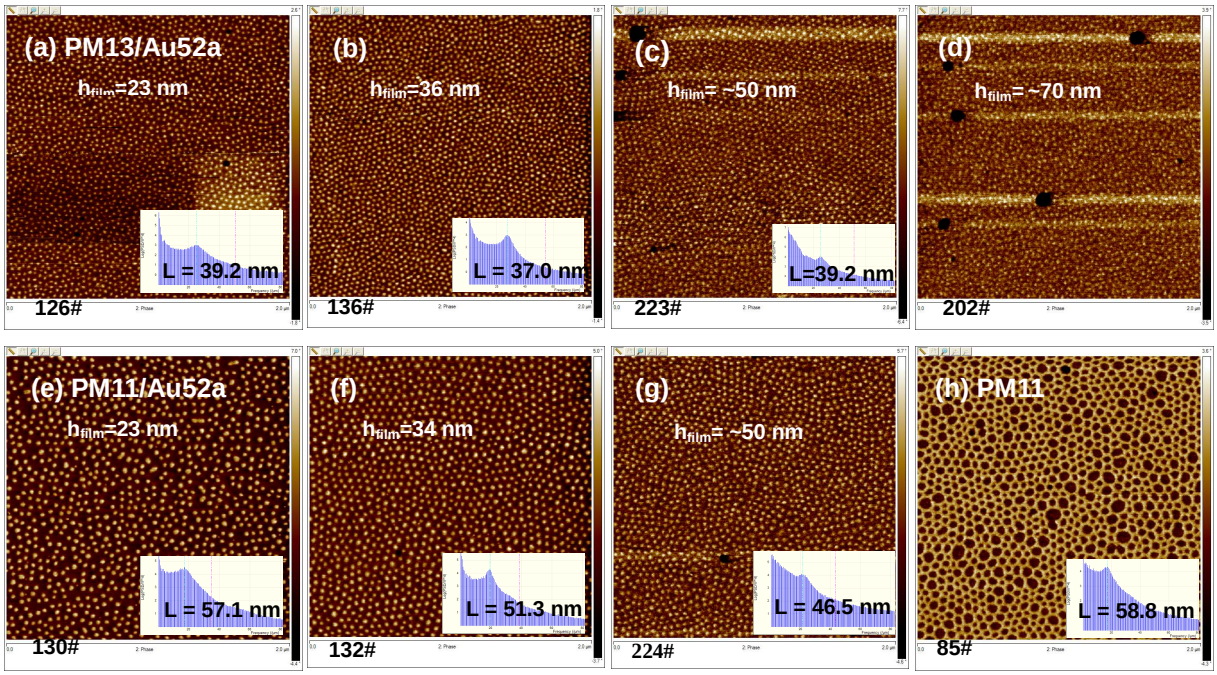

Figure 5-9. Thin film morphology completely switched to perpendicular cylinders at 1 wt% loading of Au52a (stabilized by $PPMA_{30}$-SH) for film thickness from ~20–70 nm. Neat PM13 and PM11 were shown in Figure 5-2a,c and e,g, respectively. (a–d) is PM13 with 1 wt% Au52a and (e–g) is PM11 with 1 wt% Au52a. (h) neat PM11 thin film of 22 nm. AFM phase image is in 2*2 μm^2. The inset image is FFT of the corresponding AFM.

Au52a was also incorporated into PM11 which had phase separation into lamellar morphology in bulk (**chapter 5.1.1**) and cylindrical morphology in thin film with thickness ~25 nm (**chapter 5.1.2**). The AFM results showed that PPMA-cylinders (darker areas in **Figure 5-9h**) changed into PMMA-cylinders (brighter areas **Figure 5-9e–g**) for 1 wt% of Au52a. The cylinders oriented perpendicular to the substrate. Some nanoparticles were well discernible in PPMA-domain. This is due to preferential interaction of Au52a (stabilized by PPMA) with PPMA-domain of block copolymer. Compared to the much higher loading of homopolymer PPMA (50 wt% in **Figure 5-14**) to get a complete change of the nanostructure orientation from parallel to perpendicular, only a very small amount of AuNPs coated by PPMA was needed for the same evolution, here 1 wt% of Au52a (corresponding to 11.5 wt% of PPMA). We suppose that PPMA stabilized nanoparticles decreased the interface tension of the two blocks dramatically, thus induced the re-orientation of the microdomains and the phase transition at very low loading of NPs (1 wt%)[18,28,208,209]. This is consistent with the decreasing tendency of domain size, from 40.8 nm to 37.0 nm for PM13 and from 58.8 nm to 51.3 nm for PM11, respectively, at 1 wt% of Au52a as shown in **Figure 5-9b,f,** which was induced by the decreased interface tension, leading to decreased stretching of segmental chains.

P4VP$_6$-*b*-PPMA$_{107}$, which stabilized Au85b with PPMA as outer layer, also directed the cylindrical domain partially from parallel to perpendicular at film thickness of ~45 nm (**Figure 5-7b**). **A conclusion** here is that AuNPs modified by homopolymer PPMA (as outer layer) corresponding to the component of lower surface energy of block copolymer PPMA-*b*-PMMA are more powerful to get standing cylinders in thin films, which can serve as a guideline to other BCP/NP hybrid thin film systems.

5.4.2 15 wt% of AuNPs: hybrid thin films with topography of holes and islands

As discussed previously, the AuNPs modified by homopolymer PPMA directed the lying cylinders of BCP thin film to standing cylinders at low nanoparticles loading, 1 wt% of Au52a. However, AuNPs stabilized by dodecanethiol, fluorinated thiol or PMMA encountered film thickness limit. The cylindrical domain orientation had no change when the film thickness increased to ~45 nm. Higher amount of AuNPs, 15 wt%, was incorporated into PM13. As shown in **Figure 5-10**, PMMA-cylinder orientation had a complete switch from parallel (neat PM13 in **Figure 5-2a**) to perpendicular to the substrate (**Figure 5-10a,d,g**). However, bumps and holes in topography appeared at such high amount of AuNPs as shown in the AFM height images (**Figure 5-10c,f,i**).

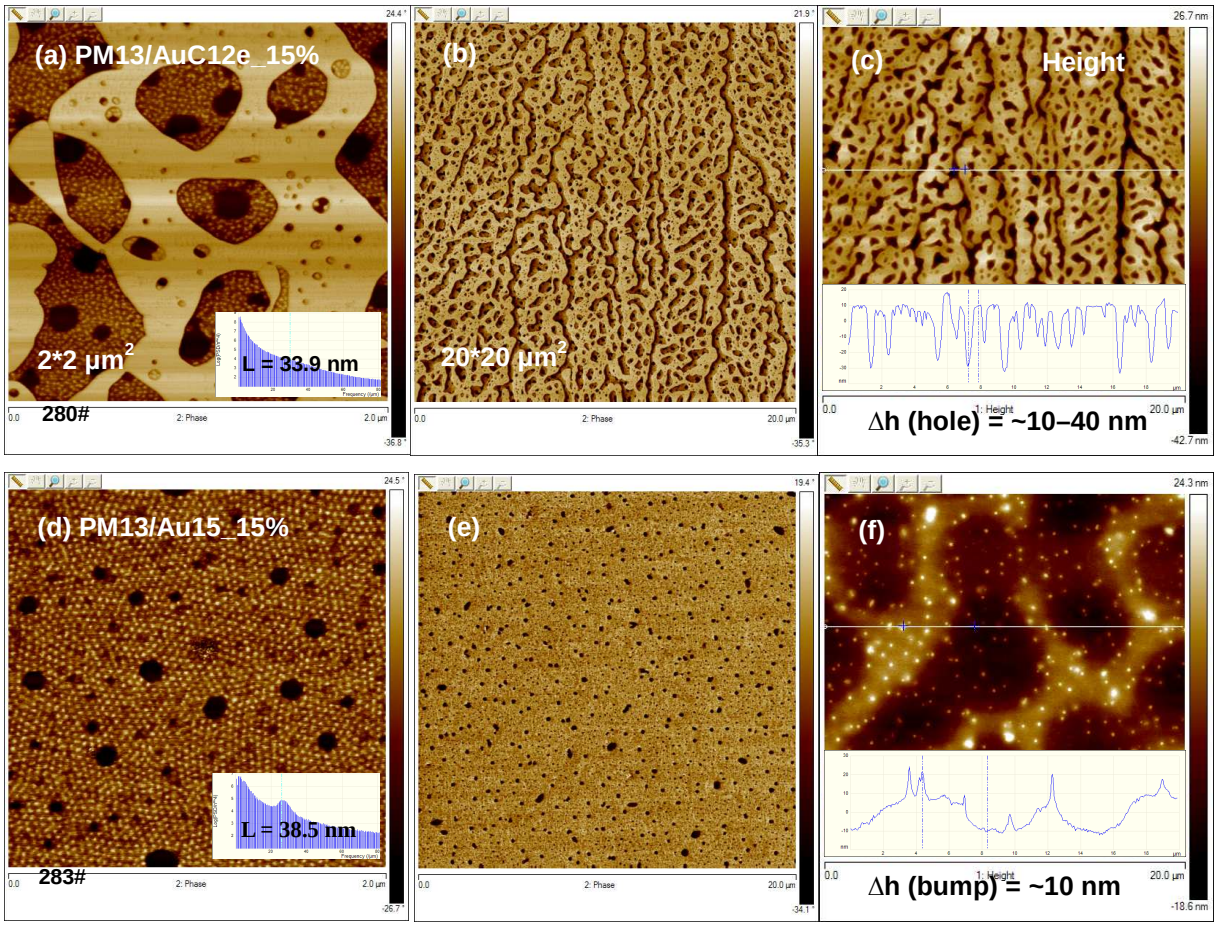

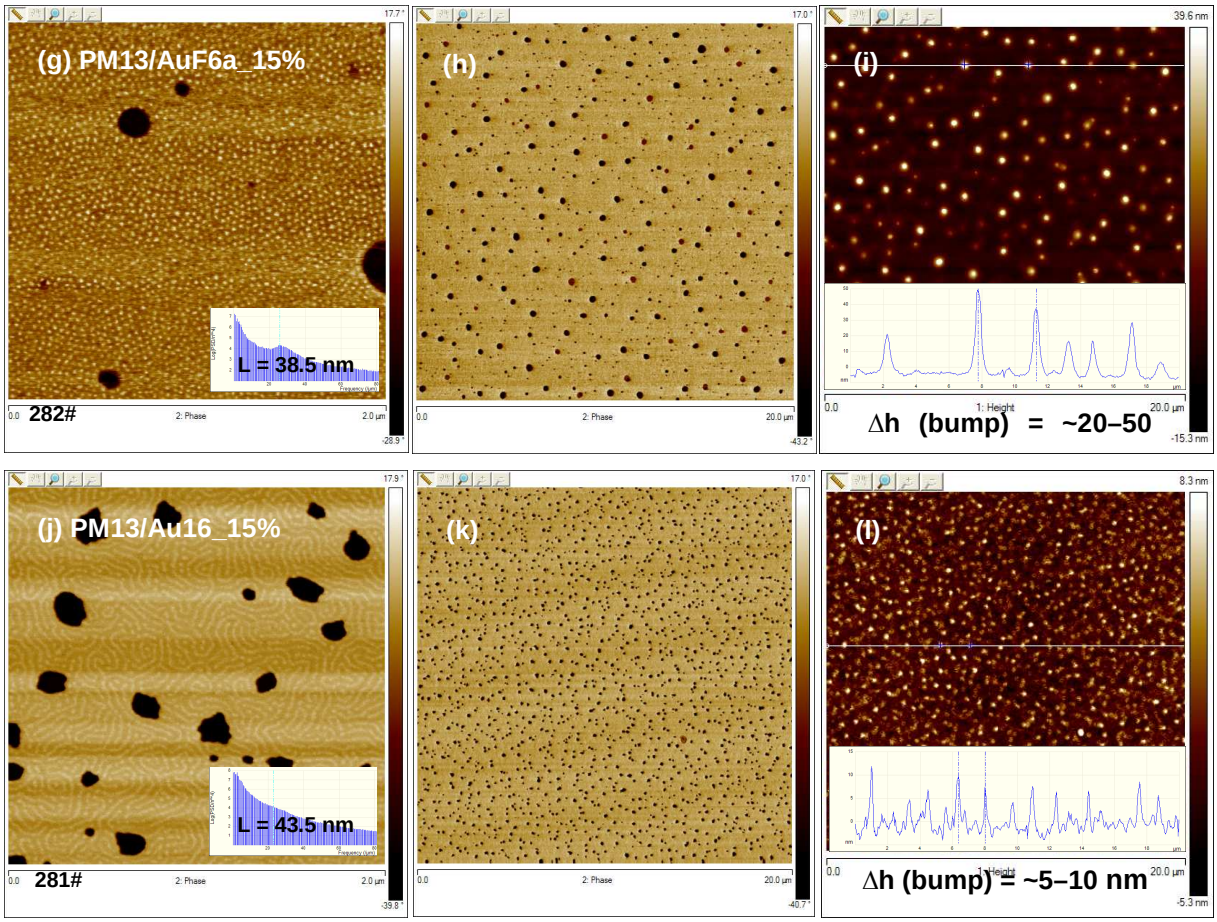

Figure 5-10. AFM images of PM13/AuNP hybrid thin film with 15 wt% of AuNP. Film thickness is ~45 nm. (a–c) AuC12e stabilized by dodecanethiol; (d–f) Au15 stabilized by dodecanethiol; (g–i) AuF6a stabilized by $CF_3(CF_2)_5CH_2CH_2$-SH; (j–l) Au16 stabilized by $CH_3O(CH_2CH_2O)_6CH_2CH_2$-SH. AFM image is in 2*2 μm^2 for a,d,g and the rest is in 20*20 μm^2.

Conclusion of the thin film nanostructure re-orientation:

The nanoscopic cylinders re-oriented from parallel to perpendicular to the substrate corresponding to decreased lateral distance at addition of AuNPs regardless of small or big ones (low or high molecular weight species stabilized). The decrease tendency of lateral distance was more pronounced when the cylinder orientation had a complete change. The contraction of microdomains was attributed to the reduced segmental interface tension by adding AuNPs, leading to decreased segment length by decreased chain stretching.

Solvent annealing is the most widely used method to improve and direct the thin film nanostructure into ordered[24,157,158]. However, the annealing parameters such as solvent, annealing time and withdraw rate are different from case to case. The addition of NPs provided a simple and general way to improve the nanostructure and the order as well as the orientation.

5.5 Investigation of AuNP location in the hybrid thin films by electron microscopy

To further investigate “where are the AuNPs in BCP thin film”, the BCP/AuNP hybrid thin films were studied by SEM, as well as plan-view and cross-sectional view TEM. The stained thin film was firstly deposited an amorphous carbon layer to avoid damage by focused electron beam as shown in **Scheme 5-1**.

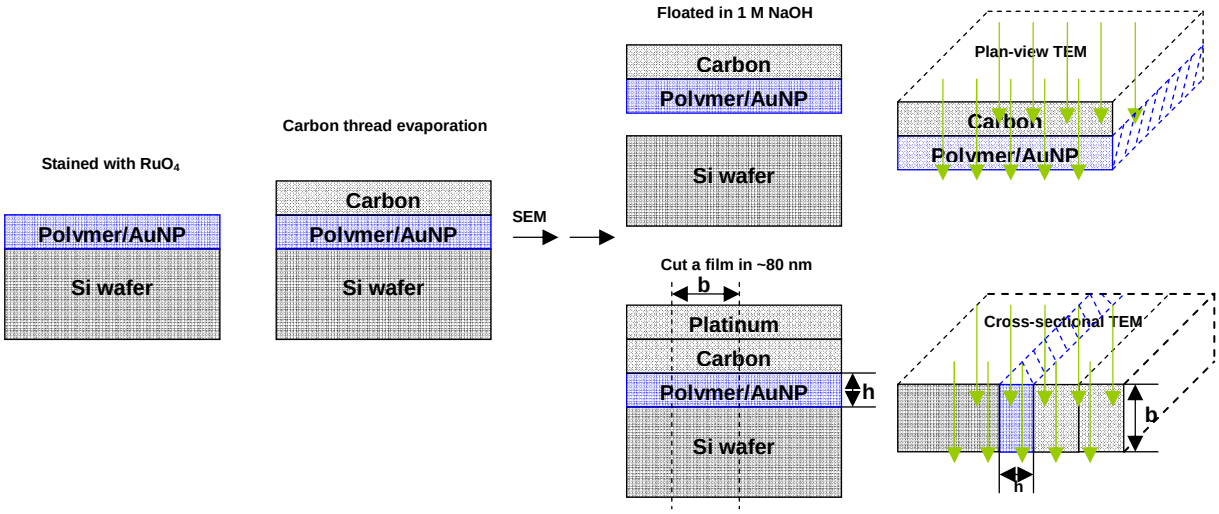

Scheme 5-1. The pre-treatment of BCP/AuNP hybrid thin film species for SEM, planview and cross-sectional view TEM.

Figure 5-11 showed SEM images of the hybrid thin films. AuNPs were easily discernible except for those very small ones with d < 5 nm (**Figure 5-11e**). Both low molecular weight thiol and polymer thiol stabilized AuNPs dispersed very well in the polymer matrix with scarce agglomeration. Specific AuNPs, Au16, Au15 and AuF6c were in form of homogeneous clusters constituted of several (5–10) nanoparticles per cluster (**Figure 5-11a,f,h**). These clusters dispersed separately, however, not in order. The mechanism of the formation of clusters is not yet clear.

For the hybrid thin film of PM13 with 15 wt% of Au-PEO, nanostructures could be seen from SEM (**Figure 5-11b**). However, for most of the cases, the nanostructures of PPMA-*b*-PMMA in thin films were difficult to see by SEM although very pronounced microphase separated domains were confirmed by AFM. This is due to the low contrast of the components, PPMA and PMMA, which are chemically similar. SEM with lower voltage may be applicable to see the nanostructure.

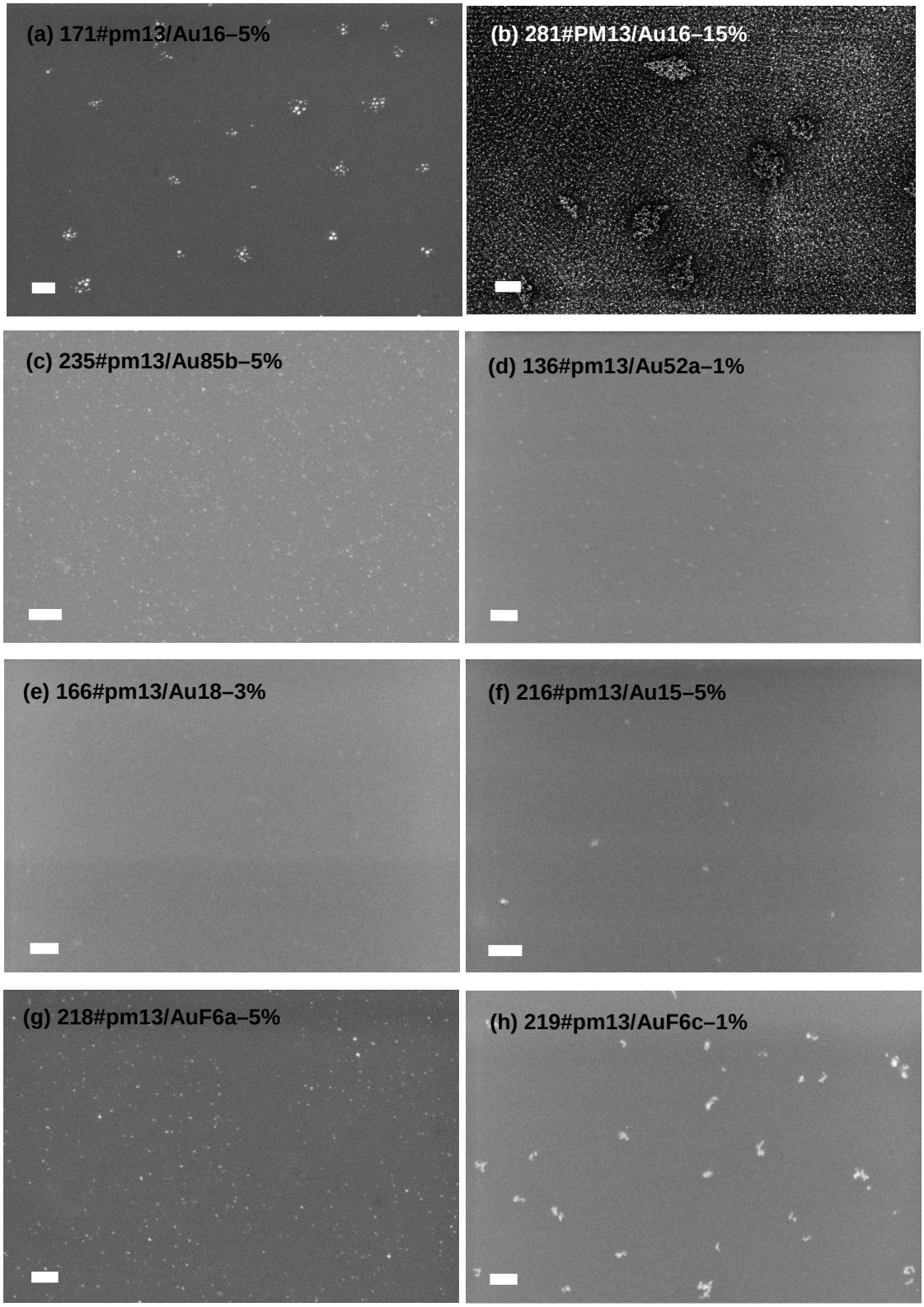

Figure 5-11. SEM (Scale bar of 200 nm) of PM13/AuNP hybrid thin films (thickness of 45–70 nm). (a,b) 5 and 15 wt% of Au16 stabilized by PEO-SH, (c,d) AuNPs stabilized by PPMA, (e,f) AuNPs stabilized by $C_{12}H_{25}$-SH, (g,h) AuNPs stabilized by $CF_3(CF_2)_5CH_2CH_2$-SH.

Another platinum layer was coated on the hybrid thin film and a lamellae of ~80 nm was then cut for cross-sectional TEM. From **Figure 5-12a,b** of PM13/Au16 hybrid thin films, a layer of AuNPs was clearly seen at polymer/Si substrate interface. In the dip-coating procedure, the thin film forms by drawing the Si-wafer out of BCP/AuNP solution in the direction along the Si-wafer plane. Thus AuNPs could not be deposited to the substrate by gravity during dip-coating. B. J. Kim et al. discussed the gravitational settling of AuNPs in polymer film[215]. The gravitational energy, given by Δmgh ($\Delta m = m_{AuNP} - m_{matrix}$) is much less than the thermal energy, k_BT (k_B is Boltzmann constant). The gravitational height h when $\Delta mgh = k_BT$ is 2.8 m for 2.5 nm gold nanoparticles in PSt-*b*-P2VP. The gravity is irrelevant over the micrometer length scales for the deposition of AuNPs in depth. Au16 stabilized by PEO-SH ($CH_3O(CH_2CH_2O)_6CH_2CH_2$-SH) were hydrophilic and had preferential interaction with Si substrate which was pre-treated by piranha solution. Thus, Au16 are supposed to disperse to the polymer/Si interface during dip-coating by preferential interaction with Si surface.

Au51h and Au51i stabilized by $PMMA_{75}$-SH with surface tension γ_{PMMA} = ~40 mN/m were similarly hydrophilic compared to Au16 stabilized by PEO-SH (γ_{PEO} = ~35 mN/m). As shown in **Figure 5-12e,f** for PM13/Au51h and Au51i hybrid thin films, most of AuNPs dispersed near the Si substrate, however, with some exception for Au51i (**Figure 5-12f** red arrows marked). AFM analysis showed that the cylindrical domains of PM13/Au51h oriented paralleled to the substrate (inset in **Figure 5-12e**). For PM13/Au51i, the cylinders had mixed orientation, partially perpendicular to the substrate (inset in **Figure 5-12f**). Further more, there was no NP showing in PPMA-domain from AFM analysis. Based on TEM and AFM results, Au-PMMA were verified to locate in PMMA-phase and near the bottom as shown in the scheme of **Figure 5-12g**. The NPs partially locating near the top induced the cylinders oriented partially perpendicular to the substrate (**Figure 5-12h**).

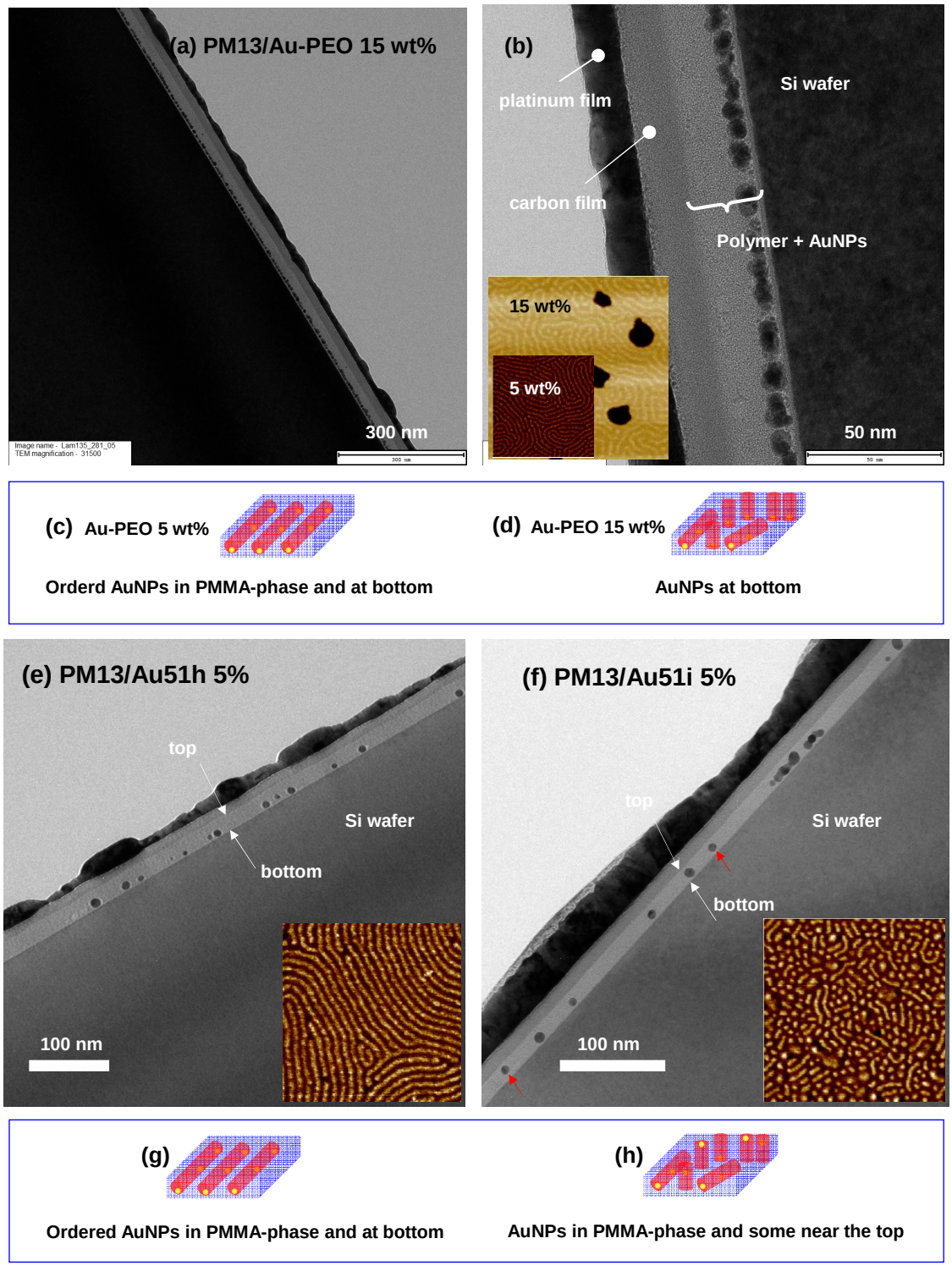

Figure 5-12. Cross-sectional views of hybrid thin film by TEM: (a,b) PM13 with 15 wt% of Au16 stabilized by $CH_3O(CH_2CH_2O)_6CH_2CH_2$-SH, (e) PM13 with 5 wt% of Au51h stabilized by $PMMA_{75}$-SH, (f) PM13 with 5 wt% Au51i stabilized by $PMMA_{75}$-SH. Inset images are the AFM phase images (1*1 μm^2). (c,d,g,h) are the proposed AuNP arrays in BCP thin film based on the corresponding TEM and AFM analysis.

The effect of AuNP location at bottom on the nanostructure orientation of thin film was similar to the modification of substrate with an organic layer. From the cross-view of the

hybrid thin film of PM13/Au16 in **Figure 5-12a,b**, all nanoparticles dispersed to the Si substrate. The AFM images (inset in **Figure 5-12b**) show that PMMA-cylinders were in mixed orientation at addition of 15 wt% Au16. However, 15 wt% of AuNPs stabilized by dodecanethiol and semifluorinated thiol induced all the PMMA-cylinders to re-orient perpendicularly to the substrate (**Figure 5-10a,d,g**). Due to the higher hydrophilicity of PEO compared to dodecane and semifluorinated species (**Table 5-3**), Au16 stabilized by PEO-SH was more preferable to the hydrophilic Si substrate (pre-cleaned by Piranha solution). Furthermore, the polarity of PEO (surface tension γ = ~35 mN/m) is closer to PMMA-domain (γ = ~40 mN/m) than PPMA-domain (γ = ~25 mN/m) thus, nanoparticles Au-PEO are preferable to PMMA-domain. This was further confirmed by AFM analysis (insets in **Figure 5-12b**). There was no particle showing in PPMA-domain. Based on TEM and AFM results, Au-PEO were verified to locate in PMMA-phase and near the bottom as shown in the scheme of **Figure 5-12c,d**. A layer of nanoparticles Au-PEO on the Si substrate induced the PMMA-cylinders in higher potential to orient parallel to the substrate. By increasing amount of Au-PEO from 5 to 15 wt%, PMMA-domains still oriented partially parallel to the substrate (insets in **Figure 5-12b**), while 15 wt% of other AuNPs induced all PMMA-domains to orient perpendicularly (**Figure 5-10a,d,g**).

5.6 Homopolymer/block copolymer blends

5.6.1 PPMA/PPMA-*b*-PMMA

Homopolymer $PPMA_{70}$ synthesized by living anionic polymerization, with degree of polymerization n = 70 and dispersity Đ = 1.05, was introduced into block copolymer PM13 and PM11 by mixing the polymer solution in THF followed by dip-coating onto the Si substrate. For PM13, addition of $PPMA_{70}$ induced a PMMA-cylinder orientation change from parallel to perpendicular to the substrate (**Figure 5-14a–d**). The tendency was more pronounced as $PMMA_{70}$ content increased. By adding 50 wt% $PPMA_{70}$ (PPMA/PM13 = 50:100, m/m), all PMMA-cylinders oriented perpendicularly to the substrate and in hexagonal packing (**Figure 5-14c**). For PM11, addition of $PPMA_{70}$ induced the phase transition from lamellar morphology to cylindrical morphology (**Figure 5-14e–g**). The cylinder orientation evolved from parallel to perpendicular to the substrate. By adding 100 wt% $PPMA_{70}$ (PPMA/PM13 = 100:100, m/m), all PMMA-cylinders oriented perpendicularly to the substrate (**Figure 5-14g**). For both cases of PM13 and PM11, the lateral distance (L) firstly increased and then decreased by increasing homopolymer $PPMA_{70}$. The inflection point (at which the lateral distance was in maximum value) was different, 30 wt% and 50 wt% of $PPMA_{70}$ for PM13 and PM11, respectively (**Figure 5-13**). However, from the view of morphology evolution, the lateral distance started to decrease when more than half lying cylinders switched to standing cylinders (red circles marked) and had the lowest value when all the cylinders oriented perpendicular to the substrate (green circles marked) (**Figure 5-13**).

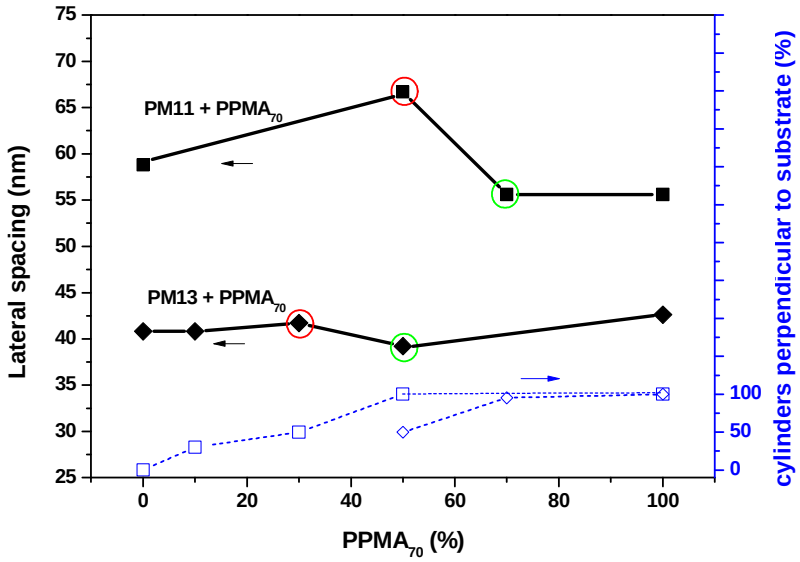

Figure 5-13. The lateral distance of the nanostructure in thin films (obtained from the first-order peak in FFT of AFM in Figure 5-12) versus weight percentage of incorporated homopolymer $PPMA_{70}$. $PPMA_{70}$ % = $PPMA_{70}$/PM13 and $PPMA_{70}$/PM11, m/m.

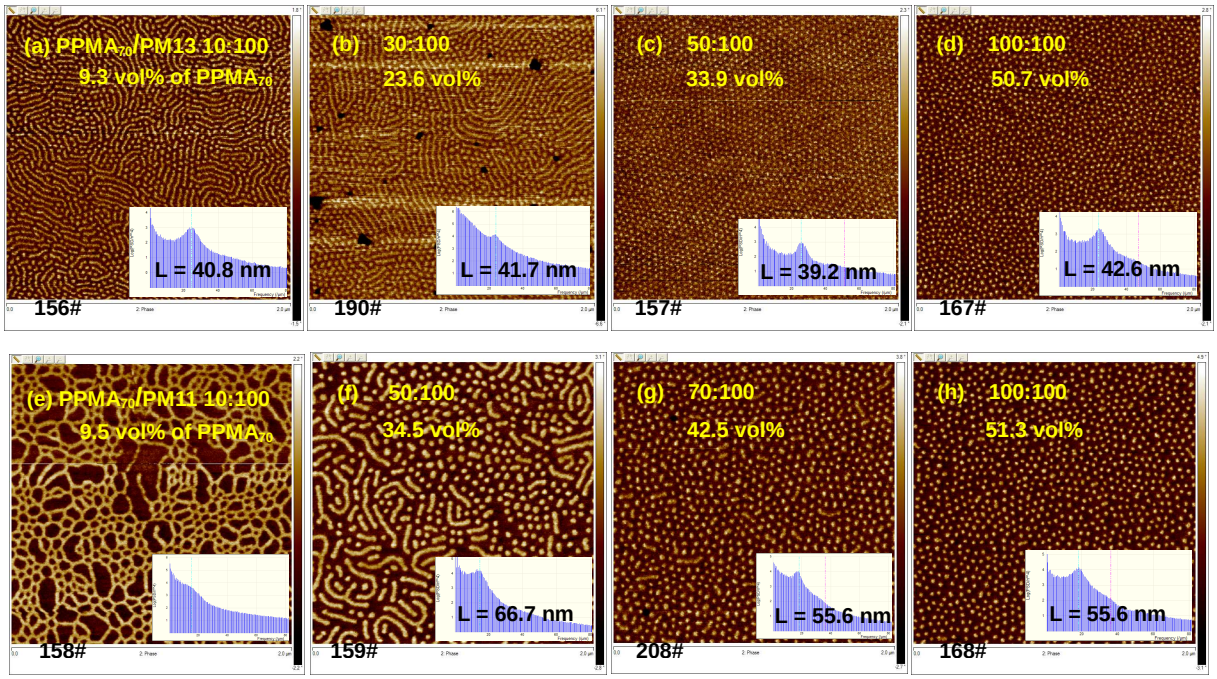

Figure 5-14. AFM phase image (2*2 μm^2) of blends of homopolymer $PPMA_{70}$ (n = 70, PDI = 1.05) with block copolymer PM13 (film thickness of ~25 nm) at weight ratio $PPMA_{70}$/PM13 of (a) 10:100, (b) 30:100, (c) 50:100, (d) 100:100; $PPMA_{70}$+PM11 blends at weight ratio $PPMA_{70}$/PM11 of (e) 10:100, (f) 50:100, (g) 70:100, (h) 100:100 of $PPMA_{70}$. Neat block copolymers PM13 and PM11 were shown in Figure 5-2a and Figure 5-2e. The inset image is FFT of the corresponding AFM.

As the degree of polymerization N_H (70, $PPMA_{70}$) is << N_{BCP} (PM13 of 386, PM11 of 428 based on NMR and GPC analysis), homopolymer PPMA chains are supposed to segregate into preferred PPMA-domain and to distribute throughout the whole domain[162]. The lateral swelling of PPMA-domain necessitated the shrinking of PMMA-domain to maintain uniformed density throughout the film. The swelling of PPMA-domain outweighed the shrinking of PMMA-domain, leading to an increase of domain spacing (**Figure 5-14a,b** and **e,f**). However, at further increasing homopolymer $PPMA_{70}$ content, the microdomain orientation had a complete change from parallel to perpendicular to the substrate. The segmental chains re-oriented and arrayed more compactly and orderly, leading to decreased domain size (lateral distance) as seen in **Figure 5-14c,g**. With further increase of $PPMA_{70}$, after the nanostructure fully re-oriented, the microdomains expanded again (**Figure 5-14d,g**).

5.6.2 PMMA/PPMA-*b*-PMMA

Homopolymer $PMMA_{95}$ synthesized by living anionic polymerization, with degree of polymerization n = 95 and dispersity Đ = 1.04, was introduced into block copolymer PM13 and PM11. The incorporation of $PMMA_{95}$ into PM13 induced the expansion of microdomains (lateral distance L increased) as shown in **Figure 5-15a–c**. The reason for the increase of

lateral distance by adding $PMMA_{95}$ was similar to the case of $PPMA_{70}$ addition as discussed previously. The penetration of $PMMA_{95}$ chains into preferred PMMA-domain caused the overall expansion of microdomain size (**Figure 5-15a,b**).

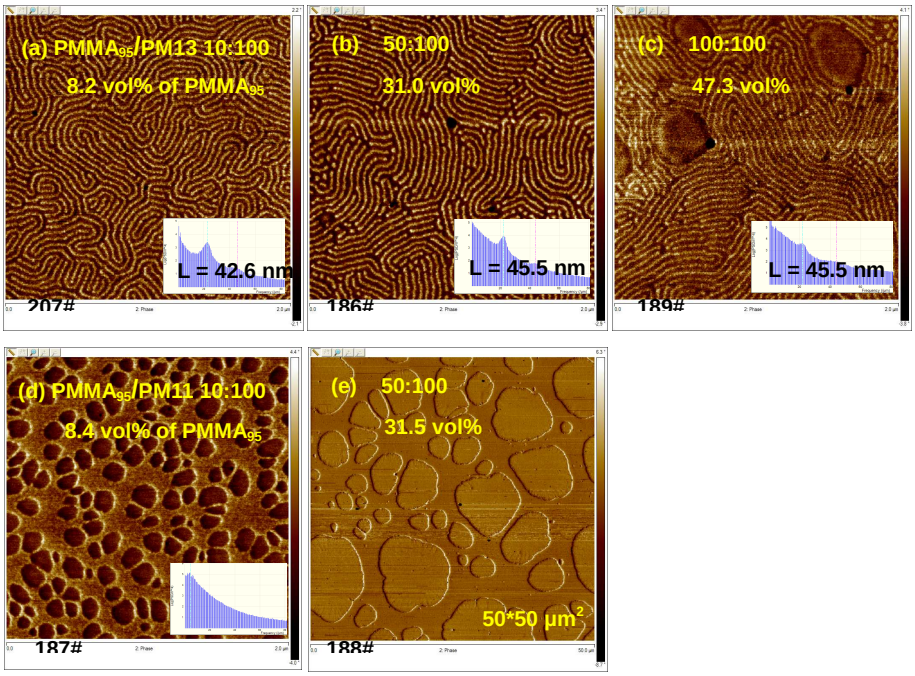

Figure 5-15. AFM phase images (2*2 μm^2 except e) of $PMMA_{95}$+PM13 blends (film thickness of ~25 nm) at weight ratio $PMMA_{95}$/PM13 of (a) 10:100, (b) 50:100, (c) 100:100 of $PMMA_{95}$ (n = 95, PDI = 1.04); $PMMA_{95}$+PM11 blends at weight ratio $PMMA_{95}$/PM11 of (e) 10:100, (f) 50:100 of $PPMA_{95}$. Neat PM13 and PM11 without $PMMA_{95}$ addition was shown in Figure 5–2a and Figure 5–2e. The inset image is FFT of the corresponding AFM.

However, the microdomain orientation showed no change when incorporating homopolymer $PMMA_{95}$. The PMMA-cylinders still oriented parallel to the substrate at adding 47.3 vol% of $PMMA_{95}$ where macrophase separation appeared (**Figure 5-15c**), whilst 31.5 vol% of $PMMA_{95}$ into PM11 caused the macrophase separation (**Figure 5-15e**). Jeong et al.[216] investigated the phase separation behavior of PSt-*b*-PMMA/PMMA blend in thin films. 33 vol% of PMMA induced the PMMA-domain orientation change from perpendicular to partially parallel to the substrate. Upon further increasing PMMA to 55 vol%, macrophase separation appeared. In this study, 47.3 vol% of $PMMA_{95}$ into PM13 induced the macrophase separation. With 50.7 vol% of $PPMA_{70}$ into PM13 there was no macrophase separation. The distribution of homopolymers in the BCP depends on the molecular weight of homopolymer to BCP, $M_{n,H}/M_{n,BCP}$ and the volume fraction of homopolymer[162,212]. When $M_{n,H}/M_{n,BCP} < 0.5$, the homopolymers dispersed uniformly in the preferred domain. When $M_{n,H}/M_{n,BCP} >> 1$, macrophase separation occurred. And when $Ø_H > Ø_C$ ($Ø_C$, solubility limit of homopolymer in BCP), macrophase separation also happened. Due to the composition of PM13, with

PPMA/PMMA = 82/18 in volume ratio, the solubility limit of homopolymer PPMA in PM13 is higher than PMMA when M_n (PPMA) ≈ M_n (PMMA). Thus PM13 accommodated higher amount of $PPMA_{70}$ (M_n ≈ 11000 g/mol) than $PMMA_{95}$ (M_n ≈ 9500 g/mol) without macrophase separation.

Conclusion of the block copolymer/homopolymer blends:

Homopolymer PPMA, corresponding to the lower surface energy component of PPMA-*b*-PMMA, induced the PMMA-domain re-orientation from parallel to perpendicular to the substrate. The domain size increased with increasing homopolymer. However, the domain size had lowest value when all the lying PMMA-cylinders changed into standing ones.

Homopolymer PMMA, corresponding to the higher surface energy component of PPMA-*b*-PMMA, had no effect on the nanostructure orientation of both PM13 and PM11 but only induced the microdomain expansion until macrophase separation happened.

5.7 Electrical conductivity of BCP/AuNP hybrid thin films

The macroscopic electrical conductivity properties of BCP/AuNP thin films were investigated by 2-probe DC electrical resistance measurements. Two-point probe experiments were carried out with applying voltage from -0.01 to +0.01 V. The electrical properties were measured in different regions for each thin film sample. Similar behavior was observed indicating the reproducibility of the results.

The neat block copolymer PPMA-*b*-PMMA thin film did not show any current passing through the sample when a voltage of 0.01 V was applied. As shown in **Figure 5-16**, the BCP/AuNP hybrid thin films responded to the applied voltage without hysteresis, independent of the applied voltage range. The curves were almost equal for the measurements performed at voltage range from +0.01 to -0.01 V and from -0.01 to +0.01 V.

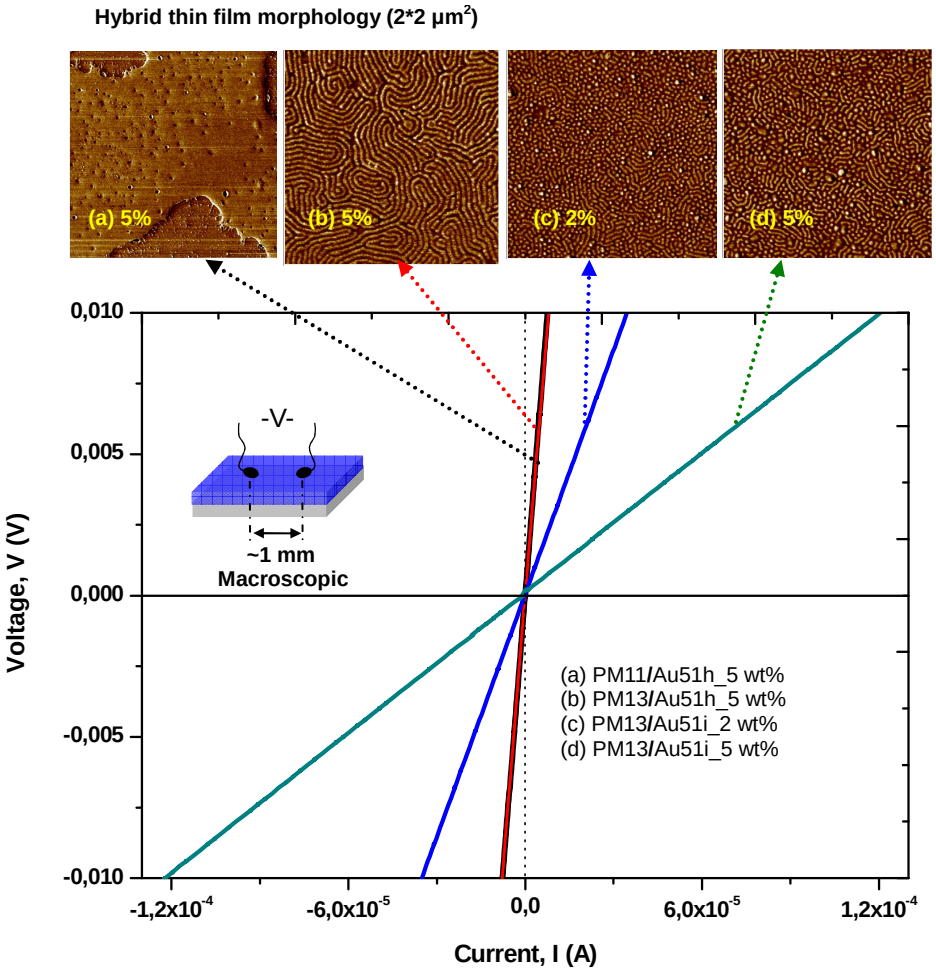

Figure 5-16. DC-electrical resistance measurements of hybrid thin films on Si wafer (film thickness of ~25 nm). (a) PM11 with 5 wt% Au51h, (b) PM13 with 5 wt% Au51h, (c) PM13 with 2 wt% Au51i, (d) PM13 with 5 wt% Au51i.

The thicknesses of the hybrid thin films for the measurement shown in **Figure 5-16** were

comparably equal of ~25 nm to avoid confusion in results interpretation since the response of the samples is proportional to the applied bias and inversely proportional to the thickness. The sample PM13/Au51i (**Figure 5-16d**) reached the highest current level under the same measurement conditions. It can be observed that the current level was amplified by increasing amount of AuNP in the BCP film (**Figure 5-16c,d**). This once more confirmed that the conductive properties of the investigated systems strongly depended on the amount of AuNPs in the systems. Furthermore, the location of AuNPs played an important role on the conductive behaviors of the hybrid thin film. Thin film with AuNPs near or at the polymer/air interface showed a higher conductivity compared to those with AuNPs buried inside the film (**Figure 5-16 a,b** and **c,d**).

Here it should be pointed out that the good distribution of AuNPs in the BCP templates resulted in good reproducibility of the electrical properties of each material exposed[217], since only these AuNPs responded to the current transported throughout the designed materials.

6 Summary and outlook

The aim of this work was to study how the incorporation of gold nanoparticles (AuNPs) affects the morphology and nanostructure orientation of block copolymer PPMA-*b*-PMMA thin films and to get hybrid BCP/AuNP thin films with ordered and oriented nanostructures. To achieve the goal, micro-phase separated block copolymer PPMA-*b*-PMMA and AuNPs with varied size and modification were the main synthetic goals (**Scheme 6-1** and **6-2**) and then BCP/AuNP thin films were profoundly investigated with regard to morphology and nanostructure orientation by AFM, GISAXS, TEM and SEM.

Synthetic part 1

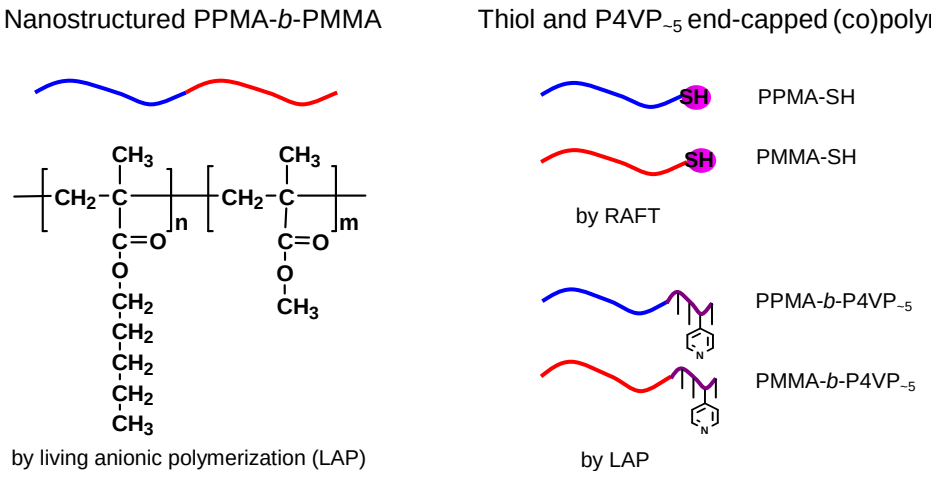

Scheme 6-1. The synthesized block copolymers and end-functionalized polymers.

Nanostructured block copolymers PPMA-*b*-PMMA were successfully synthesized via sequential living anionic polymerization under standard conditions for PMMA. Block copolymers with pre-determined molecular weight and segmental molar ratio as well as narrow dispersity Đ = ~1.1 were successfully prepared. Two block copolymers were chosen for further investigation of hybrid thin films. PM11 with molar ratio of PPMA/PMMA = 49/51 and PM13 with PPMA/PMMA = 72/28 were employed in the hybrid thin films. PM11 phase-separated into lamellar structure with $d_{(100)}$ = 55.5 nm and PM13 showed cylindrical structure with $d_{(100)}$ = 38.5 nm (a_{hex} = 44.5 nm) as measured by T-SAXS.

To introduce thiol end-groups, functionalized terminator of alkyl chloride with protected thiol group was synthesized. Both alkyl chloride and dimethylchlorosilane were successful in terminating PSt^- in anionic polymerization of styrene which was confirmed by ^1H and ^{13}C NMR. However, these terminators could not end-cap anionic $PMMA^-$ which is attributed to

the lower electronegativity of the carbanion of $PMMA^-$ compared to PSt^-.

In order to improve the interaction of block copolymers PPMA-*b*-PMMA with AuNPs, thiol terminated polymers PMMA-SH and PPMA-SH for stabilizing AuNPs were successfully synthesized by RAFT followed by aminolysis. Dithioester end-capped PMMA-SCS were synthesized by RAFT method with molecular weight ranging from 2000-20000 g/mol and dispersity ~1.2. Dithioester end-capped block copolymers PMMA-*b*-PPMA-SCS were also synthesized in a controlled way with dispersity ~1.2 by using the first-synthesized PMMA-SCS as macro-CTA. The dithioester end-group was then cleaved by aminolysis to get thiol-terminated polymers which were confirmed by ^1H and ^{13}C NMR as well as by GPC.

A short P4VP-block was also introduced into block copolymers in order to stabilize AuNPs by pyridine/Au^{3+} interaction. $P4VP_n$-*b*-PMMA and -PPMA with short (n = 5–10) and long P4VP-block were successfully synthesized by living anionic polymerization. MMA had to be polymerized from $P4VP^-$ since polymerization of 4VP from $PMMA^-$ was not applicable due to the higher base of $P4VP^-$. Short P4VP-block was synthesized in THF at -78 ℃ , similar as the PMMA system. Long P4VP-block was synthesized in pyridine at elevated temperature of -12 ℃, however, the polymerization proceeded in a cont rolled way with dispersity Đ = ~1.2–1.3.

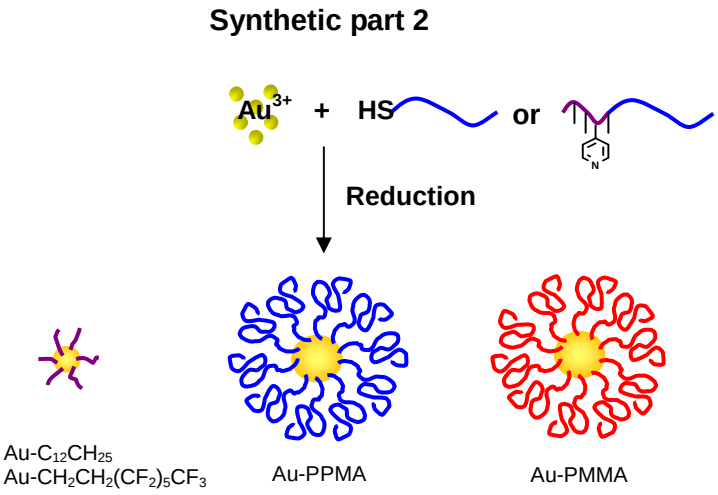

Scheme 6-2. The synthesized AuNPs stabilized by varied species.

AuNPs with varied size and stabilizing species were synthesized in controlled manner either by two-phase method (Brust-Schiffrin method) or by one-phase method in THF and characterized by DLS, UV-Vis and TEM (**Figure 6–1**). Varied ligands were used. $CH_3(CH_2)_{10}CH_2$-SH, $CH_3O(CH_2CH_2O)_6CH_2CH_2$-SH (PEO-SH), $CF_3(CF_2)_5CH_2CH_2$-SH, the synthesized PMMA-SH, PPMA-SH, and P4VP-based block copolymers were employed in stabilizing AuNPs and the mechanism was studied.

Thiol-terminated species were grafted to AuNP surface via S-Au bond. The nanoparticle size depended on the molar ratio of SH/Au^{3+} and increased with decreasing SH amount.

Thiol-terminated polymers were weaker ligands than small thiol molecules in stabilizing AuNPs due to steric effect. Since tetraoctylammonium bromide (TOAB) was required in two-phase method as phase-transfer agent, thiol-terminated polymers were applied in one-phase method to avoid the competitive stabilizer of TOAB. Only small thiol molecules (much stronger ligand than TOAB for Au) were used in two-phase method.

P4VP-based block copolymers were employed successfully in stabilizing AuNP with P4VP as inner core due to the interaction of pyridine group with Au^{3+} and the other block as outer shell. P4VP-based polymers were weaker ligand than thiol-terminated polymers in stabilizing AuNPs.

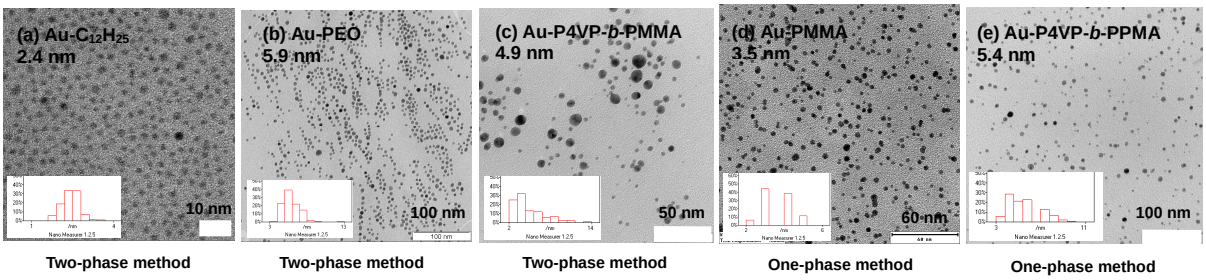

Figure 6–1. TEM images (Au core was visible) of AuNPs stabilized by different species of (a) dodecanethiol, (b) $CH_3O(CH_2CH_2O)_6CH_2CH_2$-SH, (c) $P4VP_8$-*b*-$PMMA_{148}$, (d) $PMMA_{28}$-SH, and (e) $P4VP_6$-*b*-$PPMA_{107}$. Inset: histogram of size distribution.

The AuNPs with varied stabilizing species were applied in hybrid thin films to investigate **how the AuNP size and stabilizing species affect the morphology and nanostructure orientation of PPMA-*b*-PMMA thin films** (**Scheme 6-3**).

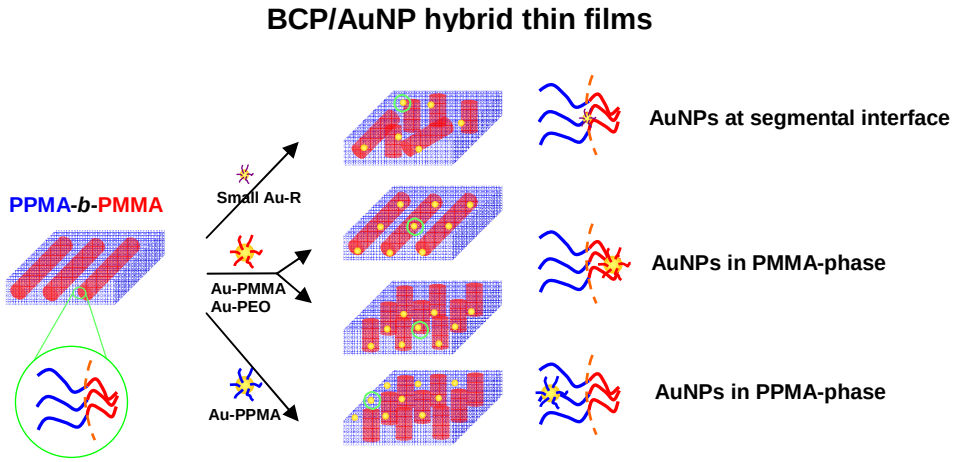

Scheme 6-3. BCP/AuNP hybrid thin films with AuNPs selective location in the preferred microdomain or at segmental interface.

Small nanoparticles stabilized by low molecular weight thiols dispersed at the segmental interface and induced the **contraction** of microdomains by reduced interfacial tension, so that the lateral distance decreased (**Figure 6–2f**). A part of cylindrical domains re-oriented from parallel to perpendicular to the substrate. High AuNP loading (15 wt%) was needed to get complete re-orientation.

Big nanoparticles stabilized by high molecular weight species (polymers) preferably located in the specific domains and induced the **expansion** of microdomains which was due to the extension of segmental chains to accommodate the incoming NPs, so that the lateral distance increased (**Figure 6–2c,g**).

The **location** of AuNPs depended on the modification. Hydrophilic species (PEO–, PMMA–) stabilized AuNPs preferred to PMMA-domain. Hydrophobic species ($C_{12}H_{25}$–, PPMA–, $CF_3(CF_2)_5CH_2CH_2$–) stabilized AuNPs preferred to PPMA-domain.

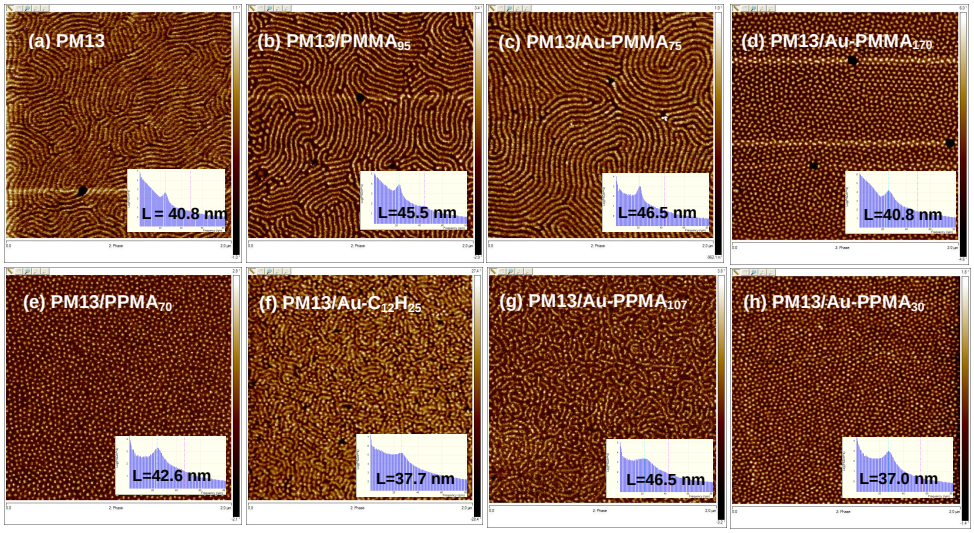

Figure 6-2. Thin films of PPMA-*b*-PMMA with AuNPs stabilized by different species. (a) neat block copolymer PM13, (b) PM13 with homopolymer $PMMA_{95}$ of 50/100 m/m, (c) PM13 with 1 wt% Au-$PMMA_{75}$, (d) PM13 with 3 wt% Au-$PMMA_{170}$, (e) PM13 with homopolymer $PPMA_{70}$ of 100/100 m/m, (f) PM13 with 5 wt% of Au-$C_{12}H_{25}$, (g) PM13 with 5 wt% Au-$PPMA_{107}$, and (h) PM13 with 1 wt% Au-$PPMA_{30}$. Film thickness of ~25 nm.

The **re-orientation** of cylindrical domains depended on the modification of AuNPs. PPMA-coated AuNPs were most powerful in directing the cylinders from parallel to perpendicular to the substrate. When the cylinders re-oriented from parallel to perpendicular to the substrate, the microdomains contracted regardless adding small or big nanoparticles (low or high molecular weight species stabilized) (**Figure 6–2d,h**). The domain contraction was more pronounced when the orientation had a complete change.

To get a further understanding of the relation between stabilizing species of AuNPs and thin film nanostructure re-orientation, **homopolymer/BCP blends** were investigated.

Homopolymer PPMA induced the microdomain re-orientation from parallel to perpendicular to the substrate (**Figure 6–2e**). However, higher amount of PPMA were needed to get a complete re-orientation compared to Au-PPMA. **Homopolymer PMMA** had no effect on the nanostructure orientation of PPMA-*b*-PMMA (**Figure 6–2b**). But PMMA caused the expansion of the microdomains.

Based on these studies, the conclusion can be drawn that AuNPs are powerful in directing the nanostructure orientation of block copolymers to get perpendicular nano-cylinders which is critical for application in nanotechnology. The results provide a general guide for other BCP/inorganic NP hybrid systems for desired morphology and nanostructure orientation.

Macroscopic measurements of the conductivity of BCP/AuNP thin films were carried out which showed that the thin films with AuNPs near the polymer/air interface owned ~10^3 higher conductivity than that with NPs buried inside the film. Possible applications that can be proposed are incorporation in microelectronic devices as well as solar cells in which the polymer/AuNP thin films act as functional layer.

7 Experimental and analysis

7.1 Materials and chemical purification

7.1.1 List of chemicals

1,1-Diphenylethylene (DPE)	99 %, Acros
1,2-Dibromoethane	98 %, Aldrich
1-Dodecanethiol	≥ 98 %, Aldrich
2,2′-Azobis(2-methylpropionitrile) (AIBN)	98 %, Aldrich
2,5,8,11,14,17,20-Heptaoxadocosane-22-thiol ($CH_3O(CH_2CH_2O)_6CH_2CH_2$-SH)	polypure
2-Phenyl-2-propyl benzodithiolate	99 % (HPLC), Aldrich
2-Propene-1-thiol	~60 % (GC), Fluka
3,3,4,4,5,5,6,6,7,7,8,8,8-Tridecafluoro-1-octanethiol ($CF_3(CF_2)_5CH_2CH_2$-SH)	97 %, Aldrich
3-Bromo-1-propanethiol	93 %, Angene International Limited
3-Chloro-1-propanethiol	98 %, Aldrich
4-(Dimethylamino)pyridine (DMAP)	≥ 99 %, Aldrich
4-Vinylpyridine (4VP)	95 %, Aldrich
Ammonium chloride (NH_4Cl)	≥ 99.5 %, Sigma-Aldrich
Azobisisobutyronitrile (AIBN)	98 %, Aldrich
Benzophenone	99 %, Sigma-Aldrich
Calcium hydride (CaH_2)	95 %, Aldrich
Chlorodimethylsilane	98 %, Aldrich
Lithium chloride (LiCl)	≥ 99.99 %, Aldrich
sec-Butyllithium (sec-BuLi)	1.3 M solution in cyclohaxane/haxane (92/8), Acros
Cyclohexane	99.5 %, Sigma-Aldrich

Dichloromethane (CH_2Cl_2)	≥ 99.8, Sigma-Aldrich
Ethanol	laboratory reagent, Fisher Chemical
Gold(III) chloride hydrate ($HAuCl_4$)	~50 % Au basis, Aldrich
Hexane	Laboratory reagent, Fisher Chemical
Hexylamine	99 %, Acros
Magnesium sulfate ($MgSO_4$)	97 %, Acros
Methanol (MeOH)	99.8 %, Sigma-Aldrich
Methyl methacrylate (MMA)	99 %, Aldrich
n-Pentyl methacrylate (PMA)	Scientific Polymer Product, Inc.
Phenolphthalein	ACS reagent, Sigma-Aldrich
Platinum(0)-1,3-divinyl-1,1,3,3-	
Tetramethyldisiloxane complex solution	in xylene, Pt ~2 wt%, Aldrich
Potassium (K)	98 %, Aldrich
Potassium hydroxide (KOH)	≥ 85 %, Sigma-Aldrich
Propylene sulfide	≥ 96 %, Aldrich
Pyridine	99.8 %, Sigma-Aldrich
Sodium (Na)	≥ 99.8 %, Aldrich
Sodium borohydride ($NaBH_4$)	98 %, Aldrich
Tetrahydrofurane (THF)	≥ 99.9 %, Acros
Tetraoctylammonium bromide (TOAB)	98 %, Aldrich
***tert*-Butyldimethylsilyl chloride** (TBDMS)	98 %, Acros
Toluene	99.8 %, Sigma-Aldrich
Triethylaluminum (TEAl)	1.0 M in hexanes, Aldrich
Triethylamine (TEA)	≥ 99 %, Sigma-Aldrich
Triethylborohydride	
(Superhydride, $Li(C_2H_5)_3BH$)	1.0 M in THF, Aldrich
Triethylsilane	99 %, Aldrich

7.1.2 Purification

Tetrahydrofurane was stirred over KOH for 2 days and distilled over Ar. Sodium in small pieces was added into the flask, followed by reflux for 2 days and cooled to RT before adding ~0.1 wt% benzophenone. THF was heated to reflux again until dark blue appeared which indicating dryness and was kept under reflux until needed. Before anionic polymerization, THF was distilled from the reflux flask and transferred to the solvent vessel on the Schlenk line followed by titration with DPE/sec-Butyllithium until the red color persisted. After stirring over sec-Butyllithium for >12 h, THF was condensed to the reaction vessel. Methyl methacrylate and n-pentyl methacrylate were distilled twice over calcium hydride (CaH_2) under Ar with reduced pressure and stored over CaH_2 at -18 ℃. Prior to use, triethylaluminium solution in hexane (1.0 M) was transferred into a distillation bridge, and the solvent was removed by vacuum. The monomer was added to the dry triethylaluminium and stirred for several minutes followed by distillation in vacuum before polymerization. 1,1-Diphenylethylene was distilled under reduced pressure, stored at -18 ℃ with Ar and condensed in vacuum prior to use. Methanol (for termination) was degassed and stored at RT. 4-Vinyl pyridine (4VP) was distilled over CaH_2 under Ar with reduced pressure and stored over CaH_2 at -18 ℃. 4VP was distilled again and kept at < ~ -20 ℃ before it was transferred to the reaction vessel. Pyridine was distilled over CaH_2 and stored under Ar. Before used as solvent for anionic polymerization of 4VP, pyridine was distilled again and transferred into the solvent vessel and followed by the same procedure as THF. All reactions (monomer distillation and anionic polymerization) were carried out under argon 5.0, which was further purified by HydrosorbVC and OxisorbVC cartridges. Toluene was distilled over CaH_2 and stored under Ar before used in RAFT. The other solvent and chemicals which are not described here were used as received without further purification.

7.2 Experimental

7.2.1 PPMA-*b*-PMMA and P4VP-*b*-PMMA by living anionic polymerization

PPMA-b-PMMA by sequential living anionic polymerization

Block copolymers PPMA-*b*-PMMA were synthesized by living anionic polymerization as described in previous reports[180,218,219]. In a typical procedure (PM11), 28 mg LiCl was added into a vessel which was attached to the Schlenk line and dried over 330 ℃ with heat gun under vacuum. 60 ml of THF, which was fresh distilled over sec-BuLi/DPE with characteristic color of red, was then transferred to the vessel via syringe. 14 mg, 15 µl of DPE was added into the vessel. 25 µl of sec-BuLi (1.3 M in hexane) was added until the red color persisted

and followed by another 50 µl. The vessel with solvent THF, LiCl, and initiator sec-BuLi/DPE was then cooled to -78 ℃ with a liquid N_2/ethanol bath. The first monomer PMA, 1.55 ml, was added into the reactor with disappearance of the red color immediately. After 0.5 h, the second monomer MMA, 1.75 ml was added and the reaction was continued for another 0.5 h before terminated by degassed MeOH. The as synthesized block copolymer in THF was precipitated into 900 ml hexane and dried over vacuum at room temperature (RT). 3.05 g of crude product with monomer conversion of ~100% was finally obtained. Further purification, by re-dissolving in THF and precipitated into MeOH, was carried out for two more times before further application.

P4VP-*b*-PMMA and -PPMA polymerized in THF and pyridine

The synthesis of P4VP-based block copolymers by living anionic polymerization was similar to PPMA-*b*-PMMA except consideration of the solubility in THF. With THF as solvent, short P4VP-block, repeating units < ~20 could be obtained. At adding monomer 4VP, the red solution (dipehnylhexyllithium) turned to be yellow orange and persisted until adding second monomer MMA. However, even with low molecular weight, P4VP solution in THF was not clear, indicating the poor solubility in THF.

Mixed solvent THF/pyridine (50/50, v/v) or pyridine was employed in order to improve the solubility. The polymerization in pyridine was conducted at elevated temperature of -12 ℃ (ice + NaCl) compared to -78 ℃ in THF.

7.2.2 Terminators for LAP and end-functionality by LAP

Alkyl halides terminator: *tert*-butyldimethylsilyl 3-chloropropyl sulfide (TDSCS)

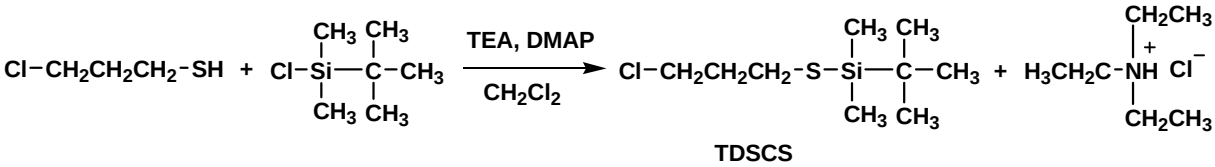

TDSCS

Scheme 7-1. Synthesis of terminator TDSCS.

In a typical procedure, 3-chloro-1-propanethiol (20 mmol, 2.212 g) was dissolved in 40 ml dry CH_2Cl_2 in a two-neck flask under Ar. Triethylamine (TEA) (24 mmol, 2.64 g) and 4-(dimethylamino)pyridine (2 mmol, 0.244 g) were added into the flask and stirred for 5 min until dissolved. The mixture was cooled down to 0 °C in ice bath. *tert*-butyldimethylsilane (24 mmol, 3.617 g) dissolved in 10 ml of dry CH_2Cl_2 was added into the mixture. The reaction

was kept in ice bath for 2 h and then elevated to RT. After 5 h the mixture was still clear solution and white precipitate appeared within ~20 h. The reaction was carried on for 28 h and followed by purification. The mixture was washed with saturated NH_4Cl (50 ml * 4 times). The organic layer was collected and dried over $MgSO_4$ for 12 h followed by rotary evaporation to remove CH_2Cl_2. The crude product was purified by fractional distillation under Ar for twice and stored in Ar under -18 ℃ before u se.

Alkyl halides terminator: *tert*-butyldimethylsilyl 3-bromopropyl sulfide (TDSBS)

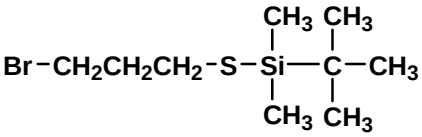

The synthesis and purification was the same with TDSCS.

Silyl halides terminator: *tert*-butyldimethylsilyl 3-(chlorodimethylsilyl)propyl sulfide (TSCSPS)

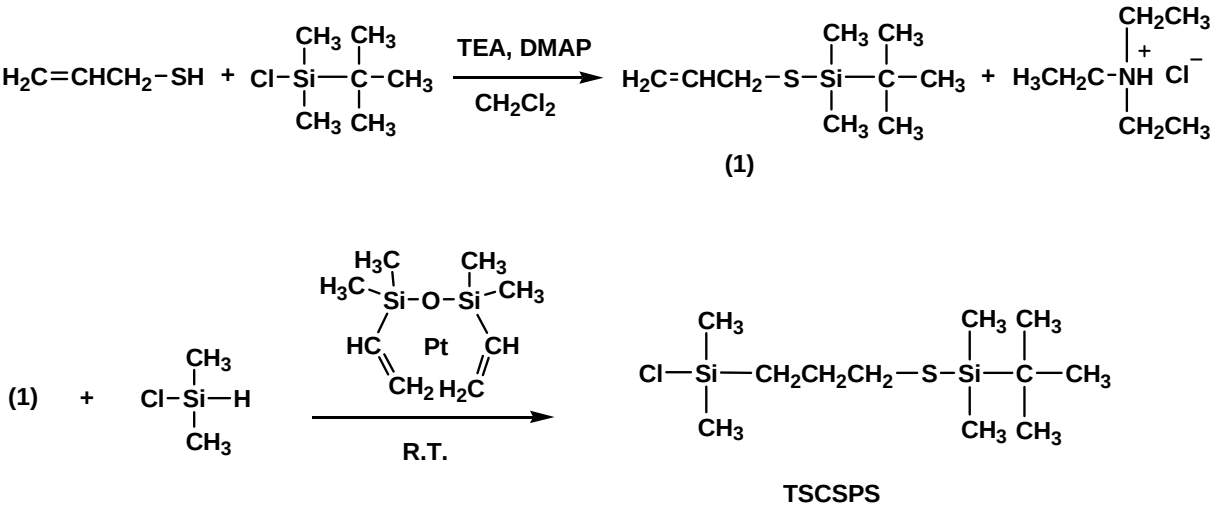

Scheme 7-2. Synthesis of terminator TDCSPS.

In a typical procedure, TSCSPS was synthesized by two steps. 2-Propene-1-thiol was reacted with *tert*-butyldimethylsilane to get *tert*-butyldimethylsilyl 2-propene sulfide in the similar procedure of TDSCS. 2-Propene-1-thiol (0.1 mol, 7.41 g) was dissolved in 200 ml dry CH_2Cl_2 in a two-neck flask under Ar. (TEA) (0.12 mol, 12.14 g) and 4-(dimethylamino)pyridine (0.01 mol, 0.61 g) were added into the flask and stirred for 5 min until dissolved. The mixture was cooled down to 0 ℃ in ice bath. *tert*-butyldimethylsilane (0.105 mol, 15.82 g) dissolved in 50 ml of dry CH_2Cl_2 was added into the mixture. White precipitate appeared within 0.5 h.

The reaction was kept in ice bath for 2 h and then 16 h at RT followed by purification. The mixture was washed with saturated NH_4Cl (200 ml * 4 times). The organic layer was collected and dried over CaH_2 for 20 h followed by rotary evaporation to remove CH_2Cl_2. The crude product was purified by fractional distillation under Ar and stored in Ar under -18 ℃ before use.

Dimethylchlorosilane (0.024 mol, 2.28 g) was mixed with compound (1) (0.02 mol, 3.77g) in a two-neck flask under Ar. Karstedt's Catalyst (platinum(0)-1,3-divinyl-1,1,3,3-tetramethyldisiloxane complex solution in xylene, Pt ~2 wt%) (1 g with ~0.02 Pt) was added. The solution changed into yellow in several minutes. After 24 h, the reaction mixture (yellow and clear solution) was carried out thrice of cool-pump-thaw to remove the xylene and the residual dimethylchlorosilane. The final product was stored in Ar under -18 ℃ before use.

7.2.3 PMMA-SH, PPMA-SH and PPMA-*b*-PMMA-SH synthesized by RAFT followed by aminolysis

Thiol-terminated polymers, here including PMMA-SH, PPMA-SH and PMMA-b-PPMA-SH were synthesized by RAFT method followed by cleaving the dithioester end-group with hexylamine to finally get the thiol end-group. In a typical procedure (PMMA-SH), AIBN of 49 mg (0.3 mmol), PPBD (2-phenyl-2-propyl benzodithiolate) of (3 mmol) were added into a 100 ml flask with a magnetic stirrer, followed by two cycles of vacuum-flush to get argon atmosphere. 15 ml of toluene and 3 g (30 mmol) of MMA were transferred into the flask by syringe under Ar. The polymerization was carried on for 16 h at 70 ℃ before stopped by liquid N_2, precipitated into 400 ml hexane and dried under vacuum at RT. Pink powder of 2.0 g product PMMA, with conversion of 67 wt%, was obtained and with repeating units of n=18 from NMR.

The dithioester end-group of PMMA was reduced into thiol end-group by hexylamine with molar ratio of dithioester/hexyamine = 1/1.5 (0.9 g PMMA with 0.05 g hexyamine into 5 ml THF) under Ar at RT. The red color changed into orange in 15 min and finally became yellow-orange in 2 h. The reaction was carried out overnight to make sure a complete reduction, followed by precipitated into hexane and dried over vacuum at RT. The final product, PMMA-SH, colorless powder, was confirmed from NMR.

Thiol-terminated block copolymers with group were prepared in a similar procedure but the first-synthesized PMMA was used as macro-CTA.

7.2.4 AuNPs synthesized by Brust-Schiffrin method

The stabilizing agent used in this method included $CH_3(CH_2)_{10}CH_2$-SH (noted as C12-SH),

$CF_3(CF_2)_5CH_2CH_2$-SH (noted as F6C2-SH) and $CH_3O(CH_2CH_2O)_6CH_2CH_2$-SH (noted as PEO-SH)

The AuNPs were prepared by Brust-Schiffrin method in separated toluene layer. In a typical procedure for Au18, 3 ml of 30 mM aqueous solution of $HAuCl_4$ was added to 8 ml of 50 mM TOAB in toluene under vigorous stirring for 0.5 h until all $AuCl_4^-$ transferred to the organic layer (aqueous layer became colorless). The organic phase was separated and followed by adding 18 mg (0.09 mmol) dodecanethiol and with further stirring for 0.5 h. Freshly prepared 2.5 ml of 0.4 M aqueous solution of $NaBH_4$ was slowly added under vigorous stirring and a characteristic color of wine-red appeared in several seconds. Finally, the organic layer was separated, dialyzed against THF and finally stored under dark for further use.

7.2.5 AuNPs synthesized by one-phase procedure in THF

The stabilizing agent used in this method included P4VP-based block copolymers and thiol-terminated polymers.

When the thiol-terminated polymer ligand, prepared by RAFT, was used to stabilize AuNPs, THF was applied as solvent instead of toluene/H_2O mix solvent to avoid the phase transfer agent of TOAB, which is a competitive ligand with thiol-terminated polymer. In a typical procedure (Au55F), 8 mg of $HAuCl_4$ in 4 ml dry THF (bright green) was mixed with 70 mg of PMMASH51 in 12 ml dry THF. The mixed solution was further stirred for 2 h (without obvious color change but less bright) followed by adding reducing agent of 10 mg triethylsilane. Red color appeared after ~10 min. (for Au55G, the color changed into light brown after 40 min and finally brown in 10 more min; for Au55H and Au55I, the color immediately changed into old wine-red, details see the result and discussion). The reaction was stopped by adding the AuNP solution into 50 ml of fresh THF and stirred overnight. The free polymers were purified by membrane (cut-off 14000) dialysis against THF for over 4 times and over 24 h for each time.

The purified AuNPs was analyzed by DLS, UV-Vis, TEM and TGA and used in the block copolymer thin films.

7.2.6 Preparation of BCP/AuNP hybrid thin films

The thin films were prepared by dip-coating method. The BCPs were dissolved in THF and incorporated with AuNPs colloids in THF followed by stirring for over 2 h to get final BCP/AuNP solution with polymer concentration of 0.5-1 wt% and different content of AuNPs. The as-prepared homogeneous solutions were dip-coated onto silica wafer with different pull-

out speed from 0.5–2.0 mm/s aiming to get thin films with varied thickness. The Si wafers were pre-cleaned in piranha solution at 80 ℃ for 0 .5 h, followed by thoroughly rinsing with deionized water and drying with pressurized N_2.

The vapor annealing was carried out by putting the thin films in the glass chamber with saturated THF vapor for 0.5 h and drying for over 5 h at RT before further analysis.

7.3 Analysis

Gel Permeation Chromatography (GPC) was used to analyze the molecular weight and dispersity of polymers. Measurements were performed using a Varian GPC 50plus system with ResiPore© column (PL) and refractive index (RI) detector with THF as eluent at a flow rate of 1.0 mL/min at 40 ℃. Narrow distributed PMM A samples were used as calibration.

Nuclear Magnetic Resonance (NMR) measurements were carried out on a Bruker DRX 500 NMR spectrometer at 500 MHz for ^{1}H spectra and at 125 MHz for ^{13}C spectra. Deuterated chloroform ($CDCl_3$) was used as solvent for all samples except the polymers by RAFT for which CD_2Cl_2 was used as solvent to discern the dithioester end-group. The spectra were referred to the solvent signal (δ (^{1}H) = 7.26 ppm, δ (^{13}C) = 77.0 ppm for $CDCl_3$; δ (^{1}H) = 5.31 ppm, δ (^{13}C) = 53.7 ppm for CD_2Cl_2.

Transmission Electron Microscopy (TEM) images in different magnifications were obtained with in Libra200 TEM (Carl Zeiss Microscopy GmbH, Oberkochen, Germany) at an acceleration voltage of 200kV. The AuNPs solution in THF was drop-casted on the carbon-coated copper grids (Type S160-4, Plano GmbH, Germany) and dried over 2 h at RT before investigation.

For BCP/AuNP hybrid thin films, to obtain top-view TEM images, the specimens were first coated with 20 nm amorphous carbon film (SCD 500 Sputter Coater, Leica Microsystems GmbH, Wetzlar, Germany). The thin films were then detached from the silicon substrate in 1M NaOH. The detached films were picked up onto holey-carbon TEM grid (Type S147-3, Plano GmbH, Wetzlar, Germany) and investigated in Libra200 TEM with a use of energy filter (zero-loss imaging).To obtain cross-sectional TEM images, the thin films were coated with a platinum layer after a carbon layer. A lamella of ~80 nm was cut for cross-sectional TEM.

Scanning Electron Microscopy (SEM) were used to analysis the thin film nanostructures. The specimens for SEM were stained in RuO_4 gas for 30 min and coated with 20 nm amorphous carbon film followed by coating with 30 nm platinum film. The specimens were then investigated at 5.00 kV in NEON 40 SEM (Carl Zeiss Microscopy GmbH, Oberkochen, Germany) using a SE2 detector. Lower acceleration voltage (EHT) of 3.00 or 1.00 kV and the detector of InLens or ESB were used to get further images.

Ellipsometry was used to determine the thickness of the polymer thin films by an SE400

ellipsometer (SENTECH Instruments GmbH, Germany) with a 632.8 nm laser at a 70° incident angle.

Height and phase images of the thin films were recorded simultaneously by **Atomic Force Microscopy (AFM)** with Nanoscope III Dimension 3100 (Veeco) in tapping mode. Silicon cantilevers (BudgetSensors Multi75) with spring constant of 4 N/m and tip radius below 10 nm were used. The scan conditions (scan rate < 1 Hz, target amplitude ~4 V, peak offset 0 %, proportional gain > 3, integral gain ~10 % of proportional gain) were chosen to get viscoelasticity contrast in the phase image according to Magonov[220]. Bright regions in the phase image have higher stiffness than dark areas. To further investigate the AuNP location in the thin film, a conductive tip was applied to get electrical force microscopy (EFM). The scan conditions were set as that in the previous tapping mode to get a good height and phase image and then scanned the surface in Lift Mode (with scanning parameters of Anolog 2 (applied voltage on the tip) ~-10 V, lift start height ~100 nm, lift scan height ~100 nm) to get information about the variations in the electric field gradient above the sample in the form of height and phase images. Here the brighter area indicated a higher electrical field for a smooth sample without large differences in topography (sharp points on the surface also contribute the field gradient).

Characterization of BCP phase separation in bulk was performed by **temperature-dependent small-angle X-ray measurements (T-SAXS)** at beamline A2 (HASYLAB, DESY Hamburg). The 1D pattern was recorded by a linear detector within a scattering range of 5–90 nm, based on calibrations with silver behenate and rat tail collagen (the accuracy of *d*-values higher as ~60 nm is limited).

Grazing-incidence small-angle X-ray scattering experiments (GISAXS) of the thin films at RT were performed at beamline BW4 (HASYLAB at DESY Hamburg). 2D patterns were recorded by a MARCCD detector in the incidence angle at range of (0.03…0.30°), close to critical angles α_c of the polymer film (e.g., for pure PMMA and λ = 0.138 nm: α_c = 0.148°) and of the substrate (SiOx, α_c = 0.20°).

List of abbreviation and symbols

⊥	Microdomain perpendicular to the substrate
═	Microdomain parallel to the substrate
α	Incident angle
γ	Surface energy
δ	Chemical shift
χ	Flory-Huggins segmental interaction parameter
$\mathbf{a_{hex}}$	Length (a-axis) of the hexagonal cell
$\mathbf{d_{(100)}}$	d-Value of the first observable reflection
$\mathbf{h_{film}}$	Thickness of the thin film
n	Degree of polymerization of the second block
m	Degree of polymerization of the first block
AFM	Atomic Force Microscopy
AuNP	Gold nanopaticle
BCP	Block copolymer
BSM	Brust-Schiffrin method
CTA	Chain transfer agent
Đ	Dispersity of polymers
DFT	Density Functional Theory
DLS	Dynamic Light Scattering
FFT	Fast Fourier Transition
GC-MS	Gas Chromatography coupled with Mass Spectroscopy
GISAXS	Grazing-Incidence Small Angle X-ray Scattering
GPC	Gel Permeation Chromatography
HRTEM	High-Resolution Transmission Electron Microscopy
L	Lateral distance of thin film with NPs
$\mathbf{L_0}$	Lateral distance of thin film without NPs

LAP	Living Anionic Polymerization
M_n	Number averaged molecular weight
M_w	Weight averaged molecular weight
MMA	Methyl methacrylate
MW	Molecular Weight
N_{BCP}	Degree of polymerization of block copolymer
N_H	Degree of polymerization of homopolymer
NP	Nanoparticle
NMR	Nuclear Magnetic Resonance
P4VP	Poly(4-vinyl pyridine)
PMA	n-Pentyl methacrylate
PMMA	Poly(methyl methacrylate)
PPMA	Poly(n-pentyl methacrylate)
PPMA-*b*-PMMA	Poly(n-pentyl methacrylate)-*block*-Poly(methyl methacrylate)
PSt	Polystyrene
PSt-*b*-PMMA	Polystyrene-*block*-poly(methyl methacrylate)
PSt-*b*-P2VP	Polystyrene-*block*-poly(2-vinyl pyridine)
PtBA	Poly(tert-butyl acrylate)
R_h	Hydrodynamic radius
RAFT	Reversible Addition-Fragmentation Chain Transfer
RT	Room Temperature
SAXS	Small Angle X-ray Scattering
SCFT	Self-Consistent Field Theory
SCS	Dithioester group, -S-(C=S)-
SEM	Scanning Electron Microscopy
SFM	Scanning Force Microscopy
SPR	Surface Plasmon Resonance
St	Styrene

TDSBS	tert-Butyldimethylsilyl 3-bromopropyl sulfide
TDSCS	tert-Butyldimethylsilyl 3-chloropropyl sulfide
TEM	Transmission Electron Microscopy
TGA	Thermal Gravimetric Analysis
T_{ODT}	Order-disorder transition temperature
T-SAXS	Temperature-dependent Small Angle X-ray Scattering
TSCSPS	tert-Butyldimethylsilyl 3-(chlorodimethylsilyl)propyl sulfide
UV-Vis	Ultraviolet-Visible spectroscopy

References

[1] M. Templin, A. Franck, A. D. Chesne, H. Leist, Y. Zhang, R. Ulrich, V. Schädler, and U. Wiesner. Organically modified aluminosilicate mesostructures from block copolymer phases. Science 1997, 278, 1795–1798.

[2] M. R. Bockstaller, Y. Lapetnikov, S. Margel, and E. L. Thomas. Size-selective organization of enthalpic compatibilized nanocrystals in ternary block copolymer/particle mixtures. J. Am. Chem. Soc. 2003, 125, 5276–5277.

[3] M. R. Bockstaller, R. A. Mickiewicz, and E. L. Thomas. Block copolymer nanocomposites: perspectives for tailored functional materials. Adv. Mater. 2005, 17, 1331–1349.

[4] B. J. Kim, J. J. Chiu, G. R. Yi, D. J. Pine, and E. J. Kramer. Nanoparticle-induced phase transitions in diblock-copolymer films. Adv. Mater. 2005, 17, 2618–2622.

[5] Y. Lin, A. Böker, J. He, K. Sill, H. Xiang, C. Abetz, X. Li, J. Wang, T. Emrick, S. Long, Q. Wang, A. Balazs, and T. P. Russell. Self-directed self-assembly of nanoparticle/copolymer mixtures. Nature 2005, 434, 55–59.

[6] F. S. Bates. Polymer-polymer phase behavior. Science 1991, 251, 898–905.

[7] H. L. Hsieh. Kinetics of polymerization of butadiene, isoprene, and styrene with alkyllithiums. Part II. Rate of initiation. J. Polym. Sci. A Polym. Chem. 1965, 3, 163–172.

[8] A. Hirao and M. Hayashi. Recent advance in syntheses and applications of well-defined end-functionalized polymers by means of anionic living polymerization. Acta Polym. 1999, 50, 219–231.

[9] M. Tohyama, A. Hirao, S. Nakahama, and K. Takenaka. Synthesis of end-functionalized polymer by means of living anionic polymerization, 5[a)] Syntheses of polystyrenes and polyisoprenes with hydroxyl and mercapto end groups by reactions of the living polymers with haloalkanes containing silyl ether and silyl thioether functions. Macromol. Chem. Phys. 1996, 197, 3135–3148.

[10] M. C. Daniel and D. Astruc. Gold nanoparticles assembly, supramolecular chemistry, quantum-size-related properties, and applications toward biology, catalysis, and nanotechnology. Chem. Rev. 2004, 104, 293–346.

[11] G. J. Hutchings, M. Brust, and H. Schmidbaur. Gold-an introductory perspective. Chem. Soc. Rev. 2008, 37, 1759–1765.

[12] B. J. Kim, J. Bang, C. J. Hawker, and E. J. Kramer. Effect of areal chain density on the location of polymer-modified gold nanoparticles in a block copolymer template. Macromolecules 2006, 39, 4108–4114.

[13] B. J. Kim, G. H. Fredrickson, and E. J. Kramer. Effect of polymer ligand molecular weight on polymer-coated nanoparticle location in block copolymers. Macromolecules 2008, 41, 436–447.

[14] B. J. Kim, J. Bang, C. J. Hawker, J. J. Chiu, D. J. Pine, S. G. Jang, S.-M. Yang, and E. J. Kramer. Creating surfactant nanoparticles for block copolymer composites through surface chemistry. Langmuir 2007, 23, 12693–12703.

[15] M. R. Bockstaller, Y. Lapetnikov, S. Margel, and E. L. Thomas. Size-selective organization of enthalpic compatibilized nanocrystals in ternary block copolymer/particle mixtures. J. Am. Chem. Soc. 2003, 125, 5276–5277.

[16] R. J. Spontak, R. Shankar, M. K. Bowman, A. S. Krishnan, M. W. Hamersky, J. Samseth, M. R. Bockstaller, and K. Ø. Rasmussen. Selectivity- and size-induced segregation of molecular and nanoscale species in microphase-ordered triblock copolymers. Nano Lett. 2006, 6, 2115–2120.

[17] M. Brust, M. Walker, D. Bethell, D. J. Schiffrin, and R. J. Whyman. Synthesis of thiol-derivatised gold nanoparticles in a two-phase liquid-liquid system. J. Chem. Soc., Chem. Commun. 1994, 801–802.

[18] M. Yoo, S. Kim, S. G. Jang, S.-H. Choi, H. Yang, E. J. Kramer, W. B. Lee, B. J. Kim, and J. Bang. Controlling the orientation of block copolymer thin films using thermally-stable gold nanoparticles with tuned surface chemistry. Macromolecules 2011, 44, 9356–9365.

[19] M. Komura and T. Iyoda. AFM cross-sectional imaging of perpendicularly oriented nanocylinder sructures of microphase-separated block copolymer films by crystal-like cleavage. Macromolecules 2007, 40, 4106–4108.

[20] J. R. Levine, J. B. Cohen, Y. W. Chung, and P. Georgopoulos. Grazing-incidence small-angle X-ray scattering: new tool for studying thin film growth. J. Appl. Cryst. 1989, 22, 528–532.

[21] D.-M. Smilgies, P. Busch, D. Posselt, and C. M. Papadakis. Characterization of polymer thin films with small-angle X-ray scattering under grazing incidence (GISAXS). Synchrotron Radiation News, 2002, 15, 35–41.

[22] J. Y. Wang, S. Park, and T. P. Russell. Chapter 1 Block copolymer thin films. Polymer thin films, O. K. C. Tsui and T. P. Russell edited. Published by World Scientific Publishing Co. Pte. Ltd.

[23] J. N. L. Albert and T. H. Epps III. Self-assembly of block copolymer thin films. Materialtoday 2010, 13, 24–33.

[24] S. H. Kim, M. J. Misner, T. Xu, M. Kimura, and T. P. Russell. Highly oriented and ordered arrays from block copolymers via solvent evaporation. Adv. Mater. 2004, 16, 226–231.

[25] R. B. Thompson, V. V. Ginzburg, M. W. Matsen, and A. C. Balazs. Predicting the mesophases of copolymer-nanoparticle composites. Science 2001, 292, 2469–2472.

[26] J. Y. Lee, Z. Y. Shou, and A. C. Balazs. Predicting the morphologies of confined copolymer/nanoparticle mixtures. Macromolecules 2003, 36, 7730–7739.

[27] V. Pryamitsyn and V. Ganesan. Strong segregation theory of block copolymer-nanoparticle. Macromolecules 2006, 39, 8499–8510.

[28] S. C. Park, B. J. Kim, C. J. Hawker, E. J. Kramer, J. Bang, and J. S. Ha. Controlled ordering of block copolymer thin films by the addition of hydrophilic nanoparticles. Macromolecules 2007, 40, 8119–8124.

[29] D. Baskaran and A. H. E. Müller. Anionic vinyl polymerization—50 years after Michael Szwarc. Prog. Polym. Sci. 2007, 32, 173–219.

[30] M. Szwarc, M. Levy, and R. Milkovich. Polymerization initiated by electron transfer to monomer. A new method of formation of block copolymers. J. Am. Chem. Soc. 1956, 78, 2656–2657.

[31] M. Szwarc. 'Living' polymers. Nature 1956, 178, 1168–1169.

[32] M. Levy and F. Cohen-Bosidan. Studies of electron transfer initiation of polymerization by pyrene and anthracene anions. Polymer 1960, 1, 517–518.

[33] H. Hsieh and A. V. Tobolsky. Polymerization of isoprene by n-butyllithium. J. Polym. Sci. 1957, 25, 245–247.

[34] H. L. Hsieh and W. H. Glaze. Kinetics of alkyllithium initiated polymerizations. Rubber Chem. Technol. 1970, 43, 22–73.

[35] H. L. Hsieh. Kinetics of polymerization of butadiene, isoprene, and styrene with alkyllithiums. Part II. Rate of initiation. J. Polym. Sci. A Polym. Chem. 1965, 3, 163–172.

[36] D. M. Wiles and S. Bywater. Polymerization of methyl methacrylate initiated by 1,1-diphenylhexyl lithium. Trans. Faraday Soc., 1965, 61, 150–158.

[37] K. Ishizu, K. Mitsutani, and T. Fukutomi. Synthesis of poly(t-butyl-methacrylate) macromonomer. J. Polym. Sci. C Polym. Lett. 1987, 25, 287–291.

[38] R. K. Graham, D. L. Dunkelberger, and W. E. Goode. Anionic copolymerization: the inability of the poly (methyl methacrylate) anion to initiate the polymerization of styrene. J. Am. Chem. Soc. 1960, 82, 400–403.

[39] T. G. Fox, B. S. Garrett, W. E. Goode, S. Gratch, J. F. Kincaid, A. Spell, and J. D. Stroupe. Crystaline polymers of monomethacrylate. J. Am. Chem. Soc. 1958, 80, 1768–1769.

[40] R. M. Fuoss. Ionic association. III. The equilibrium between ion pairs and free ions. J. Am. Chem. Soc. 1958, 80, 5059–5061.

[41] S. Winstein, E. Clippinger, A. H. Fainberg, and G. C. Robinson. Salt effects and ion-pairs in solvolysis. J. Am. Chem. Soc. 1954, 76, 2597–2598.

[42] M. Szwarc. Living polymers and mechanisms of anionic polymerization. Adv. Polym. Sci. 1983, 49, 1–177.

[43] T. Ellingsen and J. Smid. Studies of contact and solvent separated ion pairs of carbanions. VI. Conductivities and thermodynamics of dissociation of fluorenyl alkali salts in THF and DME. J. Phys. Chem. 1969, 73, 2712–2719.

[44] R. M. Fuoss and C. A. Kraus. Properties of electrolytic solutions, IV. The conductance minimum and the formation of triple ions due to the action of Coulomb forces. J. Am. Chem. Soc. 1933, 55, 2387–2399.

[45] C. Geactinov, J. Smid, and M. Szwarc. Kinetics of anionic polymerization of styrene in THF. J. Am. Chem. Soc. 1962, 84, 2508–2514.

[46] C. Carvajal, K. J. Tölle, J. Smid, and M. Szwarc. Studies of solvation phenomena of ions and ion pairs in DME and THF. J. Am. Chem. Soc. 1965, 87, 5548–5553.

[47] F. S. Dainton, G. C. East, G. A. Harpbell, N. R. Hurworth, K. J. Ivin, R. T. Laflair, R. H. Pallen, and K. M. Hui. The kinetics of anionic polymerization of styrene and a-methylstyrene. Effects of counterion and solvent. Macromol. Chem. Phys. 1965, 89, 257–262.

[48] B. J. Schmitt and G. V. Schulz. The influence of polar solvents on ions and ion pairs in the anionic polymerization of styrene. Eur. Polym. J. 1975, 11, 119–130.

[49] T. Shimomura, J. Smid, and M. Szwarc. Reactivities of contact and solvent-separated ion pairs. Anionic polymerization of styrene in dimethoxyethane. J. Am. Chem. Soc. 1967, 89, 5743–2749.

[50] M. Szwarc and A. Rembaum. Polymerization of methylmethacrylate initiated by an electron transfer to the monomer. J. Polym. Sci. 1956, 22, 189–191.

[51] D. L. Glusker, I. Lysloff, and E. Stiles. The mechanism of the anionic polymerization of methyl methacrylate. II. The use of molecular weight distribution to establish a mechanism. J. Polym. Sci. 1961, 49, 315–334.

[52] D. L. Glusker, R. A. Gallucio, and R. A. Evans. The mechanism of the anionic polymerization of methyl methacrylate III. Effects of solvents upon stereoregularity and rates in fluorenyl-lithium initiated polymerizations. J. Am. Chem. Soc. 1964, 86, 187–196.

[53] S. Krause, L. Defonso, and D. L. Glusker. Mechanism of the anionic polymerization of methyl methacrylate. IV. Calculated molecular weight distributions resulting from a reversible termination by a bimolecular exchange reaction. J. Polym. Sci. A 1965, 3, 1617–1630.

[54] K. Hatada, T. Kitayama, K. Fujikawa, K. Ohta, and H. Yuki. Polym. Studies on the anionic polymerization of methyl methacrylate with butyl-lithium using perdeuterated monomer. Bull (Berlin) 1978, 1, 103–108.

[55] F. J. Gerner, H. Höcker, A. H. E. Müller, and G. V. Schulz. On the termination reaction in the anionic polymerization of methyl methacrylate in polar solvents. 1. Kinetic studies. Eur. Polym. J. 1984, 20, 349–355.

[56] B. A. Feit. Anionic oligomerization of acrylic esters. Eur. Polym. J. 1967, 3, 523–534.

[57] W. K. Busfield and J. M. Methven. Anionic polymerization of methyl acrylate. Polymer

1973, 14, 137–144.

[58] S. Bywater. Kinetic studies and reaction mechanisms in homogeneous anionic polymerization. Pure Appl. Chem. 1962, 4, 319–332.

[59] D. M. Wiles and S. Bywater. Polymerization of methyl methacrylate initiated by 1.1-diphenyl-hexyl-lithium. Trans. Faraday Soc. 1965, 61, 150–158.

[60] B. C. Anderson, G. D. Andrews, P. Arthur Jr,, H, W. Jacobson, L. R. Melby, A. J. Playtis, and W. H. Sharkey. Anionic polymerization of methacrylates. Novel functional polymers and copolymers. Macromolecules 1981, 14, 1599–1601.

[61] H. L. Hsieh and R. P. Quirk. Anionic polymerization: principles and practical applications. Marcel Dekker, New York, 1996.

[62] S. M. Ptacek. Funktionalisierte Alkylmethacrylat-Blockcopolymere als Template zur Darstellung geordneter Silica-Strukturen. Dissertation 2009.

[63] W. S. Matthews, J. E. Bares, J. E. Bartmess, F. G. Bordwell, F. J. Cornforth, G. E. Drucker, Z. Margolin, R. J. McCallum, G. J. McCollum, and N. R. Vanier. Equilibrium acidities of carbon acids. VI. Establishment of an absolute scale of acidities in dimethyl sulfoxide solution. J. Am. Chem. Soc. 1975, 97, 7006–7014.

[64] F. G. Bordwell. Equilibrium acidities in dimethyl sulfoxide solution. Acc. Chem. Res. 1988, 21, 456–463.

[65] F. G. Bordwell and H. E. Fried. Acidities of the H-C protons in carboxylic esters, amides, and nitriles. J. Org. Chem. 1981, 46, 4327–4331.

[66] C. Eaborn and W. Stancyk, Base cleavage of R-Si bonds of silanols $RSiMe_2OH$. A proposed new mechanism of substitution at silicon. J. Chem. Soc., Perkin Trans. 2 1984, 12, 2099–2103.

[67] G. Löhr and G. V. Schulz. Kinetics of anionic polymerization of methyl methacrylate with caesium and sodium as counterions in THF. Eur. Polym. J. 1974, 10, 121–130.

[68] H. Jeuck and A. H. E. Müller. Kinetics of the anionic polymerization of methyl methacrylate in tetrahydrofuran using lithium and potassium as counterions. Makromol. Chem., Rapid Commun. 1982, 3, 121–125.

[69] R. Kraft, A. H. E. Müller, H. Höcker, and G. V. Schulz. Kinetics of anionic polymerization of methyl methacrylate in 1, 2-dimethoxyethane. Makromol. Chem., Rapid Commun. 1980, 1, 363–368.

[70] C. B. Tsvetanov, A. H. E. Müller, and G. V. Schulz. Dependence of the propagation rate constants on the degree of polymerization in the initial stage of the anionic polymerization of methyl methacrylate in tetrahydrofuran. Macromolecules 1985, 18, 863–868.

[71] D. Kunkel, A. H. E. Müller, L. Lochmann, and M. Janata. The role of association/complexation equlibria in the anionic polymerization of (meth)acrylates. Makromol. Chem., Macromol Symp. 1992, 60, 315–326.

[72] G. Litvinenko and A. H. E. Müller. General kinetic analysis and comparison of MWD's for various mechanisms of activity exchange in living polymerizations. Macromolecules 1997, 30, 1253–1266.

[73] R. Fayt, R. Forte, C. Jacobs, R. Jerome, T. Ouhadi, Ph. Teyssie, and S. K. Varshney. New initiator system for the ''living'' anionic polymerization of tert-alkyl acrylates. Macromolecules 1987, 20, 1442–1444.

[74] R. P. Quirk and D. L. Pickel. Macromolecular architectures and soft nano-objects. 6.10 – Controlled end-group functionalization (including telechelics). Polym. Sci.: Compreh. Refer. 2012, 6, 351–412.

[75] J. Jagur-Grodzinski. Functional polymers by living anionic polymerization. J. Polym. Sci. A Polym. Chem. 2002, 40, 2116–2133.

[76] R. P. Quirk, T. Yoo, Y. Lee, J. Kima, and B. Lee. Applications of 1,1-diphenylethylene chemistry in anionic synthesis of polymers with controlled structures. Adv. Polym. Sci. 2000, 153, 67–162.

[77] R. P. Quirk, S. H. Jang, and J. Kim. Recent advances in anionic synthesis of functionalized elastomers using functionalized alkyllithium initiators. Rubb. Chem. Technol. 1996, 69, 444–461.

[78] A. Takano, T. Furutani, and Y. Isono. Preparation of a polystyrene macromonomer with a novel anionic initiator containing an olefinic vinyl group. Macromolecules 1994, 27, 7914–7916.

[79] A. Touris, J. W. Mays, and N. Hadjichristidis. Acetylene-functionalized lithium initiators for anionic polymerization. powerful precursors for "click" chemistry. Macromolecules 2011, 44, 1886–1893.

[80] R. P. Quirk, R. T. Mathers, C. Wesdemiotis, and M. A. Arnould. Investigation of ethylene oxide oligomerization during functionalization of poly(styryl)lithium using MALDI-TOF MS and NMR. Macromolecules 2002, 35, 2912–2918.

[81] R. P. Quirk and G. M. Lizárraga. Investigation of the reaction of poly(styryl)lithium with propylene oxide. Macromolecules 1998, 31, 3424–3430.

[82] R. P. Quirk, Q. Ge, M. A. Arnould, and C. Wesdemiotis. Functionalization of poly(styryllithium) with 1-butene oxide. Macromol. Chem. Phys. 2001, 202, 1761–1767.

[83] F. G. Bordwell, H. M. Andersen, and B. M. Pitt. The reaction of thiacyclopropanes (olefin sulfides) and thiacyclobutanes with organolithium compounds. J. Am. Chem. Soc. 1954, 76, 1082–1085.

[84] R. P. Quirk, M. Ocampo, M. J. Polce, and C. Wesdemiotis. Functionalization of poly(styryl)lithium with thiiranes sulfur extrusion vs ring-opening mechanisms. Macromolecules 2007, 40, 2352–2360.

[85] S. Nakahama and A. Hirao. Protection and polymerization of functional monomers-Anionic

living polymerization of protected monomers. Prog. Polym. Sci. 1990, 15, 299–335.

[86] M. A. Peters, A. M. Belu, R. W. Linton, L. Dupray, T. J. Meyer, and J. M. DeSimone. Termination of living anionic polymerizations using chlorosilane derivatives: a general synthetic methodology for the synthesis of end-functionalized polymers. J. Am. Chem. Soc. 1995, 117, 3380-3388.

[87] A. R. Luxton, A. Quig, M. -J. Delvaux, and L. J. Fetters. Star-branched polymers: 2. linking reaction involving 2- and 4-vinyl pyridine and dienyland styryllithium chain ends. Polymer 1978, 19, 1320–1324.

[88] M. Tardi and P. Sigwalt. Etude de la nature des especes ioniques intervenant au cours de la polymerisation anionique de la vinyl-4 pyridine. Eur. Polym. J. 1973, 9, 1369–1379.

[89] S. K. Varshney, X. F. Zhong, and A. Eisenberg. Anionic homopolymerization and block copolymerization of 4-vinylpyridine and its investigation by high-temperature size-exclusion chromatography in N-methyl-2-pyrrolidinone. Macromolecules 1993, 26, 701–706.

[90] S. Creutz, P. Teyssié, and R. Jérôme. Living anionic homopolymerization and block copolymerization of 4-vinylpyridine at “elevated” temperature and its characterization by size exclusion chromatography. Macromolecules, 1997, 30, 1–5.

[91] G. Huynh-Ba and J. E. McGrath. Pyridine-mediated anionic homo- and copolymerization of alkylmethacrylate. Recent advances in anionic polymerization, T. Hogen-Esch and J. Smid edited. New York, Elsevier, 1987, 173–184.

[92] K. Arai, T. Kotaka, Y. Kitano, and K. Yoshimura. Synthesis and morphological behavior of a new ABC three-block polymer. Macromolecules 1980, 13, 457–459.

[93] I. Kudose and T. Kotaka. Morphological and viscoelastic properties of poly(styrene-b-butadiene-b-4-vinylpyridine) three-block polymers of the ABC type. Macromolecules 1984, 17, 2325–2332.

[94] S. Creutz, P. Teyssié, and R. Jérôme. Anionic block copolymerization of 4-vinylpyridine and tert-butyl methacrylate at “elevated” temperatures: influence of various additives on the molecular parameters. Macromolecules 1997, 30, 5596–5601.

[95] K. Arai, T. Kotaka, Y. Kitano, and K. Yoshimura. Poly(styrene-b-butadiene-b-4-vinylpyridine) three-block polymers. synthesis, characterization, morphology, and mechanical properties. Macromolecules 1980, 13, 1670–1678.

[96] H. J. Mencer and Z. Grubisic-Gallot. Influence of solvent polarity on elution volume in the case of polar polymers. J. Liq. Chromatogr. 1979, 2, 649–662.

[97] J. Pan, M. Chen, W. Warner, M. He, L. Dalton, and T. E. Hogen-Esch. Synthesis of block copolymers containing a main chain polymeric NLO Segment. Macromolecules 2000, 33, 4673–4681.

[98] S. H. Han, D. H. Lee, and J. K. Kim. Phase behavior of poly(2-vinylpyridine)-block-poly(4-vinylpyridine) copolymers. Macromolecules 2007, 40, 7416–7419.

[99] J. Chiefari, Y. K. Chong, F. Ercole, J. Krstina, J. Jeffrey, T. P. T. Le, R. T. A. Mayadunne, G. F. Meijs, C. L. Moad, G. Moad, E. Rizzardo, and S. H. Thang. Living free-radical polymerization by reversible addition-fragmentation chain transfer: the RAFT process. Macromolecules 1998, 31, 5559–5562.

[100] G. Moad, E. Rizzardo, and S. H. Thang. Living radical polymerization by the RAFT process. Aust. J. Chem. 2005, 58, 379–410.

[101] G. Moad, E. Rizzardo, and S. H. Thang. Living radical polymerization by the RAFT process-a first update. Aust. J. Chem. 2006, 59, 669–692.

[102] G. Moad, E. Rizzardo, and S. H. Thang. Living radical polymerization by the RAFT process-a second update. Aust. J. Chem. 2009, 62, 1402–1472.

[103] G. Moad, E. Rizzardo, and S. H. Thang. Chapter 6 Fundamentals of RAFT polymerization. Fundamentals of Controlled/Living Radical Polymerization, B. Z. Tang, N. V. Tsarevsky, and B. S. Sumerlin edited, 2013.

[104] A. B. Lowe. Chapter 2 End-group functionalization of RAFT-prepared polymers using thiol-X chemistries. Thiol-X chemistries in polymer and materials science, A. Lowe and C. Bowman edited, 2013.

[105] M. A. Harvison, P. J. Roth, T. P. Davis, and A. B. Lowe. End group reactions of RAFT-prepared (co)polymers. Aust. J. Chem. 2011, 64, 992–1006.

[106] M. Deletre and G. Levesque. Kinetics and mechanism of polythioamidation in solution. 1. Reaction of mono- and bis(dithioester)s with excess amine. Macromolecules 1990, 23, 4733–4741.

[107] G. Moad, E. Rizzardo, and S. H. Thang. End-functional polymers, thiocarbonylthio group removal/transformation and reversible addition fragmentation chain transfer (RAFT) polymerization. Polym. Int. 2011, 60, 9–25.

[108] W. Shen, Q. Qiu, Y. Wang, M. Miao, B. Li, T. Zhang, A. Cao, and Z. An. Hydrazine as a nucleophile and antioxidant for fast aminolysis of RAFT Polymers in Air. Macromol. Rapid Commun. 2010, 31, 1444–1448.

[109] J. Turkevitch, P. C. Stevenson, and J. Hillier. Nucleation and growth process in the synthesis of colloidal gold. Discuss. Faraday Soc. 1951, 11, 55–75.

[110] G. Frens. Controlled nucleation for the regulation of the particle size in monodisperse gold suspensions. Nature: Phys. Sci. 1973, 241, 20–22.

[111] G. Schmid, R. Pfeil, R. Boese, F. Bandermann, S. Meyer, G. H. M. Calis, and J. W. A. van der Velden. $[Au_{55}[P(C_6H_5)_3]_{12}Cl_6]$ – A gold cluster of unusual size. Chem. Ber. 1981, 114, 3634–3642.

[112] M. Giersig and P. Mulvaney. Preparation of ordered colloid monolayers by electrophoretic deposition. Langmuir 1993, 9, 3408–3413.

[113] M. Brust, J. Fink, D. Bethell, D. J. Schiffrin, and C. Kiely. Synthesize and reaction of

functionalised gold nanoparticles. J. Chem. Soc., Chem. Commun. 1995, 1655–1656.

[114] M. M. Alvarez, J. T. Khoury, T. G. Schaaff, M. Shafigullin, I. Vezmar, and R. L. Whetten. Critical sizes in the growth of Au clusters. Chem. Phys. Lett. 1997, 266, 91–98.

[115] A. G. Kanaras, F. S. Kamounah, K. Schaumburg, C. J. Kiely, and M. Brust. Thioalkylated tetraethylene glycol – a new ligand for water soluble monolayer protected gold clusters. Chem. Commun. 2002, 2294–2295.

[116] I. Hussain, S. Graham, Z. Wang, B. Tan, D. C. Sherrington, S. P. Rannard, A. I. Cooper, and M. Brust. Size-controlled synthesis of near-monodisperse gold nanoparticles in the 1−4 nm range using polymeric stabilizers. J. Am. Chem. Soc. 2005, 127, 16398–16399.

[117] I. Hussain, Z. Wang, A. I. Cooper, and M. Brust. Formation of spherical nanostructures by the controlled aggregation of gold colloids. Langmuir 2006, 22, 2938–2941.

[118] Z. Wang, B. Tan, I. Hussain, N. Schaeffer, M. F. Wyatt, M. Brust, and A. I. Cooper. Design of polymeric stabilizers for size-controlled synthesis of monodisperse gold nanoparticles in water. Langmuir 2007, 23, 885–895.

[119] E. Boisselier and D. Astruc. Gold nanoparticles in nanomedicine: preparations, imaging, diagnostics, therapies and toxicity. Astruc. Chem. Soc. Rev. 2009, 38, 1759–1782.

[120] R. Sardar, A. M. Funston, P. Mulvaney, and R. W. Murray. Gold nanoparticles: past, present, and future. Langmuir 2009, 25, 13840–13851.

[121] R. Jin. Quantum sized, thiolate-protected gold nanoclusters. Nanoscale, 2010, 2, 343–362.

[122] X. Huang, B. Li, H. Zhang, I. Hussain, L. Lianga, and B. Tan. Facile preparation of size-controlled gold nanoparticles using versatile and end-functionalized thioether polymer ligands. Nanoscale 2011, 3, 1600–1607.

[123] M. Brust, N. Stuhr-Hansen, K. Norgaard, J. B. Christensen, L. K. Nielsen, and T. Bjornholm. Langmuir−blodgett films of alkane chalcogenide (S, Se, Te) stabilized gold nanoparticles. Nano Lett. 2001, 1, 189–191.

[124] C. K. Yee, A. Ulman, J. D. Ruiz, A. Parikh, H. White, and M. Rafailovich. Alkyl selenide- and alkyl thiolate-functionalized gold nanoparticles: Chain packing and bond nature. Langmuir, 2003, 19, 9450–9458.

[125] B. S. Zelakiewicz, T. Yonezawa, and Y. Y. Tong. Observation of selenium-77 nuclear magnetic resonance in octaneselenol-protected gold nanoparticles. J. Am. Chem. Soc. 2004, 126, 8112–8113.

[126] P. J. G. Goulet and R. B. Lennox. New insights into Brust−Schiffrin metal nanoparticle synthesis. J. Am. Chem. Soc. 2010, 132, 9582–9584.

[127] R. G. Nuzzo, F. A. Fusco, and D. L. Allara. Spontaneously organized molecular assemblies. 3. Preparation and properties of solution adsorbed monolayers of organic disulfides on gold surfaces. J. Am. Chem. Soc. 1987, 109, 2358–2368.

[128] C. D. Bain, E. B. Troughton, Y. T. Tao, J. Evall, G. M. Whitesides, and R. G. Nuzzo. Formation of monolayer films by the spontaneous assembly of organic thiols from solution onto gold. J. Am. Chem. Soc. 1989, 111, 321–335.

[129] C. D. Bain, H. A. Biebuyck, and G. M. Whitesides. Comparison of self-assembled monolayers on gold: coadsorption of thiols and disulfides. Langmuir 1989, 5, 723–727.

[130] P. Ionita, A. Caragheorgheopol, B. C. Gilbert, and V. Chechik. EPR Study of a place-exchange reaction on Au nanoparticles: two branches of a disulfide molecule do not adsorb adjacent to each other. J. Am. Chem. Soc. 2002, 124, 9048–9049.

[131] Y. Li, O. Zaluzhna, B. Xu, Y. Gao, J. M. Modest, and Y. Y. J. Tong. Mechanistic insights into the Brust-Schiffrin two-phase synthesis of organo-chalcogenate-protected metal nanoparticles. J. Am. Chem. Soc. 2011, 133, 2092–2095.

[132] Y. Li, O. Zaluzhna, and Y. Y. J. Tong. Identification of a source of size polydispersity and its solution in Brust–Schiffrin metal nanoparticle synthesis. Chem. Commun. 2011, 47, 6033–6035.

[133] C. K. Yee, R. Jordan, A. Ulman, H. White, A. King, M. Rafailovich, and J. Sokolov. Novel one-phase synthesis of thiol-functionalized gold, palladium, and iridium nanoparticles using superhydride. Langmuir 1999, 15, 3486–3491.

[134] M. K. Corbierre, N. S. Cameron, M. Sutton, S. G. J. Mochrie, L. B. Lurio, A. Rühm, and R. B. Lennox. Polymer-stabilized gold nanoparticles and their incorporation into polymer matrices. J. Am. Chem. Soc. 2001, 123, 10411–10412.

[135] A. B. Lowe, B. S. Sumerlin, M. S. Donovan, and C. L. McCormick. Facile preparation of transition metal nanoparticles stabilized by well-defined (co)polymers synthesized via aqueous reversible addition-fragmentation chain transfer polymerization. J. Am. Chem. Soc. 2002, 124, 11562–11563.

[136] J. Shan, M. Nuopponen, H. Jiang, T. Viitala, E. Kauppinen, K. Kontturi, and H. Tenhu. Amphiphilic gold nanoparticles grafted with poly(N-isopropylacrylamide) and polystyrene. Macromolecules 2005, 38, 2918–2926.

[137] S. K. Jewrajka and U. Chatterjee. Block copolymer mediated synthesis of amphiphilic gold nanoparticles in water and an aqueous tetrahydrofuran medium: an approach for the preparation of polymer–gold nanocomposites. J. Polym. Sci. A Polym Chem. 2006, 44, 1841–1854.

[138] J. Shan, M. Nuopponen, H. Jiang, T. Viitala, E. Kauppinen, K. Kontturi, and H. Tenhu. Amphiphilic gold nanoparticles grafted with poly(N-isopropylacrylamide) and polystyrene. Macromolecules 2005, 38, 2918–2926.

[139] X. Li, H. Yang, L. Xu, X. Fu, H. Guo, and X. Zhang. Janus micelle formation induced by protonation/deprotonation of poly-(2-vinylpyridine)-block-poly(ethylene oxide) diblock copolymers. Macromol. Chem. Phys. 2010, 211, 297–302.

[140] L. Bronstein, D. Chernyshov, and P. Valetsky. Laser photolysis formation of gold colloids in block copolymer micelles. Langmuir 1999, 15, 83–91.

[141] T. Azzam, L. Bronstein, and A. Eisenberg. Water soluble surface-anchored gold and palladium nanoparticles stabilized by exchange of low molecular weight ligands with biamphiphilic triblock copolymers. Langmuir 2008, 24, 6521–6529.

[142] C. Lee, S. H. Kim, and T. P. Russell. Controlling orientation and functionalization in thin films of block copolymers. Macromol. Rapid Commun. 2009, 30, 1674–1678.

[143] W. Lee, S. Y. Lee, R. M. Briber, and Oded Rabin. Self-assembled SERS substrates with tunable surface plasmon resonances. Adv. Funct. Mater. 2011, 21, 3424–3429.

[144] Z. H. Mbhele, M. G. Salemane, C. G. C. E. van Sittert, J. M. Nedeljković, V. Djoković, and A. S. Luyt. Fabrication and characterization of silver-polyvinyl alcohol nanocomposites. Chem. Mater. 2003, 15, 5019–5024.

[145] I. Hussain, M. Brust, A. J. Papworth, and A. I. Cooper. Preparation of acrylate-stabilized gold and silver hydrosols and gold-polymer composite films. Langmuir 2003, 19, 4831–4835.

[146] J. P. Spatz, A. Roescher, and M. Moiler. Gold nanoparticks in micellar poly(styrene)-b-poly(ethylene oxide) films-size and interparticle distance control in monoparticulate films. Adv. Mater. 1996, 8, 337–340.

[147] T. Sakai and P. Alexandridis. Mechanism of gold metal ion reduction, nanoparticle growth and size control in aqueous amphiphilic block copolymer solutions at ambient conditions. J. Phys. Chem. B 2005, 109, 7766–7777.

[148] F. S. Bates and G. H. Fredrickson. Block copolymer thermodynamics: theory and experiment. Annu. Rev. Phys. Chem. 1990, 41, 525–557.

[149] I. W. Hamley. The physics of block copolymers, Oxford Univ. Press, New York, 1998.

[150] P. F. Green and R. Limary. Block copolymer thin films: pattern formation and phase behavior. Adv. Colloid Interface Sci. 2001, 94, 53–81.

[151] R. D. Peters, X. M. Yang, T. K. Kim, and P. F. Nealey. Wetting behavior of block copolymers on self-assembled films of alkylchlorosiloxanes: effect of grafting density. Langmuir 2000, 16, 9620–9626.

[152] P. H. Liu, P. Thébault, P. Guenoun, and Jean Daillant. Easy orientation of diblock copolymers on self-assembled monolayers using UV irradiation. Macromolecules 2009, 42, 9609–9612.

[153] P. Mansky, Y. Liu, E. Huang, T. P. Russell, and C. Hawker. Controlling polymer-surface interactions with random copolymer brushes. Science 1997, 275, 1458–1460.

[154] E. Han, K. O. Stuen, Y. H. La, P. F. Nealey, and P. Gopalan. Effect of composition of substrate-modifying random copolymers on the orientation of symmetric and asymmetric diblock copolymer domains. Macromolecules 2008, 41, 9090–9097.

[155] S. Ham, C. Shin, E. Kim, D. Y. Ryu, U. Jeong, T. P. Russell, and C. J. Hawker.

Microdomain orientation of PS-b-PMMA by controlled interfacial interactions. Macromolecules 2008, 41, 6431–6437.

[156] E. Han, K. O. Stuen, M. Leolukman, C. -C. Liu, P. F. Nealey, and P. Gopalan. Perpendicular orientation of domains in cylinder forming block copolymer thick films by controlled interfacial interactions. Macromolecules 2009, 42, 4896–4901.

[157] Z. Q. Lin, D. H. Kim, X. D. Wu, L. Boosahda, D. Stone, L. LaRose, and T.P. Russell. A rapid route to arrays of nanostructures in thin films. Adv. Mater. 2002, 14, 1373–1376.

[158] Y. Xuan, J. Peng, L. Cui, H. Wang, B. Li, and Y. Han. Morphology development of ultrathin symmetric diblock copolymer film via solvent vapor treatment. Macromolecules 2004, 37, 7301–7307.

[159] G. Kim and M. Libera. Morphological development in solvent-cast polystyrene-polybutadiene-polystyrene (SBS) triblock copolymer thin films. Macromolecules 1998, 31, 2569–2577.

[160] Y. S. Jung and C. A. Ross. Solvent-vapor induced tunability of self-assembled block copolymer patterns. Adv. Mater. 2009, 21, 2540–2545.

[161] A. Knoll and R. Magerle. Phase behavior in thin films of cylinder-forming ABA block copolymers: Experiments. J. Chem. Phys. 2004, 120, 1105–1116.

[162] P. F. Green and R. Limary. Block copolymer thin films: pattern formation and phase behavior. Adv. Colloid Interface Sci. 2001, 94, 53–81.

[163] B. Hamdoun, D. Ausserré, and S. Joly. Composites copolymer-nanoparticule: courbure. J. Phys. II France 1996, 6, 1207–1217.

[164] S. H. Anastasiadis, T. P. Russell, S. K. Satija, and C. F.Majkrzak. Neutron reflectivity studies of the surface-induced ordering of diblock copolymer films. Phys. Reu. Lett. 1989, 62, 1852–1855.

[165] S. H. Anastasiadis, T. P. Russell, S. K. Satija, and C. F. Majkrzak. The morphology of symmetric diblock copolymers as revealed by neutron reflectivity. J. Chem. Phys. 1990, 92, 5677–5691.

[166] A. M. Mayes, T. P. Russell, S. K. Satija, and C. F. Majkrzak. Homopolymer distributions in ordered block copolymers. Macromolecules 1992, 25, 6523–6531.

[167] K. A. Orso and P. F. Green. Phase behavior of thin film blends of block copolymers and homopolymers: changes in domain dimensions. Macromolecules 1999, 32, 1087–1092.

[168] A. M. Mayes, T. P. Russell, V. R. Deline, S. K. Satija, and C. F. Majkrzak. Block copolymer mixtures as revealed by neutron reflectivity. Macromolecules 1994, 27, 7447–7453.

[169] M. R. Bockstaller and E. L. Thomas. Proximity effects in self-organized binary particle-block copolymer blends. Phys. Rev. Lett. 2004, 93, article 166106.

[170] V. V. Ginzburg, C. Gibbons, F. Qiu, G. W. Peng, and A. C. Balazs. Modeling the dynamic

behavior of diblock copolymer-particle composites. Macromolecules 2000, 33, 6140–6147.

[171] J. Huh, V. V. Ginzburg, and A. C. Balazs. Thermodynamic behavior of particle-diblock copolymer mixtures-simulation. Macromolecules 2000, 33, 8085–8096.

[172] R. B. Thompson, V. V. Ginzburg, M. W. Matsen, and A. C. Balazs. Block copolymer-directed assembly of nanoparticles-forming mesoscopically. Macromolecules 2002, 35, 1060–1071.

[173] A. J. Schultz, C. K. Hall, and J. Genzer. Computer simulation of block copolymer/nanoparticle composites. Macromolecules 2005, 38, 3007–3016.

[174] S. W. Sides, B. J. Kim, E. J. Kramer, and G. H. Fredrickson. Hybrid particle-field simulations of polymer nanocomposites. Phys. Rev. Lett. 2006, 96, article 250601.

[175] W. A. Lopes and H. M. Jaeger. Hierarchical self-assembly of metal nanostructures on diblock copolymer scaffolds. Nature 2001, 414, 735-738.

[176] T. Thurn-Albrecht, J. Schotter, G. A. Kästle, N. Emley, T. Shibauchi, L. Krusin-Elbaum, K. Guarini, C. T. Black, M. T. Tuominen, and T. P. Russell. Ultrahigh-Density Nanowire Arrays Grown in Self-Assembled Diblock Copolymer Templates. Science 2000, 290, 2126-2129.

[177] M. Bockstaller, R. Kolb, and E. L. Thomas. Metallodielectric Photonic Crystals Based on Diblock Copolymers. Adv. Mater. 2001, 13, 1783-1786.

[178] A. C. Balazs, T. Emrick, and T. P. Russell. Nanoparticle Polymer Composites: Where Two Small Worlds Meet. Science 2006, 214, 1107-1110.

[179] O. Glatter, O. Kratky. Small angle X-ray scattering. Academic Press Inc. (London) Ltd., 1982.

[180] R. Keska. Study of the phase behavior of poly(n-alkyl methacrylate-b-methyl methacrylate) diblock copolymers and its influence on the wettability of polymer surfaces. Dissertation, 2006.

[181] P. Du, M. Li, K. Douki, X. Li, C. B. W. Garcia, A. Jain, D.-M. Smilgies, L. J. Fetters, S. M. Gruner, U. Wiesner, and C. Ober. Additive-driven phase-selective chemistry in block copolymer thin films: the convergence of top-down and bottom-up approaches. Adv. Mater. 2004, 16, 953–957.

[182] D.-M. Smilgies. http://staff.chess.cornell.edu/~smilgies/gisaxs/GISAXS.php

[183] H.-J. Butt, B. Cappella, and M. Kappl. Force measurements with the atomic force microscope: Technique, interpretation and applications. Surf. Sci. Rep. 2005, 59, 1–152.

[184] SPM training note book. Bruker Corporation, 2011.

[185] J. J. Bozzola and L. D. Russell. Electron microscopy, 2nd Edition. Jones and Bartlett Publishers, Inc., 1998.

[186] P. Champness. Electron diffraction in the transmission electron microscope. Garland Pub. 2001.

[187] M. A. Peters, A. M. Belu, R. W. Linton, L. Dupray, T. J. Meyer, and J. M. DeSimone. Termination of living anionic polymerizations using chlorosilane derivatives: a general synthetic methodology for the synthesis of end-functionalized polymers. J. Am. Chem. Soc. 1995, 117, 3380–3388.

[188] S. K. Varshney, P. Bayard, C. Jacobs, R. Jerome, R. Fayt, and P. Teyssie. Anionic polymerization of acrylic monomers. 8. Synthesis and characterization of (meth)acrylic end-functionalized polymers: macromonomers and telechelics. Macromolecules, 1992, 25, 5578–5584.

[189] R. K. Graham, D. L. Dunkelberger, and W. E. Goode. Anionic copolymerization: the inability of the poly (methyl methacrylate) anion to initiate the polymerization of styrene. J. Am. Chem. Soc. 1960, 82, 400–403.

[190] M. N. Nguyen, C. Bressy, and A. Margaillan. Synthesis of novel random and block copolymers of tert-butyldimethylsilyl methacrylate and methyl methacrylate by RAFT polymerization. Polymer 2009, 50, 3086–3094.

[191] Mylèhe Delêtre and Guy Levesque. Kinetics and mechanism of polythioamidation in solution. 1. Reaction of mono- and bis(dithioester)s with excess amine. Macromolecules 1990, 23,4733–4741.

[192] G. Capozzi and G. Modena. Oxidation of thiols. The chemistry of the thiol Group, S. Patai edited. John Wiley and Sons: London, 1974.

[193] M. C. Dalfovo, R. C. Salvarezza, and F. J. Ibañez. Improved vapor selectivity and stability of localized surface plasmon resonance with a surfactant-coated Au nanoparticles film. Anal. Chem. 2012, 84, 4886–4892.

[194] I. Hussain, S. Graham, Z. Wang, B. Tan, D. C. Sherrington, S. P. Rannard, A. I. Cooper, and M. Brust. Size-controlled synthesis of near-monodisperse gold nanoparticles in the 1−4 nm range using polymeric stabilizers. J. Am. Chem. Soc. 2005 127, 16398–16399.

[195] S. Link and M. A. El-Sayed. Size and temperature dependence of the plasmon absorption of colloidal gold nanoparticles. J. Phys. Chem. B 1999, 103, 4212–4217.

[196] W. Haiss, N. T. K. Thanh, J, Aveyard, and D. G. Fernig. Determination of size and concentration of gold nanoparticles from UV−Vis spectra. Anal. Chem. 2007, 79, 4215–4221.

[197] C. Gao, J. Vuong, Q. Zhang, Y. Liu, and Y. Yin. One-step seeded growth of Au nanoparticles with widely tunable sizes. Nanoscale, 2012, 4, 2875–2878.

[198] D. Seo, C. I. Yoo, J. C. Park, S. M. Park, S. Ryu, and H. Song. Directed surface overgrowth and morphology control of polyhedral gold nanocrystals. Angew. Chem. Int. Ed. 2008, 47, 763–767.

[199] M. Ahmed and R. Narain. Rapid synthesis of gold nanorods using a one-step photochemical strategy. Langmuir 2010, 26, 18392–18399.

[200] L. F. Zhang and A. Eisenberg. Multiple morphologies of “crew-cut” aggregates of polystyrene-b-poly(acrylic acid) block copolymers. Science 1995, 268, 1728−1731.

[201] P. Alexandridis, B. Lindman. Amphiphilic block copolymers: self-assembly and applications. Elsevier: Amsterdam, 2000.

[202] R. Vyhnalkova, A. H. E. Müller, and A. Eisenberg. Control of corona composition and morphology in aggregates of mixtures of PS-b-PAA and PS-b-P4VP diblock copolymers: effects of pH and block length. Langmuir 2014, 30, 5031−5040.

[203] M. K. Corbierre, N. S. Cameron, and R. B. Lennox. polymer-stabilized gold nanoparticles with high grafting densities. Langmuir 2004, 20, 2867–2873.

[204] S. Sakurai, H. Umeda, C. Furukawa, H. Irie, S. Nomura, H. Hyun, and J. K. Kim. Thermally induced morphological transition from lamella to gyroid in a binary blend of diblock copolymers. J. Chem. Phys. 1998, 108, 4333–4339.

[205] Y. Matsushita, H. Momose, Y. Yoshida, and I. Noda. Lamellar domain spacing of the ABB graft copolymers. Polymer, 1997, 38, 149–153.

[206] B. Lee, I. Park, J. Yoon, S. Park, J. Kim, K.-W. Kim, T. Chang, and M. Ree. Structural analysis of block copolymer thin films with grazing incidence small-angle X-ray scattering. Macromolecules 2005, 38, 4311–4323.

[207] D. Jehnichen, D. Pospiech, R. Keska, S. Ptacek, A. Janke, S. S. Funari, A. Timmann, and C. M. Papadakis. Analysis of thin nanostructured block copolymer films by GISAXS and AFM. J. Nanostruct. Polym. Nanocomp. 2008, 4, 119–128.

[208] B. J. Kim, G. H. Fredrickson, C. J. Hawker, and E. J. Kramer. Nanoparticle surfactants as a route to bicontinuous block copolymer morphologies. Langmuir 2007, 23, 7804–7809.

[209] B. J. Kim, G. H. Fredrickson, J. Bang, C. J. Hawker, and E. J. Kramer. Tailoring core-shell polymer-coated nanoparticles as block copolymer surfactants. Macromolecules 2009, 42, 6193–6201.

[210] S. G. Jang, B. J. Kim, C. J. Hawker, and E. J. Kramer. Bicontinuous block copolymer morphologies produced by interfacially active, thermally stable nanoparticles. Macromolecules 2011, 44, 9366–9373.

[211] B. J. Kim, G. H. Fredrickson, and E. J. Kramer. Effect of polymer ligand molecular weight on polymer-coated nanoparticle location in block copolymers. Macromolecules 2008, 41, 436–447.

[212] C. -C. Chang and C. -T. Lo. Effect of particles on the structure of solvent-annealed block copolymer/nanoparticle composite thin film. J. Phys. Chem. B 2011, 115, 2485–2493.

[213] J. Brandrup, E. H. Immergut, E. A. Grulke. Polymer handbook 4th edition. John Wiley and Sons, New York, 1999.

[214] Hannu Häkkinen. Atomic and electronic structure of goldclusters: understanding flakes, cages and superatoms from simple concepts. Chem. Soc. Rev. 2008, 37, 1847–1859.

[215] B. J. Kim, J. J. Chiu, G.-R. Yi, D. J. Pine, and E. J. Kramer. Nanoparticle-induced phase transitions in diblock copolymer films. Adv. Mater. 2005, 17, 2618–2622.

[216] U. Jeong, D. Y. Ryu, D. H. Kho, D. H. Lee, J. K. Kim, and T. P. Russell. Phase behavior of mixtures of block copolymer and homopolymers in thin films and bulk. Macromolecules 2003, 36, 3626–3634.

[217] A. Tercjak, J. Gutierrez, and I. Mondragon. Conductive properties of photoluminescent Au/Ps-b-PEO inorganic/organic hybrids containing nematic liquid crystals. J. Phys. Chem. C 2011, 115, 1643–1648.

[218] R. Keska, D. Pospiech, K. Eckstein, D. Jehnichen, S. Ptacek, L. Häußler, P. Friedel, A. Janke, and B. Voit. Study of the phase behaviour of Poly(pentylmethacrylate-b-methylmethacrylate) diblock copolymers. J. Nanostruct. Polym. Nanocomp. 2006, 2, 43–52.

[219] S. Werner, D. Pospiech, D. Jehnichen, K. Eckstein, H. Komber, P. Friedel, A. Janke, F. Näther, U. Reuter, B. Voit, R.Taurino, and M. Messori. Synthesis and phase-separation behavior of a,x-difunctionalized diblock copolymers. J. Polym. Sci. A Polym. Chem. 2011, 49, 926–93.

[220] S. N. Magonov, V. Elings, and M.-H. Whangbo, Phase imaging and stiffness in tapping-mode atomic force microscopy. Surf. Sci. 1997, 375, L385–L391.

Versicherung

Hiermit versichere ich, dass ich die vorliegende Arbeit ohne unzulässige Hilfe Dritter und ohne Benutzung anderer als der angegebenen Hilfsmittel angefertigt habe; die aus fremden Quellen direkt oder indirekt übernommen Gedanken sind als solche kenntlich gemacht. Die Arbeit wurde bisher weder im Inland noch im Ausland in gleicher oder ähnlicher Form einer anderen Prüfungsbehörde vorgelegt.

Die vorliegende Arbeit wurde in der Zeit von Februar 2011 bis Juni 2014 am Leibniz-Institut für Polymerforschung Dresden e.V. im Rahmen des Projektes zum Thema: “Functionalized polymethacrylate diblock copolymers as templates for gold and metal oxide nanoparticles“ unter wissenschaftlicher Betreuung von Frau Dr. habil. Doris Pospiech und Frau Prof. Brigitte Voit durchgeführt.

Frühere Promotionsverfahren haben nicht stattgefunden.

Ich erkenne die Promotionsordnung der Fakultät Mathematik und Naturwissenschaften der Technischen Universität Dresden vom 23.02.2011 in vollem Umfang an.

Guping He
Dresden, 24/07/2014